STUDY OF ATOMIC LAYER DEPOSITION: THIN FILM CONTINUITY AND TECHNIQUES TO MODULATE SURFACE REACTIVITY

A Dissertation

Presented to the Faculty of the Graduate School

of Cornell University

in Partial Fulfillment of the Requirements for the Degree of

Doctor of Philosophy

by

Wenyu Zhang

February 2016

STUDY OF ATOMIC LAYER DEPOSITION: THIN FILM CONTINUITY AND TECHNIQUES TO MODULATE SURFACE REACTIVITY

Wenyu Zhang

Cornell University 2016

Abstract

Atomic layer deposition (ALD) is a deposition technique capable of achieving highly conformal thin films, with excellent control over thin film thicknesses. With these advantages, research in ALD processes and conditions for numerous applications has increased exponentially over the last few decades. With device feature sizes decreasing every generation, and the appearance of 3D structures such as FinFET transistors, and 3DNAD devices, ALD is a promising technology to deposit conformal thin films without defects.

The focus of the work presented here is twofold. First, we discuss the use of two powerful analysis techniques: X-ray Photoelectron Spectroscopy (XPS) and Low Energy Ion Scattering Spectroscopy (LEISS). These techniques can determine growth modes of ultrathin ALD films, as well as determine, both *in situ* and *ex situ*, if these films are continuous. Second, we demonstrate the development of techniques for area-selective deposition, so that materials (either dielectrics or metals) can be deposited on a surface where film growth is desired and blocked on the surface where growth is not desired, without the use of photolithography.

We begin with an *ex situ* sputter depth profile study of commercially deposited tantalum nitride (TaN_x) thin films deposited via ALD on three different substrates (SiO_2, low- κ and Cu). We employed ex situ angle-resolved XPS (ARXPS), LEISS, and atomic force microscopy (AFM) to determine the continuity of these thin films, and by implication, the abruptness of the thin film/substrate interface. On SiO_2 and low- κ, we find similar results: both ARXPS and AFM indicate that smooth, uniform thin films are deposited, consistent with nearly layer-by-layer growth of TaN_x on these surfaces. Examination of these films using LEISS revealed that while the 10 Å TaN_x thin films are continuous, the 5 Å TaN_x thin films are not continuous and may possess on the order of ~10% exposed substrate in the form of small sub-nanometer inclusions. On Cu, the situation is quite different. The TaN_x thin films on these surfaces are not continuous, and our results point to a mixed layer of TaN_x and Cu forming during ALD. Combined, the results for ARXPS, LEISS and AFM indicate that the TaN_x thin films on Cu are not conformal, the TaN_x|Cu interface is not abrupt, and the near surface layers consist of a mixture of both TaN_x and Cu. In all cases, if one were to rely solely on results from ARXPS, the picture would be incomplete as the results from LEISS are ultimately decisive concerning thin film continuity, especially for these ultrathin ALD films.

Next, we move to the study of modulating the surface reactivity of different substrates, using both self-assembled monolayers (SAMs) as blocking layers as well as techniques that do not require the use of SAMs to modify the surface chemistry of different substrate surfaces.

First, we examined the effect of two molecules that form self-assembled monolayers (SAMs) on the subsequent growth of TaN_x by atomic layer deposition (ALD) on two

substrate surfaces, SiO_2 and Cu. The SAMs that we have investigated include two vapor phase deposited, fluorinated alkyl silanes: $Cl_3Si(CH_2)_2(CF_2)_5CF_3$ (FOTS) and $(C_2H_5O)_3Si(CH_2)_2(CF_2)_7CF_3$ (HDFTEOS). Both the SAMs themselves and the TaN_x thin films, grown using $Ta[N(CH_3)_2]_5$ and NH_3, were analyzed *ex situ* using contact angle, spectroscopic ellipsometry, x-ray photoelectron spectroscopy (XPS), and low energy ion-scattering spectroscopy (LEISS). First, we find that both SAMs on SiO_2 are nominally stable at T_s ~300 °C, the substrate temperature used for ALD, while on Cu, we find that HDFTEOS thermally desorbs, while FOTS is retained on the surface. The latter result reflects the difference in the head groups of these two molecules. We found that both SAMs strongly attenuate the ALD growth of TaN_x on SiO_2, by about a factor of 10, while on Cu, the SAMs have no effect on ALD growth. Results from LEISS and XPS are decisive in determining the nature of the mechanism of growth of TaN_x on all surfaces. Growth on SiO_2 is 2D and approximately layer-by-layer, while on the surfaces terminated by the SAMs, it nucleates at defect sites, is islanded, and is 3D. In the latter case, our results support growth of the TaN_x thin film over the SAM, with a considerable delay in formation of a continuous thin film. Growth on Cu, with or without the SAMs, is also 3D and islanded, and there is also a delay in the formation of a continuous thin film as compared to growth on SiO_2. These results highlight the power of coupling measurements from both LEISS and XPS in examinations of ultrathin films formed by ALD.

Most approaches taken to date concerning selective area growth have involved the use of masking layers consisting of photoresists or SAMs. While some success has been achieved with this approach there are a number of disadvantages intrinsic to these methods. SAMs are very difficult to form defect free, and second, and perhaps more important, these

masking layers themselves must be patterned or deposited selectively. A second approach to selective area ALD relies on intrinsic reactivity differences between exposed surfaces, which, unfortunately, may be limited to a few special cases.

Here we seek to develop a more general approach to achieving selective area growth – modulating the surface chemistry of a substrate surface without the use of SAMs. We are examining two specific approaches to the surface chemistry: (*i*) the use of adsorption reversal agents; and (*ii*) the use of molecular blocking agents. Here for a thin film precursor we examine transition metal complexes with the generic structure, $M(XR_m)_n$, where *M* is the transition metal and XR_m is the coordinating ligand. In pursuing strategy (*i*) we examine the introduction of a second species in the first half-cycle that can act as a coordinating ligand, e.g., HXR'_m, or $HXR'_{m-1}R''$, etc. In pursuing strategy (*ii*) species (*Y*) are selected that can effectively compete for adsorption sites, dependent on the composition of the substrate. Concerning strategy (*i*) we are currently investigating reactions between transition metal amido compounds [pentakis dimethylamido tantalum, $Ta[N(CH_3)_2]_5$, PDMAT and tetrakis(ethylmethylamino)zirconium ($Zr[N(CH_3)(CH_2CH_3)]_4$, TEMAZ] and a series of amines (*X* = *N*). Certain amines (concentrations) showed promise in the complete blockage of chemisorption on the metal (Cu) surface and no effect on the dielectric surface (SiO_2). For strategy (*ii*), a molecular blocking agent with the structure *HSR″* [ethanedithiol, EDT], gave encouraging results. We recognize that we are initially focusing on the first half-cycle of ALD, where demonstrating selectivity for this part of the ALD process is a necessary, but not sufficient condition for selective area growth.

Biographical Sketch

Wenyu Zhang was born in Harbin, China. He moved to Singapore at age four, and to Colorado at age sixteen. His one memory of his time in China was visiting a zoo with his grandfather, eating a corn on the cob, throwing it at an elephant and running away. After obtaining straight A's in his GCSE O levels in Singapore, Wen moved to Colorado where he graduated *cum laude* in Chemical Engineering at the University of Colorado at Boulder. Wenyu worked with Prof Will Medlin there working on using a high energy electron loss spectrometer (EELS) and temperature programed desorption (TPD). He obtained good results on the decomposition of several compounds on Pd and Pt crystals. Wen then joined Prof James Engstrom's group at Cornell for his graduate work where his studied atomic layer deposition processes with focuses on thin film continuity of ultrathin ALD films as well as exploring different techniques to modulate surface reactivity of different substrates. There he familiarized himself with powerful analysis techniques such as X-ray photoelectron spectroscopy (XPS) and low-energy ion scattering spectroscopy (LEISS). Wen is fluent in English and Chinese (Mandarin), and knows some basic German. After graduation Wenyu went on to work as a process engineer at Applied Materials in Santa Clara, CA.

Dedicated to my grandparents,

Who taught me to never give up,

no matter the circumstance…

Acknowledgements

I could have not completed this journey on my own, and there are countless people whom have helped shape the experience I have had at here at graduate school.

First, I would like to thank my advisor, Prof. Jim Engstrom. The generous feedback I received from him helped me think critically about our results, write eloquently, and countless other skills that will stay with me for the rest of my personal and professional career. My other committee members Prof. Tobias Hanrath and Prof. Darrell Schlom provided great ideas and discussion that have guided me in developing ideas for film growth kinetics.

Next, Engstrom group members, both past and present have been extremely valuable. I especially want to thank Dr. Kevin Hughes, who has guided me in my early years on the maintenance and operation of the 312 chamber, as well as many sample preparation steps. Dr. Tushar Desai and Dr. Edward Kish provided valuable insights as well. Rambert Nahm have been instrumental in several sputter depth projects, taken over operation of the 312 chamber in his first year, as well as aided in the design of the new microreactor system. There will be no doubt that his skills and attitude towards research and problem solving will be much valued wherever his career takes him. Jiun-Ruey Chen has played a great role in designing, simulating and testing the new microreactor system, as well as a new gas delivery system, coupled to our analysis chamber in 312, allowing us to do higher pressure reactions, and analyze samples without an air break. We have shared more than a handful frustrating

days/ nights/ week(end)s/ months troubleshooting the new system. I feel confident leaving the chamber in his hands. The new students Hugh Bullen and Taewon Suh are hardworking and humble, have provided great discussions on the problems Jiun-Ruey and I have faced, as well as aided Rambert on his synchrotron runs. I have no doubt they will do very well in the Engstrom Research group.

Within Cornell, I would like to recognize Cornell Nanofabrication Facility (CNF), Nanobiotechnology Center (NBTC) and Cornell Center for Materials Research (CCMR) for the use of their facilities. Many sample preparation steps require the use of the cleanroom in CNF, as well as chemicals available in both CNF and NBTC. Many depositions and metrology were performed and/or obtained using tools available in CNF and CCMR.

Over my years here, I have mentored several undergraduate CNF REU students in the summer months. They were hardworking, modest students, with great motivation (often pulling long hours) to obtain results. These students include Jade Noble (summer 2011), Clay Long (summer 2012), Tyler Erjavec (summer 2013) and Alicia Elliot (summer 2014). The results from these projects were instrumental in our understanding of several ALD processes, how different substrates behaved at the ALD temperatures and pressure conditions, as well as aided us in developing several new recipes to attempt selective deposition. These students are all currently perusing a graduate degree in various fields, and I am very confident they will be successful.

In the middle of my time at Cornell, a close group of friends and family helped me get through a little health “bump”. I especially want to thank Monica, Bryan, Linxiao, Mark, Katie, and countless people in Ithaca, Rochester, Colorado and Singapore who helped me get through this little event. I certainly could not have made it without your support.

Last, but most certainly not least, I would like to thank all my friends here at Cornell and in Ithaca, especially Emily, Zeta and Emme. Thank you for all the encouragements, amazing days and nights, rides to and from campus, wagging tails, love and support. This journey is not complete without you.

TABLE OF CONTENTS

LIST OF FIGURES

1. Introduction

1.2 Overview

This dissertation involves an investigation of atomic layer deposition (ALD) processes, metrology methods to determine the continuity and uniformity of these ultrathin ALD thin films (Chapter 3), as well as an initial exploration of approaches to achieve selective deposition, without the use of lithography and etching steps (Chapters 4 and 5). In the appendix, sample heater calibration study of the deposition and analysis chamber used is presented, along with some typical experimental procedures performed on Olin 312 UHV chamber.

1.3 Atomic layer deposition (ALD)

With semiconductor device requirements moving toward smaller and spatially demanding features, atomic layer deposition (ALD) has many potential advantages over alternative deposition methods such as continuous deposition techniques [e.g. chemical vapor deposition (CVD) and physical vapor deposition (PVD)]. ALD can deposit conformal films, with excellent control over thin film thickness originating from the cyclic, self-limiting nature of the ALD process. A typical ALD process is presented in Fig. 1-1 below, consisting of alternating pulses of ALD precursors with purges in between. In each individual gas-surface reaction (ALD half cycles), a precursor is pulsed onto the surface for a certain amount of time for the precursor to fully react with the surface below it through a self-

limiting reaction that leaves one monolayer deposited, with the precursor unable to react with itself. The reaction chamber is then purged of any excess precursors or reaction by-products with an inert gas (e.g. N_2 or Ar). The second precursor is then pulsed onto the surface, reacting in a self-limiting fashion, with the surface below, creating a layer of the desired material. This process can be repeated to achieve a thin film with the desired thickness.

One advantage of ALD is the precise thickness control on the monolayer level. The self-limiting aspect of ALD precursors leads to great step coverage and conformal film deposition, even on high aspect ratio structures. The self-limiting aspect of ALD also results in non-random deposition since variance in precursor flux across a substrate will no longer result in uneven deposition rates. Hence ALD films are smooth and conformal because reactions will be driven to completion every half cycle. Because all surface sites are reacted, ALD films tend to be continuous and pin-hole free, which is extremely important in many applications, including dielectric films [1], [2] and back-end-of-line processes. ALD processes can also extend to large substrates, even parallel processing of multiple substrates. The precursors used in ALD are gaseous, and can thus fill in all spaces independent of geometries and do not require line-of-sight deposition. This is advantageous, as a shift from traditional planar devices (two dimensional) to three-dimensional devices is observed recently, such as 3D FinFET transistors and 3D NAND flash technology. The precursors themselves are also separated with inert gas purges, limiting the possibility of gas phase reactions and particle contamination on the substrate.

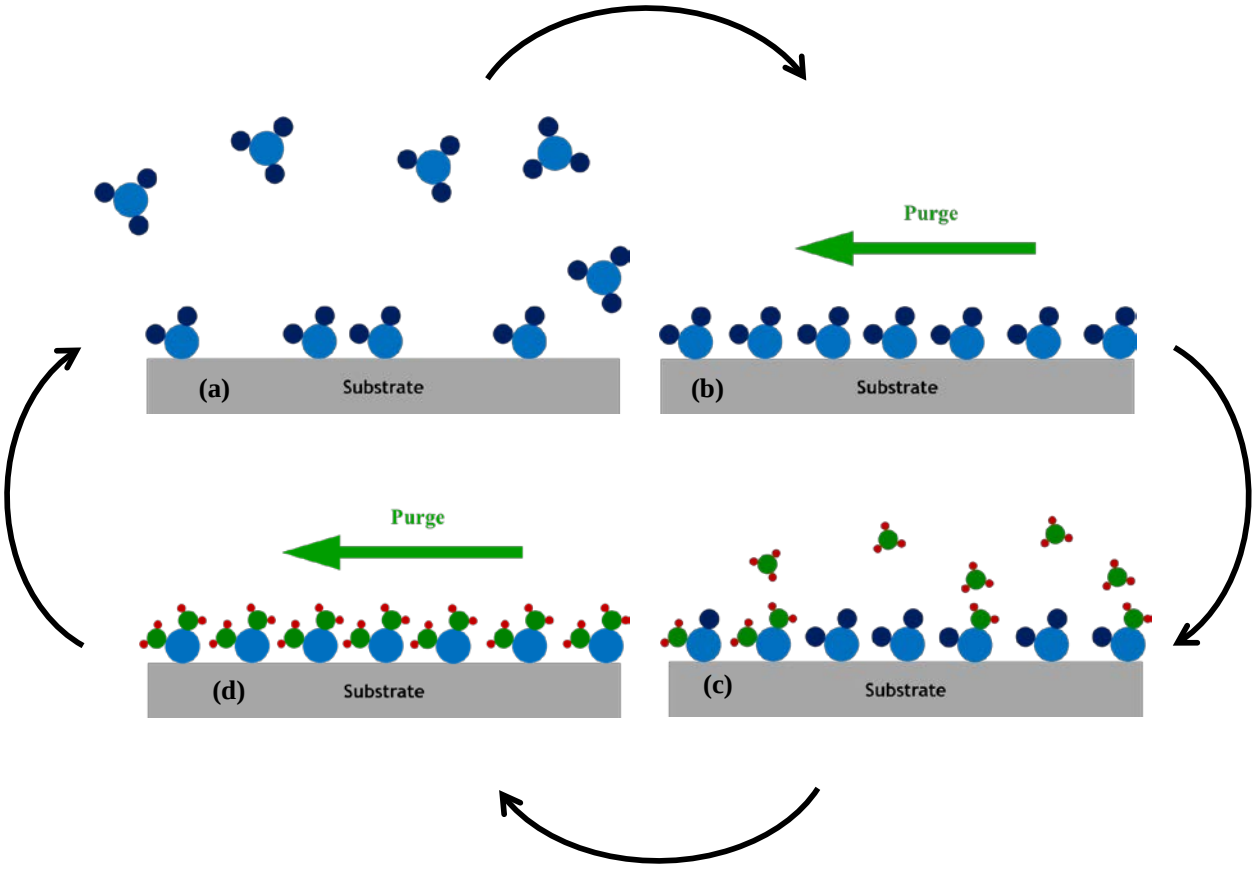

Figure 1-1 Schematic representation of an ALD process. (a) Pulse of precursor A which react only with surface below, (b) excess precursor A and by-products are purged, (c) pulse of precursor B, which react only with surface below, and (d) excess precursor B and by products are purged.

1.4 Metrology of ALD films

Atomic layer deposition (ALD) is well-suited to the formation of ultrathin films with thicknesses < 10 Å [2], particularly concerning growth on topologically complex three-dimensional device features such as those found in interconnect layers [3]. In many cases thin film continuity, i.e., complete coverage of the underlying substrate, is essential. For such ultrathin films ALD growth may be in the nucleation/incubation regime, where ideal two-dimensional steady-state growth has not been achieved. Moreover, analysis of thin film composition, continuity and uniformity is challenging for these ultrathin films.

Determination of ultrathin film continuity and uniformity represents a serious challenge to analytical techniques. Direct imaging using, for example, cross-sectioned samples and transmission electron microscopy analyzes only selected areas, and sub-10 Å resolution with chemical specificity has only been demonstrated with epitaxial thin film structures. Atomic force microscopy (AFM) lacks chemical specificity and in-plane spatial resolution. Scanning tunneling microscopy (STM) possesses the required spatial resolution, but would require operation in a spectroscopic mode to provide chemical specificity, and may also encounter serious issues when imaging insulating substrates. Techniques that provide spatially averaged information concerning thin film composition can in some cases help distinguish between limiting cases of thin film morphology—3D islands vs. uniform flat thin films. Secondary ion mass spectrometry (SIMS) is one possibility, but it can be a challenge to quantify, and it is an intrinsically invasive technique. X-ray photoelectron spectroscopy (XPS) possesses surface sensitivity, and when conducted in an angle-resolved mode (ARXPS), it can provide information concerning the spatial distribution of elements in

a thin film along the surface normal. Concerning in-plane spatial distribution, ARXPS is strongly model-dependent. Low energy ion scattering spectroscopy (LEISS) possesses the ultimate in surface sensitivity, namely the topmost monolayer. LEISS can be affected by "matrix effects," making absolute quantification of the composition of the topmost layer less straightforward when compared to techniques such as XPS [4]. Nevertheless, among all of the techniques just described, LEISS holds the most promise to determine thin film continuity and the point where the thin film "closes-out" and first covers entirely the underlying substrate.

In chapter 3, we present a sputter depth profile of commercially deposited ultrathin (~ 5 and 10 Å) tantalum nitride (TaN_x) ALD films on three different substrates: thermally grown SiO_2; a Cu thin film grown by PVD; and a carbon(C)-doped SiO_2 porous low-κ. We used a combination of ARXPS, LEISS and atomic force microscopy to determine thin film uniformity and continuity of these films.

1.5 Modulation of surface reactivity for area-selective deposition – self-assembled monolayers (SAMs)

Conformal deposition where a thin film is formed on all exposed areas of a substrate is not always desired, especially when only select features need be deposited. For example, in many device manufacturing applications, deposition may be desired on one exposed surface (e.g., metal) and not on another (e.g., dielectric). Selective deposition is a process where materials are only deposited where desired, effectively eliminating additional patterning steps using lithography and etching. Many current selective deposition

technologies rely on lithography to pattern areas and block growth on areas where thin film growth is not desired. With device features becoming three dimensional and shrinking every generation, lithography is becoming less feasible and the development of ALD processes that are selective is of increasing interest.

A common approach to achieve selective deposition is to provide a masking material over areas of the substrate where deposition is not desired. In previous work self-assembled monolayers (SAMs) have shown promise as molecular-scale masks, preventing deposition at early stages of ALD deposition [5]. With the appropriate choice of head groups, SAMs can be chosen to react selectively with one surface, while not reacting at all with another. For example, thiols (R-SH) react with metal surfaces such as Ag, Au, and Cu [6], while silanes (R-Si-X_3) react with hydroxylated (-OH) surfaces. SAMs also contain tail groups, which can effectively control the surface energy of the substrate as well as other properties. In addition, combining SAMs with ALD is a logical choice, since many substrate temperatures used for ALD are relatively low, which is important concerning the stability of SAMs and their ability to block growth.

In chapter 4, we present a study using two molecules: 1H, 1H, 2H, 2H-perfluorooctyltrichlorosilane [FOTS, $(Cl)_3Si(CH_2)_2(CF_2)_5CF_3$] and (heptadecafluoro-1,1,2,2-tetrahydrodecyl)triethoxysilane [HDFTEOS, $(CH_3CH_2O)_3Si(CH_2)_2(CF_2)_7CF_3$] [Gelest, Inc (Morrisville, PA)] to block thermal TaN_x ALD on a dielectric surface (SiO_2), while not affecting growth on a metal surface (Cu). Samples were analyzed *ex situ* using contact angle, spectroscopic ellipsometry, X-ray photoelectron spectroscopy (XPS) and low-energy ion scattering spectroscopy (LEISS) to determine not only the degree of selectivity, but also the mode of growth.

We used the same analysis techniques to analyze several other commercially deposited films such as Co, MnN_x and TaN_x.

1.6 Modulation of surface reactivity for area-selective deposition – co-exposures

The concept of using SAMs as blocking layers has its advantages, however, the stability of the organic layer is a strong function of the film deposition temperature [5], [7], [8]. Moreover, a densely packed SAM layer is required to block ALD growth, which is achievable after more than 48 hours of dipping in solution [7], or a relatively long vapor phase exposure to the SAM molecule. With device features getting smaller every generation, a new technique for selective deposition need to be developed, which we have begun exploring (*cf.* chapter 5) by modifying the standard typical ALD recipe: a *co-exposure* of the substrate to both the transition metal complex (precursor A) and *species "x"*. Molecules for *species "x"* are chosen to reverse any adsorption events that may have occurred on the surface (where film growth is not desired) or simply block the active sites on said surface. We will explore two approaches: controlling the intrinsic reactivity of the surface and making adsorption reversible.

Results for the first half ALD cycle of ZrO_x ALD using tetrakis(ethylmethylamino)zirconium ($Zr[N(CH_3)(CH_2CH_3)]_4$, TEMAZ) and multiple amines and thiol are presented.

1.7 References

[1] M. Groner, J. Elam, F. Fabreguette, and S. George, Thin Solid Films **413**, 186 (2002).

[2] S. George, Chem. Rev. **110**, 111 (2010).

[3] O.Van der Straten, S. M. Rossnagel, J. P. Doyle, K. P. Rodbell, ECS Transactions, **1**, 51 (2006).

[4] H.H. Brongersma, M. Draxler, M. de Ridder and P. Bauer, Surf. Sci. Rep. **62**, 63 (2007).

[5] X. Jiang and S.F. Bent, J. Phys. Chem. C **113**, 17613 (2009).

[6] P. Laibinis and G. Whitesides, J. Am. Chem. Soc. **113**, 7152 (1991).

[7] J. Hong, D.W. Porter, R. Sreenivasan, P.C. McIntyre, and S.F. Bent, Langmuir **27**, 1160 (2007).

[8] R. Chen, H. Kim, P.C. McIntyre, and S.F. Bent, Appl. Phys. Lett. **84**, 4017 (2004).

2. Experimental techniques

Several analytical techniques were used to probe samples. Two of the techniques (x-ray photoelectron spectroscopy and low-energy ion scattering spectroscopy) will be described in some detail in this chapter, while the others will be mentioned (wavelength dispersive spectroscopy, spectroscopic ellipsometry), with their main theory of operation stated.

2.1 Sample preparation

A 'clean' substrate, with minimal contamination is required when studying surface chemistries and how certain reactants interact with the substrate surface in the initial stages of film growth. This section describes the way we prepare the dielectric surface used most often – SiO_2, chemical oxide.

Substrates in the semiconductor industry typically consist of two different categories: dielectrics and metals. Unless otherwise specified, our model surfaces are SiO_2 (chemical oxide) for dielectrics, and Cu [~a 900 Å thick Cu thin film deposited on SiO_2 via physical vapor deposition (PVD] for metals. Most Cu samples were used "as-received", albeit the presence of a Cu oxide layer, while chemical oxide samples require sample cleaning and oxide formation.

Silicon samples (full 100mm wafers or 17 × 17 mm^2 coupons, p-type) were first subjected to a 10 min sonication in chloroform ($CHCl_3$) followed by a rinse in deionized (DI) water and dried with nitrogen, all in Nanobiotechnology Center (NBTC). The samples were

then transferred into Cornell Nanofabrication Facility (CNF) where they were first submerged in buffered oxide etch (BOE, hydrofluoric acid, HF, buffered with ammonium fluoride, NH_4F) to remove the native oxide layer, creating a hydrogen terminated Si-H surface. This is followed by a submergence Nanostrip (mixture of sulfuric acid, H_2SO_4, hydrogen peroxide, H_2O_2 and peroxymonosulfuric acid, H_2SO_5) at an elevated temperature of ~70-80 °C for 15 min to form the thin SiO_2 (chemical oxide) layer. DI water rinse and N_2 drying were followed after each of these acid treatments. These acid treatments (BOE and Nanostrip) and DI water rinse/N_2 drying were repeated twice to ensure consistent SiO_2 thickness and (-OH) densities on the substrate surface. BOE etch step were performed in a Teflon or plastic container, while Nanostrip dip were done in a glass beakers. The resulting "chemical oxide" (SiO_2) has a thickness of ~17 – 25 Å, measured using spectroscopic ellipsometry (SE; Woollam, Lincoln NE).

2.2 X-ray photoelectron spectroscopy (XPS)

X-ray photoelectron spectroscopy (XPS) is a surface sensitive analysis technique that can be used to analyze the surface chemistry of a material. It can measure the elemental composition, chemical and electronic state of the elements that exist within a material. XPS spectra are obtained by irradiating a solid surface with a beam of 'soft' x-rays (usually Al Kα, ~1486.6 eV or Mg Al Kα, ~1253.6 eV). This x-ray beam excites the core electrons within the sample, and the excited electrons (with sufficient energy) can escape the sample surface and be detected by an analyzer. Most of the electrons excited by the incoming x-ray will be reabsorbed by other atoms in the sample, and only the electrons emitted from the

atoms near the sample surface can escape the sample surface (< 100 Å), hence defining the depth resolution of the XPS technique. Since most of the thin film thickness of interest to us is during the initial stages of film growth, or the nucleation stages, XPS is a perfect probe for analyzing the total coverage of material on different substrates.

For our analysis, XPS was carried out in a UHV system using an Omicron Sphera U5 concentric hemispherical electron energy analyzer (Omicron Nanotechnology USA, Eden Prairie, MN), operated at a constant pass energy of 50 eV. Non-monochromated Mg Kα x-rays (1253.6 eV excitation energy) and Al Kα x-rays (1486.7 eV excitation energy) were produced using an Omicron DAR 400 twin anode source operated at 300 W (15 kV anode potential, 20 mA emission current). For angle-resolved XPS (ARXPS) measurements, the takeoff angle was varied by rotating the sample with respect to the analyzer axis. Background subtraction was carried out using the Shirley method [1] Peak areas were calculated by fitting spectra to a Gaussian/Lorentzian product formula with a mixing ratio of 0.7 [2]. Data analysis was carried out using CasaXPS software, version 2.3.15. For detailed description of the XPS hardware, angled-resolved XPS models used etc., please refer to Chapters 3 and 4, as well as Kevin Hughes thesis (Ph.D, 2011).

2.3 Low-energy ion scattering spectroscopy (LEISS)

Low-energy ion scattering spectroscopy (LEISS) is a unique tool in surface analysis, since it provides the atomic composition of the outermost atomic layer. The outer surface atoms are of interest in many applications, including adhesion, catalysis, electron emission, growth and wetting. In our work studying the initial stages of ALD, thin film continuity is

often of the utmost interest. For many semiconductor devices to function, a continuous (defect-free) thin film is required. For example, in back-end-of-line processing, a thin diffusion barrier layer (Ta/TaN layer stack) need to be deposited to prevent the Cu from diffusing into the surrounding dielectric. There are two requirements for this barrier layer. First, it needs to be continuous and defect free. Second, it needs to be a thin layer, so the resistance of the Cu lines can be maintained.

2.3.1 Fundamentals of LEISS

In LEISS, a sample is bombarded with noble gas ions (e.g. He^+, Ne^+ or Ar^+) with low incident energies (E_0) between 500 and 10000 eV. The incident ion beam is directed towards the surface (at an angle α with respect to the surface normal) and only projectiles that are backscattered into a certain solid angle $d\Omega$ (at a scattering angle θ, where the analyzer is located) are analyzed (see Fig. 2-1). In this low energy regime, ions scattered from surface atoms are almost exclusively from elastic binary collisions.

In an elastic binary collision of an incident ion of mass M_0 with a target atom of mass M_1 at rest, the energy transfer only depends on the scattering angle θ. The ratio of detected mass over incident ion energy (E/E_0) can be calculated from simple momentum and energy conservation equations to yield Eqn 1 below [3]:

$$\frac{E}{E_0} = \left(\frac{M_0}{M_0 + M_1}\right)^2 \left[\cos\theta \pm \sqrt{\left(\frac{M_1}{M_0}\right)^2 - sin^2\theta}\right]^2 \qquad [1]$$

Where the positive sign (+) applies to cases where $M_1/M_0 \geq 1$ while both signs are solutions for $|\sin\theta| \leq M_1/M_0 \leq 1$.

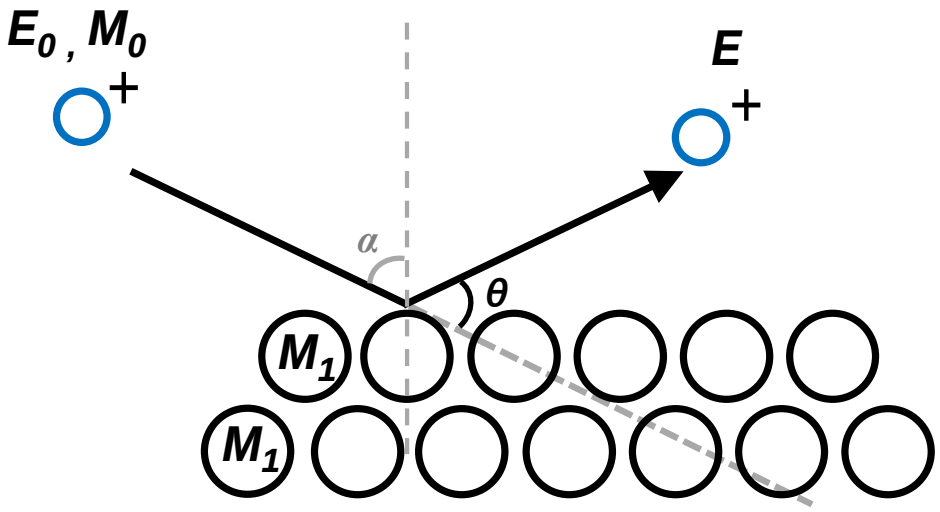

Figure 2- 1 Schematic representation of experimental conditions for LEISS, with incident ion beam (mass M_0, energy E_0, striking the sample surface at an angle α to the surface normal) and the detected ion (mass M, energy E, at a scattering angle θ).

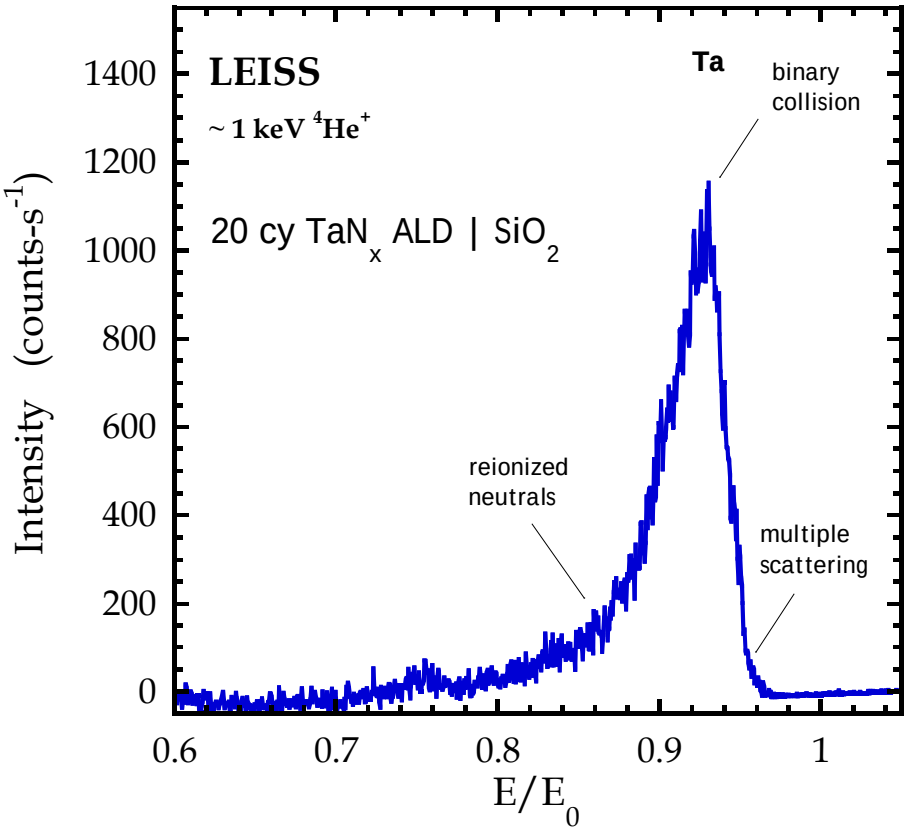

Figure 2- 2 LEIS spectra of ~ 1keV He^+ scattered over a 20cy TaN_x ALD film on SiO_2, θ = 140°, α = 0°, showing the different regions of a LEIS Ta peak, and their corresponding contributors

A typical LEIS spectrum as a function of the energy ratio E/E_0 is presented in Fig. 2-2 above. ~ 1 keV He^+ ions were scattered on a sample of 20 cy of TaN_x deposited on SiO_2 via ALD (θ = 140°, α = 0°). The main peak observed is due to He^+ ions that are backscattered on a single collision from a Ta atom on the sample surface (binary collision). The signal at higher energies (E/E_0 ratios) originates from double and multiple scattering of He^+ ions. The background at lower energies (E/E_0 ratios) is a result from backscattering in deeper layers. This 'tail' can provide non-destructive in-depth information. For multi-component samples, the masses of the different atoms can be derived from the positions of the binary collision peaks, and the integrated intensities of each of the peaks can be used as a measure for the surface concentrations. Since the background between different elemental peaks are due to other scattering events (backscattering from deeper layers, > 1ML, or multiple scattering), it has been suggested that a flat background suggests films grow in a layer-by-layer fashion, while a sloping background indicates islanded growth with agglomeration [4].

The yield of ions, S_i, backscattered from a sample surface atom of mass m_i, is a measure for the atomic surface concentration N_i, described by Eqn. 2 below [5]:

$$S_i = \frac{I_p}{e} \cdot t \cdot \xi \cdot R \cdot n_i \cdot N_i \qquad [2]$$

where

I_p – the primary ion beam current

e – the elementary charge

t – the acquisition time

ξ – instrumental factor (includes factors such as detector solid angle, detector efficiency, and analyzer transmission etc.)

R – factor accounting for surface roughness and shielding

n_i – the elemental sensitivity factor

Compositional analysis in LEISS is based on the principle that only ions backscattered from a single binary collision contribute to the peaks observed in the spectra. Since noble gases are usually used in LEIS, effective neutralization strongly reduces the contributions from multiple scattering processes.

For LEISS, both the spread in the incident ion energy (E_0) and the scattering angle (angular spread in incident ion beam and analyzer acceptance) will contribute to the width of the peak. For energies used in LEISS, the actual scattering process, during which the momentum and energy of the incident ion change significantly, is much shorter than a characteristic vibration time of the sample atom (which is not exactly a free atom, because it is bound to other atoms of the same or different elemental composition). A Doppler broadening effect can thus be observed, causing a shift in the observed peak to be tens of eV lower than what it is predicted (*cf.* Eqn. 1).

Because of the surface sensitivity (the outermost monolayer of a sample) of LEISS, impurities, or surface 'contamination' will have a dramatic effect on the LEIS spectra obtained. When analyzing samples *ex-situ*, the surface of a sample is generally contaminated to some degree by water and organic molecules (see Fig. 2-3 below). Because the underlying surface (beneath the 'contamination layer') is often of interest, certain procedures are essential for LEIS measurements. Common procedures include sputter etch, heating and chemical treatments. For our experiments, we found that a short Ar^+ sputter etch (1 min, ~3keV) was sufficient to remove the majority of the surface contaminants, while not doing

significant damage to the underlying thin film and substrate (see Chapter 3). From Fig. 2-3 below (green curve), we observe a broad 'contamination' peak around $0.1 \leq E/E_0 \leq 0.5$, and a small Ta peak for the spectra taken as-received (without any cleaning procedures). After a 15min Ar^+ sputter-etch, we see the elements of interest – Ta and O.

2.3.2 Characterization of SPECS ion source / LEISS in 312 Olin

The SPECS ion source (SPECS IQE12/38) was added to the UHV system in Olin 312 in October 2010, with two noble gas sources – Argon (UHP, 99.999%, Airgas, PA) and Helium (UHP, 99.999%, Airgas, PA). This addition provided us the ability to sputter etch films (using Ar^+) to remove surface contamination as well as perform sputter depth profiles of samples using XPS. This ion gun also allowed us to perform LEISS.

The SPECS ion source was mounted on main chamber flange 10, with a scattering angle of 140° with respect to the Omicron Sphera U5 concentric hemispherical electron energy analyzer (serial no. 154/1250/U5/34/08, Omicron Nanotechnology USA, Eden Prairie, MN).

Working distance from ion source to sample is 91mm, when the sample is in the normal XPS analysis position. However, after position calibration, we do sputtering and LEISS at an x-position distance of 0.6837 (instead of 0.3645 during XPS analysis) to center the sputter spot in the middle of the sample. This increases the working distance to ~ 99mm.

After installation of the SPECS ion source onto the 312 chamber, several characterization experiments were performed to determine the best parameters to be used for both sputter etching (with Ar^+ ions) as well as LEISS (with He^+ ions), as well as determine

the optimum sample positions to be used when doing a sputter etch and LEISS. Two sets of focus settings were used for this initial test of the ion source. A maximum beam current setting was used for sputter etching, and a minimum beam diameter setting was used for LEISS.

The first characterization experiment involved sputter etching a thermal oxide film ($SiO_2|Si$) to visually observe the sputter spot on the sample. Different thicknesses of SiO_2 will result in major shifts in their perceived color, due to the variations in the reflectance of light through the SiO_2 layer [6]. A maximum beam current setting was used (Factory recall #2), and the sample was sputter etched for ~ 90 min with 3keV Ar^+ ion beam, rastered over an area of 10 × 10 mm^2. The post 90 min sample is presented in Fig. 2-4 below, along with corresponding dimensions. From this characterization, several observations could be made. First, the SiO_2 sample appeared sputter etched, with a well-defined (visually) rectangular spot. This is an obvious observation from the change in color, corresponding to a change in the thickness of the SiO_2 layer. Second, from the picture in Fig. 2-4, the sputter spot was not centered. Measurements were made after the sample was taken out in air and sample positions were calibrated such that the 10 × 10 mm^2 sputter spot is centered (moved the sample up by 0.1 in). Third, an in-air measurement of the sputter spot revealed the one of the dimension (horizontal) to be ~ 10 mm (0.426 in or 10.8mm). The other dimension (vertical), is a little shorter (0.388 in or 9.86 mm), but since the spot was off center in the vertical direction, not much can be determined there. *In-situ* XPS measurements will provide us with a better picture of the accuracy of the sputter beam spot. From these measurements, the sample position was adjusted to better center the sputter spot.

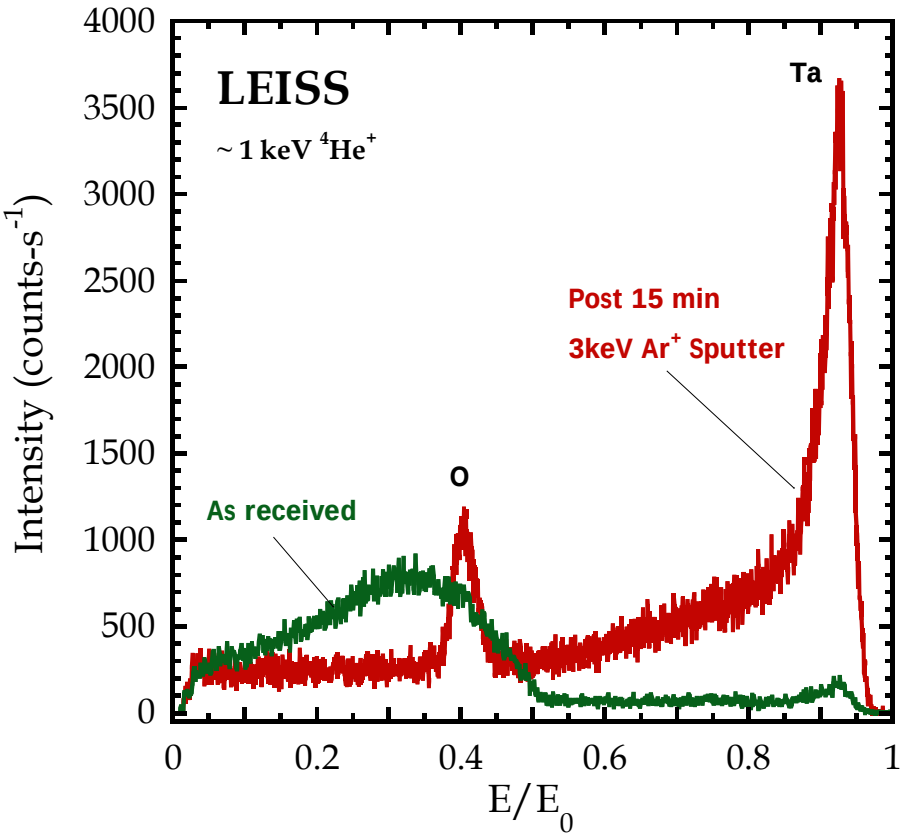

Figure 2- 3 LEIS spectra overlay of ~ 1keV He^+ scattered over a Ta film deposited on SiO_2 via physical vapor deposition, θ = 140°, α = 0°, for as received sample (green) and post 15min Ar^+ sputter etch (red)

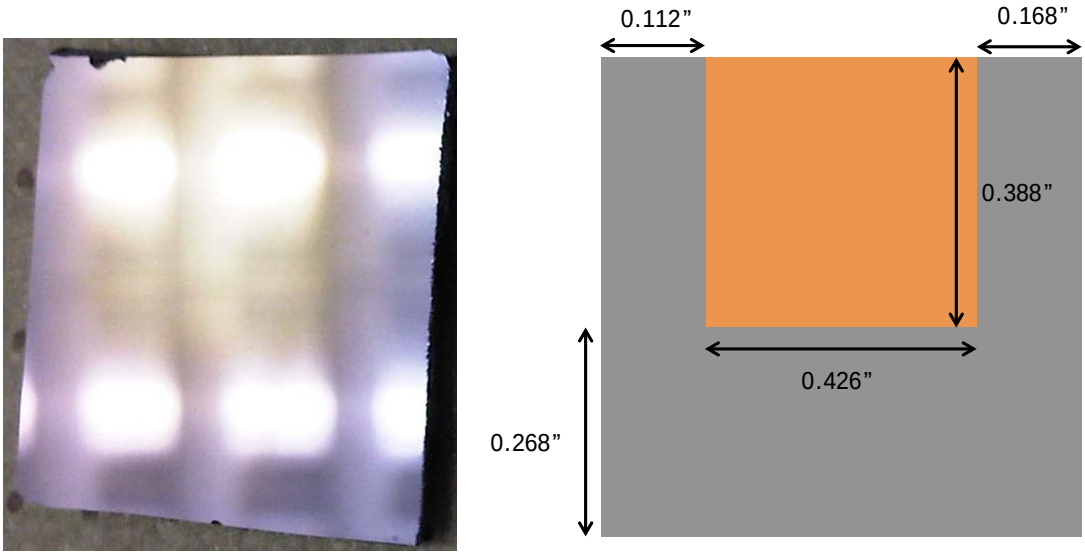

Figure 2- 4 Photo (left) of a post – 90 min 3keV Ar^+ sputter etched SiO_2 sample, along with schematic measurements of the sputter spot (right)

The next experiment involved sputter etching a native SiO_2 sample [thin SiO_2 (~ 15-25Å)|Si] for a short period (~ 3 min), using 3keV Ar^+ ions, rastered over 10mm in the vertical direction (no rastering in the horizontal axis), and a series of XPS scans were done post sputter, in both the vertical (*z*) and horizontal (*y*) directions. The goal of this experiment was to confirm the ion gun / XPS analyzer spot alignment, determine the beam spot diameter, as well as determine the amount of 'background sputter etch' observed on the areas where the ion beam was not rastered over. O(1s) XPS was obtained using an analyzer spot size diameter of ~ 0.63mm. Results of this experiment are displayed in Fig. 2-5. From Fig. 2-5(a), we observed, from the O(1s) XPS integrated intensities, that the sputter spot diameter is ~2.5mm, since no rastering was performed in the horizontal (*y*) – direction.

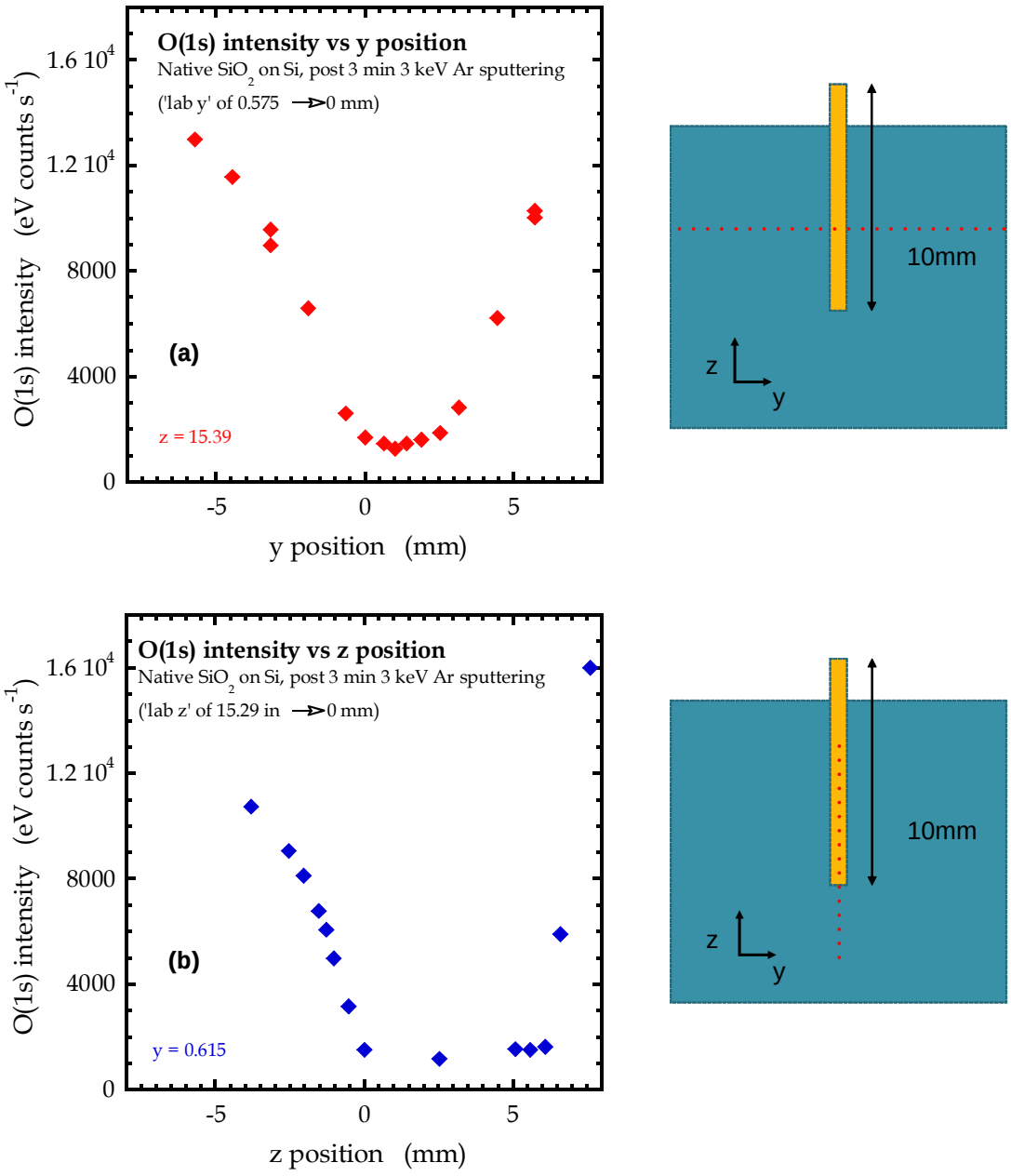

Figure 2- 5 O(1s) XPS intensities along the (a) horizontal – *y* direction and (b) vertical – *z* direction, post 3min Ar^+ sputter etched SiO_2 sample, along with schematic representation of the sputter spot and scan directions (right)

The final characterization experiment involved sputter etching a relatively thick film (~50 Å TiN | SiO_2 | Si). We wanted to determine, *in situ*, with XPS, the actual spot size of the sputtered area, as well as use the attenuation of the substrate (Si) to estimate the approximate sputter rate for this film (TiN). The sample was provided by Applied Materials, the sputter-etched spot was defined to be a 10 mm^2 rastered spot, and a setting for minimum beam diameter was usedfor the ion gun. The sample was sputter-etched in increments (1 – 105 min), with XPS scans for O, C, Ti, N and Si performed after each sputter etch step. The results are presented in Fig. 2-6 below. Carbon contamination is expected for any sample that has been air-exposed. From Fig. 2-6(a), we observed that the C signal is removed after a very short sputter-etch time (< 2min). In Fig. 2-6(b), we present the O(1s) horizontal line scan across the sample after a short sputter etch (3min, 3keV Ar^+). Since this sample was exposed to air, we would expect the top layer of the film to be oxidized from the air exposure. The decrease in O(1s) signal corresponded to the expected width of the sputter spot of approximately 0.4 in (~ 10.2mm). Lastly, we used the attenuation of the substrate, Si(2p) intensities, to approximate the sputter etch rate of TiN using 3keV Ar^+. A simple equation ($I=I_0 \exp [-d/(\lambda \cos \theta)]$*) was used, and an approximate sputter rate of ~0.42 Å / min was obtained.

* $d/\lambda = 0.63$, $d \sim 12.6$ Å

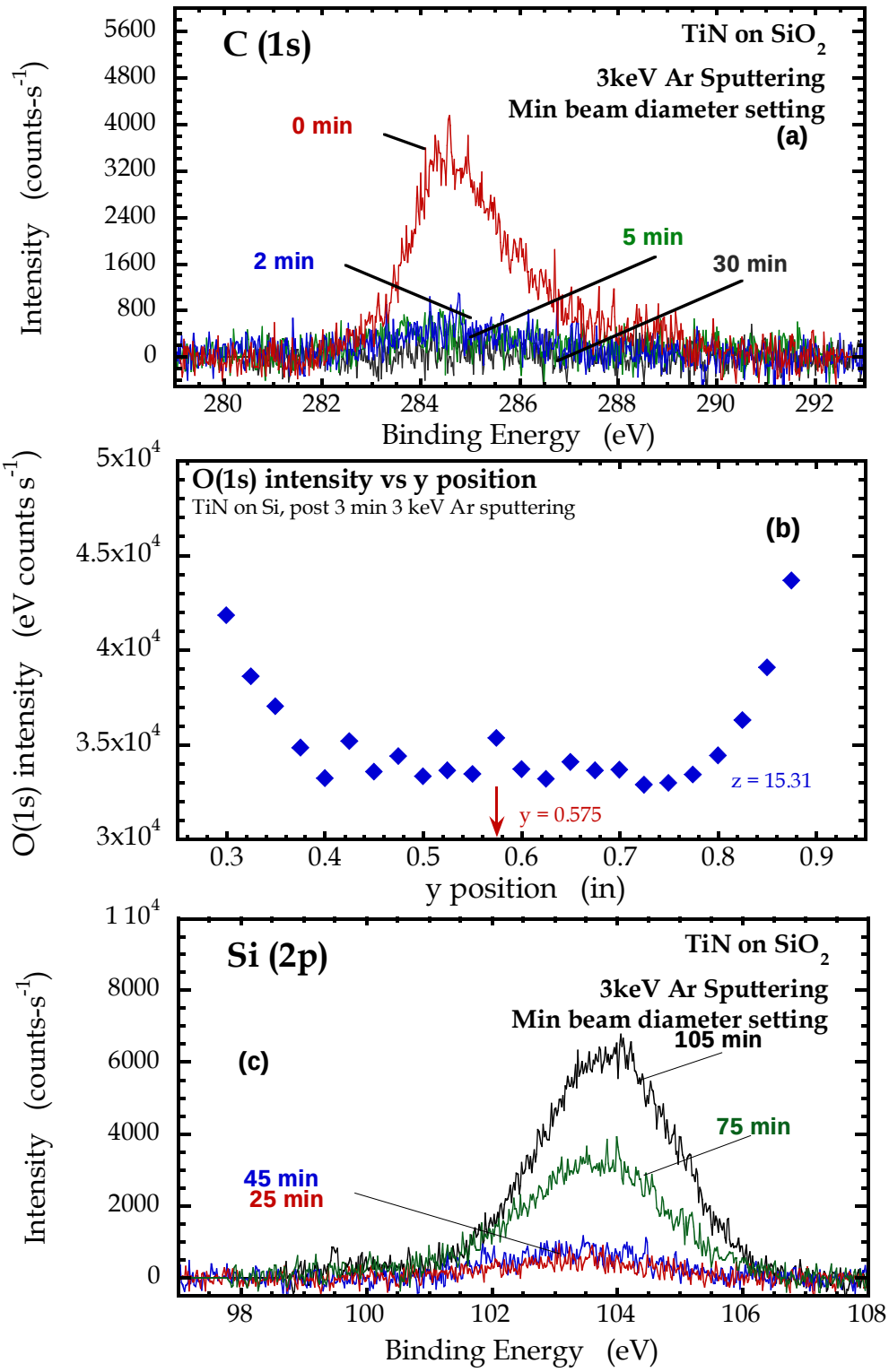

Figure 2- 6 (a) C(1s) XP spectra as a function of sputter time, (b) O(1s) XPS intensity across the sample surface after 3min sputter etch, and (c) Si(2p) spectra as a function of sputter time

2.3.3 LEISS hardware in 312 Olin

For all LEISS experiments in this thesis, it was carried out in a UHV system using an Omicron Sphera U5 concentric hemispherical electron energy analyzer, operated at a fixed retard ratio (FRR) of 5. Helium ions possessing 1000 eV of kinetic energy were produced using a differentially pumped scanning small spot ion source (SPECS ion source IQE 12/38). The axis of the ion source is 40° off the axis the analyzer, resulting in an effective scattering angle (θ) for LEISS of 140°. For LEISS samples were oriented such that they were normal to the ion beam (α = 0°), and all samples were exposed to the ion beam for two minutes before the start of data collection to ensure a stable and constant ion beam current. A typical scan over the range of kinetic energies (1-1000 eV) would take approximately 10 min. For Ar^+ sputtering, a beam of ~ 136 μm dia., with a current of ~ 0.6 μA was rastered over an area of 1 × 1 cm^2, producing a time- averaged ion current density of 0.6 μA-cm^{-2}. For LEISS, the He^+ beam was ~ 146 μm dia., with a current of ~ 0.082 μA. Data analysis was carried out using CasaXPS software, version 2.3.15. Background subtraction was carried out assuming a linear baseline. Peak areas were calculated by fitting spectra to a Gaussian/Lorentzian product formula with a mixing ratio of 0.7. Asymmetry of the peaks was accounted for by using asymmetric line- shape functions in CasaXPS.

Some experimental conditions used during Ar^+ sputter etch as well as LEISS:

Parameters for Ar^+ sputter etching:

x = 0.6837

y = 0.575

z = − 0.1 in from XPS/LEISS analysis position

10mm × 10mm raster

Max beam current setting (Factory recall #6)

47 μA leakage current, $P_{main} \sim 10^{-7} – 10^{-6}$ Torr

Omicron Sphera U5 concentric hemispherical electron energy analyzer is pulled back to the green line

Parameters for LEISS:

x = 0.6837

y = 0.575

z =

No raster

y – deflect = – 2.54 mm (0.1in correction for z-position difference between ion source and analyzer)

Minimum beam diameter setting (Factory recall #7)

7 μA leakage current, $P_{main} \sim 10^{-7}$ Torr

Omicron Sphera U5 concentric hemispherical electron energy analyzer is pulled back to the second dotted line away from user

2.4 Wavelength dispersive x-ray spectroscopy (WDX)

When an electron beam with sufficient energy interacts with a sample surface, matter and energy can be liberated from the sample [see Fig. 2-7]. Accelerated electrons can pass through the sample without interaction, undergo elastic scattering and can be inelastically scattered. Elastic and inelastic scattering result in a number of signals that are used for imaging, quantitative and semi-quantitative information of the target sample and generation of an x-ray source. Typical signals used for imaging include secondary electrons, backscattered electrons, cathodoluminescence, auger electrons and *characteristic x-rays*. Quantitative and semiquantitative analyses of materials as well as element mapping typically utilize characteristic x-rays. Bremsstrahlung radiation is a continuous spectrum of x-rays from zero to the energy of the electron beam, and forms a background in which characteristic x-ray must be considered. X-rays generated from a specific target material are used as the roughly fixed-wavelength energy source for x-ray diffraction (XRD) and x-ray fluorescence (XRF) investigations.

As an electron beam impinges on a sample surface, electron scattering and x-ray production produces in a volume [the electron interaction volume, see Fig. 2-7 (b)] that is dependent on the following factors: the energy of the incident electron beam (increasing the incident energy increases the electron interaction volume, but decreases elastic scattering), the mean atomic weight of the atoms in the sample (interaction volume decreases as atomic weight increases), and multiple electron interaction volumes developing in samples tilted relative to the incident electron beam.

When x-rays are generated in the sample, they are selected using analytical crystals with specific lattice spacing. The geometry of the sample and the crystal is important in WDX (see Fig. 2-8), such that only the x-rays that satisfy Bragg's law ($n\,\lambda = 2\,d\sin\theta$) are reflected and a single wavelength is detected by the detector. X-rays from one element can be measured at one time, since the position of the analytical crystal and the detector (relative to the sample) needs to change for each element. For each given sample, the concentration of the element is measured based on the 'counts' in the detector and a specific beam current. These x-ray intensities can then be corrected for matrix effects associated with atomic number, absorption and fluorescence. For our purposes, we simply used the raw counts (counts s^{-1} nA^{-1}), to compare the amount of element of interest (e.g. Ta).

An electron probe micro-analyzer (EPMA) – JEOL 8900 Microprobe (JEOL Ltd., Tokyo, Japan) was used to probe the sample surfaces this this thesis. A relatively low energy electron beam (~3keV) was used, and the beam current was ~$1.2\text{x}10^{-7}$ A. This tool was a Cornell Center for Materials Research (CCMR) facility and located in Snee Hall.

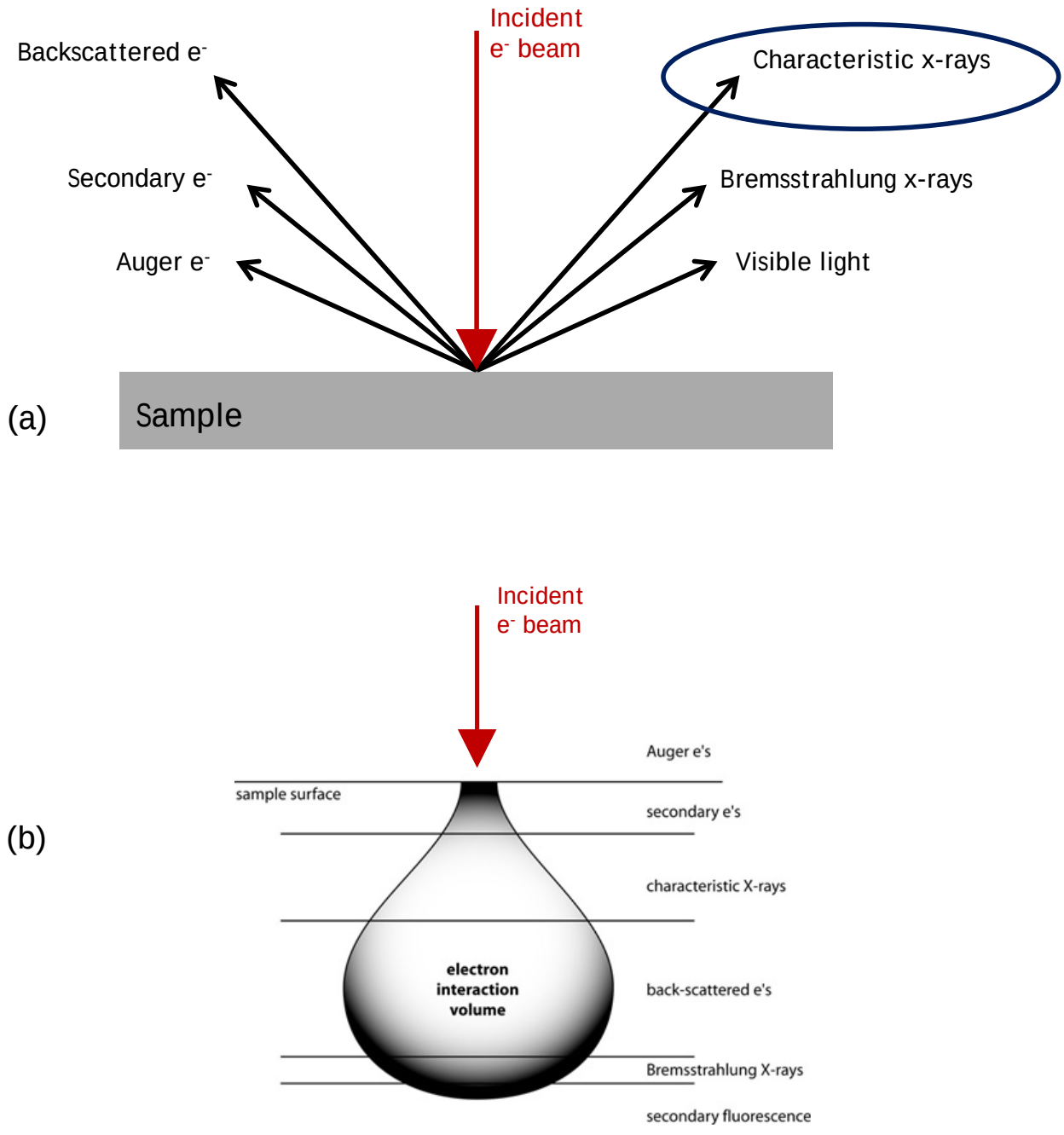

Figure 2- 7 Schematic of **(a)** events during electron beam excitation and **(b)** interaction volume and depth of incident electron beam [7]

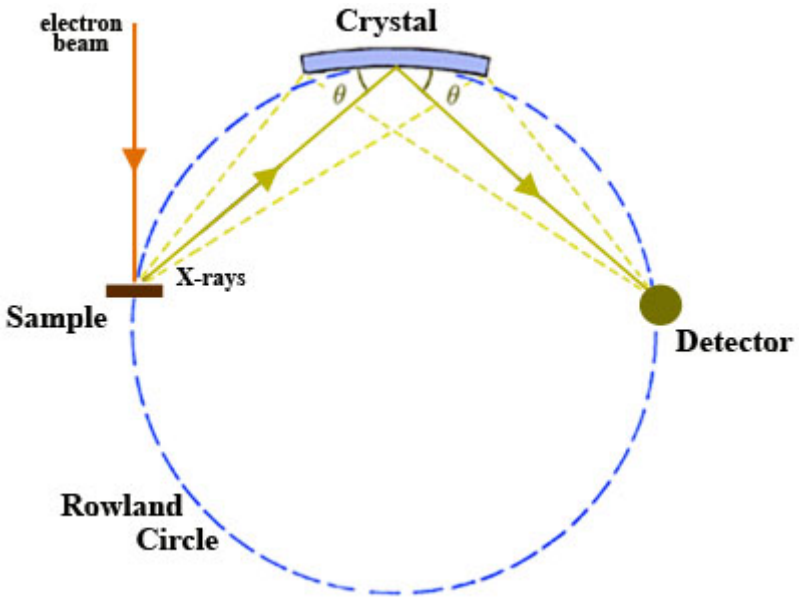

Figure 2- 8 Configuration of the sample, detector and analytical crystal used in wavelength dispersive x-ray spectroscopy [7]

2.5 References

[1] D. A. Shirley, Phys. Rev. B 5, 4709 (1972).

[2] Practical Surface Analysis: Volume I, Auger and X-ray Photoelectron Spectroscopy, 2nd ed.; Seah, M. P., Briggs, D., Eds.; John Wiley and Sons: Chichester, England (1990)

[3] H.H Brongersma and P.M. Mul, Surf. Sci. **35**, 393 (1973).

[4] A. Satta, J. Schuhmacher, C. M. Whelan, W. Vandervorst, S. H. Brongersma, G. P. Beyer, K. Maex, A. Vantomme, M. M. Viitanen, H. H. Brongersma, and W.F.A. Besling, J. Appl. Phys. **92**,12,7641 (2002).

[5] H. H. Brongersma, M. Draxler, M. de Ridder, and P. Bauer, Surf. Sci. Rep.**62**, 3, 63 (2007).

[6] J. Henrie, S. Kellis, S. Schultz, and A. Hawkins, Opt. Express **12**, 7, 1464 (2004).

[7] D. Henry and J. Goodge, "Wavelength-Dispersive X-Ray Spectroscopy (WDX)." [Online]. Available: http://serc.carleton.edu/research_education/geochemsheets/wds.html.

3. Probing ultrathin film continuity and interface abruptness with x-ray photoelectron spectroscopy and low-energy ion scattering

3.1 Abstract

We have examined ultrathin ($\leq$ 10 Å) tantalum nitride (TaN_x) thin films deposited by atomic layer deposition (ALD) on three surfaces relevant to interconnect layers in microelectronic devices: thermally grown SiO_2; a Cu thin film grown by physical vapor deposition (PVD), and a carbon(C)-doped SiO_2 porous low-κ thin film. We have employed *ex situ* angle-resolved x-ray photoelectron spectroscopy (ARXPS), low-energy ion scattering spectroscopy (LEISS) and atomic force microscopy (AFM) to determine the continuity of these thin films, and by implication, the abruptness of the thin film/substrate interface. On SiO_2 and low-κ we find similar results, both ARXPS and AFM indicate that smooth, uniform thin films are deposited, consistent with nearly layer-by-layer (LbL) growth of TaN_x on these surfaces. Examination of these films using LEISS reveals that while the 10 Å TaN_x thin films are continuous, the 5 Å TaN_x thin films are not continuous and may possess on the order of ~ 10% exposed substrate in the form of small sub-nm inclusions. On Cu the situation is quite different. The TaN_x thin films on these surfaces are not continuous, and our results point to a mixed layer of TaN_x and Cu forming during ALD. In all cases, if one were to rely solely on results from ARXPS, the picture would be incomplete as the results from LEISS are ultimately decisive concerning thin film continuity.

3.2 Introduction

Atomic layer deposition (ALD) is well-suited to the formation of ultrathin films with thicknesses < 10 Å **[1]**, particularly concerning growth on topologically complex three-dimensional device features such as those found in interconnect layers **[2]**. In many cases thin film continuity, i.e., complete coverage of the underlying substrate, is essential. For such ultrathin films ALD growth may be in the nucleation/incubation regime, where ideal two-dimensional steady-state growth has not been achieved. Moreover, analysis of thin film composition, continuity and uniformity is challenging for these ultrathin films.

Thin film continuity is of course a strong function of the mechanism of thin film growth. Historically, thin film growth has been classified in terms of three mechanisms: (*i*) Frank-van der Merwe, or 2D layer-by-layer growth (LbL); (*ii*) Stranski-Krastanov growth (S-K); and (*iii*) Volmer-Weber, or 3D islanded growth (V-W) **[3]**. These classic thin film growth mechanisms are essentially based on thermodynamic driving forces such as chemical potentials and/or substrate and thin film surface and interface energies. They can also be interpreted in terms of kinetic factors such as the rate of interlayer transport and the presence of step-edge, or Ehrlich-Schwoebel, barriers **[4,5]**. The relevance of these mechanisms to a sequential, self-limiting process such as ALD can be questioned, however. For ALD it can be argued that the density and spatial distribution of active adsorption sites after each half cycle is more relevant concerning the evolution of thin film morphology **[6,7]**. In any event, regardless of interpretation, LbL growth is clearly preferred in cases where one wishes to produce a conformal thin film possessing the smallest thickness and smoothest topology.

Determination of ultrathin film continuity and uniformity represents a serious challenge to analytical techniques. Direct imaging using, for example, cross-sectioned

samples and transmission electron microscopy analyzes only selected areas, and sub-10 Å resolution with chemical specificity has only been demonstrated with epitaxial thin film structures. Atomic force microscopy (AFM) lacks chemical specificity and in-plane spatial resolution. Scanning tunneling microscopy (STM) possesses the required spatial resolution, but would require operation in a spectroscopic mode to provide chemical specificity, and may also encounter serious issues when imaging insulating substrates. Techniques that provide spatially averaged information concerning thin film composition can in some cases help distinguish between limiting cases of thin film morphology—3D islands vs. uniform flat thin films. Secondary ion mass spectrometry (SIMS) is one possibility, but it can be a challenge to quantify, and it is an intrinsically invasive technique. X-ray photoelectron spectroscopy (XPS) possesses surface sensitivity, and when conducted in an angle-resolved mode (ARXPS), it can provide information concerning the spatial distribution of elements in a thin film along the surface normal. Concerning in-plane spatial distribution, ARXPS is strongly model-dependent. Low energy ion scattering spectroscopy (LEISS) possesses the ultimate in surface sensitivity, namely the topmost monolayer. LEISS can be affected by "matrix effects," making absolute quantification of the composition of the topmost layer less straightforward when compared to techniques such as XPS **[8]**. Nevertheless, among all of the techniques just described, LEISS holds the most promise to determine thin film continuity and the point where the thin film "closes-out" and first covers entirely the underlying substrate.

We present here a detailed examination of TaN_x thin films grown by ALD and the resulting interfaces on three surfaces relevant to interconnect layers in microelectronic devices: thermally grown SiO_2; a Cu thin film grown by PVD; and a carbon(C)-doped SiO_2

porous low-κ thin film. In all cases examined the nominal thin film thickness of the TaN_x layers is ≤ 10 Å. We employ here *ex situ* angle-resolved XPS and LEISS to examine each layer, and results from AFM will also be presented. In appropriate sections we will refer to previous work conducted on films deposited by ALD (or similar techniques) and examined via the use of LEISS **[9-23]**, ARXPS **[24-28]** and SIMS **[17]**. The goal here is to compare and contrast the effectiveness of *ex situ* analysis of ultrathin films using ARXPS and LEISS to determine thin film uniformity and continuity. We will find that the results from LEISS are ultimately decisive concerning thin film continuity.

3.3 Experimental procedures

The experiments described here involved first growth of the TaN_x thin films via ALD on 300 mm dia. Si(100) wafers possessing the thin film coatings of interest, followed by an "air break" and transfer for analysis in air (AFM) and in UHV (XPS and LEISS). TaN_x thin films were deposited by ALD using a chamber designed for 300 mm wafers and a thermal process (T_s = 230-275 °C) based on pentakis dimethylamido tantalum (PDMAT) and NH_3. TaN_x ALD was conducted on Si(100) oriented wafers with thin films of (*i*) 3000 Å thermally grown SiO_2; (*ii*) 900 Å Cu thin film grown by PVD, and (*iii*) 2000 Å C-doped SiO_2 porous low-κ (nominal κ ~ 2.3, ~ 10 Å dia. pores). For each substrate, we examined two thin films of TaN_x of nominal thicknesses of ~ 5 and 10 Å, corresponding to 10 and 20 cycles of ALD. The 300 mm. dia. wafers were cleaved into 17 × 17 mm^2 square samples and swept with a stream of dry N_2 before insertion into to the UHV chamber. No other sample preparation was employed in this study, i.e., the samples were examined "as received."

For each TaN_x thin film/substrate combination we conducted two sets of analyses. In the first set of experiments the samples were inserted into the UHV chamber and a set of XPS spectra were collected at a series of takeoff angles for the elements of interest [Ta($4d_{5/2}$), C(1s), O(1s), and Si(2p) or Cu($2p_{3/2}$)]. The features of most interest in this case are those representing photoemission from the thin film (Ta) and the substrate (Si or Cu) **[28-30]**. After one set of ARXPS data were collected, each sample was sputter etched for 1 min. using a 3 keV Ar^+ ion beam, rastered over a 10 × 10 mm^2 area. An additional set of ARXPS data was then collected. As discussed below, this short time Ar^+ ion beam sputter etch was deemed optimal to both remove most of the adventitious layer of C present on all samples, while also only minimally damaging/removing the TaN_x thin film/substrate structure that is of primary interest here. In the second set of experiments the samples were inserted into the UHV chamber, and these "as received" substrates were analyzed first using fixed takeoff angle XPS, scanning in detail the regions corresponding to the elements of interest [Ta($4d_{5/2}$), N(1s), C(1s), O(1s), and Si(2p) or Cu($2p_{3/2}$)]. This was followed by LEISS, using a primary beam of 1 keV He^+, scanning the entire range of kinetic energies (1-1000 eV). Subsequently, each sample was sputter etched for a fixed period of time using a (rastered) 3 keV Ar^+ ion beam. XPS and LEISS spectra were collected again as described above. This procedure was repeated until most of the TaN_x thin film had been removed by sputter etching. Additional details concerning the experimental methods are provided in the Supplementary Material.

3.4 Results

3.4.1 As-received samples

As described above, XPS was employed to examine the as-received samples, using both analyses at a fixed takeoff angle, and at variable takeoff angles (ARXPS). In all cases we observed the presence of a thin surface contamination layer likely associated with transfer of the samples and exposure to the atmosphere. These contamination layers consisted mostly of C and O. Assuming minimal carbon contamination of the ALD grown TaN_x thin film, only the carbon-doped SiO_2 porous low-κ thin film is expected to possess significant amounts of carbon. Likewise, the TaN_x thin films grown on Cu should not contain oxygen—the presence of O in these cases would most likely signal exchange between N bound to Ta with atmospheric oxygen, and/or possibly oxidation of the Cu atoms nearest the surface.

Detailed analysis of the C(1s) peak for the as-received samples (see Supplementary Material) reveals three distinct peaks for the TaN_x thin films on all three surfaces. In Fig. 3-1, we present two sets of results for (a) the C(1s) intensity as a function of sputter etch time (for both $TaN_x|SiO_2$ thin films); and (b) the C(1s) intensity as a function takeoff angle for the as-received sample, and one after 1 min. of Ar^+ ion sputter etching (for the 10 Å $TaN_x|SiO_2$ thin film only). From Fig. 3-1(a) we see that there is a significant drop in the C(1s) intensity after 1 min. of sputter etching (~ 70-80% of the as-received value) whereas minimal changes are observed beyond 2 min. of sputter etching. Similar results were observed on Cu and low-κ concerning the significant decrease in the C(1s) intensity after 1 min. of sputtering. On low-κ, however, after ~ 2 min. of sputtering, the C(1s) intensity began to increase nearly linearly, reaching the value approaching that for the as-received surface after 60 min. of sputtering. This is entirely consistent with the fact that the porous low-κ thin film contains carbon. Taken as a whole these results indicate that for our system configuration Ar^+ ion

sputter etching of ~ 1-2 min. represents the least invasive preparation technique to remove the adventitious C-containing layer.

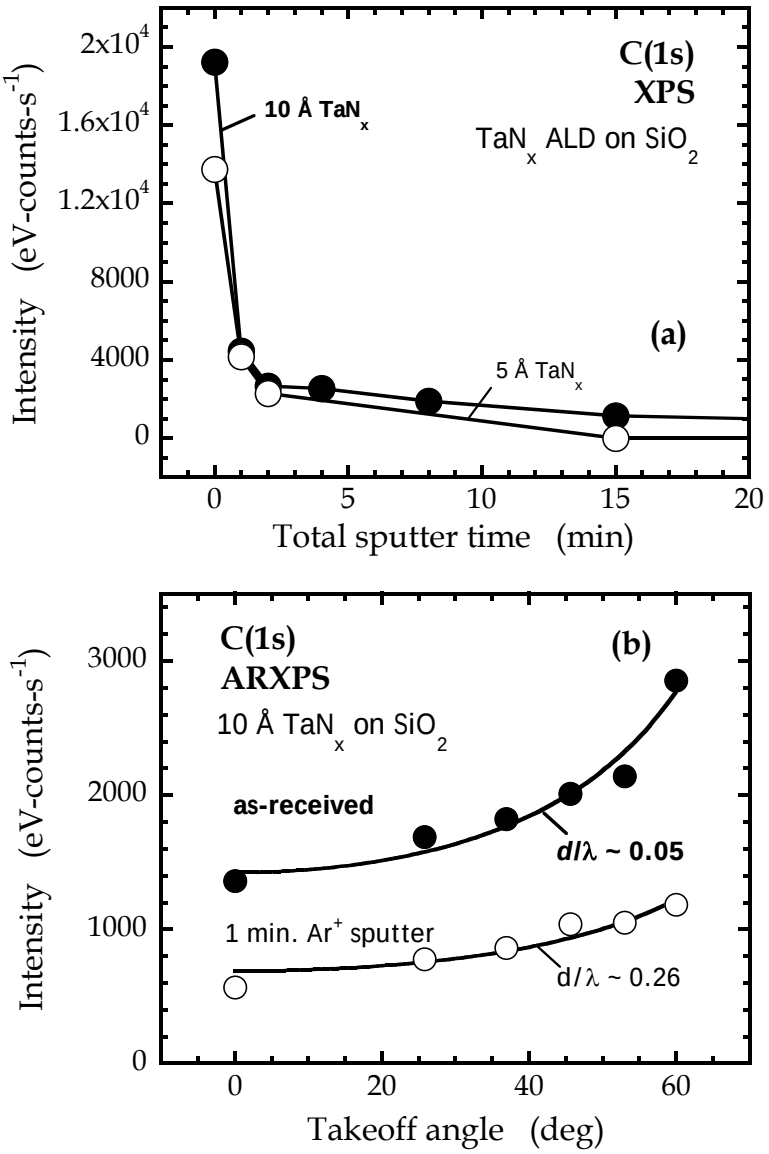

Figure 3-1 **(a)** Integrated intensity of the C(1s) peak as a function of the total Ar+ ion sputter etch time for nominal 5 and 10 Å TaN_x thin films grown by ALD on SiO_2. **(b)** Integrated intensity of the C(1s) peak as a function of the takeoff angle for a nominal 10 Å TaN_x thin film on SiO_2 for the as-received sample and one after 1 min. of Ar^+ ion sputter etching. Solid curves are a fit to Eq. [1].

In Fig. 3-1(b) we observe that both the sample as-received and after 1 min. of sputter etching exhibit an intensity that increases with takeoff angle. A fit of these data to a model (*cf.* Eq. [1] below) that assumes a uniform thin film of a carbonaceous layer covers the substrate gives the quantity d_C/λ, where d_C is the thin film thickness and λ is the attenuation length of the photoelectrons. A fit of the data for the as-received sample gives $d_C/\lambda \sim 0.05$. Assuming a reasonable value for $\lambda \sim 20$ Å **[7]** gives $d_C \sim 1$ Å, consistent with an adsorbed layer confined to the topmost surface. After 1 min. of sputter etching, we see that the C(1s) intensity decreases at all takeoff angles, but a fit to the data now gives $d_C/\lambda \sim 0.26$. This result indicates that while a considerable amount of the C is removed by sputter etching, some C is also driven into the sub-surface layers by the impacting Ar^+ ions. Similar results were observed on Cu and low-κ—in general, the value for d_C/λ increased after 1 min. of sputtering. For the as-received Cu and low-κ samples, the values for d_C/λ were somewhat larger than those observed on SiO_2, reflecting the presence of C in the underlying thin film in the case of low-κ ($d_C/\lambda \sim 0.24$), and possibly a rougher surface in the case of Cu ($d_C/\lambda \sim 0.43$).

We have also conducted a detailed analysis of the O(1s) peak for the as-received samples and those that have been sputter etched (see Supplementary Material). In the case of SiO_2 and low-κ, we clearly observe two peaks, corresponding to O bound to Ta (low binding energy) and to Si in the underlying substrate (high binding energy). On Cu, a single broad feature is observed (see Supplementary Material), which cannot be fit to a single peak with a reasonable full-width at half maximum (FWHM). Fitting this feature to two peaks gives a chemical shift of ~ 1-1.3 eV. The low binding energy peak is again best associated with O bound to Ta, while the higher binding energy peak is likely associated with O bound to Cu.

3.4.2 Angle-resolved X-ray photoelectron spectroscopy

In Fig. 3-2(a) we display the intensity from the Ta($4d_{5/2}$) peak, representing the thin film, as a function of the takeoff angle for both the nominal 5 and 10 Å TaN_x ALD thin films on SiO_2. Both of these thin films were subjected to 1 min. of Ar^+ ion sputtering, as these are largely free of the C-containing contamination layer just described in Sec. 3.4.1. In Fig. 3-2(b) we display the intensity from the Si(2p) peak, representing the substrate, as a function of the takeoff angle for these same two thin films. The photoemission intensity for elements present in a uniform, flat thin film should be described by:

$$I_{film}(\theta) = I_{0,film}\left(1 - \exp\left(-\frac{d_{film}}{\lambda_{f,film}\cos\theta}\right)\right) \quad [1]$$

where $I_{0,film}$ is the intensity of a semi-infinitely thick film, d_{film} is the thin film thickness, $\lambda_{f,film}$ is the attenuation length (specific to both the elemental component, *f*, and the attenuating medium, *film*), and θ is the takeoff angle. Similarly, the photoemission for elements present in a substrate covered by a uniform, flat thin film should be described by:

$$I_{subs}(\theta) = I_{0,subs}\exp\left(-\frac{d_{film}}{\lambda_{s,film}\cos\theta}\right) \quad [2]$$

where $I_{0,subs}$ is the intensity of a semi-infinitely thick substrate, and $\lambda_{s,film}$ is the attenuation length (specific to both the elemental component, *s*, and the attenuating medium, *film*).

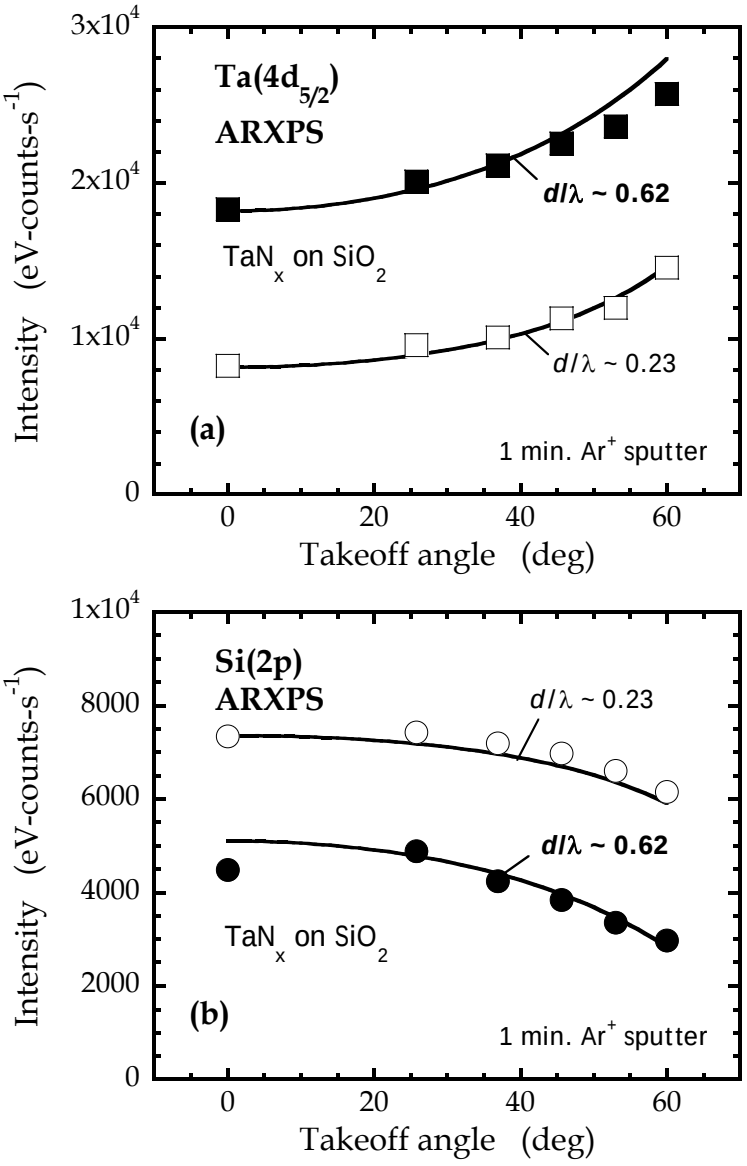

Figure 3-2 **(a)** Integrated intensity of the Ta($4d_{5/2}$) peak as a function of the takeoff angle for nominal 5 (empty squares) and 10 Å (filled squares) TaN_x thin films on SiO_2 after 1 min. of Ar^+ ion sputter etching. **(b)** Integrated intensity of the Si(2p) peak as a function of the takeoff angle for nominal 5 (empty circles) and 10 Å (filled circles) TaN_x thin films on SiO_2 after 1 min. of Ar^+ ion sputter etching. Solid curves in **(a)** and **(b)** are combined fits to Eqs. [1] and [2].

First, we see that the data displayed in Fig. 3-2 exhibit the expected dependency on the takeoff angle as described by Eqs. [1] and [2]: the intensity of the thin film component, Ta, increases with increasing takeoff angle, and that of the substrate component, Si, decreases with increasing takeoff angle. We also see that the intensity of the thin film component is larger for the thicker TaN_x thin film, while the intensity of the substrate is smaller (more attenuated) for this same thin film; both as expected. We could fit these data individually to Eq. [1] and [2], but we have taken a different approach. To constrain the fits of the data we also conducted ARXPS on a ~ 100 Å-thick TaN_x thin film deposited on SiO_2, and a bare SiO_2 substrate. Both of these samples, representing semi-infinitely thick thin films, were subjected to 1 min. of Ar^+ ion sputtering. These samples exhibited a nearly constant intensity with varying takeoff angle, as expected, and could be fit to the simple equations, $I = I_{0,film}$, and $I = I_{0,subs}$, respectively. For a final constraint, we assumed that the attenuation lengths scaled with the square root of the photoelectron kinetic energy, thus the ratio, $\lambda_{f,film}/\lambda_{s,film}$, was determined by this value.

Displayed in Fig. 3-2 as smooth curves are the results of a combined fit of the data for the Ta($4d_{5/2}$) intensity as a function of takeoff angle for both the ultrathin TaN_x film, and the 10 Å-thick TaN_x reference; and the Si(2p) intensity for the ultrathin TaN_x film and the bare SiO_2 reference. Including both ultrathin films in the analysis, this was a 4 parameter fit ($I_{0,film}$, $I_{0,subs}$, d/λ for each TaN_x thin film) to 6 sets of ARXPS data, where we minimized the square of the normalized errors between model and data. As may be seen, the data are well represented by the model. From the fit we find $d/\lambda = 0.23$ for the nominal 5 Å TaN_x thin film, and $d/\lambda = 0.62$ for the nominal 10 Å TaN_x thin film.

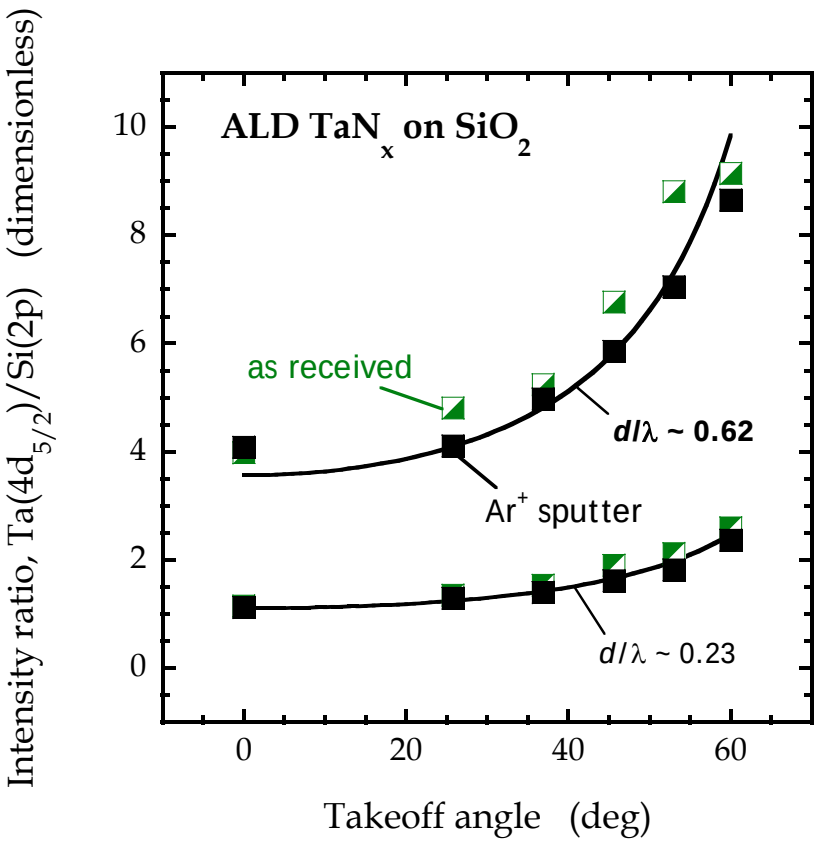

Figure 3-3 Ratio of the integrated intensities of the Ta($4d_{5/2}$) and Si(2p) peaks as a function of takeoff angle for nominal 5 and 10 Å TaN_x thin films grown by ALD on SiO_2. Half-filled (green) symbols are for the as-received samples, filled (black) symbols are after 1 min. of Ar^+ ion sputter etching. Solid lines represent the fits displayed also in Fig. 3-2.

To assess the possible effect of the 1 min. Ar^+ ion sputter etch on the analysis, including the introduction of artifacts, we present an alternative representation of the data in Fig. 3-3. Here we plot the intensity ratio, Ta($4d_{5/2}$)/Si(2p), as a function of takeoff angle for both ultrathin films, and for the as-received and 1 min. Ar^+ sputter etched samples. A possible advantage of this representation is that the effects of contamination layers on the thin film and substrate tend to cancel out (exactly for identical kinetic energy photoelectrons). We also show by the smooth line the ratio predicted by a fit of the data to Eqs. [1] and [2] for the sputter etched samples. As may be seen the model describes the data well and, more importantly, the data for the as-received and sputter etched samples are very similar. The average deviation between the as-received and sputter etched samples is ~ 10% for both ultrathin films. These results lend considerable weight to the viability of the analysis based on the 1 min. Ar^+ ion sputter etched samples.

We performed the same analysis on the films on low-κ, and the similarity between these data for ALD growth of TaN_x on low-κ, and that on SiO_2 (*cf*. Fig. 3-2) is striking. The change in both the intensity of the Ta($4d_{5/2}$) and the Si(2p) peaks with takeoff angle are very similar. Concerning the absolute intensities, we find that the intensities for the Ta($4d_{5/2}$) peak on low-κ is slightly larger (by ~ 10-20%) than that on SiO_2, whereas that for the Si(2p) peak is slightly smaller (by ~ 20-30%) on low-κ. The increased intensity of the Ta peak on low-κ likely reflects penetration of the pores by the TaN_x ALD process. On the other hand, a smaller intensity for the Si(2p) peak is expected on low-κ, due to its porosity and carbon content. Fitting our data for low-κ to Eqs. [1] and [2], we find $d/\lambda = 0.27$ for the nominal 5 Å TaN_x thin film, and $d/\lambda = 0.60$ for the nominal 10 Å TaN_x thin film. These values are within 3-14% of those found on SiO_2. From the intensity ratio Ta($4d_{5/2}$)/Si(2p), as a function of

takeoff angle for both ultrathin films, for the as-received and 1 min. Ar^+ sputter etched samples, we determined that the average deviation between the as-received and sputter etched samples is ~ 10% for both ultrathin films. Again, these results lend credence to the viability of the analysis based on the 1 min. Ar^+ ion sputter etched samples.

We now move on to the ARXPS data for the nominal 5 and 10 Å TaN_x ALD thin films on Cu. Both of these thin films were subjected to 1 min. of Ar^+ ion sputtering. In Fig. 3-4(a) we display the intensity from the Ta($4d_{5/2}$) peak as a function of the takeoff angle for both TaN_x ALD thin films. In Fig. 3-4(b) we display the intensity from the Cu($2p_{3/2}$) peak as a function of the takeoff angle for these same two thin films. The change in the intensities when comparing results from the nominal 5 and 10 Å TaN_x ALD thin films is consistent with expectations. The Ta($4d_{5/2}$) peaks for the thicker thin film are about twice those of the thinner film; while the Cu($2p_{3/2}$) peak for the thicker thin film is about half of that of the thinner film. However, these data are quite different when compared to those observed on both SiO_2 and low-κ. The dependence of both the Ta($4d_{5/2}$) and Cu($2p_{3/2}$) intensities with takeoff angle is relatively weak, not well described by Eqs. [1] and [2] (e.g., the Ta intensity for the ~ 5 Å TaN_x thin film passes through a maximum as a function of takeoff angle). Despite this, we have nevertheless fit these data to Eqs. [1] and [2] as described above, where again to constrain the fits of the data we also conducted ARXPS on a ~ 100 Å-thick TaN_x thin film, and a bare Cu substrate. As may be seen the fit to the data is fair to poor in most cases. Somewhat unexpectedly, the values implicated for d/λ in each case are reasonably similar to those found on SiO_2 and low-κ. Thus, while these results do not suggest at all that a flat uniform thin film of TaN_x is deposited on Cu, they do support that similar amounts of TaN_x are deposited on Cu.

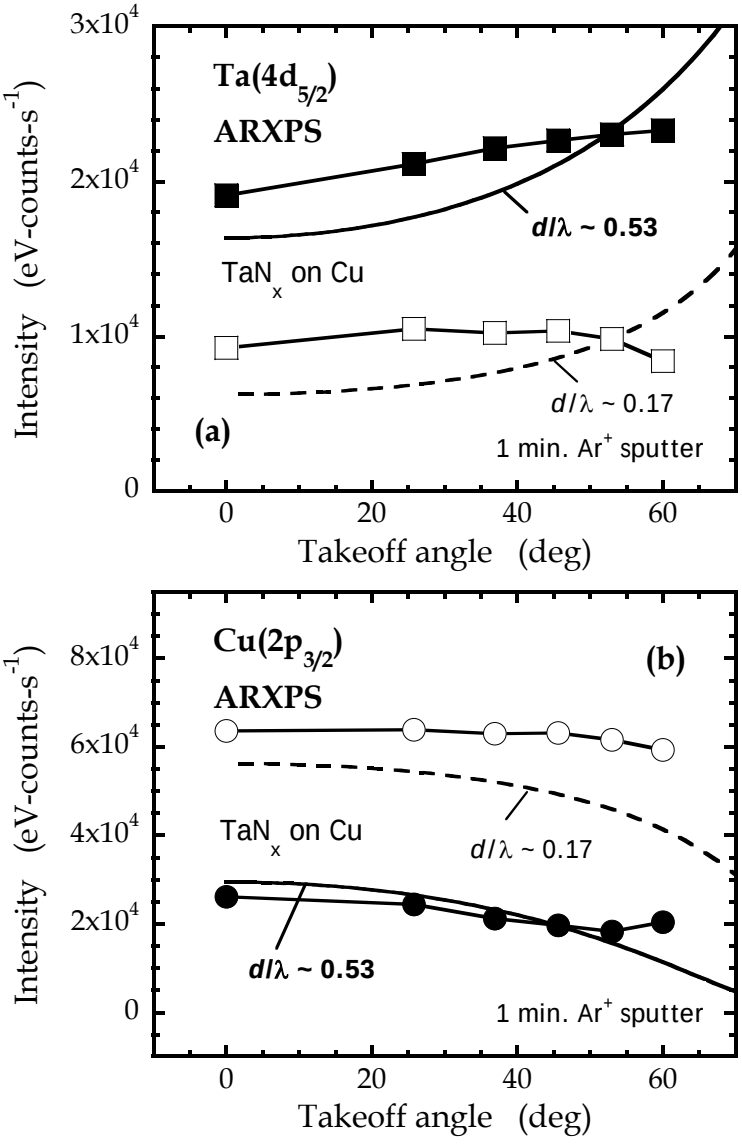

Figure 3-4 **(a)** Integrated intensity of the Ta($4d_{5/2}$) peak as a function of the takeoff angle for nominal 5 (empty squares) and 10 Å (filled squares) TaN_x thin films on Cu after 1 min. of Ar^+ ion sputter etching. **(b)** Integrated intensity of the Si(2p) peak as a function of the takeoff angle for nominal 5 (empty circles) and 10 Å (filled circles) TaN_x thin films on Cu after 1 min. of Ar^+ ion sputter etching. Solid curves in **(a)** and **(b)** are combined fits to Eqs. [1] and [2].

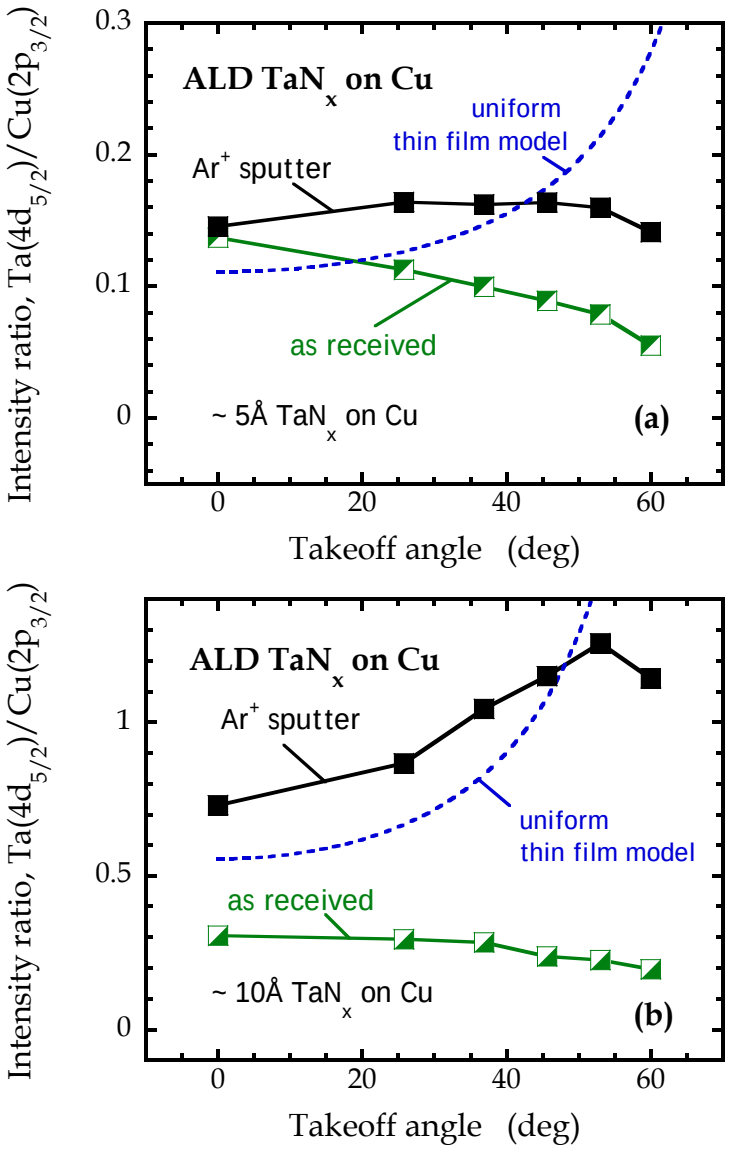

Figure 3-5 Ratio of the integrated intensities of the Ta($4d_{5/2}$) and Cu($2p_{3/2}$) peaks as a function of takeoff angle for nominal **(a)** 5 and **(b)** 10 Å TaN_x thin films grown by ALD on Cu. Half-filled (green) symbols are for the as-received samples, filled (black) symbols are after 1 min. of Ar^+ ion sputter etching. The dashed (blue) lines represent the ratio predicted by a uniform thin film model fit of the data to Eqs. [1] and [2] for the sputter etched samples.

To assess the possible effect of the 1 min. Ar^+ ion sputter etch on the analysis, we plot in Fig. 3-5 the intensity ratio, $Ta(4d_{5/2})/Cu(2p_{3/2})$, as a function of takeoff angle for the nominal (a) 5 and (b) 10 Å TaN_x ALD thin films on Cu, in each case for both the as-received and 1 min. Ar^+ sputter etched samples. Again, we also show by the dashed line the ratio predicted by a fit of the data to Eqs. [1] and [2] for the sputter etched samples. Unlike similar results for SiO_2 (Fig. 3-3) and porous low-κ, the data for Cu indicate that there is a substantial change in this ratio of intensities for the as-received vs. the 1 min. Ar^+ sputter etched samples. Specifically, the intensity ratio increases significantly, unlike the small decrease observed on SiO_2 and low-κ. This ratio can of course increase if the $Ta(4d_{5/2})$ intensity increases and/or the $Cu(2p_{3/2})$ intensity decreases as a result of sputter etching.

A closer examination of the data for all three substrates (thin film and substrate components) for the as-received and 1 min. Ar^+ sputter etched samples reveals the likely cause for the difference between the TaN_x films grown on Cu vs. SiO_2 and porous low-κ. For the latter two cases, 1 min. of Ar^+ sputter etching produced increases (typically < 40%) in both the thin film (Ta) and substrate (Si) components, and the increase in the substrate signal was always about ~ 10% larger than that from the thin film. In these two cases, these results indicate that the 1 min. of Ar^+ sputter etching removed mostly the adventitious C-containing layer, and a small amount of the TaN_x thin film, leaving the underlying substrate essentially untouched. For TaN_x on Cu, in contrast, 1 min. of Ar^+ sputter etching produced increases in the Ta signal by factors of ~ 2-7, with the largest increases occurring at the largest takeoff angles. These results on Cu would suggest that a C-containing contamination layer may be removed to a greater extent from areas where the surface is terminated by Ta, while Cu is

also being removed in regions where it is on the surface, relatively bare of a contamination layer.

In Table I we summarize our results for ARXPS for all samples investigated. Here, to quote a physical thickness for the TaN_x thin films we make use of an estimate for the attenuation length of the photoelectrons of $\lambda = 20.8$ Å [normalized to emission from Si(2p) excited by MgKα] **[31]**. As may be seen, on SiO_2 and porous low-κ, the calculated thicknesses are within expectations for the nominal 5 Å TaN_x ALD thin films (4.6-5.2 Å), and for the 10 Å TaN_x ALD thin film (11.8-12.2 Å). In addition, although the fits to the data are poor to fair, the calculated thicknesses on Cu are also in line with expectations. In summary, it is clear that the TaN_x ALD thin films formed on Cu are quite different than those on SiO_2 and porous low-κ, particularly in light of the results from ARXPS. While the results from ARXPS suggest that uniform, flat thin films are formed on SiO_2 and porous low-κ, they fall sort in terms of definitely determining thin film continuity. Additional experimental evidence concerning these issues will now be presented.

Table I

Properties of TaN_x ALD thin films

Substrate	ALD cycles	Thickness from ARXPS (Å)	Quality of ARXPS fit	Roughness, AFM (Å)	In-plane feature size (Å)	Ar^+ etch to reveal bulk ISS substrate peak (min.)
SiO_2	0	-	-	1.90	940	-
	10	4.6	very good	1.65	620	≤ 0
	20	12.2	very good	1.95	480	3
low-κ	0	-	-	3.98	580	-
	10	5.2	very good	4.15	270	≤ 0
	20	11.8	very good	4.32	290	3
Cu	0	-	-	56.6	380	-
	10	3.4	fair to poor	13.7	750	6
	20	10.5	fair to poor	21.8	320	8

3.4.3 Low energy ion scattering spectroscopy

Among all surface-sensitive techniques, LEISS is perhaps the most surface sensitive, giving information about the composition of only the topmost layer. In Fig. 3-6 we present representative LEIS spectra for ~ 1 keV He^+ scattered from nominal 10 Å TaN_x on (a) SiO_2 and (b) low-κ, at fixed Ar^+ ion sputter etch times. We resolve clearly three peaks: O, Si and Ta. N is not observed, consistent with exchange of surface N with atmospheric O_2 and/or H_2O **[32-34]**. This is even the case while a N(1s) peak is observed in XPS for these same sets of experiments, which indicates some sub-surface N is retained. We also do not observe a C peak in LEISS, which is often the case with adventitious C-containing layers **[8]**. The two peaks of most interest here are that due to the thin film (Ta) and the substrate (Si).

In Fig. 3-7 we present an analysis of the LEIS spectra of TaN_x thin films on SiO_2, where we plot the integrated peak areas for Ta and Si as a function of Ar^+ ion sputter etch time, for (a) the entire range of data; and (b) focusing on < 10 min. of sputtering. From (a) we observe, after a short-lived transient associated with removal of the adventitious C layer, a continuous decrease in the Ta signal, and a continuous increase in the Si signal. We also observe a larger Ta signal, and a smaller Si signal for the 10 Å TaN_x thin film for all sputter etch times. Once a thin film completely covers the substrate, one would expect that the signal from the components in the thin film should saturate. Thus, this suggests that the nominal 5 Å TaN_x thin film may not be continuous, or its microstructure is such that subsurface layers may also be contributing to the Ta signal.

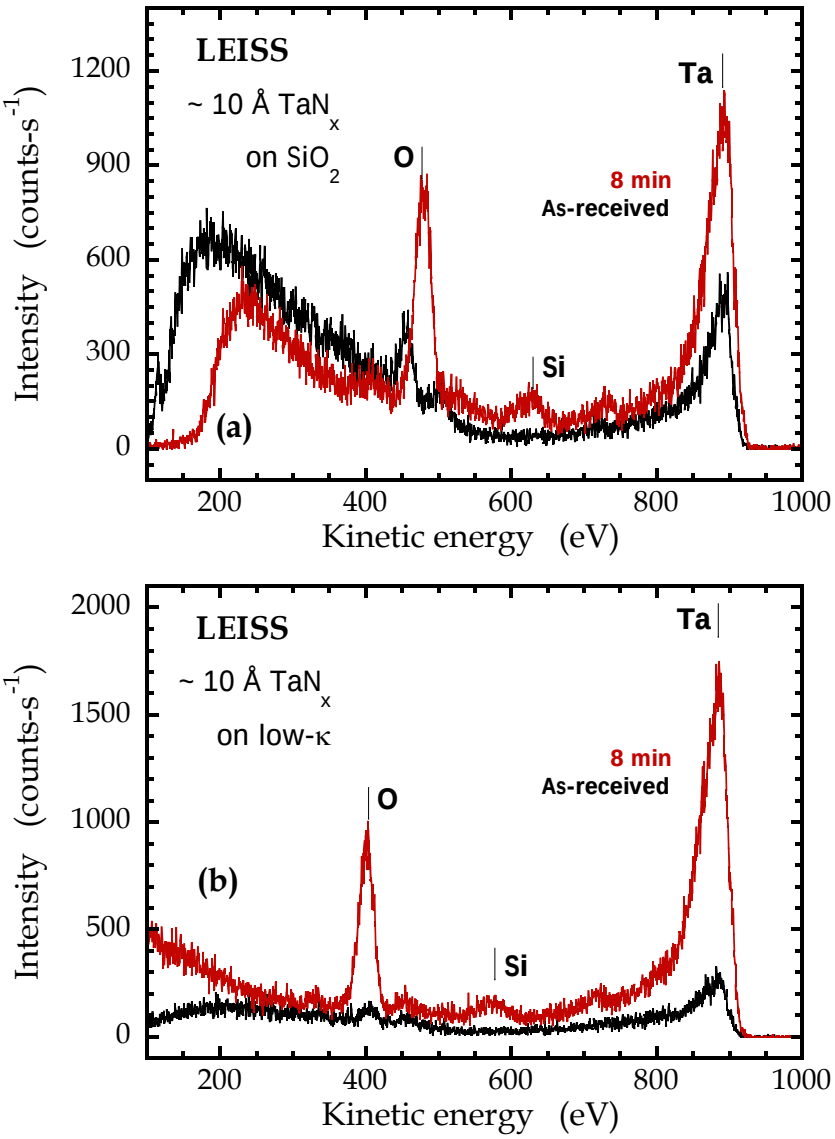

Figure 3-6 Representative LEIS spectra for ~ 1 keV He^+ scattered from nominal 10 Å TaN_x on **(a)** SiO_2 and **(b)** low-κ, for as-received and 8 min Ar^+ sputter etching.

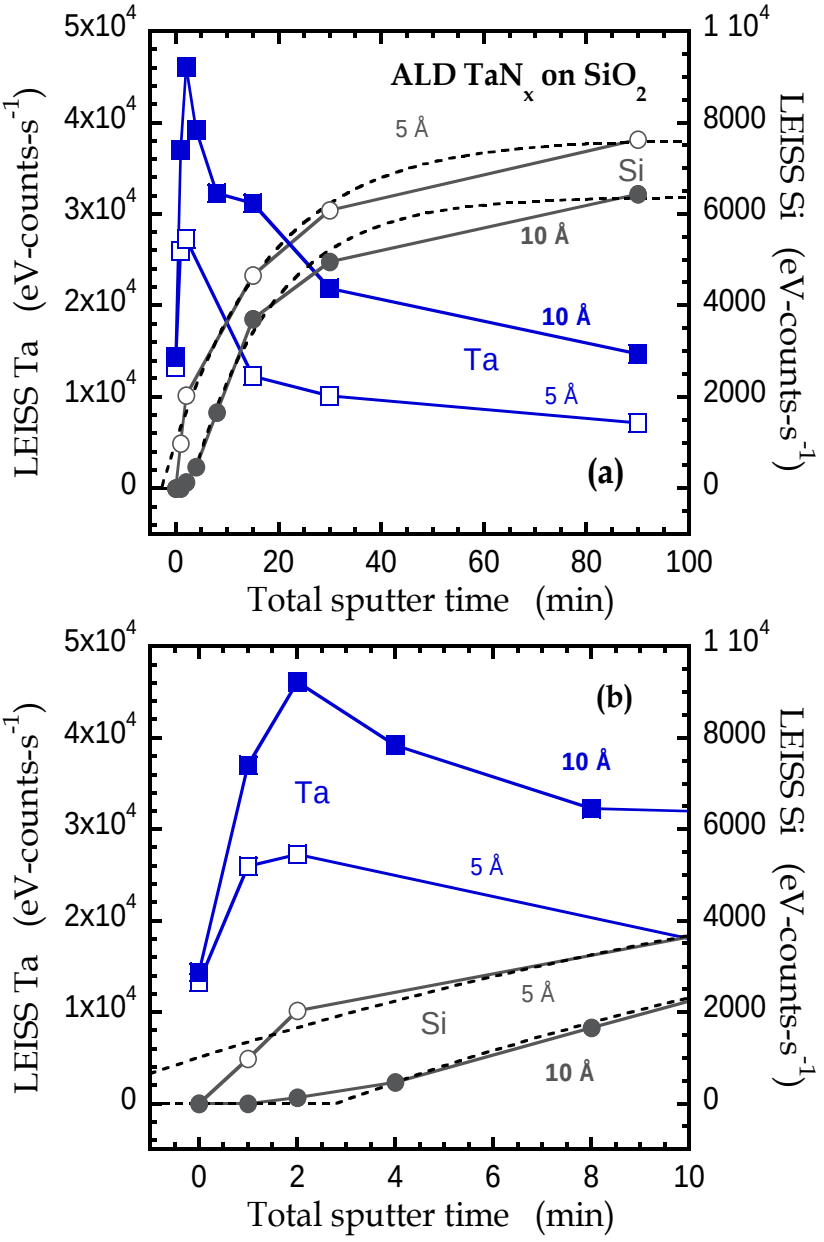

Figure 3-7 Integrated intensities of the LEISS Ta (left ordinate) and Si (right ordinate) peaks as a function of the total Ar^+ sputter etch time for nominal 5 and 10 Å TaN_x ALD thin films on SiO_2. A short Ar^+ etch time set of data are shown in **(b)**. The dashed lines represent fits of the Si intensities to a simple model (see text).

The results shown in Fig. 3-7(b) support the conclusion that the two ultrathin films are not equivalent in terms of their continuity, unlike what may have been concluded from ARXPS. As may be seen, although a Si peak is not observed on the as-received sample for the ~ 5 Å TaN_x thin film, it is observed after only 1 min. of Ar^+ ion sputter etching. In contrast, for the ~ 10 Å TaN_x thin film, a finite Si peak is observed after 4 min. of Ar^+ ion sputter etching. The presence of the adventitious C layer complicates these observations. Longer (etch) time behavior of the LEISS peaks should be much less dependent on this ultrathin contamination layer, thus, they can contribute to the analysis. Due to the stochastic nature of the sputtering process, and effects such as ion induced mixing, we do not expect a step-function change in the thin film component signal with etch time, even for an atomically flat uniform thin film. Rather, an exponentially damped approach to a signal representing the bare substrate should describe the data better. We have fit the data shown in Fig. 3-7(a) to a simple model (excluding the data where the Si peak is ~ 0), given by, $I = I_\infty\{1 - exp[(t - t_0)/\tau]\}$, and these are shown by the dashed lines. As may be seen, the data are described well by this simple function. A key result of this fit is the value for the offset t_0, which represents the minimum etch time to observe a substrate LEISS peak. For the ~ 10 Å TaN_x thin film, we find t_0 = 2.8 ± 0.8 min., while for the 5 Å thin film, t_0 = -2.8 ± 1.2 min. Concerning the latter result, a linear extrapolation of the data for 1 and 2 min. of sputtering, would give t_0 ~ 0. In any event, the threshold to observe a LEISS substrate peak on the thinner 5 Å TaN_x thin film is close to zero etch time. Thus, these data from LEISS support the conclusion that the 10 Å TaN_x thin film is continuous, while the 5 Å TaN_x thin film may represent the borderline of continuity.

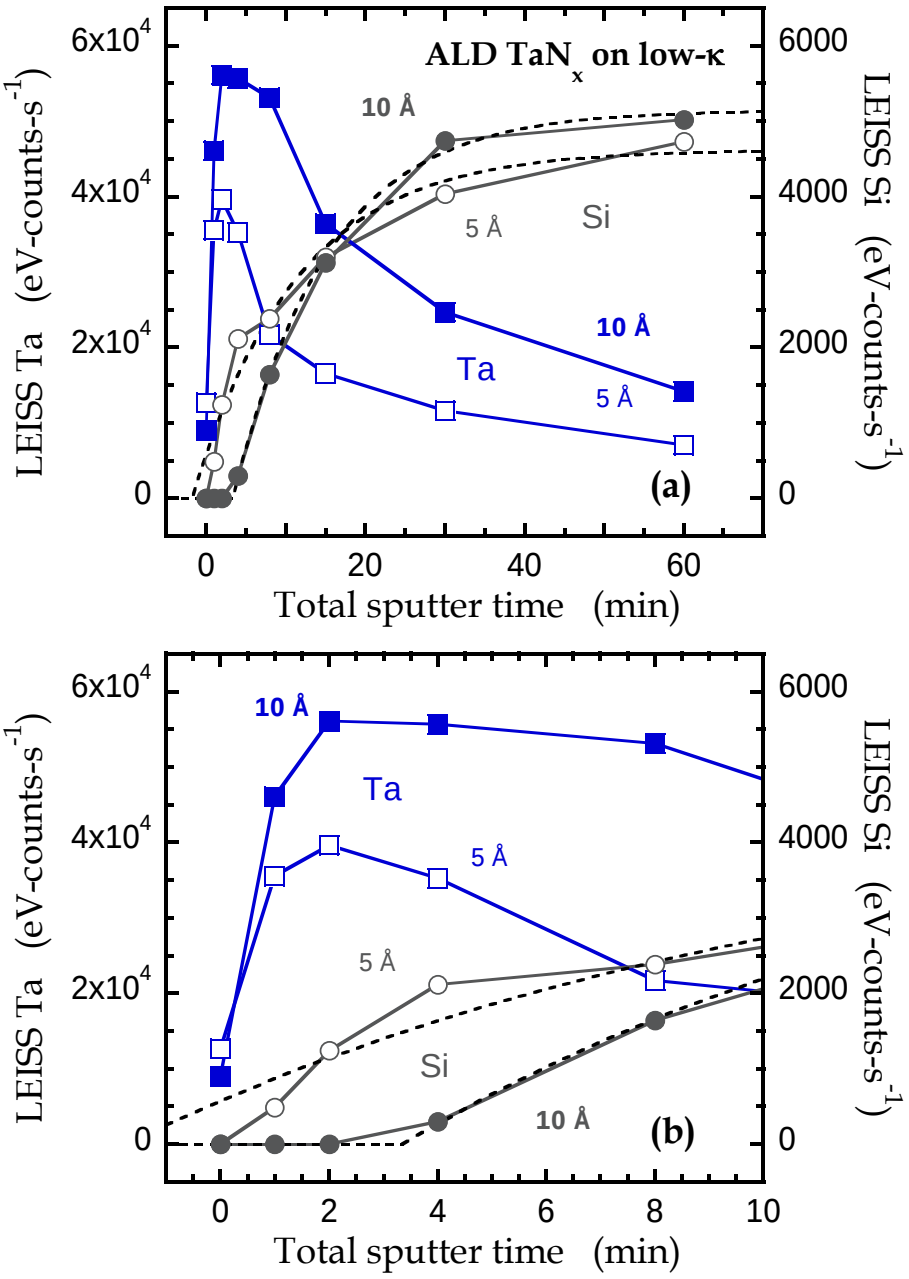

Figure 3-8 Integrated intensities of the LEISS Ta (left ordinate) and Si (right ordinate) peaks as a function of the total Ar^+ sputter etch time for nominal 5 and 10 Å TaN_x ALD thin films on low- κ. A short Ar^+ etch time set of data are shown in **(b)**. The dashed lines represent fits of the Si intensities to a simple model (see text).

In Fig. 3-8 we present an analysis of the LEIS spectra for TaN_x thin films on low-κ, where we plot the integrated peak areas for Ta and Si as a function of Ar^+ ion sputter etch time, for (a) the entire range of data; and (b) focusing on < 10 min. of sputtering. Again, we note the similarity of these data for TaN_x|low-κ to those for $TaN_x|SiO_2$, *cf*. Fig. 3-7. After a short-lived transient, there is a continuous decrease in the Ta signal and a continuous increase in the Si signal. We also observe a larger Ta signal for the 10 Å TaN_x thin film for all sputter etch times. For TaN_x|low-κ, however, there is a cross-over of the Si signal for the two TaN_x ultrathin films. The reason for this difference is not obvious, but it seems to suggest a difference in the rate of sputter etching not seen for the $TaN_x|SiO_2$ samples.

The results shown in Fig. 3-8(b) support the conclusion that the two ultrathin TaN_x|low-κ films are not equivalent in terms of their continuity, similar to that observed for the $TaN_x|SiO_2$ samples. Following the procedure described above we have fit the data shown in Fig. 3-8(a) to a simple model given by, $I = I_\infty\{1 - exp[(t - t_0)/\tau]\}$, and these are shown by the dashed lines. As may be seen, the data are described well by this simple function (better in the case of the thicker TaN_x thin film). For the ~ 10 Å TaN_x thin film, we find the offset t_0 = 3.4 ± 0.3 min., while for the 5 Å thin film, t_0 = -1.7 ± 1.3 min. Concerning the latter result, a linear extrapolation of the data for 1, 2 and 4 min. of sputtering, would give t_0 ~ 0. Thus, these data from LEISS support the conclusion that the 10 Å TaN_x thin film on porous low-κ is continuous, while the 5 Å TaN_x thin film may, again, represent the borderline of continuity.

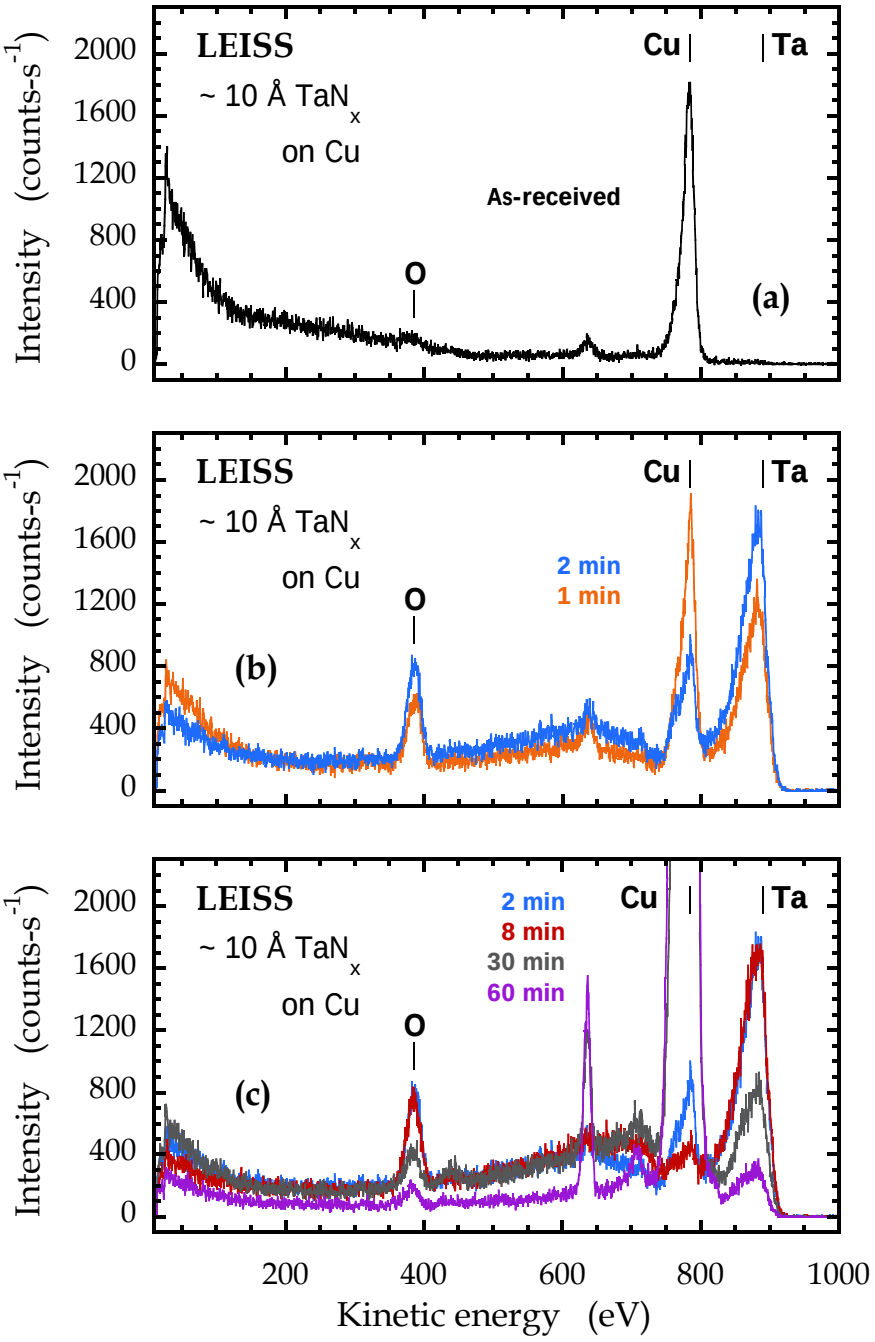

Figure 3-9 LEIS spectra for **(a)** as-received, **(b)** after 1, 2, **(c)** 2, 8, 30 and 60 min. of Ar^+ sputter etching. Results are for ~ 1 keV He^+ scattered from a nominal 10 Å TaN_x ALD thin film on Cu.

We now consider the results from LEISS for the TaN_x|Cu thin films, which we display in Fig. 3-9. These results are for ~ 1 keV He^+ scattered from nominal 10 Å TaN_x on Cu. First, for clarity in (a) we show the LEIS spectrum for just the as-received sample. This spectrum exhibits clear differences to both spectra observed on SiO_2 and low-κ (*cf.* Fig. 3-6), namely, *we observe no LEIS peak for Ta* for the as-received sample. As may be seen, *we also observe a strong Cu peak* for this sample, as well as smaller features associated with O and, at this time, an unknown contributor (E ~ 640 eV). There are at least two possible explanations for this spectrum, specifically concerning the absence of the Ta peak: (*i*) there is no Ta at the surface of the as-received thin film, or (*ii*) the Ta is covered (perhaps preferentially) by a contamination (e.g., C) layer. The appearance of a Cu peak would seem to indicate that the TaN_x thin film is not continuous, even for this nominal 10 Å thickness.

In Fig. 3-9(b) we present the results for ~ 1 keV He^+ scattered from nominal 10 Å TaN_x on Cu after 1 and 2 min. of Ar^+ ion sputter etch time. There are obvious changes in these spectra compared to those observed for the as-received sample—the Ta peak now appears, as does the Cu peak. After 1 min. of Ar^+ sputtering we see that the Cu peak is nearly as intense as that for the as-received sample. After 2 min. of Ar^+ sputtering the Cu peak actually decreases, while the Ta peak gains in intensity. The O peak appears to track the Ta peak, indicating that it may be associated with post-deposition exchange of N for O in TaN_x upon exposure to air. The peak at ~ 640 eV seems to scale with the size of Cu peak, decreasing in size from 1 to 2 min. of sputter etching. In Fig. 3-9(c) we present the results for ~ 1 keV He^+ scattered from nominal 10 Å TaN_x on Cu after 2, 8, 30 and 60min. of Ar^+ ion sputter etch time. As the time for sputter etching is increased from 2 to 8 min. we see that the Ta peak is approximately constant, while the Cu peak almost vanishes. As the time

for sputter etching increases further to 30 and then 60 min., we observe a substantial increase in the Cu peak (the peaks are clipped in this presentation), and a strong decrease in the Ta peak.

In Fig. 3-10 we present an analysis of the spectra shown in Fig. 3-9, where we plot the integrated peak areas for Ta and Cu as a function of Ar^+ ion sputter etch time, for (a) the entire range of data; and (b) focusing on < 20 min. of sputtering. First, beyond ~ 10 min. of Ar^+ ion sputter etching the behaviors of the thin film (Ta) and substrate components (Cu) with etch time are not so different from those observed on SiO_2 and low-κ: a continuous decrease in the former, and a continuous increase in the latter. Clearly, however, there are substantial differences in the transition regime of 0-8 min. of sputter etching, where the substrate Cu peak passes through a minimum with etch time. As with the data for SiO_2 and low-κ (*cf*. Figs. 3-7 and 3-8) we can fit the long time behavior of the Cu peak to an exponentially decaying function to determine the minimum time of etching required to reveal the underlying substrate. Here we obviously ignore the initial transient. The fits to the data for Cu are shown by the dashed lines in Fig. 3-10. For the ~ 10 Å TaN_x thin film, we find the offset t_0 ~ 8 min., while for the 5 Å thin film, t_0 ~ 6 min. Both of these values exceed those observed for the other two surfaces, where in both cases the offsets were t_0 ~ 3 min. for the ~ 10 Å TaN_x thin film, and t_0 ~ 0 min. for the 5 Å thin film. Consistent with this longer time to reach the underlying substrate, we also observe that the etch time required for the Ta peak to reach a maximum is also larger for the TaN_x|Cu thin films (~ 8 min. vs. ~ 2 min. for SiO_2 and low-κ).

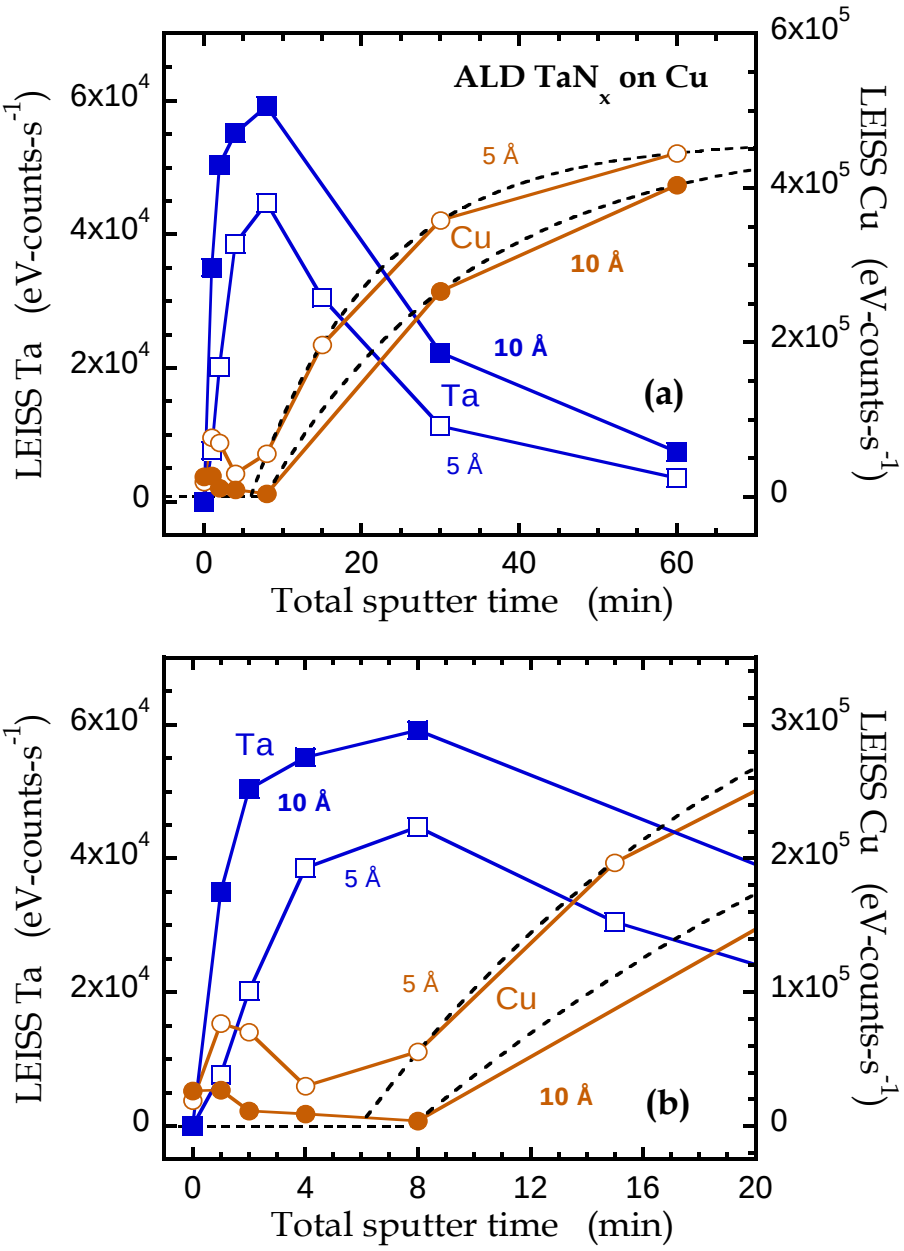

Figure 3-10 Integrated intensities of the LEISS Ta (left ordinate) and Cu (right ordinate) peaks as a function of the total Ar^+ sputter etch time for nominal 5 and 10 Å TaN_x ALD thin films on Cu. A short Ar+ etch time set of data are shown in **(b)**. The dashed lines represent fits of the Cu intensities to a simple model (see text).

3.5 Discussion

We begin first with a discussion of the results we have determined for the growth of TaN_x on SiO_2 and low-κ. To aid the discussion, in Table I we present some additional important metrics for the six thin films we have examined here and the starting substrates; namely, the RMS surface roughness and in-plane characteristic length from AFM (see Supplementary Material), and the time required of the Ar^+ ion beam etch to reveal the bulk ISS substrate peak [*cf*. Figs. 3-7(b) and 3-8(b)]. As described above in Sec. 3.4.2, our results from ARXPS are consistent with the formation of uniform flat thin films of TaN_x on both SiO_2 and low-κ, suggesting abrupt interfaces in both cases. The thin film thicknesses in all cases are consistent with a deposited thickness per cycle of ~ 0.5 Å-cycle^{-1}.

Additional information concerning the mechanism of growth and the spatial uniformity of thin film deposition can be obtained by examining the results from AFM. In one limit, in the absence of surface and/or bulk diffusion, random deposition (RD) produces a thin film that roughens relatively quickly, while the first layer fills via a decaying exponential function ("solid-on-solid" growth is described by a Poisson distribution of surface heights **[35]**). In Fig. 3-11(a) we plot the occupancy of each layer from RD (solid red lines) as a function of the mean thickness/total coverage. We also indicate the number of corresponding cycles of ALD, assuming a growth rate of 0.2 ML-cycle^{-1}. Assuming growth of cubic rocksalt TaN along the (111) direction **[36]**, this value corresponds to our measured rate of growth of 0.5 Å -cycle^{-1}. For RD, we see that ~ 5% of the substrate is still exposed after growth of 3 ML, which drops further to ~ 2% and ~ 1% after 4 and 5 MLs. In Fig. 3-11(b) we plot the RMS surface roughness as a function of the mean thickness. As may be seen, for RD the roughness grows rapidly with the square root of the thin film thickness (Poisson

statistics). In the other limit, in the presence of fast surface diffusion and rapid interlayer transport, growth can be layer-by-layer (LbL) **[35]**. In this mode, each layer fills sequentially, as shown by the solid black lines in Fig. 3-11(a). Here the substrate is completely covered by the thin film after a total coverage of 1 ML. For LbL the roughness oscillates be 0 and 0.5 ML as each layer is deposited, as displayed in Fig. 3-11(b).

In Fig. 3-11(b) we plot the RMS surface roughness measured by AFM (see Supplementary Material) for TaN_x ALD on SiO_2 and low-κ. To convert the roughness measured by AFM in Å, we have assumed that a thickness of 2.5 Å corresponds to a monolayer. Here we ignore any potential effects on the surface morphology due to the *ex situ* analysis and exposure to air. We also plot as dotted lines the predicted evolution of the surface roughness if growth on these two surfaces involved random deposition. As may be seen, there is little change in the roughness of the TaN_x thin films for 10 and 20 cycles of ALD, and the data are not well described by RD. Thus, the results from AFM favor smooth LbL growth of the TaN_x thin films on these two surfaces for this range of thicknesses.

The assignment of LbL growth up to at least 10 Å or ~ 4 MLs is tempered by our results from LEISS. If growth were truly LbL for 5 and 10 Å we would have expected a finite time of Ar^+ ion beam etching to reveal the bulk ISS substrate peak. From experiment, however, we observe a bulk ISS substrate peak for the 5 Å thick thin films once the adventitious carbon layer has been removed by Ar^+ ion sputter etching. Thus, while the thin films may be smooth from AFM, LEISS indicates that the 5 Å films are likely not continuous. We are left to conclude that while the results from ARXPS and AFM indicate that the TaN_x thin films are uniform and smooth, these results fall short in terms of

determining thin film continuity. This observation highlights the importance of using LEISS to address issues concerning thin film continuity.

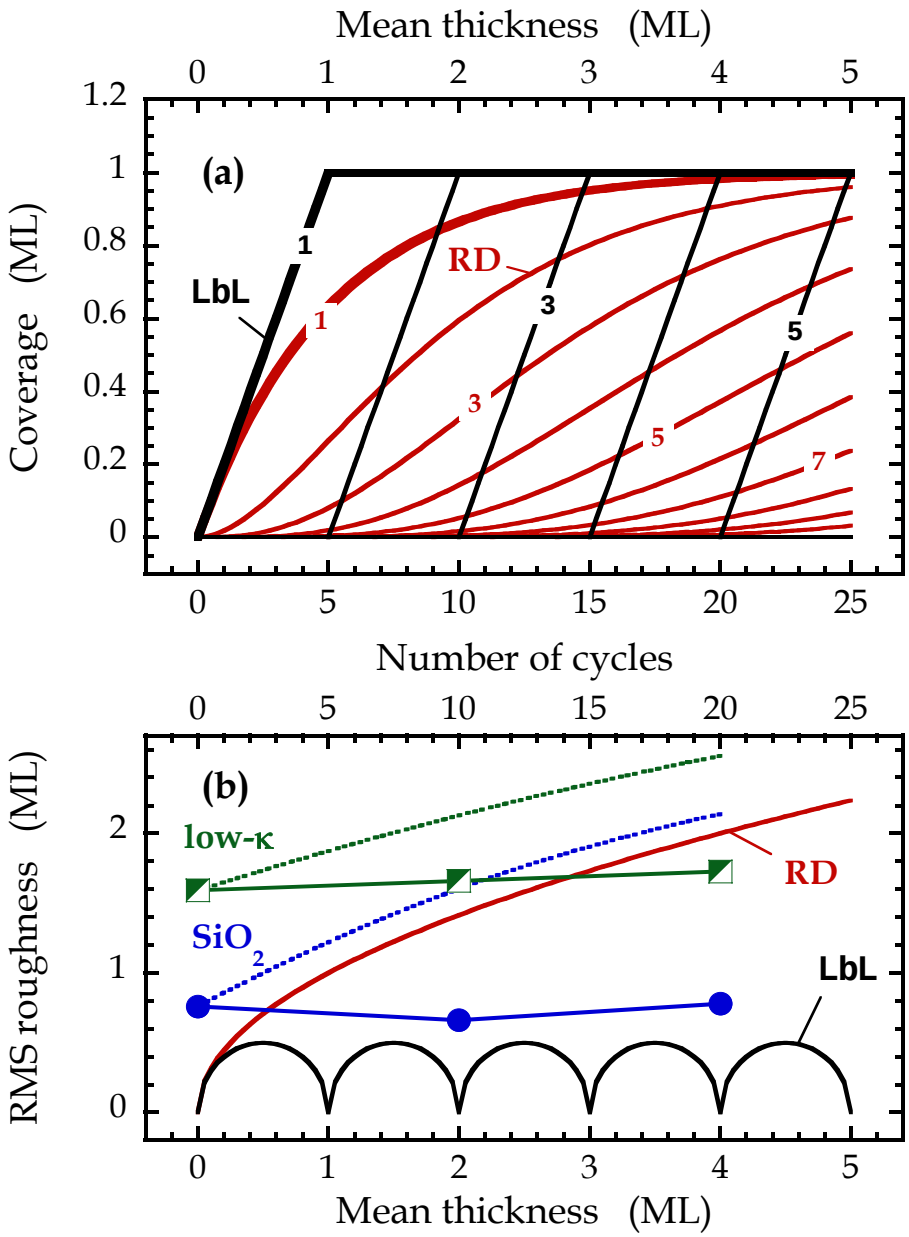

Figure 3-11 **(a)** Predicted layer occupancies as a function of the number of ALD cycles (lower abscissa) for two extremes of growth: layer-by-layer (LbL) growth (black lines) and random deposition (RD) (red lines). The assumed rate of ALD growth is 0.2 ML-cycle^{-1}. **(b)** RMS surface roughness vs. the mean thickness measured for TaN_x ALD growth on SiO_2 (blue) and low-κ (green). The dashed lines show the predicted roughness evolution if ALD growth on SiO_2 and low-κ was described by random deposition. The solid lines (black and red) represent the predicted evolution of the RMS surface roughness for the two models considered in **(a)**, assuming growth from a perfectly flat surface.

Our results for TaN_x ALD on Cu are quite distinct from those for the SiO_2 and low-κ surfaces. While analysis of the ARXPS data gave physical thicknesses for the TaN_x thin films that were reasonably in line with expectations, the qualitative nature of these data were not consistent with the formation of a uniform, smooth thin film with an abrupt interface. The results from LEISS confirmed this analysis, as a bulk ISS substrate peak was observed even for the as-received samples possessing the adventitious carbon contamination layer. In addition, the time required for Ar^+ ion etching to reach the true substrate signal was more than that observed on either the SiO_2 or low-κ surfaces. These results are best interpreted if we assume that a mixed TaN_x/Cu layer is formed on these surfaces.

Examination of the results from AFM for TaN_x|Cu are useful to further describe this situation. As may be seen from Table I the roughness of the starting substrate for the Cu thin films is considerably larger (~ 1 to 1-½ orders of magnitude) than that for the SiO_2 or low-κ surfaces we have examined. Perhaps most interesting is that we observe considerable smoothing of the surface after TaN_x ALD, where the change in the RMS surface roughness greatly exceeds the thickness of the deposited thin films. This can only occur if there is considerable mass transport of mostly Cu during or subsequent to the TaN_x ALD. Examination of line scans of the AF micrographs for all samples (see Supplementary Material) reveals the presence of pits or relatively deep (~ 150-200 Å) trenches/valleys for the Cu substrate, while these features are largely absent for the two TaN_x thin films. These pits/trenches present on the Cu substrate are still rather low aspect ratio features, appearing trapezoidal in cross-section and being ~ 1000 Å in width at the top, and ~ 300 Å in width at their base. A classic conformal ALD process depositing a 10 Å thick thin film on these features should have resulted in no change in the surface roughness. Clearly, this was not the

result. We are left to conclude that the ALD process itself has facilitated rather large scale mass transport of the Cu atoms in the substrate in this case, resulting in significant changes in the surface morphology. This is not totally unexpected in this case due to the expected much larger diffusivity of Cu with respect to Si in either SiO_2 or low-κ. The substrate temperature employed during ALD clearly plays a role in the evolution of the surface morphology, and we observe some changes in morphology due simply to annealing (see Supplementary Material). Nevertheless the presence of the ALD precursors also must play a role, as the films are smoothest following ALD. The strongest evidence for the latter is the observation of a change in the surface roughness between the 5 Å TaN_x thin film (~ 14 Å) and the 10 Å TaN_x thin film (~ 22 Å) that exceeds the nominal change in the TaN_x thickness.

3.6 Summary and Conclusions

We have presented a detailed examination of TaN_x thin films formed by ALD on thermally grown SiO_2; a Cu thin film grown by PVD; and a carbon(C)-doped SiO_2 porous low-κ thin film. We focused on thin films representing nominal thicknesses of 5 and 10 Å. The primary goal was to determine the effectiveness of *ex situ* analysis of ultrathin films using ARXPS, AFM, and LEISS and to determine thin film uniformity and continuity. First, an ultrathin layer of adventitious carbon was found on all surfaces, and it could be largely removed by a sufficiently short Ar^+ ion sputter etch. Analysis of the TaN_x thin films on SiO_2 and low-κ by ARXPS were consistent with the formation of smooth, uniform thin films with abrupt interfaces are formed. These results from ARXPS fall short in concluding absolute thin film continuity, however. For these two surfaces, analysis of the ratio of signals coming from the thin film and the substrate was nearly equivalent for the as-received samples and

those that had been subjected to a short Ar^+ ion sputter etch to remove adventitious carbon. Analysis of the TaN_x thin films on Cu by ARXPS, in contrast, gave results that were not consistent with smooth, uniform thin films, and abrupt interfaces. These results also changed quite significantly after removal of the majority of the adventitious carbon layer, suggesting that for these samples there was a non-uniform spatial distribution of this carbon layer, perhaps due to a corresponding variation of the composition of the surface of the deposited thin film/substrate.

Analysis of the substrates using LEISS both confirmed some of the results from ARXPS, but also revealed new features. Concerning the TaN_x thin films on SiO_2 and low-κ LEISS gave results that indicated that the thin films of ~ 10 Å thickness were continuous, covering essentially the entire substrate. Such is not the case for thin films of ~ 5 Å in thickness, and these films may represent the borderline of continuity. In these cases we arrived at this conclusion by not only examining the LEISS signals subsequent to removal of the adventitious carbon layer, but also the evolution of the substrate LEISS signal with Ar^+ sputter etch time. Concerning results from AFM, we found that they were consistent with layer-by-layer growth of the TaN_x thin films on these two substrates. These results do not contradict those from LEISS since AFM lacks the spatial resolution of LEISS in detecting sub 10 Å in-plane defects present at a few % in areal coverage. Thus, LEISS is decisive in determining thin film continuity.

The results from LEISS for the TaN_x thin films on Cu are quite different than those from the two SiO_2-based substrates. First, we observed a substrate (Cu) LEISS peak even for the as-received substrates. The Cu LEISS peak was observed to pass through a maximum with Ar^+ ion sputter etch time, consistent with the diffuse interface indicated from ARXPS.

The results from AFM indicated that TaN_x ALD resulted in considerable changes in the morphology of the Cu surface, much more than could be expected from thin film deposition alone. Combined, the results for ARXPS, LEISS and AFM indicate that the TaN_x thin films on Cu are not conformal, the TaN_x|Cu interface is not abrupt, and the near surface layers consist of a mixture of both TaN_x and Cu. In all cases we found the application of LEISS to be extremely useful and decisive in determining thin film continuity and interface abruptness for these ultrathin films.

3.7 Supplementary material

3.7.1 Experimental procedure

3.7.1.1 X-ray photoelectron spectroscopy

XPS was carried out in a UHV system using an Omicron Sphera U5 concentric hemispherical electron energy analyzer (Omicron Nanotechnology USA, Eden Prairie, MN), operated at a constant pass energy of 50 eV. Non- monochromated Mg Kα x-rays (1253.6 eV excitation energy) and Al Kα x-rays (1486.7 eV excitation energy) were produced using an Omicron DAR 400 twin anode source operated at 300 W (15 kV anode potential, 20 mA emission current). For angle-resolved XPS (ARXPS) measurements, the takeoff angle was varied by rotating the sample with respect to the analyzer axis. Background subtraction was carried out using the Shirley method [S-1] Peak areas were calculated by fitting spectra to a Gaussian/Lorentzian product formula with a mixing ratio of 0.7 [S-2]. Data analysis was carried out using CasaXPS software, version 2.3.15.

3.7.1.2 Low-energy ion scattering spectroscopy

LEISS was carried out in a UHV system using an Omicron Sphera U5 concentric hemispherical electron energy analyzer, operated at a fixed retard ratio (FRR) of 5. Helium ions possessing 1000 eV of kinetic energy were produced using a differentially pumped scanning small spot ion source (SPECS ion source IQE 12/38). The axis of the ion source is 40° off the axis the analyzer, resulting in an effective scattering angle for LEISS of 140°. For LEISS samples were oriented such that they were normal to the ion beam, and all samples were exposed to the ion beam for two minutes before the start of data collection to ensure a stable and constant ion beam current. A typical scan over the range of kinetic energies (1-1000 eV) would take approximately 10 min. For Ar^+ sputtering, a beam of ~ 136 μm dia., with a current of ~ 0.6 μA was rastered over an area of 1 × 1 cm^2, producing a time- averaged ion current density of 0.6 μA-cm^{-2}. We estimate a nominal sputter etch rate of TaN_x by these 3 keV Ar+ ions of 0.3 Å-min^{-1}. For LEISS, the He+ beam was ~ 146 μm dia., with a current of ~ 0.082 μA. Data analysis was carried out using CasaXPS software, version 2.3.15. Background subtraction was carried out assuming a linear baseline. Peak areas were calculated by fitting spectra to a Gaussian/Lorentzian product formula with a mixing ratio of 0.7. Asymmetry of the peaks was accounted for by using asymmetric line- shape functions in CasaXPS.

3.7.1.3 Atomic force microscopy

Atomic force microscopy (AFM) was carried out using a Digital Instruments Dimension 3100 atomic force microscope (Veeco Instruments, Woodbury, NY) in tapping mode. Images were analyzed using Gwyddion software, version 2.30.

3.7.2 Results and discussion

3.7.2.1 XPS of the C(1s) region

In Fig. 3S-1 we present results for XPS of the C(1s) region for nominal 10 Å thick TaN_x thin films on the three substrates we have examined here. For all three cases these are as-received samples that have not been subjected to Ar^+ ion sputter etching. As may be seen, we have fit this region to 3 peaks, the lowest binding energy (284.6 eV) representing aliphatic carbon. For the SiO_2 and low-κ samples, the aliphatic peak represents about 70-80% of the total C(1s) intensity, while the highest binding energy feature (~ 288.5 eV) is about 10%. In contrast, on Cu the the aliphatic peak represents about 60% of the total C(1s) intensity, while the highest binding energy feature is about 25%. The binding energy shift for the highest binding energy peak is ~ +3.9 eV. This value can be compared to expectations for carbonyl ($R_2C=O$) and ester functional groups [RO(C=O)R] of ~ +2.9 and 4.1 eV, respectively **[S-3]**. CO bound molecularly to Cu surfaces has been reported to exhibit strong shake-up features from ~ +3 to +7 eV in binding energy. We take note, however, that CO bound molecularly to Cu surfaces thermally desorbs at about 220 K **[S-4]**, well below the temperature where these XPS spectra were acquired.

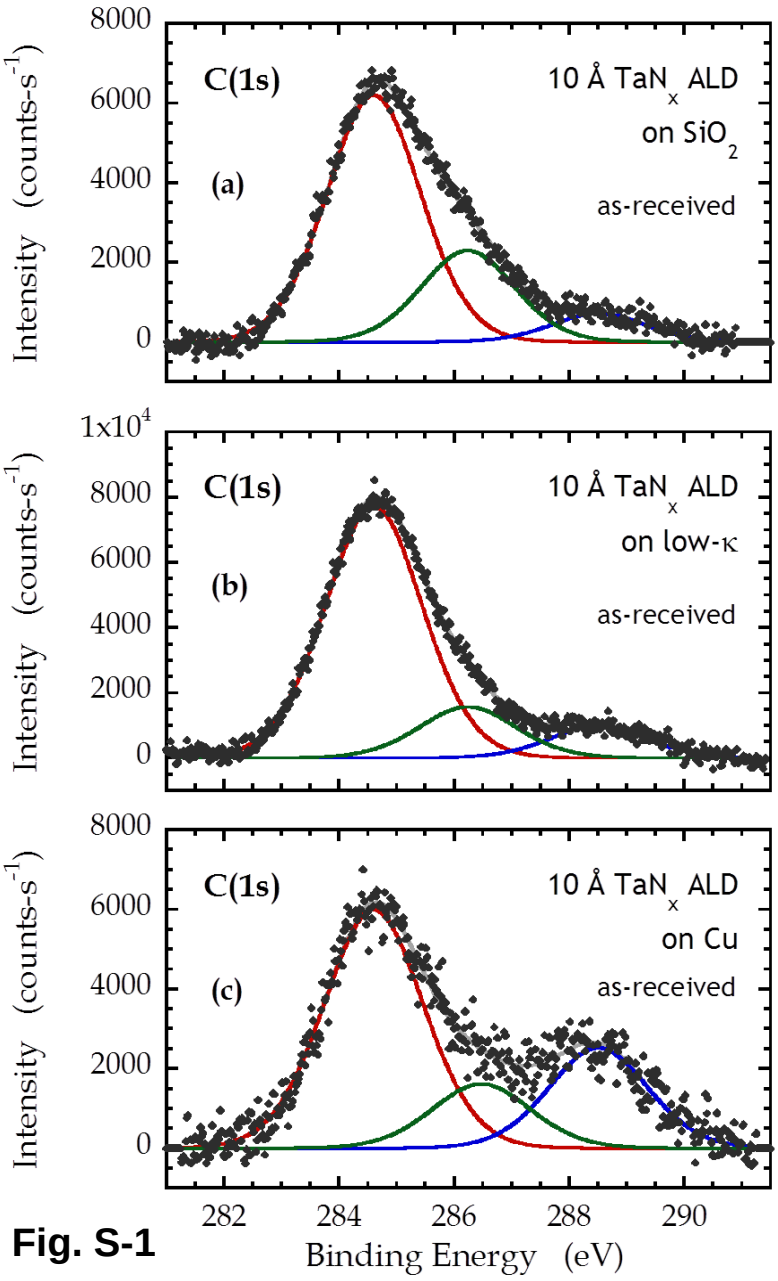

Fig. S-1

Figure 3S- 1 XPS C(1s) spectra for nominal 10 Å thick TaN_x films on **(a)** SiO_2, **(b)** low-κ and **(c)** Cu. These "as-received" samples that have not been subjected to Ar^+ ion sputter etching

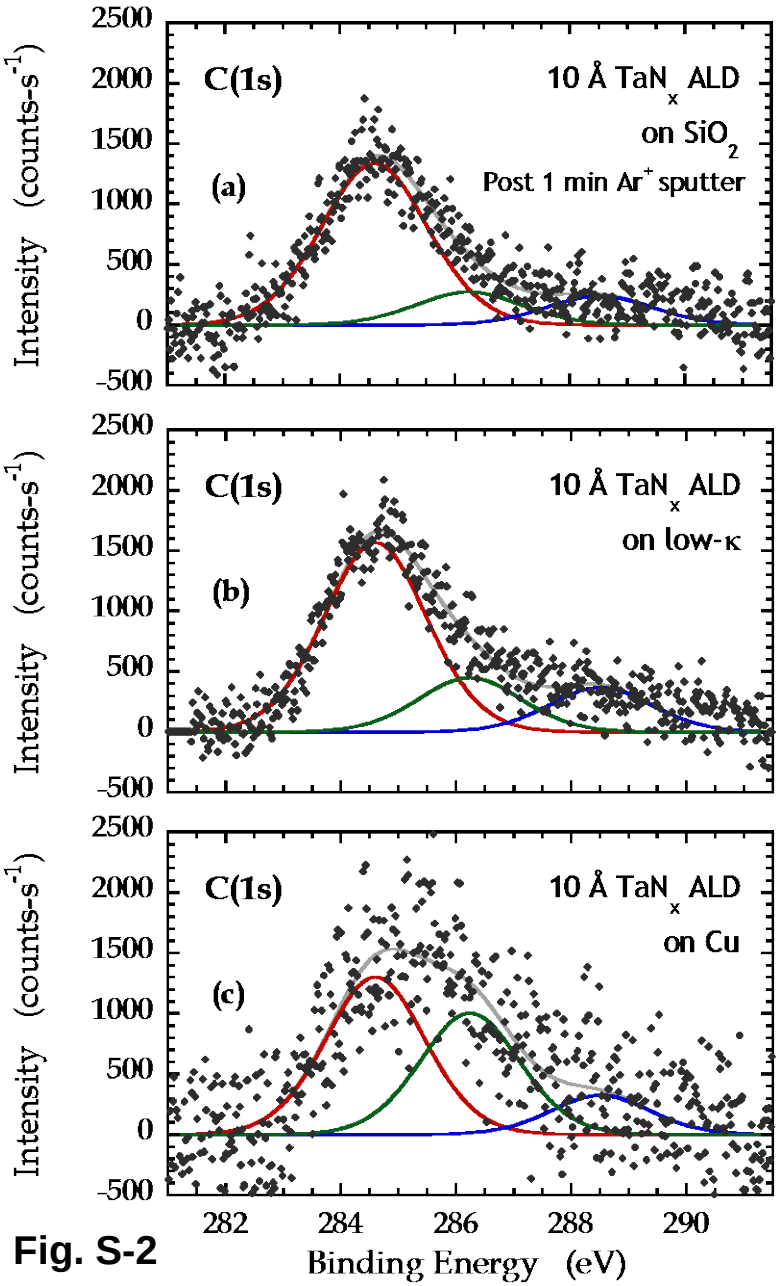

Fig. S-2

Figure 3S- 2 XPS C(1s) spectra for nominal 10 Å thick TaN_x films on **(a)** SiO_2, **(b)** low-κ and **(c)** Cu. These samples that have been subjected have been subjected to 1 min. of 3keV Ar^+ ion sputter etching

In Fig. 3S-2 we present spectra for the C(1s) region for nominal 10 Å thick TaN_x thin films on the three substrates we have examined here. For all three cases these are after the samples have been subjected to 1 min. of Ar^+ ion sputter etching. In all cases the total intensity for the C(1s) is about ¼ of that found for the as-received samples. We also observe that the fraction now associated with the high binding energy feature is quite close for all 3 of these sputter etched samples, all being in the range of 13-16% of the total intensity. We are left to conclude that the high binding energy feature (whatever species it is), present in the greatest concentration for the as-received samples for TaN_x on Cu, may be adsorbed preferentially on regions of the surface that are unique to them, namely, exposed Cu. This proposition provides an excellent explanation for the significant changes we observed in the ratio of intensities, $Ta(4d_{5/2})/Cu(2p_{3/2})$, for as-received and after 1 min. of Ar^+ ion sputter etching for only the TaN_x thin film samples on Cu (*cf*. Fig. 3-7).

3.7.2.2 XPS of the O(1s) region

In Fig. 3S-3 we present results for XPS of the O(1s) region for nominal 10 Å thick TaN_x thin films on the three substrates we have examined here. For all three cases these are as-received samples that have not been subjected to Ar+ ion sputter etching. In the case of SiO_2 and low-κ, we clearly observe two peaks, corresponding to O bound to Ta (low binding energy) and to Si in the underlying substrate (high binding energy). The chemical shift between these two peaks is ~ 2.0 eV. If we average over all values obtained as a function of Ar^+ sputter etch time we find that the mean shift for both samples is ~ 1.6 eV. These values can be compared to the expected shift for the two stoichiometric oxides: Ta_2O_5 and SiO_2,

which is ~ 2.0-4.5 eV **[S-3]**. While the SiO_2 substrate examined here is certainly stoichiometric oxide, the Ta is not; as there is considerable N content in the as-received thin films. Thus, a smaller shift reflecting the presence of TaN_xO_y is reasonable. On Cu, a single broad feature is observed, which cannot be fit to a single peak with a reasonable full-width at half maximum (FWHM). Fitting this feature to two peaks gives a chemical shift of ~ 1.3 eV. The low binding energy peak is again best associated with O bound to Ta, while the higher binding energy peak is likely associated with O bound to Cu.

A good indicator that the low binding energy O(1s) peak is associated with bonding to Ta can be found by plotting the intensity of both the Ta($4d_{5/2}$) and the low-binding energy O(1s) feature vs. the Ar^+ sputter etch time. These data are plotted in Fig. 3S-4 for all three surfaces, all possessing nominal 10 Å thick TaN_x thin films. In all cases the intensities are normalized to the values observed after 1 min. of Ar^+ sputter etching. We see that there is an excellent correlation between these two components, particularly at short Ar^+ sputter etch times. Eventually (t > 4 min.), the low-binding energy O(1s) feature decays more rapidly, which most probably reflects a difference in the sputter etch yield for O vs. Ta.

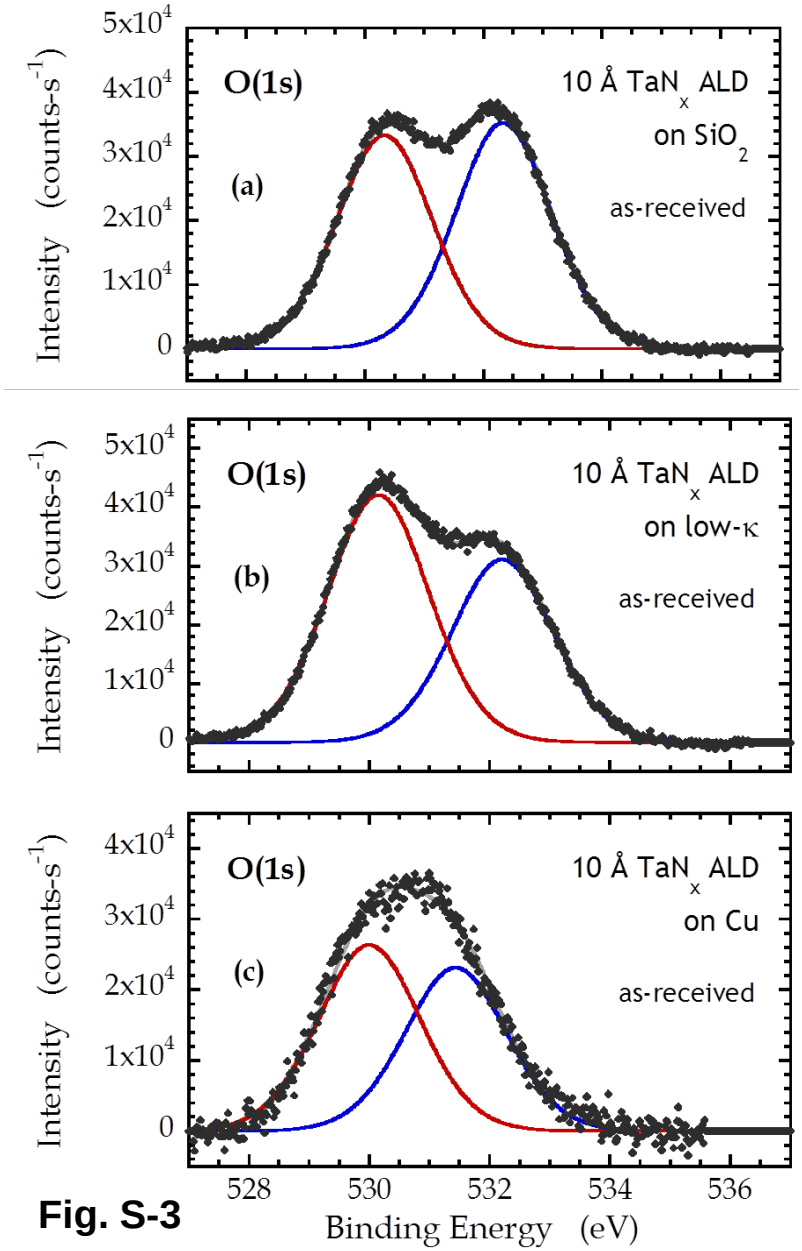

Fig. S-3

Figure 3S- 3 XPS O(1s) spectra for nominal 10 Å thick TaN_x films on **(a)** SiO_2, **(b)** low-κ and **(c)** Cu. These "as-received" samples that have not been subjected to Ar^+ ion sputter etching

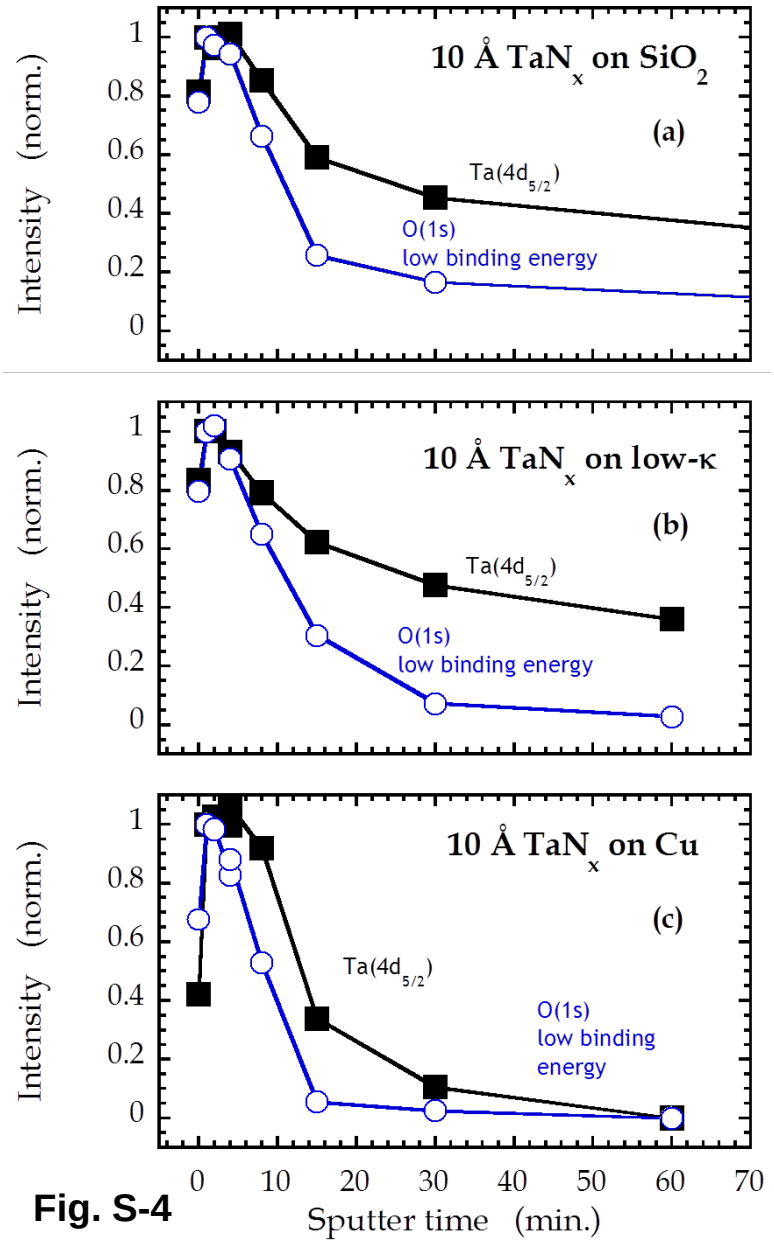

Fig. S-4

Figure 3S- 4 Normalized integrated intensity of Ta($4d_{5/2}$) and the low-binding energy O(1s) feature vs. the Ar^+ sputter etch time for nominal 10 Å thick TaN_x films on **(a)** SiO_2, **(b)** low-κ and **(c)** Cu.

3.7.2.3 XPS of the N(1s) region

In Fig. 3S-5 we display XPS spectra of the N(1s) and Ta($4p_{3/2}$) region for a nominal 10 Å thick TaN_x thin film on SiO_2 [(a) as received, and (b) after 1 min. of Ar^+ sputter etching], and a much thicker (~ 140 Å) TaN_x thin film, on SiO_2 and after 2 min. of Ar^+ sputter etching. From Fig. 3S-5(a) and (b) we see that there are only modest changes in the spectra for the as-received and after 1 min. of Ar^+ sputter etching. After removal of most of the adventitious carbon layer with 1 min. of Ar^+ sputter etching, both the N(1s) and Ta($4p_{3/2}$) peaks increase by ~ 10%. The computed elemental ratio N/Ta for the two samples is (a) 0.32 and (b) 0.30. These results can be compared to those for the much thicker 140 Å TaN_x thin film. For this film we find a N/Ta ratio of 0.91.

Returning to the results for the 5 and 10 Å thick TaN_x thin films we have observed considerable incorporation of oxygen, as discussed above in connection with Figs. 3S-3 and 3S-4. If we assign the low binding energy component O(1s) to atoms bound to Ta, we can compute the fraction that is associated with nitride vs. oxide.

Assuming a simple mixture of two compounds, $(TaN)_y(TaO_{5/2})_{1-y}$, for the samples subjected to 1 min. Ar^+ sputter etching we find values for the fraction of nitride (y) for nominal 5 and 10 Å TaN_x thin films of y ~ 0.17 and 0.24 on SiO_2; and 0.09 and 0.19 on low-κ. On both of these surfaces we see that the thinner films are susceptible to more significant oxidation. We do not report a similar value here for the TaN_x thin films on Cu, as there is poor separation of the O peaks associated with Ta and, presumably Cu. For example, for the 5 Å TaN_x thin film on Cu the calculated elemental ratio O/Ta [using O(1s)low] exceeds 5/2.

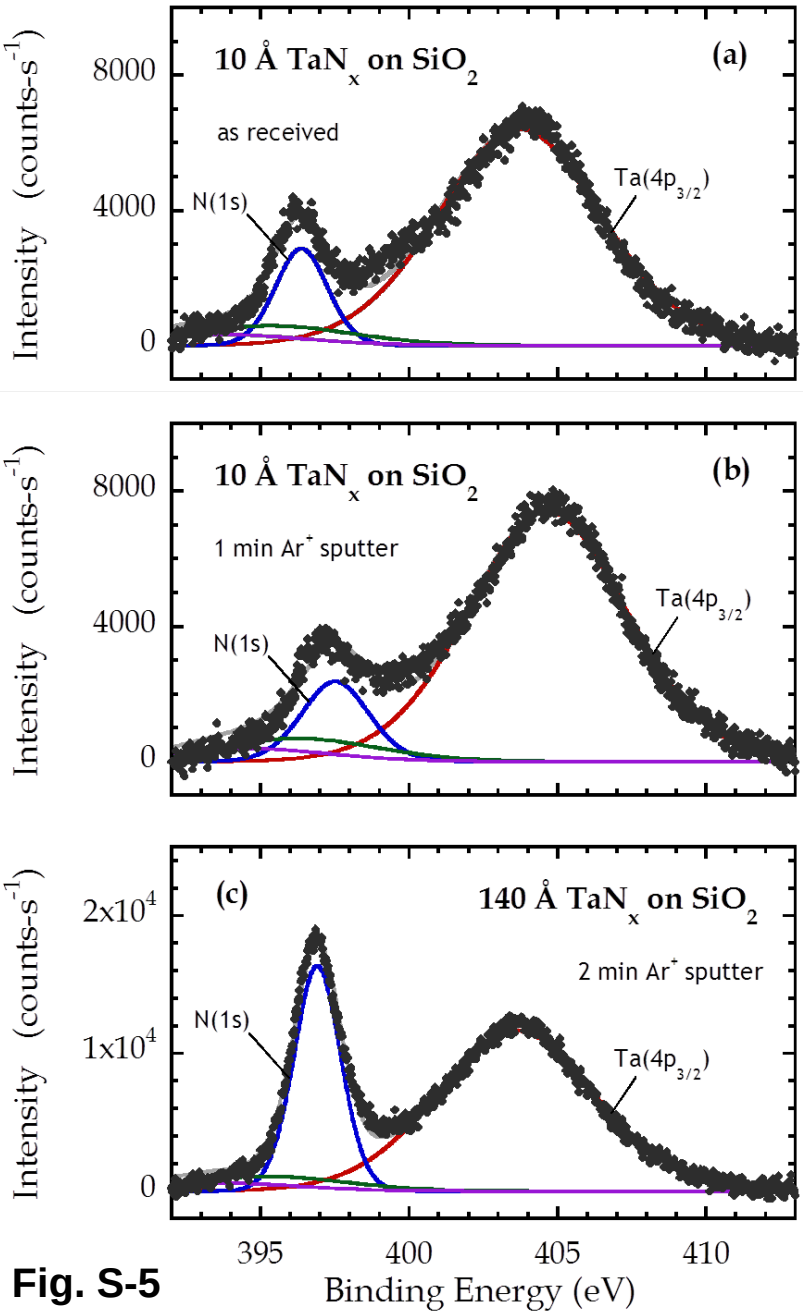

Fig. S-5

Figure 3S- 5 XPS spectra of the N(1s) and Ta($4p_{3/2}$) region for a nominal 10 Å thick TaN_x thin film on SiO_2 [**(a)** as received, and **(b)** after 1 min. of Ar+ sputter etching], and a much thicker (~ 140 Å) TaN_x thin film, on SiO_2 and after 2 min. of Ar+ sputter etching

In Fig. 3S-6 we plot the elemental N/Ta ratio for all six thin films examined here. These results confirm that the TaN_x thin films have been depleted of N by exposure to air. The thinner films, particularly on SiO_2 and low-κ, exhibit a greater loss of N. The more rapid extinction of the N signal on Cu with sputter etch time could reflect weaker binding of this element to the underlying substrate, e.g., ion-induced mixing during sputtering could produce stronger covalent Si-N bonds on SiO_2 and low-κ. Similar bonds cannot form on Cu.

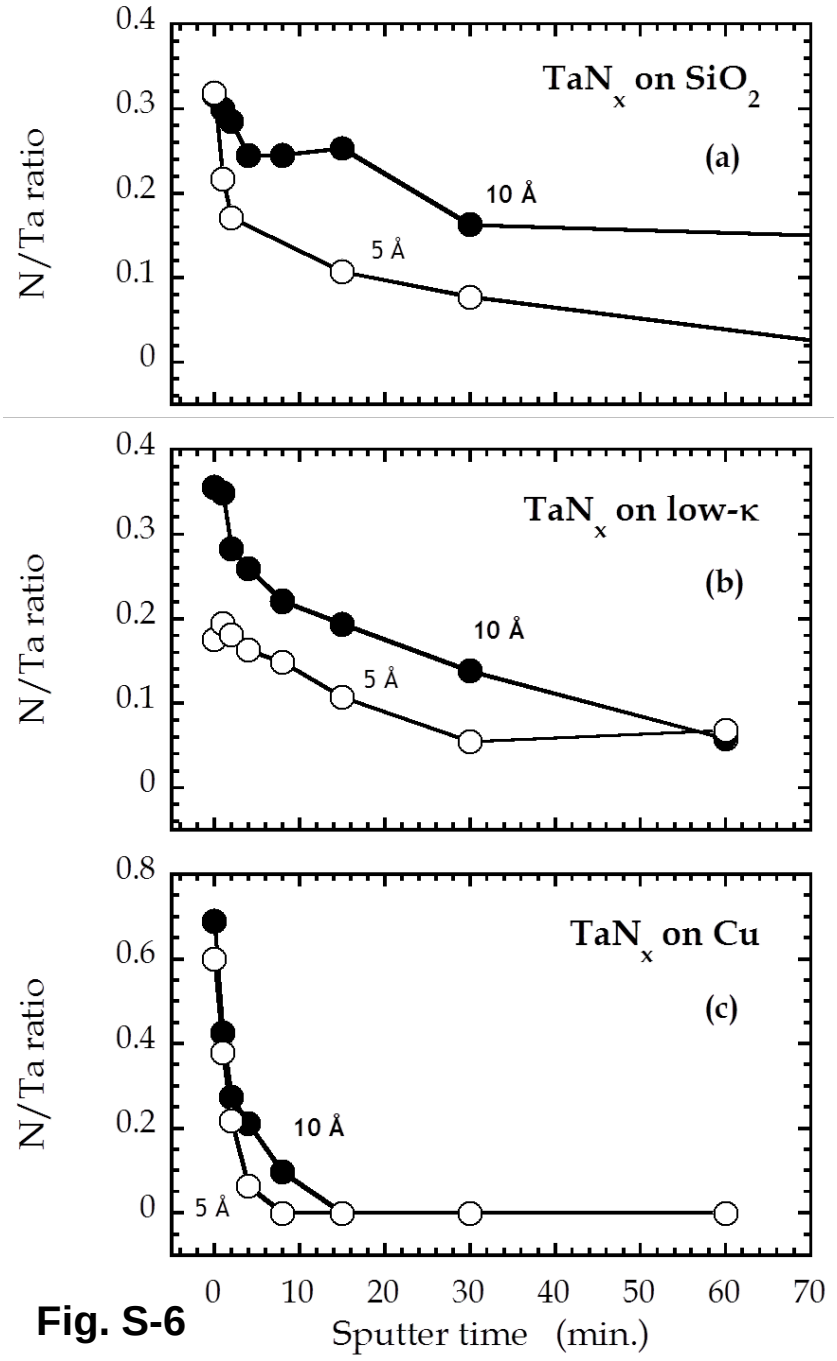

Fig. S-6

Figure 3S- 6 Calculated elemental N/Ta ratio vs. the Ar^+ sputter etch time for nominal 5 Å and 10 Å thick TaN_x films on **(a)** SiO_2, **(b)** low-κ and **(c)** Cu

3.7.2.4 Atomic force microscopy

In Fig. 3S-7 we present atomic force micrographs concerning our results on SiO_2 for the as-received substrate and after 10 and 20 cycles of TaN_x ALD. Also shown are representative line scans for each of these cases. As may be seen on SiO_2 there is little change in the surface morphology after 10 and 20 cycles of TaN_x ALD. There appears to be modest smoothening after 10 cycles of ALD, but the total change in the RMS surface roughness is ~ 0.03 nm. These results are consistent with the formation of a uniform and smooth TaN_x thin film for these thicknesses.

In Fig. 3S-8 we present atomic force micrographs concerning our results on low-κ for the as-received substrate and after 10 and 20 cycles of TaN_x ALD. Also shown are representative line scans for each of these cases. As may be seen on low-κ there is little change in the surface morphology after 10 and 20 cycles of TaN_x ALD, similar to the results for SiO_2. The change in the RMS surface roughness is 0.017 and 0.034 nm after 10 and 20 cycles of ALD. These values suggest that ALD growth is uniform and smooth.

Before moving on to the results for Cu we first touch on the effects of the finite tip radius in AFM. Tip convolution effects are complex, particularly concerning tapping-mode AFM, but a simple analysis is still illustrative. In our case the AFM tips possess a radius of curvature of ~ 9 ± 2 nm. Using this value, contact mode of a spherical tip over a surface possessing 1 nm rectangular trenches (approximate pore size in the low-κ) will give a peak-to-peak corrugation of ~ 0.014 nm. Increasing the trench width to 2 nm would give a corrugation of 0.056 nm. These values are on the order of the changes in RMS surface roughness on both SiO_2 and low-κ, which gives one pause. This simple analysis indicates

that thickness variations that are on the order of 1 nm in the plane of the surface will be nearly impossible to assess using AFM. Thus we are mostly blind to sub-1 nm in-plane defects, which may, nevertheless, be visible to the probe He^+ ions used in LEISS.

In Fig. 3S-9 we present atomic force micrographs concerning our results on Cu for the as-received substrate and after 10 and 20 cycles of TaN_x ALD. Also shown are representative line scans for each of these cases. Unlike the two SiO2-based surfaces, the change in surface morphology after 10 cycles of TaNx ALD on Cu is striking. The ~ 10-20 nm deep trenches apparent on the as-received sample are absent after the deposition of a nominal 0.5 nm thick TaN_x thin film. The ALD thin film can of course not fill trenches of this size, thus considerable mass transport of Cu atoms in the substrate is implicated. The roughness increases from 10 to 20 cycles, again to an extent that cannot be explained by thin film deposition alone.

To assess the in-plane structure and feature size of the 9 samples investigated here we have conducted a statistical analysis of the AF micrographs. Two examples are shown in Fig. 3S-11, where we plot the 1D power spectral density (PSD) vs. the spatial frequency. For surfaces that are self-affine, the one-dimensional power spectral density exhibits two linear regions on a log-log plot: a plateau region at low spatial frequencies denoting the absence of correlations, and a frequency–dependent, fall-off region indicative of the self–affine nature of the film **[S-4]**. Where these two regions intersect defines a correlation length, ξ. From these two examples, as received Cu, and a 10 Å TaN_x thin film on low-κ, we compute correlation lengths of 38 and 27 nm respectively.

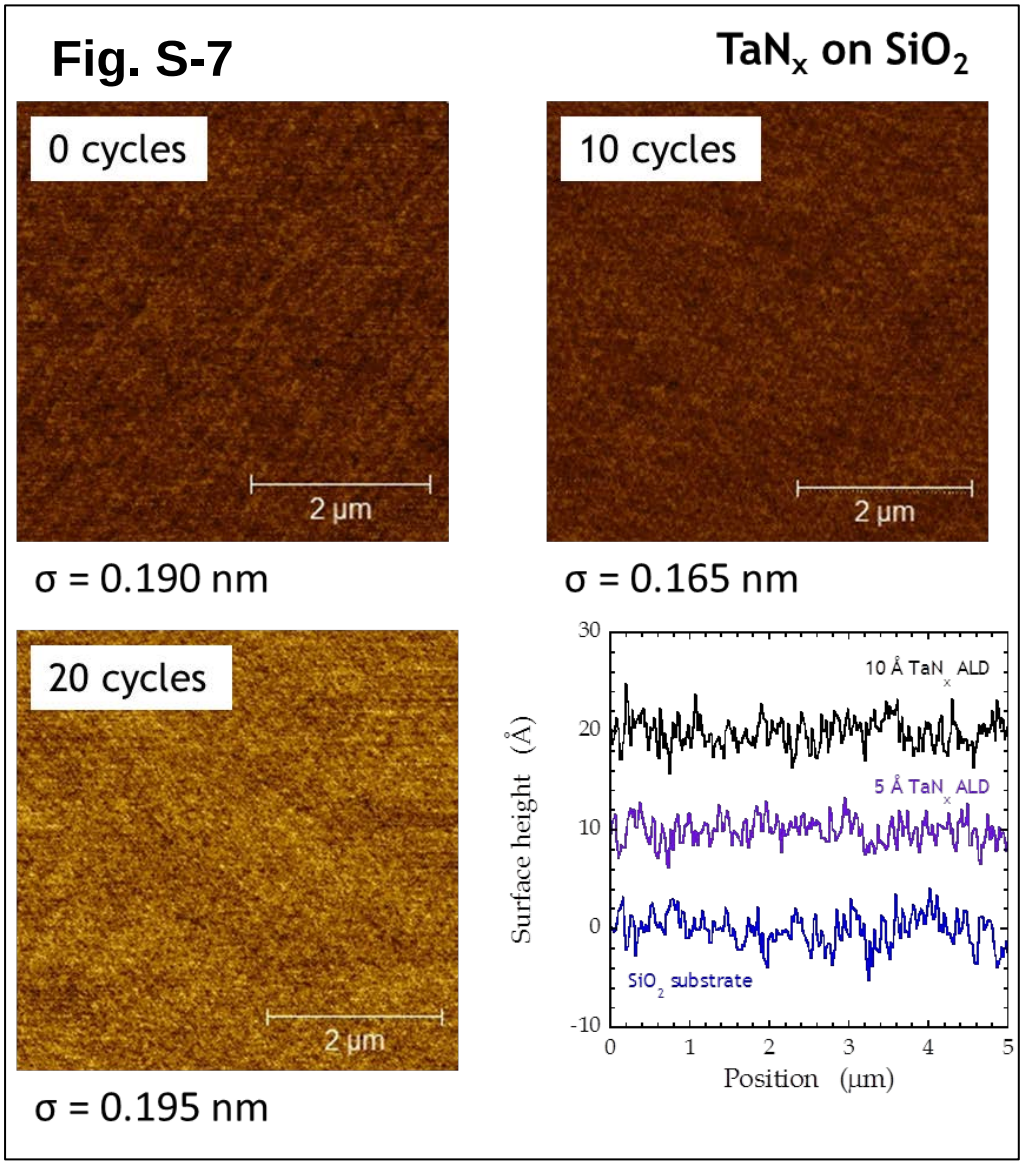

Figure 3S- 7 Atomic force micrographs on SiO_2, the as-received substrate, after 10 and 20 cycles of TaN_x ALD, and a representative line scan for each case

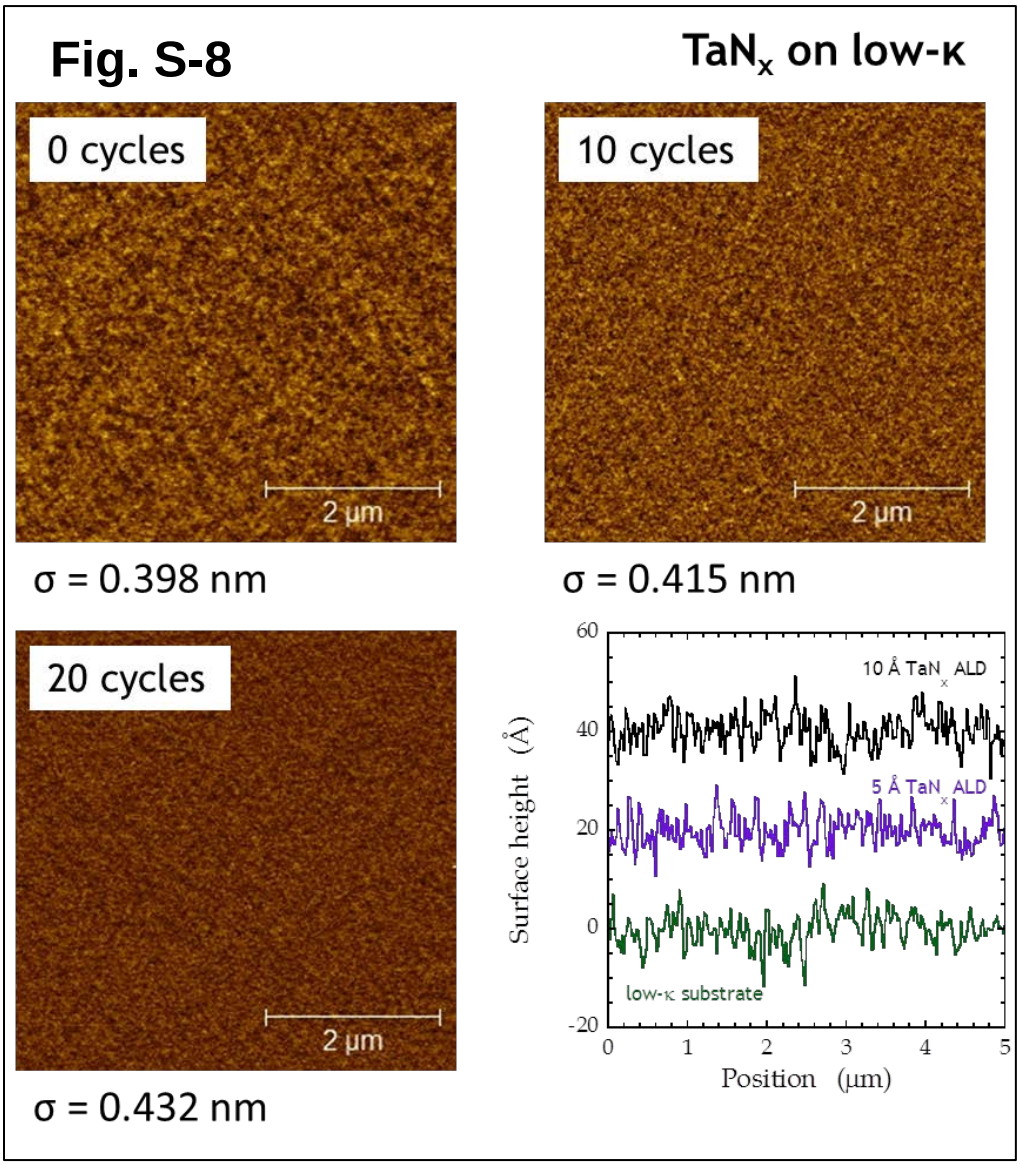

Figure 3S- 8 Atomic force micrographs on low-κ, the as-received substrate, after 10 and 20 cycles of TaN_x ALD, and a representative line scan for each case

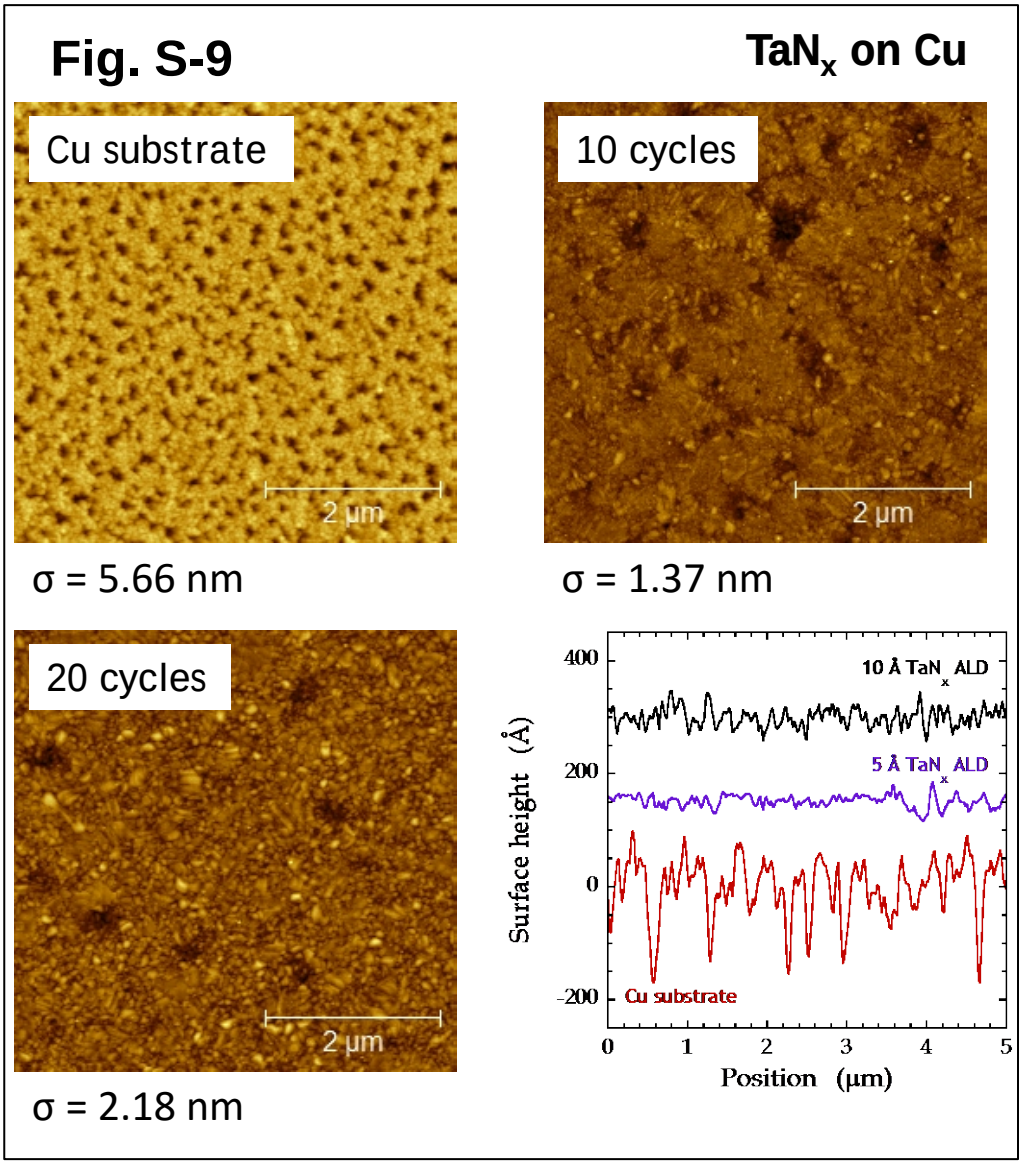

Figure 3S- 9 Atomic force micrographs on Cu, the as-received substrate, after 10 and 20 cycles of TaN_x ALD, and a representative line scan for each case

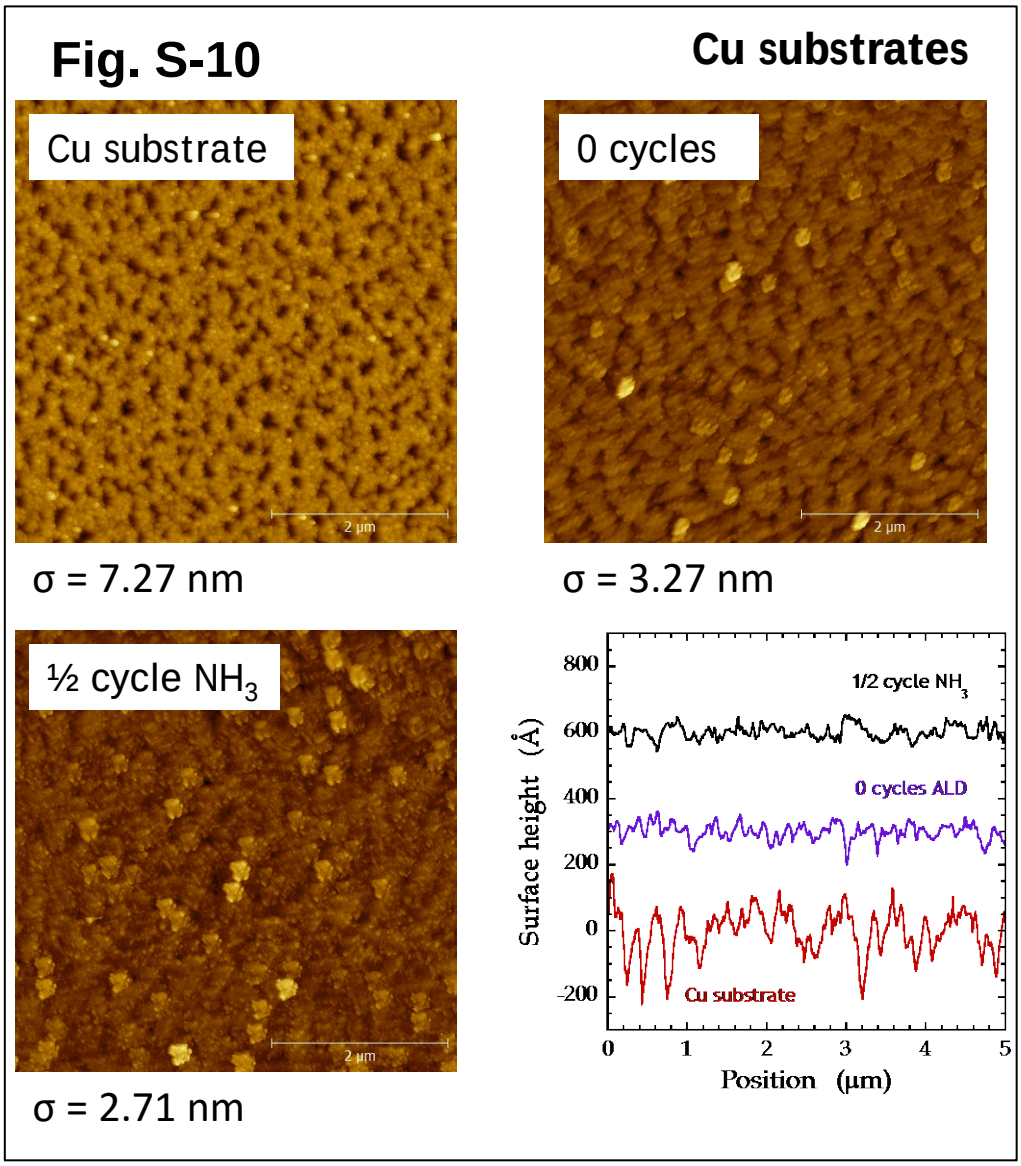

Figure 3S- 10 Atomic force micrographs on as received Cu substrate, post 5 min ALD temperature anneal in Ar, post 5 min ALD temperature anneal in NH_3, and a representative line scan for each case

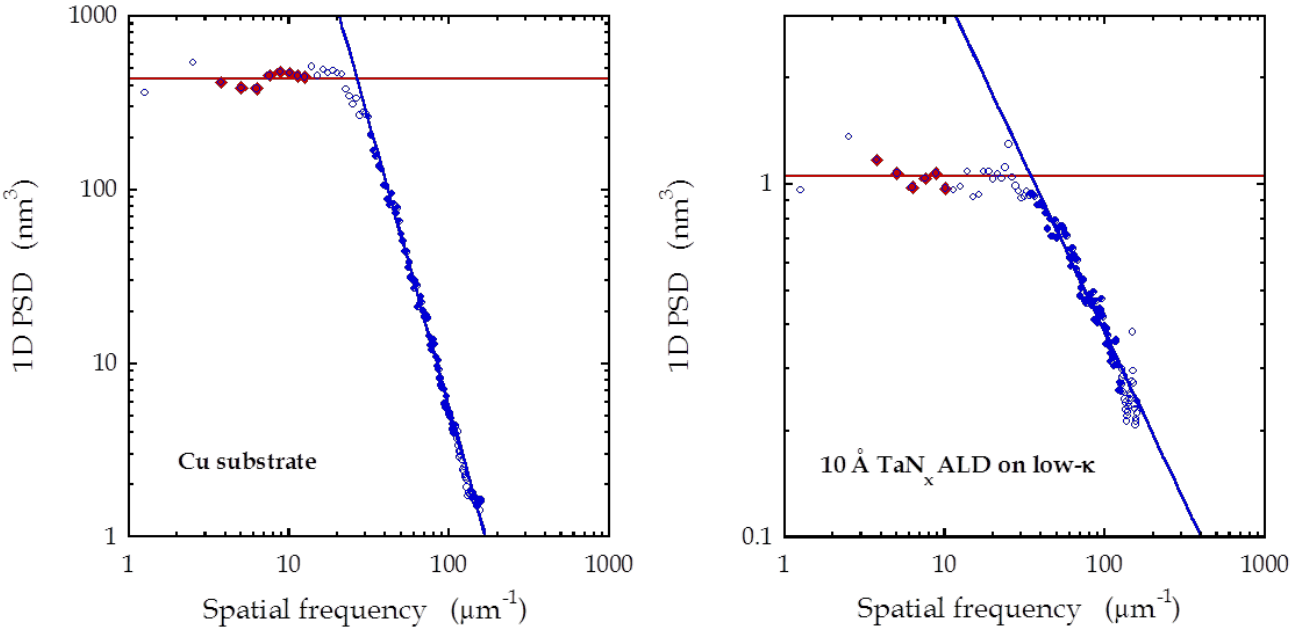

Figure 3S- 11 1D power spectral density (PSD) vs. the spatial frequency for Cu substrate and a nominal 10 Å thick TaN_x films on low-κ

3.8 Acknowledgements

The authors would like to thank Harris C. Karsch for technical contributions. This work made use of the shared facilities of the Cornell Center for Materials Research, which was supported through the NSF MRSEC program (DMR- 1120296). R.K.N. acknowledges support from the NSF IGERT program in Materials for a Sustainable Future (DGE-0903653).

3.9 References

[1] S. George, Chem. Rev. **110**, 111 (2010).

[2] O.Van der Straten, S. M. Rossnagel, J. P. Doyle, K. P. Rodbell, ECS Transactions, **1**, 51 (2006).

[3] M. Ohring, *The Materials Science of Thin Films* (Academic Press, London, United Kingdom, 1992).

[4] R. L. Schwoebel and E. J. Shipsey, J. Appl. Phys. **37**, 3682 (1966).

[5] G. Ehrlich and F. G. Hudda, J. Chem. Phys. **44**, 1039 (1966).

[6] A. Dube, M. Sharma, P. F. Ma, P. A.Ercius, D. A. Muller and J. R. Engstrom, J. Phys. Chem. C **111**, 11045 (2007).

[7] K. J. Hughes and J. R. Engstrom, J. Vac. Sci. Technol. A **28**, 1033 (2010).

[8] H.H. Brongersma, M. Draxler, M. de Ridder and P. Bauer, Surf. Sci. Rep. **62**, 63 (2007).

[9] H.H. Brongersma and J. Jacobs, Appl. Surf. Sci. **75,** 133 (1994).

[10] Y. Luo, D. Slater, M. Han, J. Moryl, R. M. Osgood, Jr. and J. G. Chen, Langmuir **14,** 1493 (1998).

[11] T. Nakamura, H. Inada, M. Iiyama, Appl. Surf. Sci. **130-132**, 576 (1998).

[12] M. de Ridder, P. C. van de Ven, R. G. van Welzenis, S. Helfensteyn, C. Creemers, P. Van Der Voort, M. Mathieu, E. F. Vansant and H. H. Brongersma, *J. Phys. Chem. B.* **106**, 13146 (2002).

[13] E.B.O. da Rosa, C. Krug, C. Radtke, R. P. Pezzi, L. Miotti, R. Brandão, J. Morais, I.J.R. Baumvol, F.C. Stedile, Surface Rev. Lett. **9**, 393 (2002).

[14] A. Satta, J Schuhmacher, C. M. Whelan, W. Vandervorst, S. H. Brongersma, G. P. Beyer, K. Maex, A. Vantomme, M. M. Viitanen, H. H. Brongersma and W. F. A. Besling, J. Appl. Phys. **92**, 7641 (2002).

[15] T. Conard, W. Vandervorst, J. Petry, C. Zhao, W. Besling, H. Nohira and O. Richard, Appl. Surf. Sci. **203–204**, 400 (2003).

[16] R.L. Puurunen, W. Vandervorst, W. F. A. Besling, O. Richard, H. Bender,T. Conard, C. Zhao, A. Delabie, M. Caymax, S. De Gendt, M. Heyns, M. M. Viitanen, M. de Ridder, H. H. Brongersma, Y. Tamminga, T. Dao, T. de Win, M. Verheijen, M. Kaiser and M. Tuominen, J. Appl. Phys. **96**, 4878 (2004)

[17] P. D. Kirsch, J. H. Sim, S. C. Song, S. Krishnan, J. Peterson, H. J. Li, M. Quevedo-Lopez, C. D. Young, R. Choi, N. Moumen, P. Majhi, Q. Wang, J. G. Ekerdt, G. Bersuker and B. H. Lee, Solid-State Device Research Conference, ESSDERC, Proceedings of 35th European, 367 (2005).

[18] M. Stokhof, H. Sprey, W. Li, S.Haukka, M. Ridder de, H. Bringsersma, ECS Trans. **1**, 71 (2006).

[19] Y. Lebedinskii, A. Zenkevich, G. Scarel and M. Fancciulli, Rare Earth Oxide Thin Films, Topics Appl. Phys. **106**, 127 (2007).

[20]L. Miotti, R. P. Pezzi, M. Copel, C. Krug, and I. J. Baumvol, Appl. Phys. Lett. **90**, 052913 (2007)

[21] J. Yoshihara, S. C. Parker, C. T. Campbell, J. Vac. Sci. Technol. A **28**, 1033 (2010).

[22]Q. Ma, H. Guo, R. G. Gordon and F. Zaera, Chem. Mater. **22,** 352 (2010)

[23]R. ter Veen, M. Fartmann, R. Kersting, and B. Hagenhoff, J. Vac. Sci. Technol. A **31**, 01A113 (2013)

[24] R.G. Vitchev, J.J. Pireaux, T. Conard, H. Bender, J. Wolstenholme, Chr. Defranoux, Appl. Surf. Sci. **235**, 21 (2004).

[25] P. Mack, R.G. White, J. Wolstenholme, T. Conard, Appl. Surf. Sci. **252**, 8270 (2006).

[26] K. J. Hughes and J. R. Engstrom, J. Vac. Sci. Technol. A **30**, 01A102 (2012).

[27] S. Hofmann, Surf. Interface Anal. **2**, 148 (1980).

[28] M. Zier, S. Oswald, R. Reiche, and K. Wetzig, Appl. Surf. Sci. **252**, 234 (2005).

[29] (a) M. P. Seah and S. J. Spencer, J. Vac. Sci. Technol. A **21**, 345 (2003); (b) M. P. Seah and S. J. Spencer, Surf. Interface Anal. **33**, 640 (2002); (c) M. P. Seah and R. White, Surf. Interface Anal. **33**, 960 (2002).

[30] R. Champaneria, P. Mack, R. White and J. Wolstenholme, Surf. Interface Anal. **35**, 1028 (2003).

[31] S. Tanuma, C. J. Powell, D. R. Penn, Surf. Interface Anal. **21**, 165 (1993).

[32] E. Taglauer, W. Heiland, Appl. Phys. **9,** 261 (1976).

[33] C. Somerton, D. King, Surf. Sci. **89**, 391 (1979).

[34] R. Spitzl, H. Niehus, G. Comsa, Surf. Sci. Lett. **250**, 355 (1991).

[35] A.-L. Barabási and H. E. Stanley, *Fractal Concepts in Surface Growth* (Cambridge University Press, Cambridge, United Kingdom, 1995).

[36] R. Sreenivasan, T. Sugawara, K. C. Saraswat, P. C. McIntyre, Appl. Phys. Lett. **90**, 102101 (2007).

[S-1] D. Briggs and G. Beamson, Anal. Chem. **64**, 1729 (1992).

[S-2] See, e.g., J. A. Rodriguez, W. D. Clendening and C. T. Campbell, J. Phys. Chem. **93**, 5238-5248 (1989).

[S-3] NIST X-ray Photoelectron Spectroscopy Database, Version 4.1 (National Institute of Standards and Technology, Gaithersburg, 2012); http://srdata.nist.gov/xps/

[S-4] A.-L. Barabási and H. E. Stanley, *Fractal Concepts in Surface Growth*; Cambridge University Press: Cambridge, United Kingdom (1995).

4. The effect of substrate composition on selective area atomic layer deposition using self-assembled monolayers as blocking layers

4.1 Abstract

We have examined the effect of two molecules that form self-assembled monolayers (SAMs) on the subsequent growth of TaN_x by atomic layer deposition (ALD) on two substrate surfaces, SiO_2 and Cu. The SAMs that the authors have investigated include two vapor phase deposited, fluorinated alkyl silanes: $Cl_3Si(CH_2)_2(CF_2)_5CF_3$ (FOTS) and $(C_2H_5O)_3Si(CH_2)_2(CF_2)_7CF_3$ (HDFTEOS). Both the SAMs themselves and the TaN_x thin films, grown using $Ta[N(CH_3)_2]_5$ and NH_3, were analyzed *ex situ* using contact angle, spectroscopic ellipsometry, x-ray photoelectron spectroscopy (XPS), and low energy ion-scattering spectroscopy (LEISS). First, the authors find that both SAMs on SiO_2 are nominally stable at T_s ~ 300 °C, the substrate temperature used for ALD, while on Cu, the authors find that HDFTEOS thermally desorbs, while FOTS is retained on the surface. The latter result reflects the difference in the head groups of these two molecules. The authors find that both SAMs strongly attenuate the ALD growth of TaN_x on SiO_2, by about a factor of 10, while on Cu, the SAMs have no effect on ALD growth. Results from LEISS and XPS are decisive in determining the nature of the mechanism of growth of TaN_x on all surfaces. Growth on SiO_2 is 2D and approximately layer-by-layer, while on the surfaces terminated by the SAMs, it nucleates at defect sites, is islanded, and is 3D. In the latter case, our results support growth of the TaN_x thin film over the SAM, with a considerable delay in formation of a continuous thin film. Growth on Cu, with or without the SAMs, is also 3D and islanded,

and there is also a delay in the formation of a continuous thin film as compared to growth on SiO_2. These results highlight the power of coupling measurements from both LEISS and XPS in examinations of ultrathin films formed by ALD.

4.2 Introduction

Atomic layer deposition (ALD) is well-suited to the formation of ultrathin films **[1]**, particularly concerning growth on topologically complex three-dimensional device features such as those found in interconnect layers **[2]**. However, conformal deposition where a thin film is formed on all exposed areas of a substrate is not always desired, especially when only select features need be deposited. For example, in many device manufacturing applications, deposition may be desired on one exposed surface (e.g., metal) and not on another (e.g., dielectric). Selective deposition is a process where materials are only deposited where desired, effectively eliminating additional patterning steps using lithography and etching. Many current selective deposition technologies rely on lithography to pattern areas and block growth on areas where thin film growth is not desired. With device features becoming three dimensional and shrinking every generation, lithography is becoming less feasible and the development of ALD processes that are selective is of increasing interest.

A common approach to achieve selective deposition is to provide a masking material over areas of the substrate where deposition is not desired. In previous work self-assembled monolayers (SAMs) have shown promise as molecular-scale masks, preventing deposition at early stages of ALD deposition **[3]**. With the appropriate choice of head groups, SAMs can be chosen to react selectively with one surface, while not reacting at all with another. For example, thiols (R-SH) react with metal surfaces such as Ag, Au, and Cu **[4]**, while silanes

($R\text{-}Si\text{-}X_3$) react with hydroxylated (-OH) surfaces. SAMs also contain tail groups, which can effectively control the surface energy of the substrate as well as other properties. In addition, combining SAMs with ALD is a logical choice, since many substrate temperatures used for ALD are relatively low, which is important concerning the stability of SAMs and their ability to block growth.

There has been significant previous work done in the area of using self-assembled monolayers (SAMs) as molecular masks to prevent ALD **[5]**, **[6]**. One recent study has examined the use of a SAM to selectively block growth ALD on one surface (Cu), while permitting it to occur on another (SiO_2) **[7]**. A modification of this approach has also shown promise concerning selective area molecular layer deposition (MLD) **[8]**. However, much of the previous work has focused on patterning a SAM that is attached to a single substrate such as SiO_2, blocking growth in areas where the SAM is present. Several techniques have been employed to deposit and/or pattern SAMs, including micro-contact printing **[3], [9]–[12]**, solution-based assembly **[3], [13]–[23]** and vapor deposition **[24]–[28]**. From this work, important relationships between the density of the SAM and its effectiveness as a molecular blocking agent have been identified **[3], [13]**.

In this study, we have investigated two molecules as blocking layers for ALD: 1H, 1H, 2H, 2H-perfluorooctyltrichlorosilane [FOTS, $(Cl)_3Si(CH_2)_2(CF_2)_5CF_3$] and (heptadecafluoro-1,1,2,2-tetrahydrodecyl)triethoxysilane [HDFTEOS, $(CH_3CH_2O)_3Si(CH_2)_2(CF_2)_7CF_3$] [Gelest, Inc (Morrisville, PA)]. Both of the SAMs, shown in Fig. 4-1 in space-filling models, can be deposited onto the substrates via vapor deposition, prior to thin film growth via ALD. Vapor deposition of the SAMs holds obvious advantages for process integration as one does not require a vacuum break between the formation of the

SAM layer and the ALD process. Concerning the SAMs themselves, both of these molecules have long fluorinated alkyl tail groups, which should be unreactive to many thin film precursors as the CF_x chains are coordinatively saturated and consist of the strongest single bond (C-F) in organic compounds. Since both molecules are silanes, they can be expected to bind preferentially to a dielectric material such as SiO_2, and not to a metal such as Cu, because of the prevalence of hydroxyl groups on SiO_2. Thus, here we will investigate the ability of these two SAMs to block ALD growth on SiO_2, while leaving growth on Cu relatively untouched. Finally we recognize that, while both molecules are silanes, they do possess different head group chemistries [$-SiCl_3$ vs. $-Si(OCH_2CH_3)_3$], which may turn out to be important in terms of their interaction with SiO_2 and Cu surfaces.

The deposition process investigated in this study is the thermal ALD of tantalum nitride (TaN_x) in a conventional viscous flow reactor using pentakis dimethylamido tantalum {$Ta[N(CH_3)_2]_5$} and NH_3 as precursors (T_s ~ 225-300 °C). TaN_x is a material currently used as a Cu diffusion barrier and relevant to interconnect layers in microelectronic devices. We have examined the ALD growth of TaN_x on SiO_2 and Cu, both clean surfaces and ones that have been exposed to FOTS and HDFTEOS. We used *ex situ* contact angle, spectroscopic ellipsometry, X-ray photoelectron spectroscopy (XPS) and low-energy ion scattering spectroscopy (LEISS) to examine both the SAMs themselves and the TaN_x thin films that were deposited. We will demonstrate that these latter two surface-sensitive probes are especially effective in determining not only the degree of selectivity, but also the mode of growth.

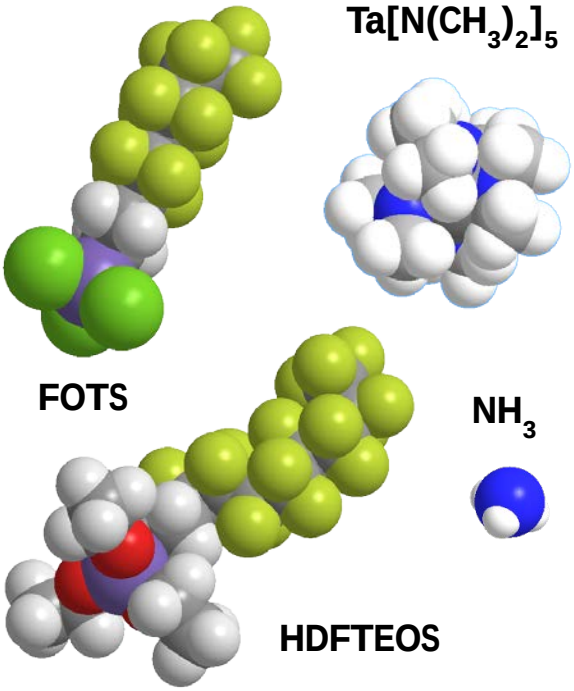

Figure 4 - 1 Space-filling models for the two reactants we consider here, $Ta[N(CH_3)_2]_5$ and NH_3, and the two SAMs: FOTS, $(Cl)_3Si(CH_2)_2(CF_2)_5CF_3$, and HDFTEOS, $(CH_3CH_2O)_3Si(CH_2)_2(CF_2)_7CF_3$.

4.3 Experimental Procedures

The experiments described here involved a sequence of steps beginning with preparation of the starting substrates (SiO_2 and Cu), formation and characterization of the SAMs, and finally, ALD TaN_x thin film growth and characterization. Complete details can be found in Supplementary Material. Following substrate preparation, the next step in most cases was the growth of the SAMs via molecular vapor deposition on the two substrates: SiO_2 (chemical oxide) and Cu [a 900 Å thick Cu thin film deposited on SiO_2 via physical vapor deposition (PVD)]. These substrate surfaces terminated with the SAMs were then characterized using a number of techniques. First we used *ex situ* measurements of the contact angle (VCA optima, Billerica MA) using water, where multiple (~ 5) contact angle measurements were obtained and then averaged. We also used *ex situ* spectroscopy ellipsometry (SE; Woollam, Lincoln NE) to estimate the thicknesses of the SAMs (only on the SiO_2 substrates). These two techniques (contact angle and SE) allow for a quick non-invasive evaluation of the SAMs, albeit lacking chemical specificity.

All substrates were placed in the viscous flow ALD reactor (Oxford FlexAL, Oxford Instruments, Oxfordshire, UK), heated to the desired temperature for growth, and exposed to a set number of cycles (0-200) of the TaN_x ALD process. Following processing in the ALD reactor a number of samples were investigated using contact angle measurements and spectroscopic ellipsometry. All samples, including some that were "as-received" and not subjected to the ALD process temperature, were transferred and placed in a custom-designed ultrahigh vacuum chamber [29], [30] for analysis using XPS and LEISS. XPS is a powerful technique for analyzing thin films that are < 10nm thick and can give absolute

densities/concentrations if appropriate calibration standards are used, and it holds the potential for depth resolution using angle-resolved XPS (ARXPS). LEISS has been shown to have extremely good surface sensitivity and is extremely useful in determining thin film continuity and interface abruptness of ultrathin films [31], [32].

4.4 Results

4.4.1 Formation and characterization of the SAMs

As described in Sec. II and in Supplementary Material the SAMs were formed via vapor deposition by exposing the substrates to FOTS or HDFTEOS. Once formed the SAMs were characterized *ex situ* using contact angle measurements, spectroscopic ellipsometry, XPS and LEISS.

In Fig. 4.2 we display results for the contact angle of samples composed of (a) SiO_2 and (b) Cu that have been exposed to HDFTEOS and FOTS. Results are shown for SiO_2 and Cu substrates, with and without a SAM, at room temperature (as received) and after annealing the samples to a temperature (~ 300 °C) that was used for TaN_x ALD. For these "0 cycles" data the atmosphere in the ALD reactor consisted of Ar (99.9999%) at a pressure of 200 mTorr. Measurement of the water contact angles on the SiO_2 surfaces (with and without SAMs) exhibited no significant time dependence. For example, for HDFTEOS|SiO_2 the contact angle was measured to be within +2°/-4° over a time period of 7 min, a range within experimental uncertainties. On the Cu surfaces, however, we observed a change in the

contact angle on the Cu surfaces as a function of time, most likely due to Cu oxidizing or reacting in the presence of water. Typically, for the first min. of exposure, the change observed was at most 4°, while after 7 min. of exposure changes of ~ 50° were observed. To minimize subjectivity in the contact angle measurements, all results (on Cu and SiO_2) were taken at the same time period after the water droplet made contact with the substrate surface (60s).

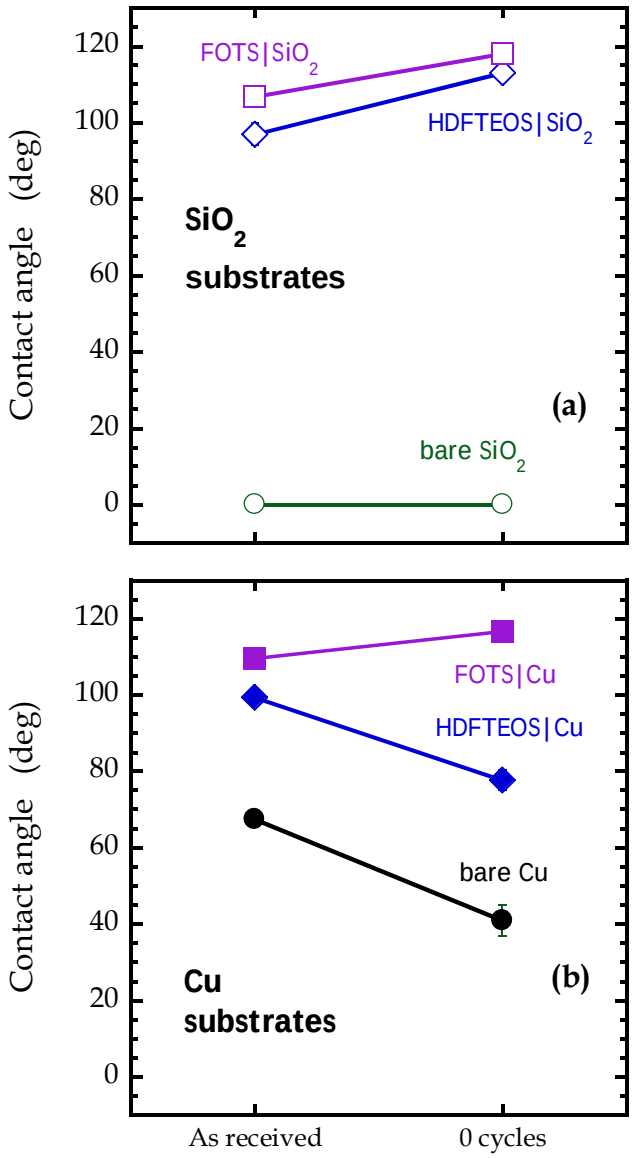

Figure 4 - 2 Contact angles measured for the six surfaces examined here for as-received samples, and those annealed to the substrate temperature for ALD (300 °C), "0 cycles": **(a)** clean SiO2 and FOTS and HDFTEOS on SiO2; **(b)** bare Cu and FOTS and HDFTEOS on Cu.

The most significant observations from these data first include the fact that the contact angles for both SAMs on the un-annealed samples are quite similar, independent of substrate, ~107° and ~109° for FOTS on SiO_2 and Cu, and ~97° and ~99° for HDFTEOS, respectively. Second, we observe that for both SAMs on SiO_2 the change in contact angle is modest (increase of ~ 11-16°) after annealing to the process temperature for ALD. This suggests that these two SAMs may be relatively intact on SiO_2 at the substrate temperature used for ALD growth here. On bare Cu substrates, however, we observed a significant decrease (~27°) in the contact angle after annealing to ALD temperatures. In a previous study, we have found that similar Cu thin film substrates undergo significant surface morphology changes at ALD temperatures, resulting in smoothening [32]. Results from XPS (*cf*. Supplementary Material) indicate that there are also chemical changes occurring on the Cu surface due to annealing to the ALD process temperature. In particular, features associated with oxides of Cu are greatly reduced after annealing. In addition, on Cu, we observe a difference in the effect of annealing on the contact angles for each SAM: for FOTS there is a modest increase (~ 7°) in the contact angle upon annealing, similar to that on SiO_2, while for HDFTEOS there is a significant decrease (~22°) in the contact angle upon annealing, and the decrease in the value is similar to that observed for bare Cu upon annealing. The change in the contact angle for HDFTEOS|Cu upon annealing could mean a number of things, including thermal desorption of the molecule from Cu at the elevated temperatures (~ 300°C) used for ALD growth, and/or possibly chemical changes in the Cu substrate itself. We will now consider those possibilities directly.

We have also used XPS to characterize the SAMs on both the SiO_2 and Cu surfaces, again for the un-annealed samples, and those that have been annealed to the process

temperature used in ALD. Here we first focus on photoemission from the F(1s) feature, since it gives us a unique signal as fluorine is only present in the SAM molecules. In Supplementary Material we also present results from analysis of the C(1s) feature, as it exhibits a distinct feature associated with the CF_x species in the SAM backbone. These results support those we report here for the F(1s). In Fig. 4-3 we present the integrated intensity of the F(1s) peak for all SAM-treated surfaces, both as-received pre- and post- "0 cycles" of ALD. After insertion into vacuum these samples received no further treatment (e.g., Ar^+ sputtering) before analysis via XPS. Halogens such as fluorine are notorious for artifacts associated with photoelectron induced desorption. To account for this, multiple F(1s) spectra were taken and the results were extrapolated to represent the signal that would have been achieved at zero X-ray exposure time. As we can see, the F(1s) intensity remained essentially constant upon annealing for three cases: both SAMs on the SiO_2 surface, and FOTS on Cu. However, for the HDFTEOS on Cu surface, a large decrease in the F(1s) intensity has been observed. This result supports the assertion, suggested by the contact angle data, that HDFTEOS or its adsorbed molecular fragment is not stable on the Cu surface and desorbs at the elevated temperature of ~300 °C investigated here for the ALD of TaN_x.

Finally, the F(1s) [and C(1s) (from CF_x)] feature observed in XPS can be used to estimate the absolute coverage of the SAMs on each of the surfaces. Details concerning this calculation, including possible effects due to the ubiquitous adventitious carbon are given in Supplementary Material. In Table I we summarize our calculations for the density of the two SAMs on the SiO_2 and Cu substrates. The range given in the table represents the two limiting assumptions: no effect of the adventitious layer (lower limit); and factoring in attenuation by the adventitious layer (upper limit). First, focusing on the densities based on

the F(1s) intensities, for both SAMs on SiO_2 we see that the values for the as-received samples and those subjected to an anneal to the ALD process temperature give similar values, within ~ 10%. Concerning the densities calculated from the C(1s)-CF_x intensities, there is an apparent modest (~ 30%) increase in the density upon annealing to the ALD process temperature for these SAMs on SiO_2. These apparent increases are not physical and could be due to decreased effects of attenuation by contamination layers after the high temperature anneal, or other effects. If we take a simple average of the lower and upper limits obtained from the F(1s) data we calculate densities of 2.51×10^{14} and 2.47×10^{14} molecules-cm^{-2} for as-received and 0 cycle ALD for FOTS|SiO_2, and 2.20×10^{14} and 2.46×10^{14} molecules-cm^{-2} for as-received and 0 cycle ALD for HDFTEOS|SiO_2. Concerning the former values, in previous work using essentially the same procedure to form the FOTS|SiO_2 layers, we reported a density of $(1.97 \pm 0.12) \times 10^{14}$ molecules-cm^{-2} based on results from synchrotron X-ray reflectivity (XRR) [33].

Moving on to the results for the SAMs on Cu, we see that for FOTS|Cu the densities found are quite similar to those found on FOTS|SiO_2. Again, using the F(1s) data we calculate densities of 2.84 and 2.83×10^{14} molecules-cm^2, for the as-received and 0 cycle TaN_x ALD samples. For HDFTEOS|Cu, however, both the F(1s) and the C(1s)-CF_x data indicate a large (~ 80-90%) decrease in the density after the high temperature anneal, from ~ 1.40 to 0.26×10^{14} molecules-cm^2, reflecting the data we have already shown in Fig. 4-3. We note also that the absolute density for the as-received HDFTEOS|Cu is also less than (~ 63%) what we observe for HDFTEOS|SiO_2, suggesting further a relatively weak interaction between HDFTEOS and the Cu surface.

Table I

Properties of self-assembled monolayers

SAM|substrate	Treatment	Density from F(1s) (molecules-cm^{-2})	Density from C(1s) (molecules-cm^{-2})
HDFTEOS|SiO_2	As-received	1.96-2.45 × 10^{14}	2.09-2.61 × 10^{14}
	0 cycles of TaN_x ALD	2.19-2.73 × 10^{14}	2.65-3.31 × 10^{14}
FOTS|SiO_2	As-received	2.23-2.79 × 10^{14}	2.21-2.75 × 10^{14}
	0 cycles of TaN_x ALD	2.20-2.74 × 10^{14}	2.81-3.51 × 10^{14}
HDFTEOS|Cu	As-received	1.24-1.55 × 10^{14}	1.61-2.01 × 10^{14}
	0 cycles of TaN_x ALD	0.23-0.29 × 10^{14}	0.19-0.24 × 10^{14}
FOTS|Cu	As-received	2.53-3.15 × 10^{14}	3.22-4.02 × 10^{14}
	0 cycles of TaN_x ALD	2.52-3.14 × 10^{14}	2.31-2.88 × 10^{14}

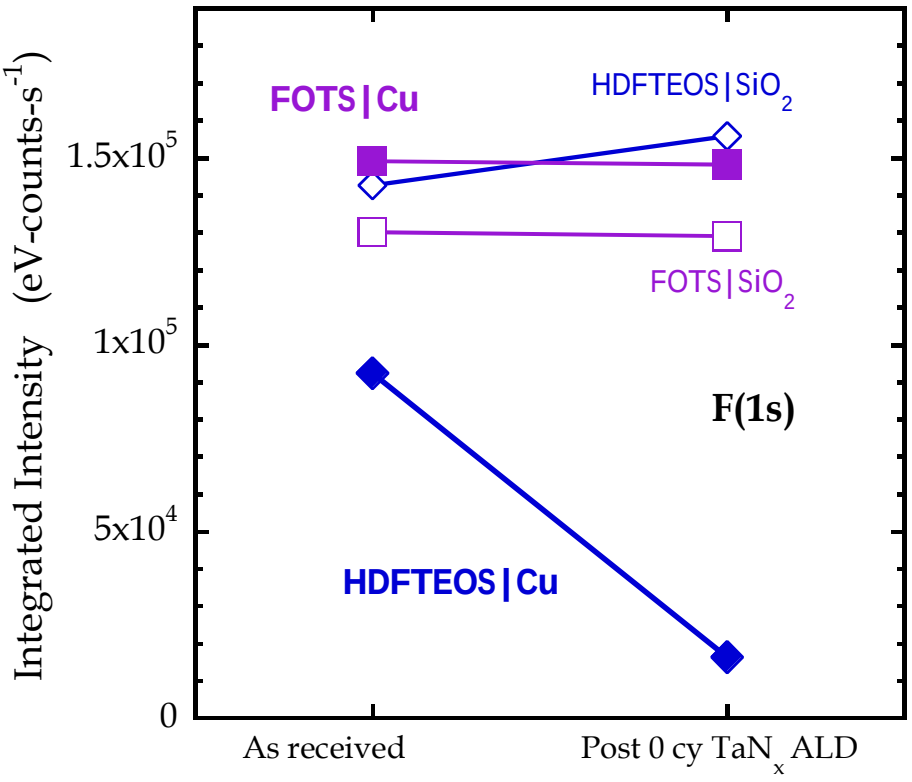

Figure 4 - 3 Integrated intensities of the F(1s) peak from XPS for FOTS (squares) and HDFTEOS SAMs formed on SiO_2 and Cu substrates for as-received samples, and those annealed to the substrate temperature for ALD (300 °C), "0 cycles".

Summarizing our results concerning just the SAMs themselves, we find that both molecules, HDFTEOS and FOTS, bind strongly to the SiO_2 surface, and form layers with a density of ~ 2-3 × 10^{14} molecules-cm^2. These layers remain essentially intact after annealed to the ALD process temperature of 300 °C in an inert environment. On the Cu surface, the behavior is quite different. For FOTS on Cu, SAMs are formed that have a density similar to those on SiO_2, and these layers are stable after annealing to the ALD process temperature in an inert environment. For HDFTEOS, however, the as-received layers that form are about 2/3 the density of those formed on SiO_2, and the density of these layers decreases further to a value that is about 10% of those formed on SiO_2.

4.4.2 ALD of TaN_x

4.4.2.1 Spectroscopic Ellipsometry

We have employed spectroscopic ellipsometry (SE) *ex situ* to measure the thickness of thin films deposited by ALD as a first check of the effect of the self-assembled monolayers on the growth of TaN_x. In Fig. 4-4 we plot the thin film thickness deduced from SE as a function of the number of ALD cycles for growth of TaN_x on bare SiO_2 (chemical oxide), and a SiO_2 surface that has a SAM formed from HDFTEOS. Here, we made use of the Cauchy dispersion relationship for the optical constants for the deposited thin film in the analysis. We found very similar results (see Supplementary Material) when we assumed that the thin film of TaN_x could be described by the optical constants for Ta_2O_5. For example, as shown in the Supplementary Material, XPS results indicate that air exposure of the thin films resulted in significant oxidation of the TaN_x thin film, particularly for thin films < 30 Å in

thickness. We can make a number of observations from the data shown in Fig. 4-4. First, there is an offset between the thin film thicknesses for growth on SiO_2 vs. HDFTEOS|SiO_2 for all conditions examined, and the value on SiO_2 is greater by ~ 9 Å. Second, an incubation period is clearly indicated for growth on HDFTEOS|SiO_2, but not on SiO_2. Third, a linear fit to the thickness (D) deposited per cycle for n = 10-200 cycles gives growth rates (dD/dn) on the two surfaces that are nearly identical: 0.385 Å-cycle^{-1} on SiO_2 and 0.383 Å-cycle^{-1} on HDFTEOS|SiO_2.

The results presented in Fig. 4-4 indicate clearly that the SAM formed by HDFTEOS has a significant effect on the early stages of growth, i.e. n < 20 cycles, or D < 10 Å. Unfortunately, analysis of TaN_x thin film formation on Cu using SE is problematic, and was not attempted here. Moreover, for many applications using ALD the goal is to form films with ultrathin thicknesses, where D < 20 Å. Thus, there is a clear need for the use of techniques that are well-suited to the analysis of ultrathin films. In the next two sections, Sec. 4.4.2.2 and Sec. 4.4.2.3, we will apply two such techniques: XPS and LEISS, and we will find that the application of these two techniques is decisive in determining the effects of the two SAMs on ALD growth of TaN_x.

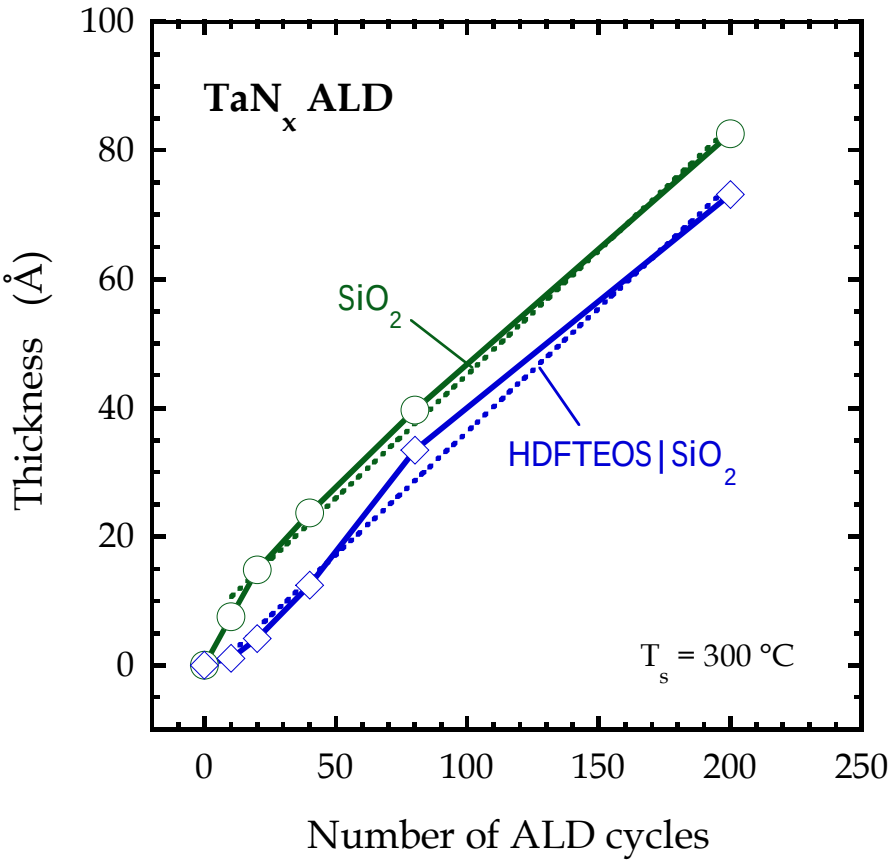

Figure 4 - 4 Thin film thickness as measured by spectroscopic ellipsometry as a function of the number of ALD cycles for the deposition of TaN_x on clean SiO_2 and HDFTEOS on SiO_2 at T_s = 300 °C. The solid lines are simply to guide the eye, while the dashed lines are linear fits of the data for n = 10-200 cycles of ALD.

4.4.2.2 X-ray photoelectron spectroscopy

In all cases to be presented below, analysis of the substrate and the thin films deposited on them were conducted *ex situ*. In these cases we always find that the samples possess an ultrathin layer of adventitious carbon. As described elsewhere [32], a short time (~ 1 min.) exposure to a 3 keV Ar^+ ion beam can remove ~ 70-80% of this contamination layer without adversely affecting the samples for subsequent analysis using XPS. Moreover, this procedure is required for LEISS (*vide infra*). We note that this previous work involved essentially exclusively analysis of 5 and 10 Å thick TaN_x thin films. Consequently, unless otherwise noted, the results presented below involve samples that have been subjected to this short time Ar^+ sputter etch. In selected cases, however, we will report analyses on "as-received" samples, similar to the results presented above in connection with the characterization of the SAMs themselves.

In Fig. 4-5(a) we present a plot of the integrated intensity of the Ta($4d_{5/2}$) peak as a function of the number of ALD cycles for growth of TaN_x on bare SiO_2, and SiO_2 modified with SAMs formed from FOTS and HDFTEOS. These results are for T_s = 300 °C, and we also observed similar behavior at T_s = 225 °C (see Supplementary Material). These intensities have been normalized to the intensity from a ~ 150 Å thick TaN_x thin film, one that is sufficiently thick that photoemission from the underlying substrate is completely extinguished and attenuation effects are saturated. We get an expected result for film growth on bare SiO_2: a decaying exponential approach to a constant value. Given the absolute growth rate from the results employing SE, and accounting for the takeoff angle of 38.5° employed for XPS in Fig. 4-5(a), the rate of the exponential decay corresponds to an effective photoelectron decay length of ~ 18 ± 3 Å, which can be compared to our previous

estimate for the attenuation length of the Ta($4d_{5/2}$) photoelectrons in TaN_x of 19.6 Å [34]. Most important, the rate of TaN_x thin film growth on both surfaces terminated with the SAMs is clearly attenuated. The intensities also exhibit upward curvature with increasing numbers of ALD cycles. For these two cases the smooth curves represent interpolation between the data points, simply to guide the eye. The dotted curves are a fit to a model we will consider below. We see that the effect of these two SAMs on the ALD growth of TaN_x on SiO_2 is essentially the same up to ~ 20 cycles of ALD.

In Fig. 4-5(b) we present a plot of the integrated intensity of the Ta($4d_{5/2}$) peak as a function of the number of ALD cycles for growth of TaN_x on bare Cu, and Cu modified with SAMs formed from FOTS and HDFTEOS. Again, the data have been normalized to the intensity from a thick TaN_x film. These results show clear differences when compared to those found on the SiO_2 surfaces. First, while these data are also well described by a decaying exponential function, the implicated rate of growth on bare Cu is ~ 0.237 ± 0.24 Å-cycle^{-1}, or about 60% of the rate of growth on bare SiO_2. The reasons for this change are not clear at the moment. Perhaps most interesting concerning these results is the fact that both SAMs do not affect TaN_x growth on the Cu surface. A simple fit to these data give values for the rate of growth of 0.236 ± 0.24 Å-cycle^{-1} on HDFTEOS|Cu, and 0.276 ± 0.29 Å-cycle^{-1} on FOTS|Cu, values that are within experimental uncertainties to that observed on bare Cu.

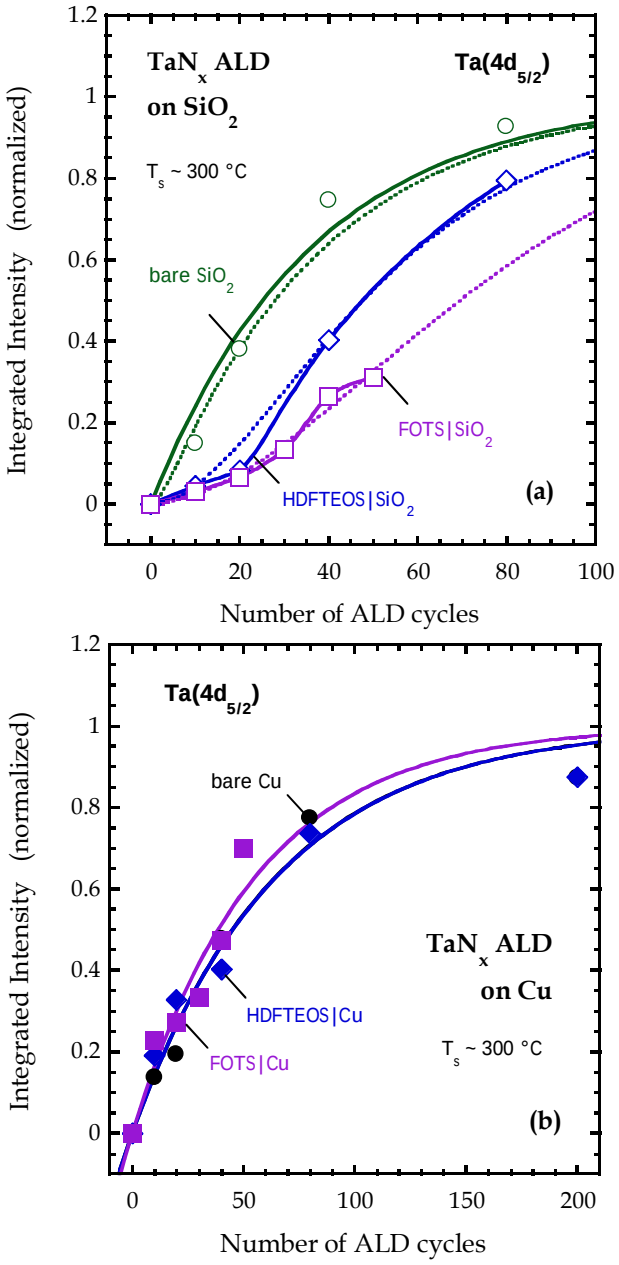

Figure 4 - 5 Integrated intensities of the peak from XPS associated with the thin film, Ta($4d_{5/2}$), as a function of the number of ALD cycles for the deposition of TaN_x at T_s = 300 °C on **(a)** clean SiO_2 and FOTS and HDFTEOS on SiO_2; and on **(b)** bare Cu and FOTS and HDFTEOS on Cu. The solid lines in (a) for bare SiO_2 and in (b) for all Cu surfaces are fits to an exponential decay function. In (a) the dashed lines for all samples represent fits to a model that accounts for an initial suppressed rate of growth that decays exponentially towards the steady-state rate of growth (see text). In (a) the solid lines for the two SAMs on SiO_2 are to guide the eye.

In Fig. 4-6 we summarize the major results from Fig. 4-5, where we plot the initial rate of ALD growth of TaN_x for all 6 surfaces examined here. Here we make use of our estimate for λ = 19.6 Å to make these rates quantitative. For the two SAMs on SiO_2, we have fit the early cycle data (0-20 cycles) shown in Fig. 4-5(a) to a straight line to assess the initial rate of growth. As may be seen, on SiO_2, we find that the initial rate of growth of TaN_x was significantly attenuated by the SAMs, by approximately a factor of 7-8. On Cu, however, we see that the SAMs have essentially no effect of the rate of growth of TaN_x on the Cu surface. The results we presented above in Sec. 4.3.2.1 can certainly shed some light on why we observe different effects of the SAMs on Cu and SiO_2. Before doing so, however, we will consider additional results for the thin films.

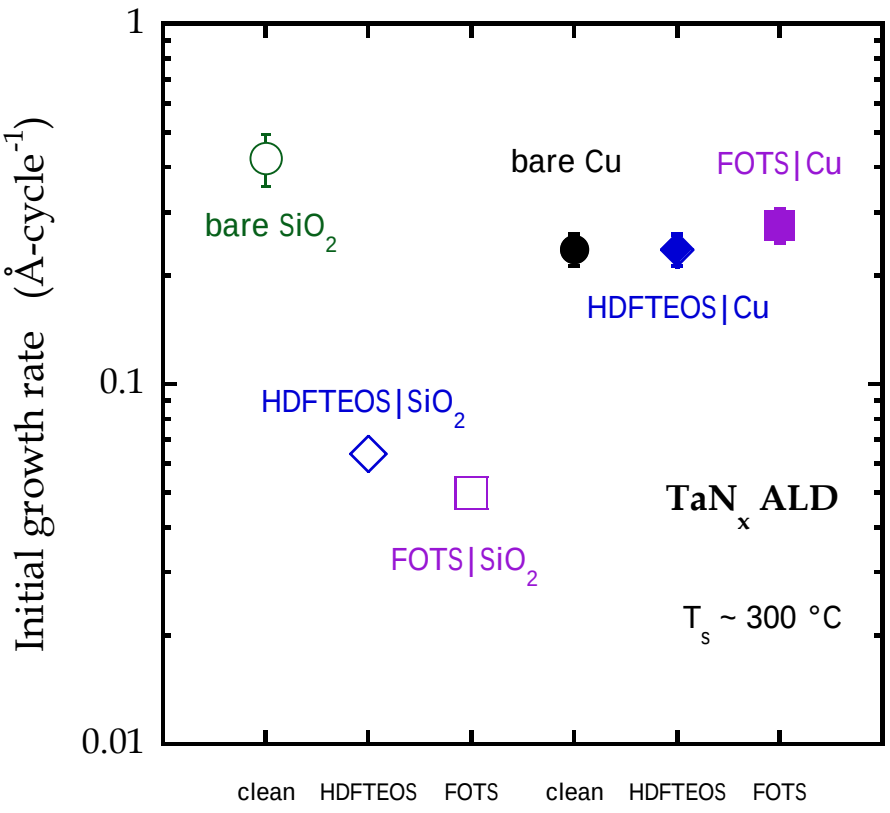

Figure 4 - 6 Initial rate of ALD of TaN_x for the six surfaces examined here. For growth on bare SiO_2 and the 3 Cu surfaces, the initial rates are derived from the fits of the Ta($4d_{5/2}$) integrated intensities to the exponential decay function displayed in Fig. 5. For the two SAMs on SiO_2 the initial rates are based on a linear fit to the data for n = 0-20 cycles.

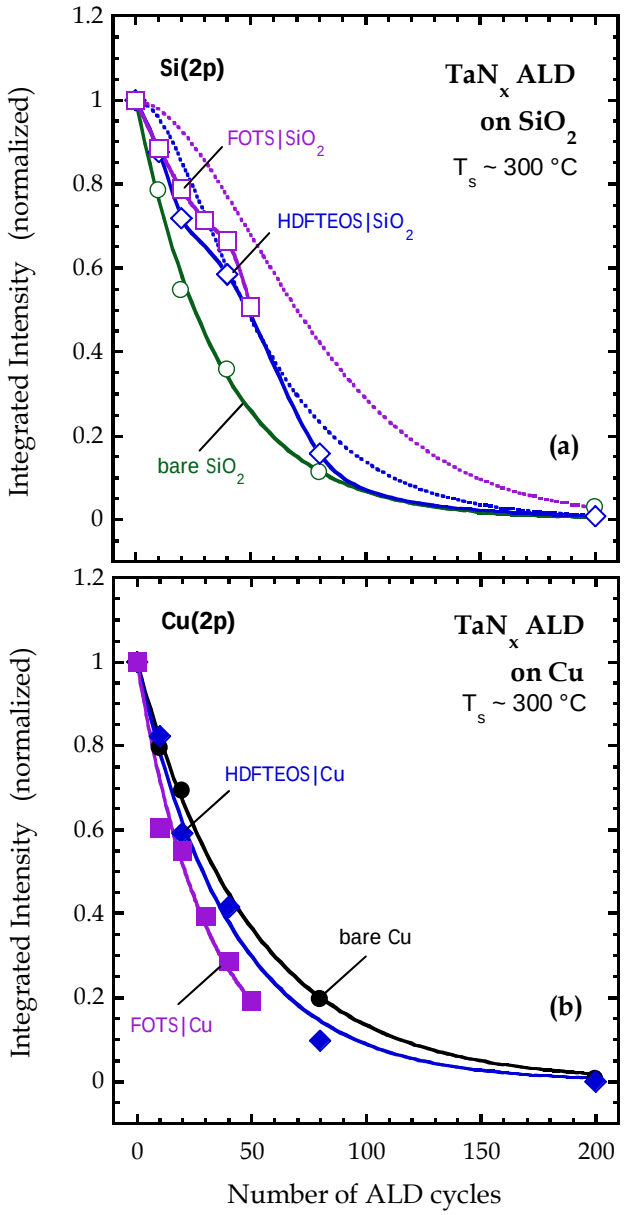

Figure 4 - 7 Integrated intensities of the peaks from XPS associated with the substrates as a function of the number of ALD cycles for the deposition of TaN_x at T_s = 300 °C on **(a)** clean SiO_2 and FOTS and HDFTEOS on SiO_2, Si(2p); and on **(b)** bare Cu and FOTS and HDFTEOS on Cu, Cu(2p). The solid lines in (a) for bare SiO_2 and in (b) for all Cu surfaces are fits to an exponential decay function. In (a) the dashed lines for all samples represent fits to a model that accounts for an initial suppressed rate of growth that decays exponentially towards the steady-state rate of growth (see text). In (a) the solid lines for the two SAMs on SiO_2 are to guide the eye.

Analysis of the features due to emission from the substrate is also useful. For example, the attenuation of the substrate signal by an overlying thin film will depend on the nature of growth, e.g., 2D layer-by-layer (LbL) vs. 3D islanded growth. In Fig. 4-7 we plot the integrated intensities of the two substrate peaks, in (a) the Si(2p); and in (b) the Cu(2p), as a function of the number of ALD cycles. All of these data have been normalized to a value of unity at 0 cycles of ALD. From Fig. 4-7(a) we see that the attenuation of the substrate signal on SiO_2 with increasing numbers of ALD cycles is fastest on the bare surface. The data for the bare surface is fit very well by a simple exponential decay as shown by the solid line. Employing an attenuation length for the Si(2p) photoelectrons (λ = 20.8 Å) the rate of the decay of the data shown in Fig. 4-7(a) indicates a rate of TaN_x growth equal to 0.44 ± 0.02 Å-cycle^{-1}, essentially identical to that found by an analysis of the data shown in Fig. 4-5(a) for Ta($4d_{5/2}$) (0.42 ± 0.07 Å-cycle^{-1}). The exponential decay observed for both the thin film and substrate signals for TaN_x growth on bare SiO_2, and the essentially identical growth rates that are implicated, are consistent with 2D LbL growth on this surface.

In the cases of the SiO_2 surface terminated by SAMs, we see that the rates of decrease/attenuation are slower, consistent with the behavior of the Ta($4d_{5/2}$) signal in Fig. 4-5(a). Even though the rate of the initial decrease is reduced, in the case of HDFTEOS|SiO_2, we see that after 200 cycles the substrate signal is essentially totally extinguished, just as it is on bare SiO_2. The data for both SAMs are not well described by a simple exponential decay. The dotted lines are the prediction of the model fit to the Ta($4d_{5/2}$) data shown in Fig. 4-5(a). This model also does not capture the rate of decay well, although the agreement is better in the case of growth on HDFTEOS|SiO_2.

We next consider the behavior of the Cu(2p) signals as a function of the number of ALD cycles. As may be seen in Fig. 4-7(b), the Cu(2p) data for bare Cu are well described by a decaying exponential. Employing an attenuation length for the Cu(2p) photoelectrons (λ = 10.9 Å), which is consistent with what we have employed for both Ta($4d_{5/2}$) and Si(2p) we find a growth rate for TaN_x of 0.172 ± 0.007 Å-cycle^{-1}. This value is ~ 23% smaller than the value implied by a fit to the Ta($4d_{5/2}$) data. The data for the two SAMs also show a decay that is approximately exponential, and the rate of decay is somewhat faster than that observed for bare Cu. Again employing an attenuation length for the Cu(2p) photoelectrons we find implicated growth rates of 0.208 ± 0.013 and 0.283 ± 0.021 Å-cycle^{-1} for HDFTEOS |Cu and FOTS|Cu. These two values are much closer (within 12% and 2%, respectively) to the values implicated from the Ta($4d_{5/2}$) results.

For a final set of results concerning the use of XPS, we will consider the evolution of the F(1s) and C(1s)-CF_x peaks as a function of the number of ALD cycles. These peaks are of course uniquely associated with the presence of the two SAMs, as there is no contribution from either the underlying substrates or the deposited thin film. If the SAMs remain intact, the ratio of these two peaks should be constant (see Supplementary Material). As described in the beginning of this section, we typically subject the sample to a short Ar^+ sputter etch before analysis by XPS. Here we report the intensities for the as-received samples as Ar^+ ion bombardment had a significant effect on these results, similar to what we observe concerning the adventitious carbon layers. For example, as shown in the Supplementary Material, for data corresponding to 0-20 cycles of ALD, the short Ar^+ sputter etch caused a decrease in the F(1s) [C(1s)-CF_x] intensities by ~ 80% [> 90%] on SiO_2, and ~ 70% [> 90%] on Cu.

First in Fig. 4-8(a) we consider the integrated (absolute) intensity of the F(1s) peak as a function of the number of ALD cycles for the two SAMs on SiO_2. The results for the two SAMs are somewhat similar, with both showing a strong decrease in intensity with increasing number of ALD cycles. The dotted lines are the prediction of the model fit to the Ta($4d_{5/2}$) data shown in Fig. 4-5(a), where we have also assumed that the TaN_x overlayer grows uniformly in thickness on the SAM covered substrate in a 2D layer-by-layer mode. The assumption of 2D layer-by-layer growth of TaN_x on the SAM surfaces can be confirmed or disregarded with other analyses, which we will consider below. We see that the model is a reasonable description of the data for both SAMs. In Fig. 4-8(b) we consider similar results for the C(1s)-CF_x intensities. These data show strong similarities to those we have just considered for the F(1s) peak. Again, the dotted lines are the prediction of the model fit to the Ta($4d_{5/2}$) data shown in Fig. 4-5(a), again assuming uniform 2D layer-by-layer growth of TaN_x. The data for FOTS|SiO_2 are in reasonable agreement with the model, whereas there is a sizable difference between the model and the results for HDFTEOS|SiO_2. The decay observed experimentally is noticeably faster than what the model predicts. These data could indicate cleavage of C-F bonds due to the ALD process, where F may be transferred to other elements present in the thin film (e.g., Ta).

In Fig. 4-8(c) we consider the integrated (absolute) intensity of the F(1s) peak as a function of the number of ALD cycles for the two SAMs on Cu. Unlike the results for SiO_2, here we observe a large difference between the two SAMs, consistent with the results presented in Fig. 4-3. After ~ 40 cycles of TaN_x ALD we see that there is no evidence of the presence of the HDFTEOS SAM on Cu. For FOTS, however, the SAM is clearly present after 50 cycles. Again, the dotted line is the prediction of the model fit to the Ta($4d_{5/2}$) data

shown in Fig. 4-5(b), where a simple exponential decay could explain both the data for Ta($4d_{5/2}$) and Cu(2p) [Fig. 4-7(b), albeit a different rate of decay]. We see that the model seems to slightly over predict the rate of decay of the F(1s) intensity. Moving on to the results for the C(1s)-CF_x intensities displayed in Fig. 4-8(d), we see that these results mostly mirror those for the F(1s) peak. The biggest difference may be associated with the larger difference observed between the results for FOTS and the prediction of the model based on the fit to the Ta($4d_{5/2}$) data shown in Fig. 4-5(b). Some of this behavior could be explained by the larger than expected F-to-CF_x ratio (~ 2.4) observed for 0 cycles and FOTS|Cu, which could again be reconciled by C-F bond cleavage and transfer of F to the Cu substrate. Thus, the data shown in Fig. 4-8(d) for the C(1s)-CF_x intensities may better represent the presence of the FOTS SAM. If this is the case, the reduced rate of decay could be explained by FOTS being at the surface, as opposed to being buried by the TaN_x thin film. Additional information concerning the mechanism of growth may be found by considering results from other analyses, which we now consider.

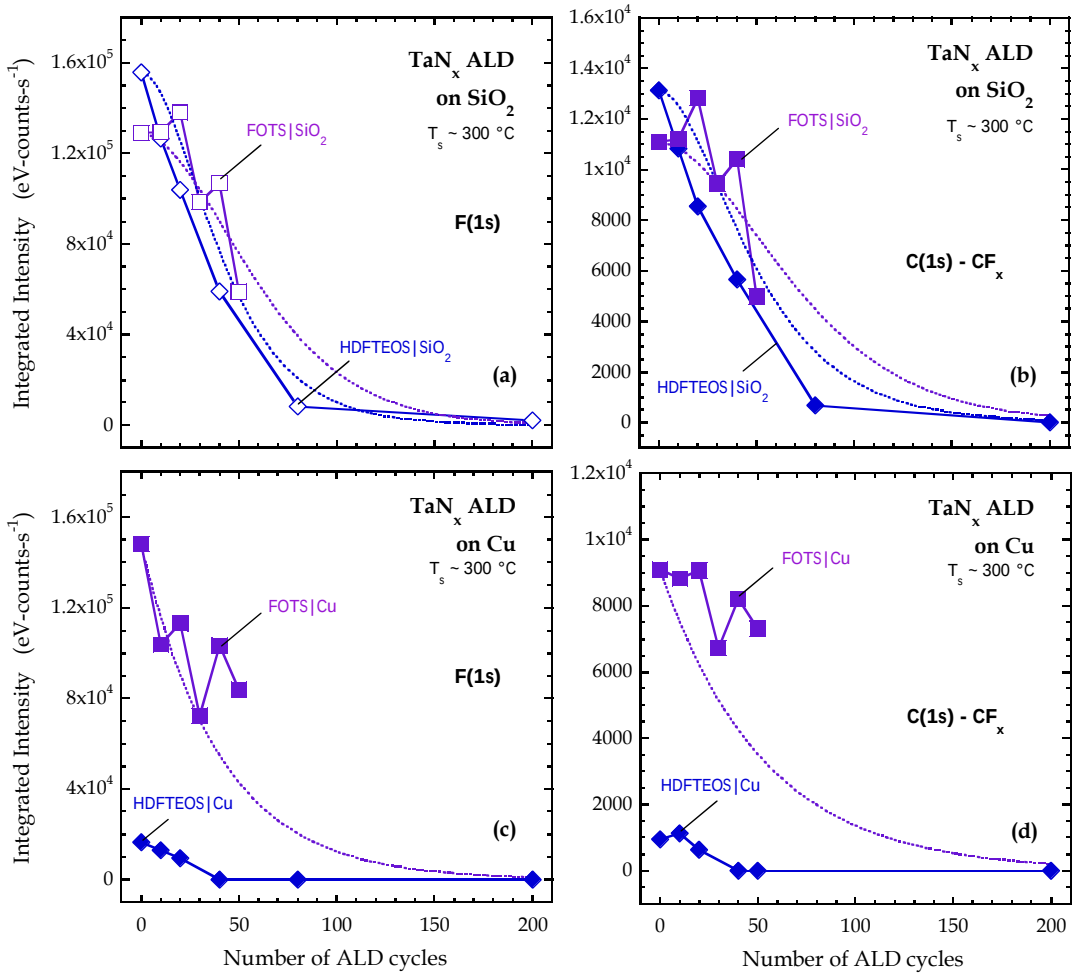

Figure 4 - 8 Integrated intensities of the peaks from XPS associated with the SAMs as a function of the number of ALD cycles for the deposition of TaN_x at T_s = 300 °C on FOTS and HDFTEOS on SiO_2, **(a)** F(1s), **(b)** C(1s)-CF_x; and on FOTS and HDFTEOS on Cu, **(c)** F(1s), **(d)** C(1s)-CF_x. In all cases the solid lines are to guide the eye. The dashed lines represent a prediction of the fits of the Ta($4d_{5/2}$) data shown in Fig. 4-5 where the SAM is assumed to be buried uniformly by the deposited TaN_x thin film.

4.4.2.3 Low-energy ion scattering spectroscopy

We now consider results from LEISS, which is extremely surface sensitive, detecting only those elements that exist in the topmost monolayer. In all cases, these samples were subjected to a short time (~ 1 min.) exposure to a 3 keV Ar^+ ion beam to remove adventitious carbon, which has a significant detrimental effect on all features observed in LEISS. Example spectra, using He^+ ions (~ 1 keV), are provided in Supplementary Material. In Fig. 4-9 we present the integrated intensities of the Ta and Si peaks from LEISS as a function of the number of ALD cycles for growth of TaN_x on (a) bare SiO_2 and (b) SiO_2 terminated by the two SAMs. First we see that on clean SiO_2 the Ta and Si signals are essentially mirror images of each other: there is a sharp linear increase (decrease) in the Ta (Si) signal up to 20 cycles, followed by a region of nearly constant intensity. This behavior indicates that the TaN_x thin film formed on SiO_2 is continuous after ~20 cycles of ALD, or ~ 0.8 nm in thickness. On the SiO_2 surfaces terminated by the SAMs the behavior of the LEISS signals is qualitatively similar in the sense that decreases in the substrate Si signal are matched by increases in the thin film Ta signal. The rate of the increase (decrease) in the Ta (Si) signal is much slower than that observed on bare SiO_2. For growth on HDFTEOS|SiO_2, for example, the substrate feature is only extinguished after ~ 200 cycles of ALD growth. This result is consistent with that suggested by the results from XPS, which we considered above in Figs. 4-5 and 4-7. There are important differences observed from the LEISS results, however, as after 80 cycles of growth the substrate is clearly not covered in the case of HDFTEOS|SiO_2, whereas the results from XPS for 80 cycles of growth were quite similar for growth on SiO_2 and HDFTEOS|SiO_2.

In Fig. 4-9 we present the integrated intensities of the Ta and Cu peaks from LEISS as a function of the number of ALD cycles for growth of TaN_x on (c) bare Cu and (d) Cu terminated by the two SAMs. For bare Cu the intensity of the Ta and Cu peaks mirror each other, exhibiting a steady increase (decrease) in the Ta (Cu) signal. Saturation is apparent at 200 cycles, where the substrate Cu signal is finally extinguished. For comparison the intensity for the Ta peak observed for TaN_x growth on clean SiO_2 is also plotted in Fig. 4-9(c) and we see that the behavior on Cu is quite different. In fact the dependence of the thin film (Ta) and substrate (Cu) peaks is much more similar to that observed on the SiO_2 surfaces covered with the two SAMs. In Fig. 4-9(d) we display the results for TaN_x growth on Cu terminated by the two SAMs. Unlike the results for SiO_2 and bare Cu, here the intensities of the thin film (Ta) and the substrate (Cu) do not mirror each other so well. For both surfaces terminated by the SAMs, there is an initial period (up to ~ 30-40 cycles) where there is little change in the substrate (Cu) signal, while there is a strong increase in the thin film (Ta) signal. These results suggest that the deposited TaN_x thin film may be replacing the SAM on the surface, either by desorption or displacement. The other feature that is obvious in Fig. 4-9(d) is the substantial difference in the intensity of the substrate (Cu) signal depending on the SAM. The Cu intensity for HDFTEOS|Cu for the first 40 cycles is essentially that for bare Cu. The much lower intensity for the Cu peak for FOTS|Cu is entirely consistent with the presence of FOTS (or molecular fragments) at the surface.

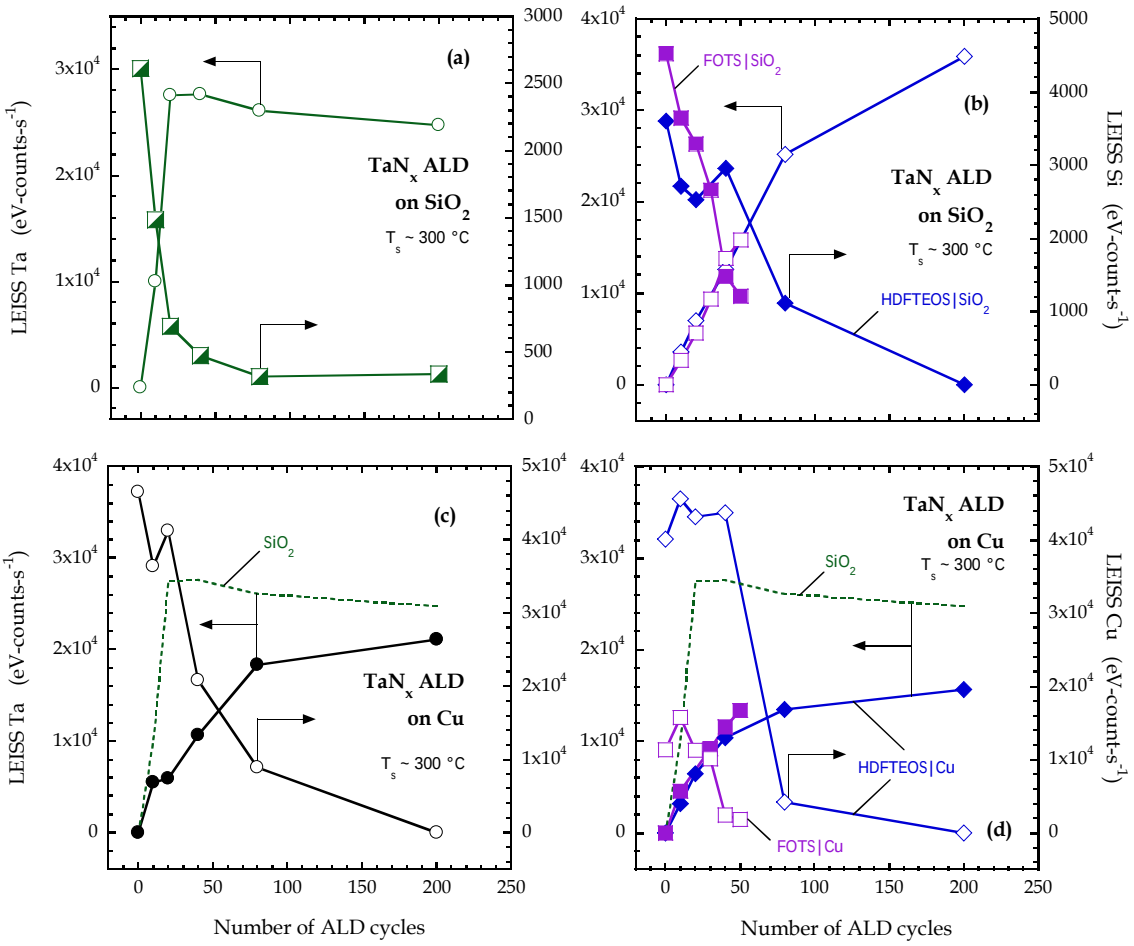

Figure 4 - 9 Integrated intensities of the peaks from LEISS associated with the thin film, Ta (left ordinate), and substrate, Si and Cu (right ordinate) as a function of the number of ALD cycles for the deposition of TaN_x at T_s = 300 °C on **(a)** clean SiO_2; on **(b)** FOTS and HDFTEOS on SiO_2, on **(c)** bare Cu; and on **(d)** FOTS and HDFTEOS on Cu. In (c) and (d) the behavior of the Ta LEISS signal for growth on clean SiO_2 is reproduced.

4.5 Discussion

We have presented results for the growth of TaN_x by ALD on two different substrates, SiO_2 and Cu, examining both the clean/bare surfaces and those that have been terminated with two SAMs. To this point we have employed four different analytical techniques and these have been applied to characterization of the substrates, the modifying SAMs, and the thin films. In this section we will attempt to reconcile all of these results in terms of a mechanistic model that is consistent with all of the data.

4.5.1 Growth on clean SiO_2 and modified SiO_2

Growth of TaN_x by ALD on SiO_2, and in particular chemical oxide, is a well-characterized system. Indeed, in previous work [32] we examined the ALD growth of ~ 0.5 (10 cycles) and 1.0 nm (20 cycles) thick TaN_x on clean SiO_2. In this previous work, we found results from XPS and LEISS that were consistent with 2D layer-by-layer growth. The results we present here are consistent with this picture. Namely from both ellipsometry and XPS there is no indication of an incubation period, and the thickness (D) deposited per cycle (n), dD/dn, is approximately constant. The dependencies of the integrated intensity from XPS for the thin film [Ta($4d_{5/2}$)] and the substrate [Si(2p)] with the number of ALD cycles are very consistent with each other. Finally from LEISS, the signal associated with the thin film saturates at ~ 20 cycles (D ~ 0.8-0.9 nm), and the signal from the Si substrate decreases approximately linearly over this same range.

Growth of TaN_x by ALD on SiO_2 surfaces modified by the SAMs is clearly different from clean SiO_2. First, we have confirmed using contact angle measurements and XPS that both SAMs on SiO_2 examined here appear to remain largely intact after annealing to the ALD process temperature of ~ 300 °C. In many previous studies, this issue—the survival of the SAMs at the ALD process temperature—goes mostly unexamined. Their presence is further verified by their effect on subsequent ALD growth of TaN_x. The amount of TaN_x deposited for the first 20 cycles of ALD is greatly reduced by the SAMs, but after about 40-50 cycles the thickness deposited per cycle begins to approach that for clean SiO_2.

As indicated above, we used a model employed in previous work [30], [34]–[37] to describe the initial attenuation of the thickness deposited per cycle ($dD/dn = D'$). As described in Supplementary Material, this model assumes that growth is initially $\alpha D'_\infty$, which decays exponentially [$\exp(-n/m)$] to the steady state rate of D'_∞. To fit the data shown in Fig. 4-5(a) we also have accounted for the attenuation of the photoelectrons by the depositing thin film. As may be seen, the fits to the data using this model shown in Fig. 4-5(a) describe the data quite well. The values determined for the attenuation of the initial thickness deposited per cycle (α) are « 1 as expected, but the exact values are not particularly significant as the uncertainty in these values are larger than the values themselves. The values for the constant that characterizes the length of the attenuated growth period (m) are more meaningful, and we find m ~ 27 and 75 cycles for HDFTEOS|SiO_2 and FOTS|SiO_2. This model predicts that the growth rate will be within ~ 5% and essentially indistinguishable of the steady-state growth rate after $n \sim 3m$ cycles, which for HDFTEOS|SiO_2 is ~ 80 cycles.

The most logical interpretation of the initial attenuation of the thickness deposited per cycle involves removal of active sites for nucleation by the chemisorption of the molecules

that constitute the SAM. Based on the steady-state growth rate and assuming deposition could be described by growth of cubic TaN along the (111) direction there is a density of Ta of 2.0×10^{14} sites-cm^2 at steady-state. This density is close to, and somewhat smaller than the density of the SAMs themselves as may be seen from the results presented in Table I. The SAMs, if uniform in density could likely block ALD growth. Thus, it is likely that growth nucleates at defect sites that are present in the SAM, e.g., areas of low local concentration, and these are at densities of much less than 10^{14} sites-cm^{-2}. In this case growth will at first be limited to defect sites, and it could be complex, depending on the fate of the SAM. Provided the SAMs are stable during ALD, thin film growth should first be mostly vertical, perpendicular to the surface. Once the ALD thin film has grown to a thickness comparable to the surrounding SAM (~ 1 nm), growth can also proceed in a horizontal direction, parallel to the surface. In this scenario forming a conformal thin film will depend on the distance between nucleation sites—thus the point at which the thin film "closes out" (i.e., becomes continuous) could be used to estimate the nucleation density. Close out is indicated directly by the disappearance of the substrate signal from LEISS, and indirectly by the deposited thickness per cycle reaching the steady-state value.

To facilitate the discussion we consider the schematic in Fig. 4-10. Here we present snapshots of layer occupancies for thin film growth that proceeds in a 2D layer-by-layer mode, and one that proceeds in a 3D island growth mode. For the latter example the layer occupancies have been chosen to also be consistent with random deposition (RD). Also displayed in this figure is a plot of the surface coverage (θ) vs. the total coverage (Θ, all layers) for these two modes of growth. As may be seen, for these two growth modes the

predicted behavior, $\theta = f(\Theta)$, is quite different, and based on these models the deviation becomes apparent for total coverages ~ $0.5 < \Theta < 3$ ML, and is largest at $\Theta = 1$ ML.

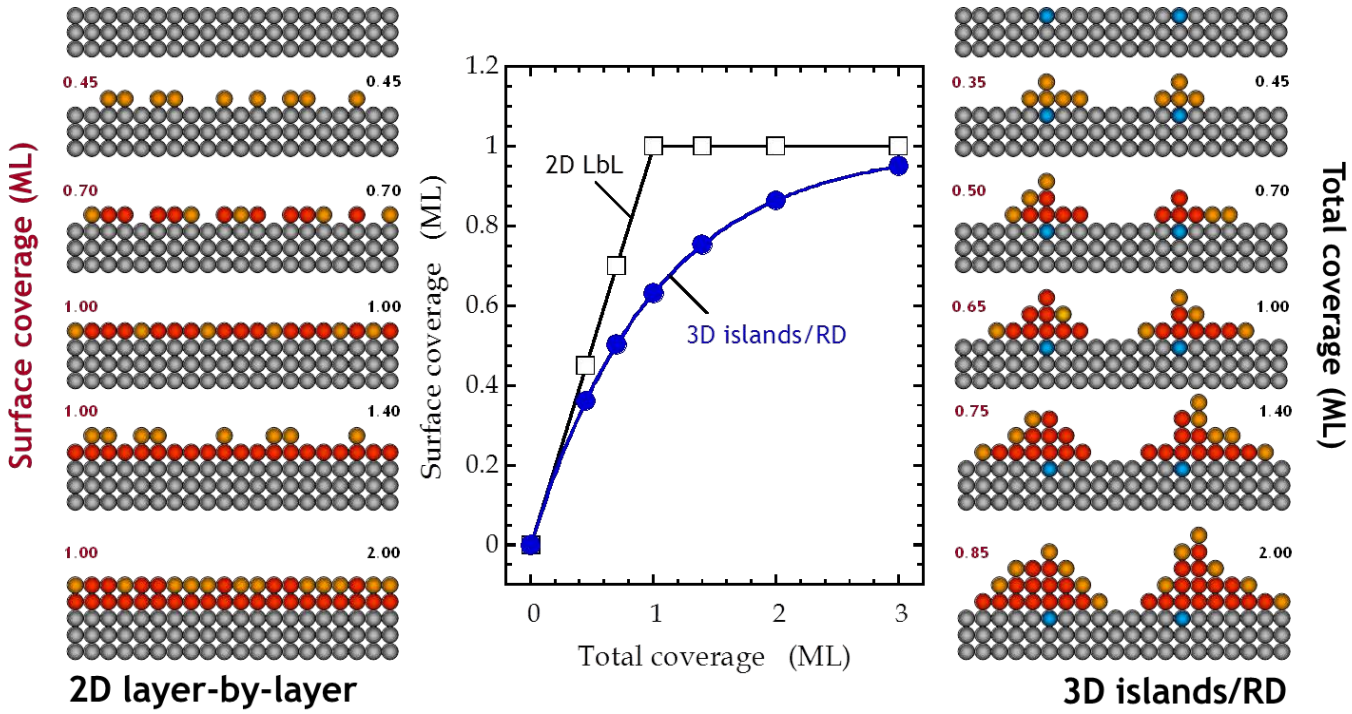

Figure 4 - 10 Simple models for thin film growth involving perfect LbL growth (left panel) and random deposition (right panel), where in the latter case, the depositing species are allowed to coalesce into islands. The central panel is a plot of the surface coverage as a function of the total coverage, which highlights the differences between the two models.

In Fig. 4-11 we consider a plot of the intensity from LEISS for the Ta peak vs. the TaN_x thin film thickness based on an analysis of the data from XPS shown in Fig. 4-5(a). In this case, the data as plotted account for attenuation effects in XPS, and conforms to the analysis as presented in Fig. 4-10. From these data we see that the results for growth on SiO_2 are very indicative of 2D layer-by-layer growth, where close-out of the TaN_x thin film occurs at a thickness of ~ 7.5 Å. This thickness corresponds to the diagonal of the cubic TaN unit cell, i.e. 3 MLs along the TaN(111) direction. Thus, for this system the depiction of 2D growth shown in Fig. 4-10 is accurate in the case where a *unit cell* thickness, and not a single *monolayer*, is required for thin film close-out. This is not unexpected as a truly 2D monolayer of TaN may not represent a stable structure (unlike, e.g., graphene), whereas a somewhat thicker thin film may provide the stability provided by more bulk like 3D bonding.

For TaN_x growth on HDFTEOS|SiO_2 we see that the shape of the curve in Fig. 4-11 is distinct from that for SiO_2; downward curvature is clearly observed, which is very indicative of 3D islanded/RD growth. Thus, combined with the attenuation of the initial rate of growth, these results clearly support islanded growth for this system, where thin film closure occurs between 80 and 200 cycles of ALD in this case. How do our other results support or possibly contradict this viewpoint? First the decay of the LEISS signal for the Si substrate shown in Fig. 4-9(b) mirrors that of the increase in the Ta signal, supporting close-out between 80 and 200 cycles. Data from XPS for both the Si substrate [Fig. 4-7(a)] and the HDFTEOS SAM [Figs. 4-8(a,b)] are described reasonably well by the model used to fit the Ta thin film signal [Fig. 4-5(a)]. Indeed, concerning the fate of the HDFTEOS SAM on SiO_2, the behavior of the F(1s) and C(1s)-CF_x signals are in good agreement with the model that assumes the SAM layer is eventually buried by the TaN_x thin film. If degradation of the

SAM were significant, we would expect a faster decay in these signals with the number of ALD cycles. We have seen similar behavior (i.e., the SAM is buried by ALD) concerning Al_2O_3 growth on top of a surface containing an ultrathin (~ 0.5 nm) poly(ethylene imine) layer [30].

For TaN_x growth on FOTS|SiO_2 these results are quite similar to those for HDFTEOS|SiO_2. For example, downward curvature is also observed for the LEISS Ta signal vs. TaN_x thickness as shown in Fig. 4-11. These data do, however, lay above those for HDFTEOS, indicating that for a nominal thickness of ~ 5 Å more of the surface is covered by TaN_x in the case of FOTS|SiO_2. The drop in the Si LEISS signal after 50 cycles for growth on FOTS|SiO_2 is also consistent with a more significant coverage of the substrate by the TaN_x thin film. These observations indicate that the growth on FOTS|SiO_2 is more 2D than that on HDFTEOS|SiO_2, suggesting that growth in-plane on FOTS|SiO_2 might be less attenuated for these thicknesses.

Finally, as indicated above, we can use the data from LEISS to estimate a defect density in the case of TaN_x growth on HDFTEOS|SiO_2. Using the disappearance of the Si LEISS signal at 200 cycles (a minimum) to represent close-out, and assuming growth proceeds at equal rates (~ 0.4 Å-cycle^{-1}) perpendicular to the surface and parallel to it we estimate a spacing of defect sites of ~ 8 nm, and a defect density of ~ 2×10^{12} cm^{-2}. This value is ~ 1% of the steady-state density of Ta deposited per cycle and corresponds to a value of $\alpha \sim 0.01$, which is within experimental uncertainties for the value of this parameter found by a fit to the data in Fig. 4-5(a).

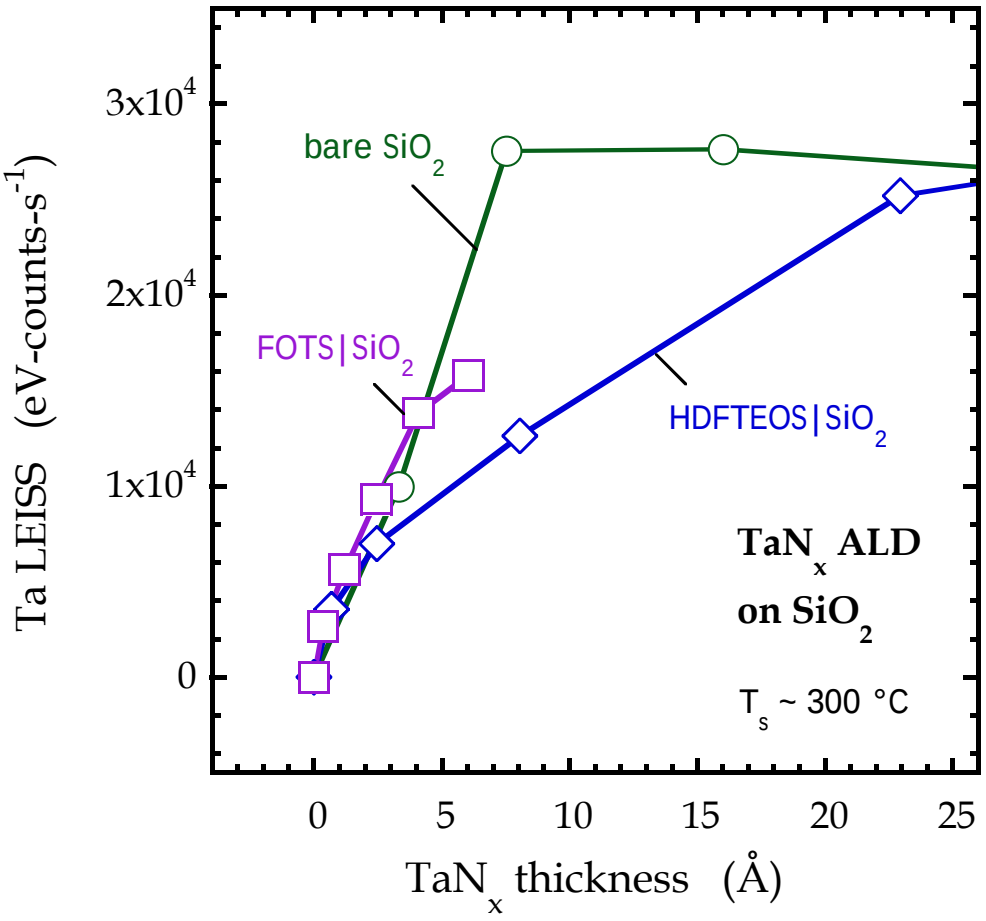

Figure 4 - 11 Integrated intensities of the peaks from LEISS associated with the thin film, Ta, as a function of the thin film thickness for the deposition of TaN_x at T_s = 300 °C on clean SiO_2 and FOTS and HDFTEOS on SiO_2. Here the TaN_x thin film thicknesses are that predicted by the fits to the Ta($4d_{5/2}$) data shown in Fig. 4-5. This representation is the equivalent to the theoretical expectation given in the central panel shown in Fig. 4-10.

4.5.2 Growth on bare and modified Cu

Growth of TaN_x on Cu, bare or modified, is different from that on SiO_2. First, for bare Cu, we found for these conditions that the data from XPS, both from the thin film [Fig. 4-5(b)] and substrate signals [Fig. 4-7(b)], indicate a steady-state rate of growth of TaN_x that is nevertheless ~ 60 % of that we find on clean SiO_2. These data are described by a model that assumes that the rate of growth is steady, and that no incubation period exists. Second, growth on the surface terminated by the SAMs is essentially the same as that on un-modified Cu. We will attempt to reconcile these observations in the following, starting first with growth on bare Cu.

Based on our prior work [32], the growth of TaN_x on Cu is indeed different from that on SiO_2. For thin films of ~ 5 and 10 Å nominal thickness we found that the TaN_x/Cu interface was not abrupt, that neither thin film was continuous at these thicknesses and that the near surface layer was likely a mixture of TaN_x and Cu. The results we present here are consistent with that viewpoint. Unlike clean SiO_2, on bare Cu complete coverage of the substrate has definitely not occurred after 80 cycles of TaN_x growth, and may not even have occurred after 200 cycles of growth based on the size of the LEISS Ta signal at this point [*cf.* Fig. 4-9(c)]. For example, after 10-20 cycles of ALD there is little change in the Cu LEISS signal, and after 40 cycles this signal is still about ½ of that for the bare Cu substrate. Thus, these results from LEISS indicate that the surface consists of a mixed TaN_x/Cu layer for at least the first 80 cycles. It is possible that clean, low index [e.g., (111)] faces of Cu do not provide active sites for TaN_x nucleation, whereas defect sites, and certainly regions where TaN_x is present could provide such sites. Thus, it is entirely feasible that the initial rate of

ALD on bare Cu may be less than that on clean SiO_2, and its rate may continue to be suppressed until the entire Cu substrate is covered. For our conditions, closure of the TaN_x thin film on bare Cu may be almost complete at ~ 200 cycles where, unfortunately, we are not particularly sensitive to changes in the growth rate due to attenuation effects on the signal from XPS. Thus, based on our calculations of the growth rate from XPS (Ta and Si signals) we estimate that a nominal thickness of ~ 35-47 Å after 200 cycles of ALD is required for closure of TaN_x on bare Cu.

Growth of TaN_x thin films on the Cu substrate modified by the two SAMs are very similar to that found for bare Cu. First, for HDFTEOS|Cu the reason for this behavior is clear. Based on results from XPS [Figs. 4-3, 4-8(c,d)] it is obvious that the majority of this SAM thermally desorbs at the substrate temperature used here for ALD. An interesting question to ask is why does HDFTEOS desorb and FOTS does not? The two molecules have similar fluorinated alkyl tail groups, $-(CH_2)_2(CF_2)_nCF_3$, where n = 5 (FOTS) and 7 (HDFTEOS). The difference in binding between these tail groups based on van der Waals interactions is expected to be small. The answer likely lies in the head groups. If, for example, the Cu surface can activate the Si-Cl bonds in the FOTS head group, but not the Si-OR bonds in the HDFTEOS head group, this could explain the observed difference.

Growth of TaN_x on FOTS|Cu occurs in the presence of a significant coverage of the FOTS SAM, or possibly partially dissociated molecular fragments of this molecule. Our results from XPS [Figs. 4-3, 4-8(c,d)] clearly indicate the presence of these species. Why do these fragments apparently affect growth so minimally? First, as discussed above, the bare Cu surface does not possess the intrinsic activity of the SiO_2 surface, even after 80 cycles of ALD and a nominal TaN_x thin film thickness of ~ 14-23 Å. As the TaN_x thin film grows,

and a mixed TaN_x/Cu surface is formed, what is a likely fate for the FOTS SAM? One possibility is that the SAM may segregate to those areas that are Cu rich, ones that may not be effective in nucleating further growth of TaN_x. If we look at the XPS results for the FOTS SAM [Fig. 4-8(c,d)] we see that the rate at which these signals are attenuated do not match the prediction of the model that assumes TaN_x overgrowth, namely the intensity from XPS is higher than what the model predicts. Also, we see from the LEISS results [Fig. 4-9(d)] that the substrate Cu signal is strongly attenuated, even for 0-30 cycles of ALD on FOTS|Cu—this signal is about 30% of that observed for bare Cu and HDFTEOS|Cu for this region of growth. These results strongly suggest that the FOTS SAM is located mostly in the Cu-rich areas of the surface, and these act to attenuate the Cu LEISS signal, while those signals associated with XPS and the SAM are not strongly attenuated.

In Fig. 4-12 we consider a construct similar to that shown in Fig. 4-11 for growth on clean and SAM-modified SiO_2, where here we plot the intensity from LEISS for the Ta peak vs. the TaN_x thin film thickness based on an analysis of the data from XPS shown in Fig. 4-5(b). Again these data for growth on Cu are plotted to account for attenuation effects in XPS, conforming to the analysis as presented in Fig. 4-10. We see that these data for all 3 cases of growth on Cu exhibit downward curvature, which is very indicative of 3D islanded/RD growth. Closer examination of these data indicate a strong similarity to the results for growth on SAMs|SiO_2. Unlike the growth of TaN_x on SAMs|SiO_2, however, the amount of material deposited per cycle on Cu, clean or modified, does not change markedly for the number of ALD cycles examined here, remaining at a value of ~ 60% of that observed on clean SiO_2. A constant, relatively high growth rate indicates that TaN_x once nucleated on Cu does not provide the only sites for further growth, otherwise the rate of growth should

accelerate as it does on SAMs|SiO_2. In particular, areas of Cu surrounding TaN_x islands must remain active for adsorption/growth. For this mechanism to be in play, material that is added in each cycle in these surrounding areas must eventually join the existing TaN_x islands via transport and incorporation. For growth to remain self-limiting, this transport most likely occurs after the half cycle involving $Ta[N(CH_3)_2]_5$, possibly during the half cycle involving the NH_3 exposure.

Is there evidence for transport in the case of growth on Cu? Unlike SiO_2, where strong covalent linkages, e.g., Ta-O-Si, will form on chemisorption of the Ta complex, no such bonds will form on the Cu surface. In previous work [32] we have shown that growth of TaN_x on Cu results in significant smoothening of the surface, and it is more than is observed to occur based on simple annealing to the ALD process temperature in either an Ar or NH_3 atmosphere. Moreover, the amount of smoothening can only be reconciled if transport of Cu is also occurring. The picture that we are left with concerning TaN_x growth on Cu, both on bare and SAM modified surfaces, is a dynamic one, where species are free to diffuse during the ALD process, perhaps most effectively during the NH_3 half-cycle. Proof of such a mechanism would likely require *in situ* surface sensitive measurements for each half-cycle, experiments that are beyond the scope of the work presented here.

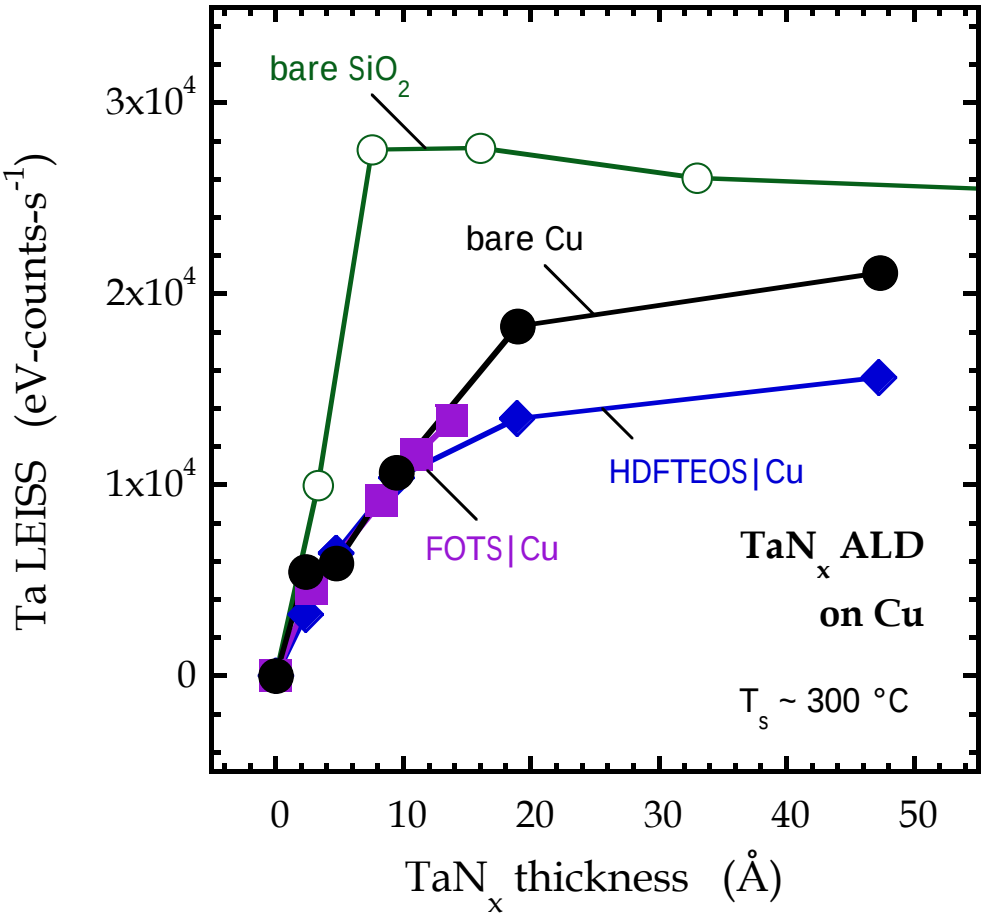

Figure 4 - 12 Integrated intensities of the peaks from LEISS associated with the thin film, Ta, as a function of the thin film thickness for the deposition of TaN_x at T_s = 300 °C on bare Cu and FOTS and HDFTEOS on Cu. Here the TaN_x thin film thicknesses are that predicted by the fits to the Ta($4d_{5/2}$) data shown in Fig. 4-5. This representation is the equivalent to the theoretical expectation given in the central panel shown in Fig. 4-10. The behavior of the Ta LEISS signal for growth on clean SiO_2 is reproduced.

4.6 Summary and Conclusions

To conclude, we present in schematic form in Fig. 4-13 our understanding of the effects of the SAMs examined here on the ALD growth of TaN_x on the SiO_2 and Cu surfaces. For growth on clean SiO_2, as may be seen in Fig. 4-13(a), the thin film roughness indicated by the cartoon is consistent with our previously reported values (~ 0.7-0.8 ML RMS) for this system for similar thicknesses [32]. On clean SiO_2, the TaN_x thin film grows mostly in a 2D layer-by-layer mode, but not strictly in the way that epitaxial growth is observed in many thin film systems where each (n) layer essentially completes before the next (n + 1) layer starts to grow. In epitaxial systems LbL growth is facilitated by interlayer transport, coupled with preferred incorporation at step edges. These features likely play a limited role in ALD, which leads to more random deposition and the observation of a continuous thin film only after the deposition of ~ 3 MLs of TaN_x.

For the ALD of TaN_x on the SiO_2 surface terminated by the SAMs, growth begins at defect sites, where free –OH(a) is present, as indicated schematically in Fig. 4-13(b). For the early stages of growth, 0-20 cycles of ALD, the amount deposited per cycle is small, and a small fraction of the surface is covered by the TaN_x thin film after 20 cycles of growth. On bare SiO_2, in contrast, the surface is nearly entirely covered by the TaN_x thin film after 20 cycles of ALD. After about 20 cycles of ALD, growth accelerates, and the amount deposited per cycle begins to approach that observed on clean SiO_2, after about 40 cycles of ALD. Although the kinetics of growth indicated by both XPS and spectroscopic ellipsometry indicate that steady-state conditions have been achieved after 40 cycles, and certainly after 80 cycles, the results from LEISS indicate that the growth is very 3D and islanded for growth on

these SiO_2 surfaces terminated by SAMs. For example, although approximately the same amount of TaN_x has been deposited after 40 cycles on SAM|SiO_2 and 20 cycles on clean SiO_2, only ~ 1/3 of the surface has been covered for the former case. Based on our results, both SAMs, FOTS and HDFTEOS, are essentially stable at the substrate temperature used here (300 °C) for ALD growth. Moreover, the rates of decay of the signals from XPS uniquely associated with fluorinated SAMs are consistent with TaN_x overgrowth of these organic monolayers, and only perhaps modest degradation during ALD.

For the ALD of TaN_x on the Cu surface, both on bare and Cu surfaces terminated by the SAMs, the situation is quite different as displayed in Fig. 4-13(c). Consistent with our previously reported work on clean Cu [32], growth differs from clean SiO_2 in that the growth is not 2D LbL, and the interface that is formed is not abrupt. First the polycrystalline Cu thin films are not nearly as smooth as the SiO_2 surface examined here, which is indicated schematically in Fig. 4-13(c). The initial rate of growth is about 60% of that observed on SiO_2, and it remains approximately constant up to the point where we are still sensitive to the growth rate measured using XPS (< 80 cycles or < 2 nm). Results from LEISS indicate 3D islanded growth, where the surface is not completely covered by the TaN_x thin film until 200 cycles of ALD. Concerning the effect of the SAMs on ALD growth on Cu, we observe with both SAMs that there is essentially no effect. In the case of HDFTEOS, results from XPS indicate that essentially all of this SAM thermally desorbs from the Cu surface at the substrate temperature examined here for ALD (300 °C), thus, no effect. For FOTS, however, this SAM is largely retained on the Cu surface at the ALD process temperature examined here. Indeed, from XPS, signals uniquely associated with this fluorinated SAMs are larger than one would expect if a TaN_x thin film were formed uniformly across the surface and

buried the SAM. On possible explanation for this observation is that the growing TaN_x thin film mostly displaces the SAM to the Cu rich parts of the surface. The difference observed between the two SAMs on Cu likely reflects the head group chemistry, where the Cu surface can activate the Si-Cl bonds in FOTS, while it does not activate Si-OR bonds nearly as effectively. Finally, the bound FOTS molecules or molecular fragments, are likely mobile on the Cu surface, where they apparently have little effect on the growth kinetics. This observation could reflect the differences between the very directional covalent bonds between the SAMs and the SiO_2 surface vs. the metallic bonding that occurs on Cu.

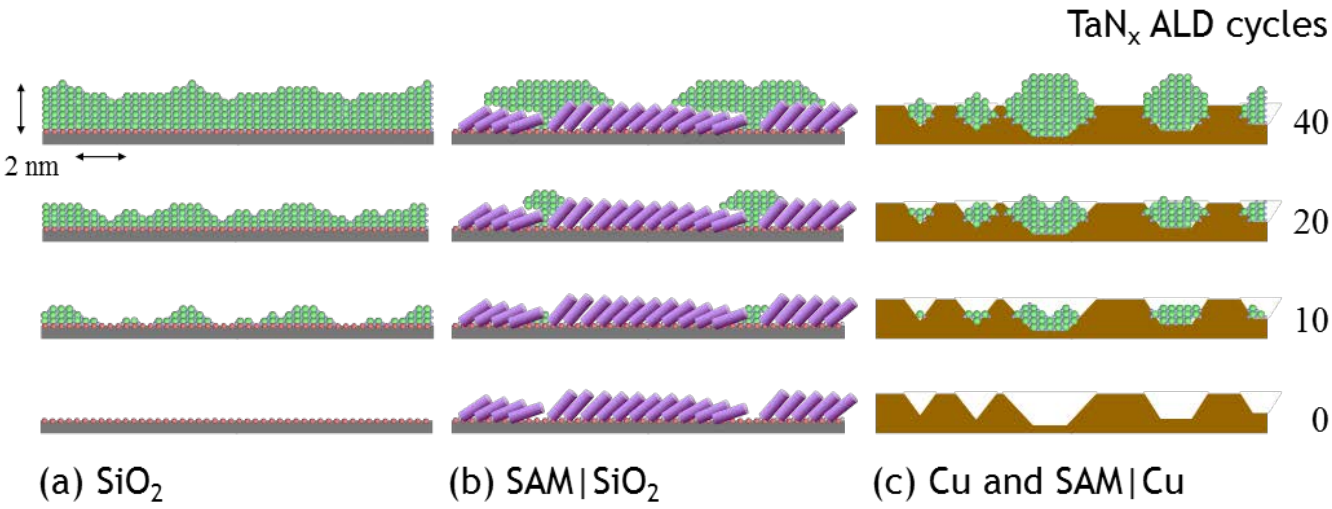

Figure 4 - 13 Schematic representation of the early stages (0-40 cycles) of ALD growth of TaN_x for the systems examined here, where these representations are designed to replicate our results from both XPS and LEISS. The systems fall into 3 classes: **(a)** quasi-2D LbL growth on SiO_2; **(b)** islanded 3D growth on SAMs|SiO_2 where the TaN_x thin film eventually overgrows the SAM; and **(c)** growth on Cu where on all surfaces growth is 3D and islanded, and the TaN_x|Cu interface is diffuse.

4.7 Supplementary Material

4.7.1 Experimental procedures

4.7.1.1 Substrate preparation

The Si substrates, approximately 17 × 17 mm^2 square samples cleaved from single-side polished, Si(100) wafers (B doped, resistivity 38-63 Ω cm), were first sonicated in $CHCl_3$, rinsed in deionized (DI) water and dried in N_2 to remove organic contaminants. The native SiO_2 layer was removed from the substrates by dipping in buffered oxide etch (BOE) for 2 minutes. The substrates were then re-oxidized by dipping in Nanostrip for 15 min at a temperature of ~75 °C. The BOE/Nanostrip treatment was then repeated. This method is known to produce a 15-20 Å layer of SiO_2. The Cu substrates (900 Å thick film of PVD Cu|SiO_2) were cleaved into 17 × 17 mm^2 square samples then used as-received.

4.7.1.2 SAM formation

The molecules used to form the self-assembled monolayers (SAMs) used in this study, 1H,1H,2H,2H-perfluorooctyltrichlorosilane (FOTS) and heptadecafluoro-1,1,2,2-tetra-hydrodecyltriethoxysilane (HDFTEOS) were purchased from Gelest, Inc. (Morrisville, PA). The SAMs were transferred to a bubbler under a nitrogen environment, which was then attached to a molecular vapor deposition tool, a MVD-100, Applied Microstructures (San Jose, CA). Substrates, prior to SAM formation in the MVD tool, were exposed to 60 s of O_2 plasma (200 W), with an O_2 flow rate of 150 standard cm^3-min^{-1} (sccm), followed by 600 s of exposure a mixture of the SAM (0.7 Torr) and H_2O (6 Torr).

4.7.1.3 Atomic layer deposition

All TaN_x thin films were deposited using a viscous flow ALD reactor (Oxford FlexAL, Oxford Instruments, Oxfordshire, UK). After insertion into the reactor the substrates were pre-heated for 3 min. to the temperature employed for ALD (300 or 225 °C) in 200 mTorr Ar, then exposed to repeated cycles of $Ta[N(CH_3)_2]_5$|Ar purge|NH_3|Ar purge, with individual cycle times of 2s|3s|5s|5s. In prior work associated with the commissioning of this ALD process on this tool these reaction conditions have been shown to produce saturation of the surface with chemisorbed species in each half-cycle at steady-state growth conditions, and adequate purging between cycles. During the $Ta[N(CH_3)_2]_5$ exposure step, the total chamber pressure was 80 mTorr, and the $Ta[N(CH_3)_2]_5$ was delivered to the chamber using a carrier gas (Ar) flow rate of 150 sccm. The $Ta[N(CH_3)_2]_5$ vessel or "bubbler" was heated to a temperature of 85 °C for delivery of the precursor. During the NH_3 exposure step the total chamber pressure was also 80 mTorr, where the flow rates of NH_3 and Ar were 50 and 150 sccm, respectively.

4.7.1.4 Spectroscopic ellipsometry

Spectroscopic ellipsometry (SE; Woollam, Lincoln NE) was employed to measure the thin film thicknesses for ALD growth of TaN_x on SiO_2 and HDFTEOS|SiO_2. We used two methods to fit the data from SE: one used the optical properties for Ta_2O_5 for the thin film, while a second used the Cauchy dispersion relationship for the optical constants. In Fig. 4S-1 we plot the TaN_x thin film thickness as a function of the number of ALD cycles for growth on SiO_2 and HDFTEOS|SiO_2. The filled symbols represent the thickness found from the

model using Ta_2O_5 and the open symbols represent those found from the Cauchy model. We see that both fits produce similar results, where the largest discrepancy is found for the thickest film grown on SiO_2., one sufficiently thick that total oxidation has not occurred.

4.7.1.5 X-ray photoelectron spectroscopy

XPS was carried out in a UHV system using an Omicron Sphera U5 concentric hemispherical electron energy analyzer (Omicron Nanotechnology USA, Eden Prairie, MN), operated at a constant pass energy of 50 eV. Non-monochromated Mg Kα x-rays (1253.6 eV excitation energy) and Al Kα x-rays (1486.7 eV excitation energy) were produced using an Omicron DAR 400 twin anode source operated at 300 W (15 kV anode potential, 20 mA emission current). For angle-resolved XPS (ARXPS) measurements, the takeoff angle was varied by rotating the sample with respect to the analyzer axis. Background subtraction was carried out using the Shirley method **[S-1]** Peak areas were calculated by fitting spectra to a Gaussian/Lorentzian product formula with a mixing ratio of 0.7 **[S-2]**. Data analysis was carried out using CasaXPS software, version 2.3.15.

4.7.1.6 Low-energy ion scattering spectroscopy

LEISS was carried out in a UHV system using an Omicron Sphera U5 concentric hemispherical electron energy analyzer, operated at a fixed retard ratio (FRR) of 5. Helium ions possessing 1000 eV of kinetic energy were produced using a differentially pumped scanning small spot ion source (SPECS ion source IQE 12/38). The axis of the ion source is 40° off the axis the analyzer, resulting in an effective scattering angle for LEISS of 140°. For LEISS samples were oriented such that they were normal to the ion beam, and all samples

were exposed to the ion beam for two minutes before the start of data collection to ensure a stable and constant ion beam current. A typical scan over the range of kinetic energies (1-1000 eV) would take approximately 10 min. For Ar^+ sputtering, a beam of ~ 136 μm dia., with a current of ~ 0.6 μA was rastered over an area of 1 × 1 cm^2, producing a time-averaged ion current density of 0.6 μA-cm^{-2}. We estimate a nominal sputter etch rate of TaN_x by these 3 keV Ar^+ ions of 0.3 Å-min^{-1}. For LEISS, the He^+ beam was ~ 146 μm dia., with a current of ~ 0.082 μA. Data analysis was carried out using CasaXPS software, version 2.3.15. Background subtraction was carried out assuming a linear baseline. Peak areas were calculated by fitting spectra to a Gaussian/Lorentzian product formula with a mixing ratio of 0.7. Asymmetry of the peaks was accounted for by using asymmetric line-shape functions in CasaXPS.

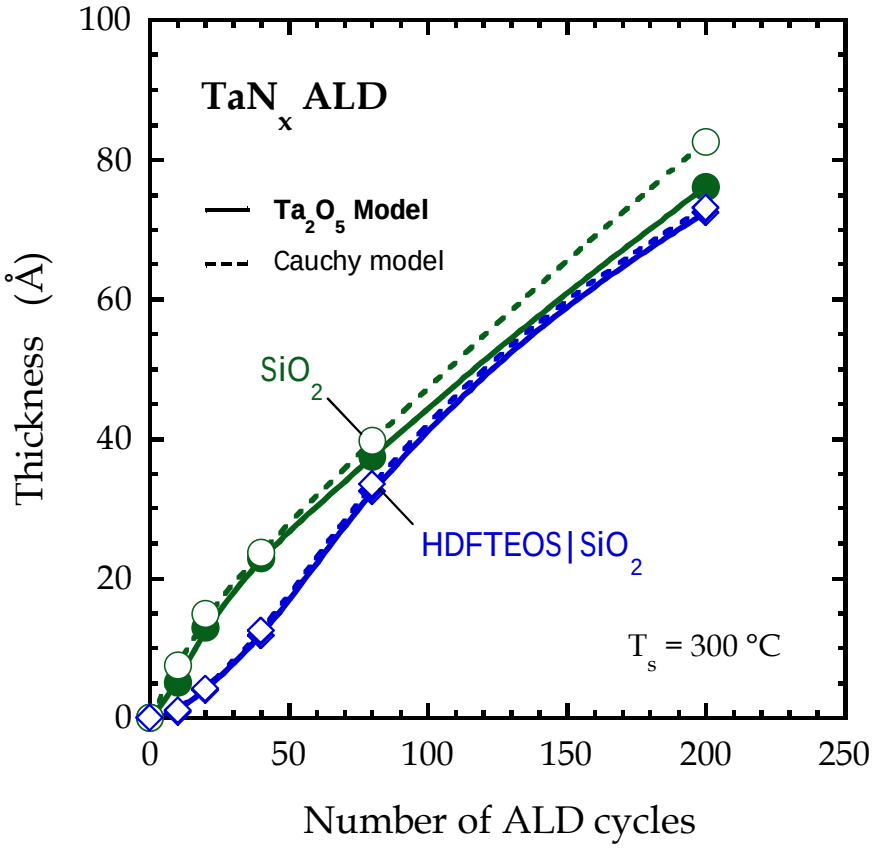

Figure 4S - 1 Spectroscopic ellipsometric TaN_x thin film thickness as a function of the number of ALD cycles for growth on SiO_2 and HDFTEOS|SiO_2. The filled symbols represent the thickness found from the model using Ta_2O_5 and the open symbols represent those found from the Cauchy model

4.7.2 Results and discussion

4.7.2.1 Calculation of the absolute sensitivity of the SAMs

This calculation requires the use of a calibration standard (we use polycrystalline thin film of Au) and the following factors: the photoelectron cross sections, σ, for the F(1s), C(1s) and the Au($4f_{7/2}$) peaks; the analyzer transmission, *T(E)*; the atomic density of the calibration standard (Au), and the attenuation length, λ, of the photoelectrons in both the standard and the sample of interest. The uncertainty is largest for the latter, i.e., the attenuation length of the F(1s) and C(1s) photoelectrons emitted from the SAMs. One complication in these calculations is the effect of adventitious carbon acting to attenuate the signals obtained from the samples, in particular those with SAMs. Based on previous studies, we have found that sputtering samples for 1 min with 3 keV Ar^+ effectively removes the majority (> 70%) of this contamination layer, while affecting minimally underlying substrates composed of Cu, SiO_2 or a TaN_x thin film. Such is not the case for these SAMs, as a 1 min. sputter removes > 90% of the coverage of either HDFTEOS or FOTS (*vide infra*). Thus, here we have calculated the SAM densities in two ways: (i) ignoring any effects of the adventitious carbon layer ; and (ii) assuming the effect of the adventitious carbon layer is the same as what we observe for the attenuation of relatively thick TaN_x samples. In the latter case, the correction to the results (the SAM density) is about a factor of 1.25.

4.7.2.2 XPS of the C(1s) region

Analysis of the C(1s) feature reveals that photoemission from samples possessing either FOTS or HDFTEOS exhibits as many as three main peaks: one associated with aliphatic and adventitious C, one from C bound to O, and one from the CF_x species in the backbone. In Fig. 4S-2 we plot spectra for the C(1s) region for a HDFTEOS|SiO_2 sample subjected to 0 cycles of ALD. First, for the pre-sputter sample, a feature appearing at a binding energy higher than that associated with aliphatic (possibly adventitious) carbon is clearly present. The size of binding energy shift (~ 7-9 eV from aliphatic C) is consistent with CF_x species **[S-3]**, where x = 2, 3. Moreover, this feature clearly consists of a peak at 291.5 eV corresponding to CF_2, and a shoulder at 293.8 eV that represents CF_3. Similar features were obtained on Cu surfaces, and for FOTS. Also plotted in Fig. 4S-2 is the spectra obtained for this same HDFTEOS|SiO_2 sample following a 1 min. Ar^+ sputter as described above. As may be seen, the feature associated with CF_x species is *totally absent*, whereas that associated with aliphatic, possibly adventitious C is nearly unchanged.

4.7.2.3 Effects of sputtering: XPS

In previous work we have shown that a short 1 min. Ar^+ sputter can be effective in terms of removing adventitious C, which can be beneficial for analysis via XPS, while also essential for analysis via LEISS. In Fig. 4S-3 we plot the integrated intensities for the Ta($4d_{5/2}$) and Si(2p) peaks as a function of the number of ALD cycles for TaN_x growth on SiO_2., measured both pre- and post-sputter. As can be seen, the short sputter leads to a modest increase in the Ta($4d_{5/2}$) intensity, and a much smaller increase in the Si(2p) signal. We consider a larger set of results in Fig. 4S-4, where we plot the Ta($4d_{5/2}$) intensity post-

sputter vs. pre-sputter, and likewise the same for the Si(2p) feature for all 3 SiO_2 substrates: SiO_2, HDFTEOS|SiO_2, and FOTS|SiO_2. As may be seen these sets of data show a very consistent relationship sample-to-sample, with and without the presence of the SAMs. We observe a similar trend concerning the results on Cu, with somewhat more scatter in the data. Finally, as seen in Fig. 4S-2, sputtering has a huge effect on the SAMs examined in this case. In Fig. 4S-5 we plot the integrated intensities for the F(1s) and the C(1s)-CF_x peaks as a function of the number of ALD cycles for TaN_x growth on HDFTEOS|SiO_2, measured both pre- and post-sputter. These results emphasize the sensitivity of the SAMs to ion bombardment.

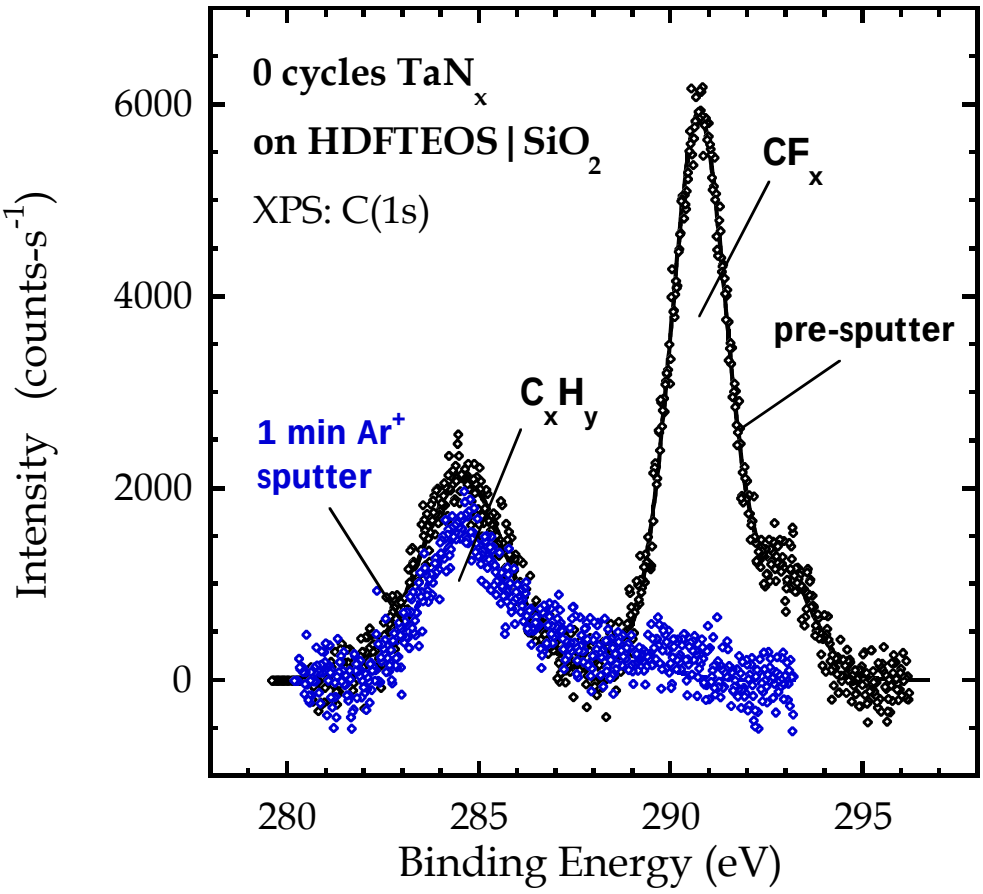

Figure 4S - 2 XPS C(1s) spectra for HDFTEOS SiO_2, subjected to 0 cycles of ALD, pre – Ar^+ sputter etch (black) and post – 1 min Ar^+ sputter etch (blue)

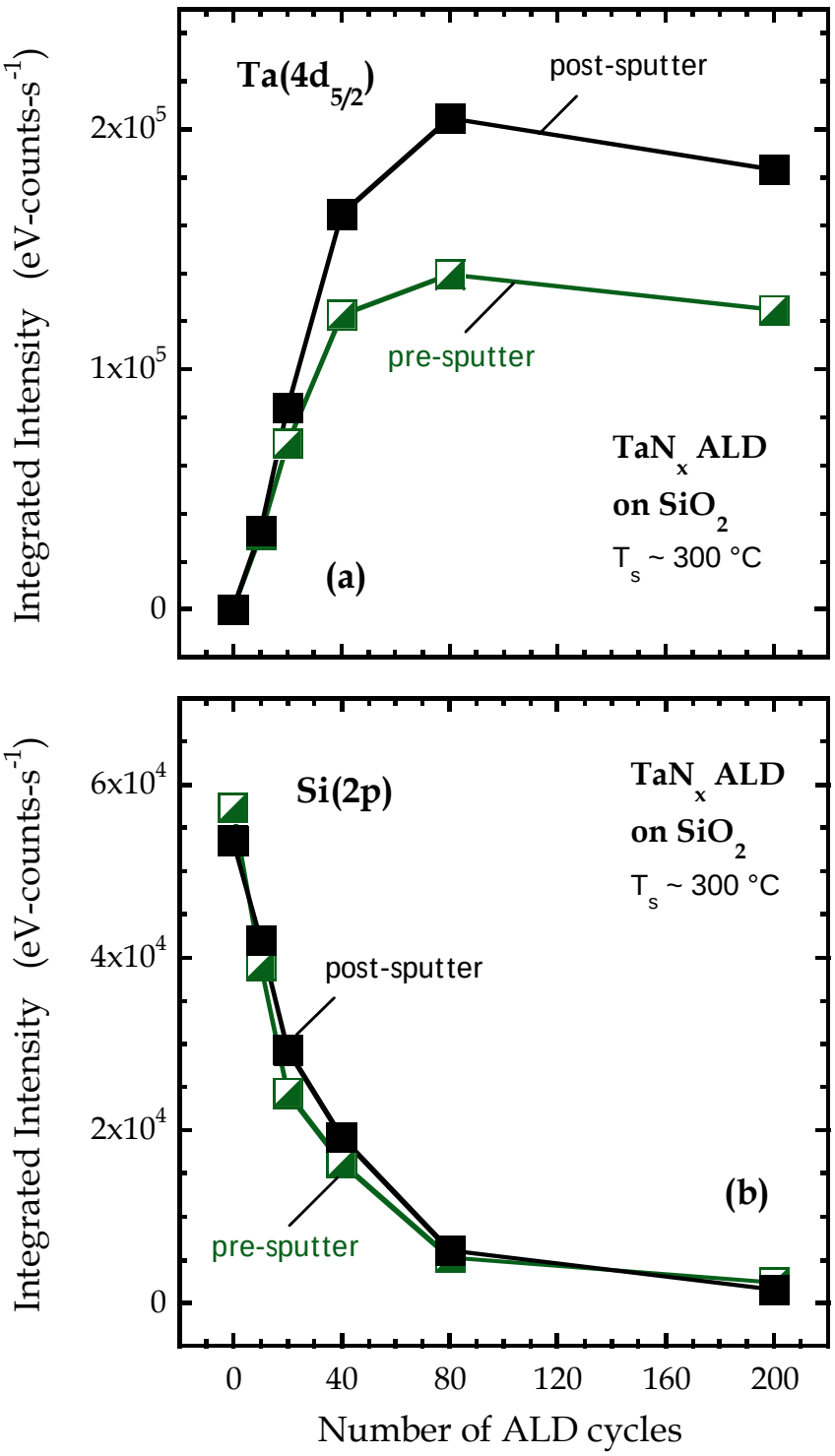

Figure 4S - 3 XPS integrated intensities for the **(a)** Ta($4d_{5/2}$) and **(b)** Si(2p) peaks as a function of the number of ALD cycles for TaN_x growth on SiO_2

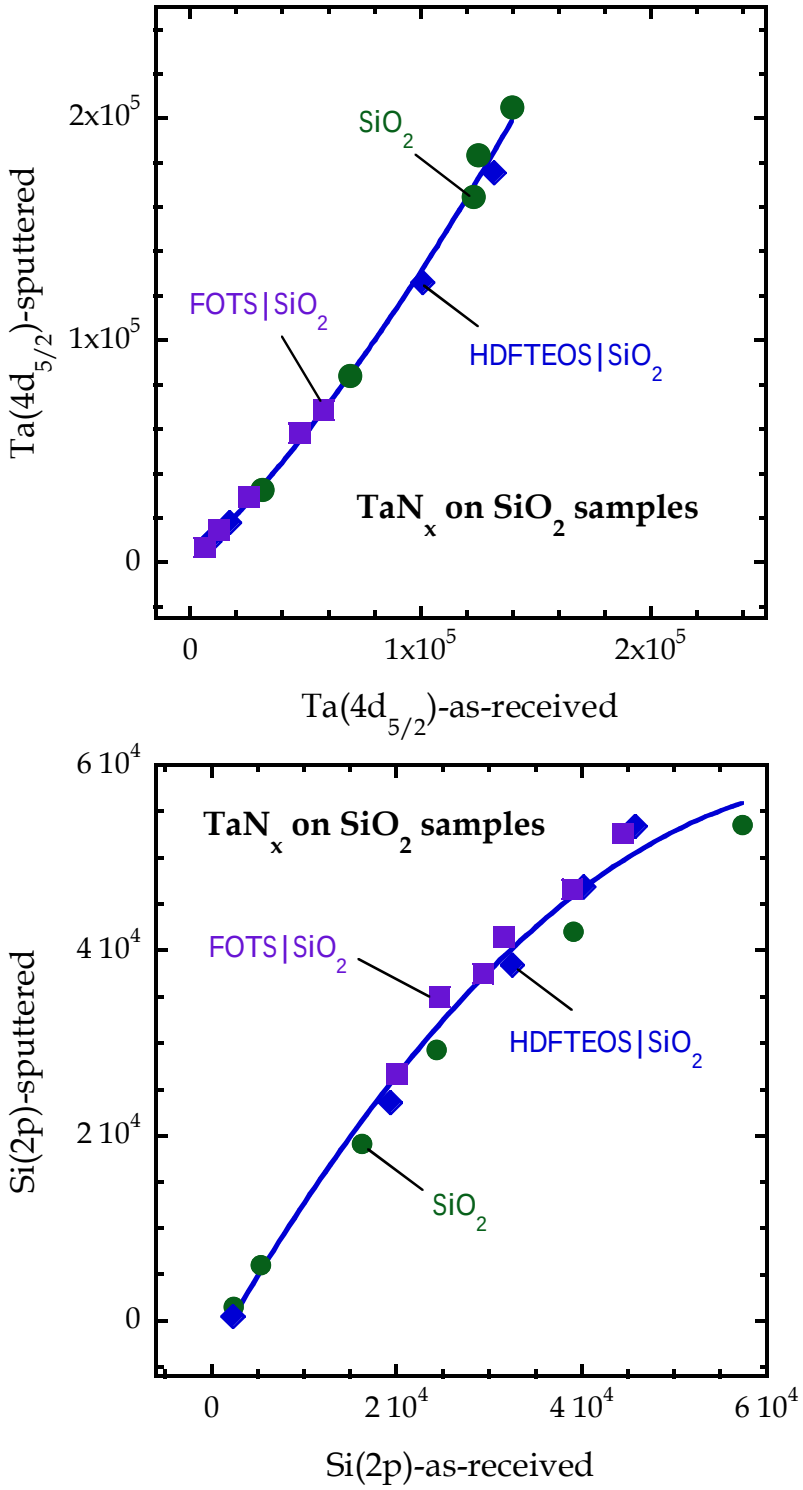

Figure 4S - 4 Ta($4d_{5/2}$) XPS integrated intensities post-sputter vs. pre-sputter, and likewise the same for the Si(2p) feature for all 3 SiO_2 substrates: SiO_2, HDFTEOS|SiO_2, and FOTS|SiO_2

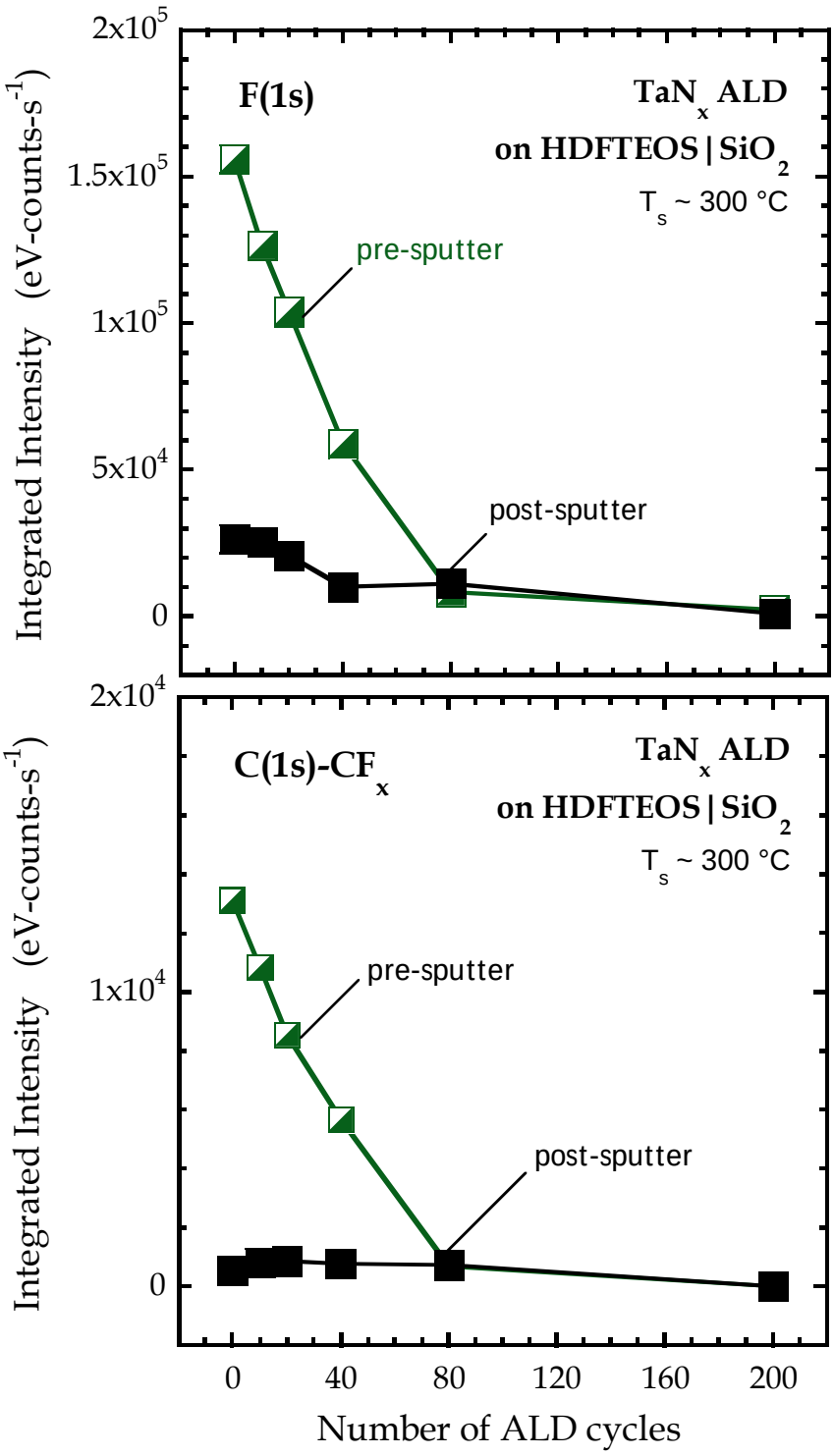

Figure 4S - 5 XPS integrated intensities integrated intensities for the F(1s) and the C(1s)-CF_x peaks as a function of the number of ALD cycles for TaN_x growth on HDFTEOS|SiO_2, measured both pre- and post-sputter

4.7.2.4 C/F ratio in the SAMs

There are 2 features in XPS that are uniquely identified with the SAMs, the F(1s) and C(1s)-CF_x peaks. We can use these peaks, along with appropriate corrections, to compute the elemental ratio F/C, counting only those C bound to F. For FOTS this ratio is 13/6 = 2.17, while for HDFTEOS it is 17/8 = 2.125. A large deviation from these values would signal that the SAMs have possibly degraded, either due to thermal treatments and/or the TaN_x ALD process itself. We plot the results of this analysis in Fig. 4S-6 for TaN_x ALD on all 4 surfaces examined here that contain either HDFTEOS or FOTS. Here the un-annealed as-received sample correspond to "-5" cycles of ALD. As may be seen, from this analysis we find that for all substrates the calculated elemental ratios lay in the range 1.50-2.60 close to the expected values, with an average value of 2.00 ± 0.34, for both the as-received samples, and those subjected to 0 cycles of TaN_x ALD. These values suggest that these SAMs are stable on these surfaces, even at the ALD process temperature.

4.7.2.5 XPS of Cu substrate

Analyses of the Cu substrates were conducted to determine the nature of both the "as-received" samples, and those that had been annealed to the temperature used for ALD ("0 cycles"). These data are displayed in Fig. 4S-7 where we plot results from XPS for the Cu(2p) region for as-received Cu, Cu (0 cycles), HDFTEOS (0 cycles) and FOTS (0 cycles). As may be seen, the as-received Cu sample exhibits peaks that indicate the presence of both metallic (Cu^0) and oxidized (Cu^{2+}) Cu. A fit of the Cu($2p_{3/2}$) peak for the as-received sample is shown in the figure. The tell-tale "shake-up" features are also observed for this oxidized surface. Upon annealing to the temperature for ALD we observe a large increase in the Cu

metallic peak, coupled with a substantial decrease in the Cu oxide peak, as well as mostly disappearance of the Cu^{2+} shake-up peaks. As may be seen in the figure, the samples with SAMs, also annealed to the temperature for ALD, exhibit spectra similar to that for "0 cycles" bare Cu. The features associated with the oxide are essentially absent. Thus, annealing samples to the temperature for ALD largely removes the Cu oxide.

4.7.2.6 Substrate temperature dependence of ALD

A set of experiments were conducted to verify that the conditions examined here were within the substrate temperature window for ALD. TaN_x ALD was performed at two different nominal substrate temperatures (T_s ~ 225 °C and 300 °C). In Fig. 4S-8 we present the integrated intensity from XPS of the Ta($4d_{5/2}$) peak as a function of the number of ALD cycles for growth of TaN_x on (a) clean SiO_2 and (b) bare Cu at these two substrate temperatures. In both cases these intensities have been normalized to the intensity from a ~ 150 Å thick TaN_x thin film, one that is sufficiently thick that photoemission from the underlying substrate is completely extinguished. As may be seen these results showed no significant differences in the amount of TaN_x deposited for these two temperatures on both substrates. Thus we are confident that these results are characteristic of the ALD window.

4.7.2.7 N/Ta ratio

Ultrathin films of transition metal nitrides are susceptible to oxidation, where O exchanges for N in the thin film. In Fig. 4S-9 we plot the elemental N/Ta ratio, computed using results from XPS, for TaN_x thin films on (a) SiO_2 and (b) Cu. These results confirm that the TaN_x thin films have been depleted of N by exposure to air. The thinner films,

exhibit a greater loss of N. At a larger number of cycles of ALD and for thicker thin films the ratio is N/Ta ~ 1.

4.7.2.8 LEISS

We consider four representative spectra for LEISS in Fig. 4S-10(a-d). In Figs. 4S-10(a,b) we consider spectra for the clean SiO_2 surface and that for 20 cycles of TaN_x ALD on clean SiO_2 and HDFTEOS|SiO_2. In (a) for growth on clean SiO_2 we see that there is the appearance of a large peak for Ta, and suppression of the Si substrate peak. The modest increase in the peak for O reflects the oxidation of the TaN_x surface due to the air break between growth and analysis. In (b) for growth on HDFTEOS|SiO_2 we see that there is a much smaller increase in the Ta peak, consistent with the attenuation of the rate of growth. There is also a new peak corresponding to F from the SAM. Spectra for growth on FOTS|SiO_2 are very similar to those shown in (b) for HDFTEOS|SiO_2. We consider growth on Cu in (c) and (d). In (c) for bare Cu we see a large Cu peak, a very small O peak, and a small peak at ~ 640 eV associated with residual (likely near sub-surface) Ar due to sputtering. After 20 cycles of TaN_x ALD, there is little change in the O and Cu peaks, while a distinct Ta peak grows in. Concerning growth on HDFTEOS|Cu, we find spectra essentially indistinguishable from those observed from clean Cu. In (d) for 20 cycles of TaN_x growth on Cu we see that a very broad feature appears, including a clearly resolved peak for F, and strong attenuation of the Cu substrate signal. On explanation for the attenuation of the Cu peak is due to the presence of the SAM, not the TaN_x thin film.

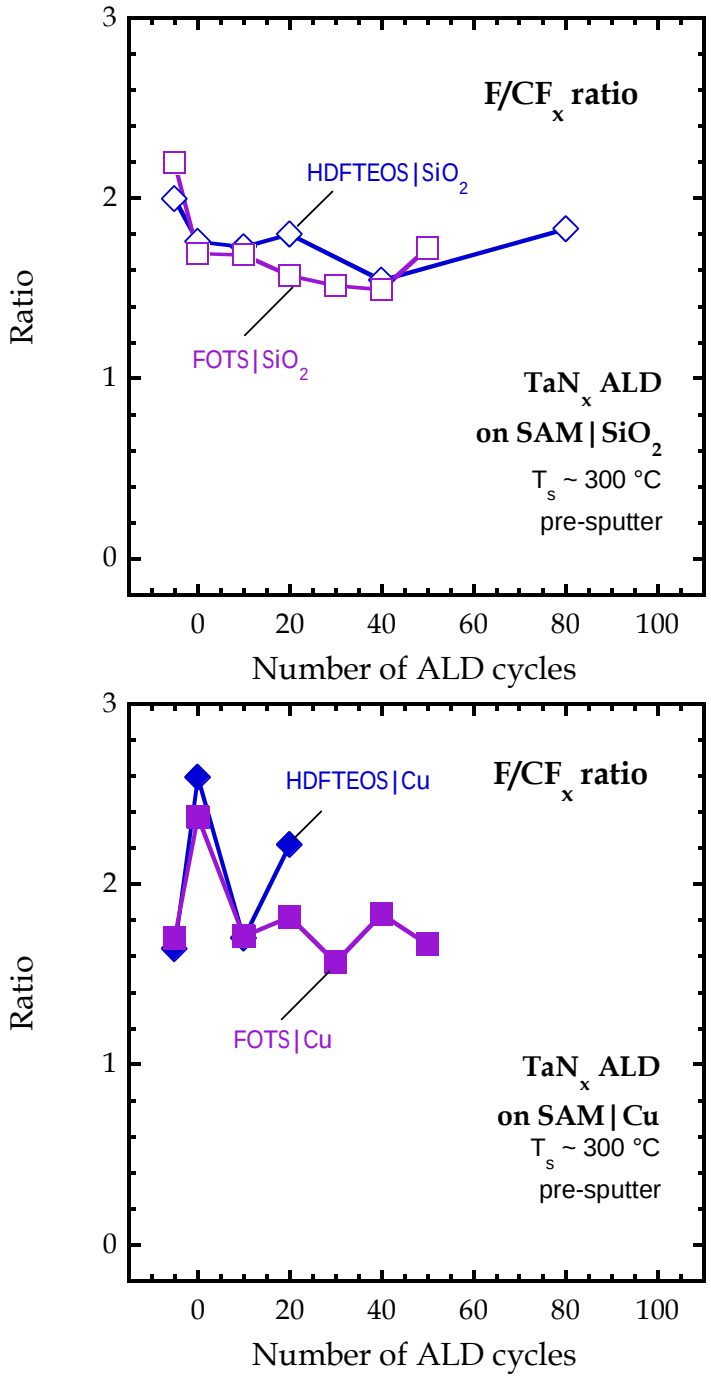

Figure 4S - 6 F/CF_x ratios for SiO_2 (top) and Cu (bottom) surfaces modified with SAMs

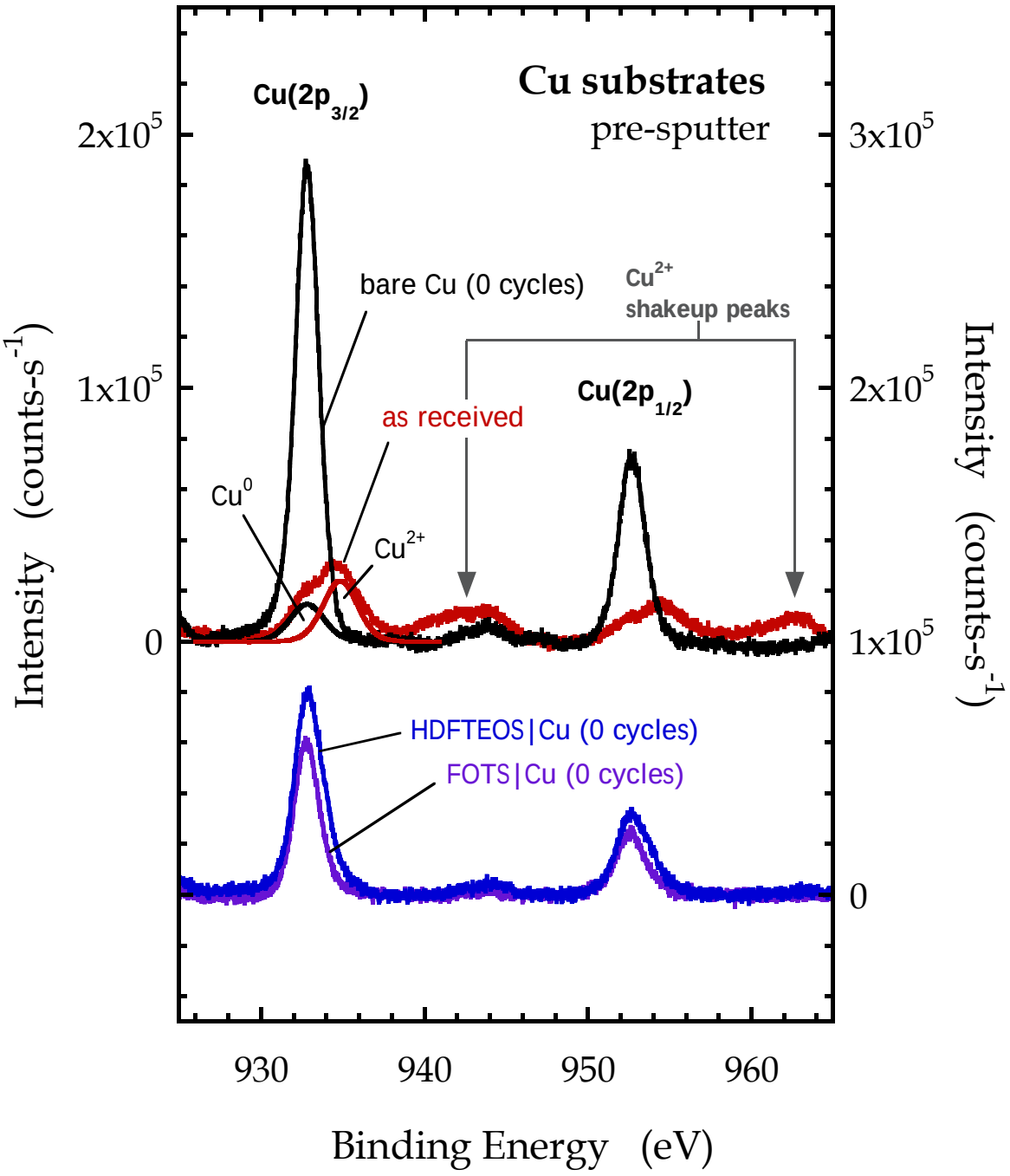

Figure 4S - 7 XPS of the Cu(2p) region for as-received Cu, Cu (0 cycles), HDFTEOS (0 cycles) and FOTS (0 cycles)

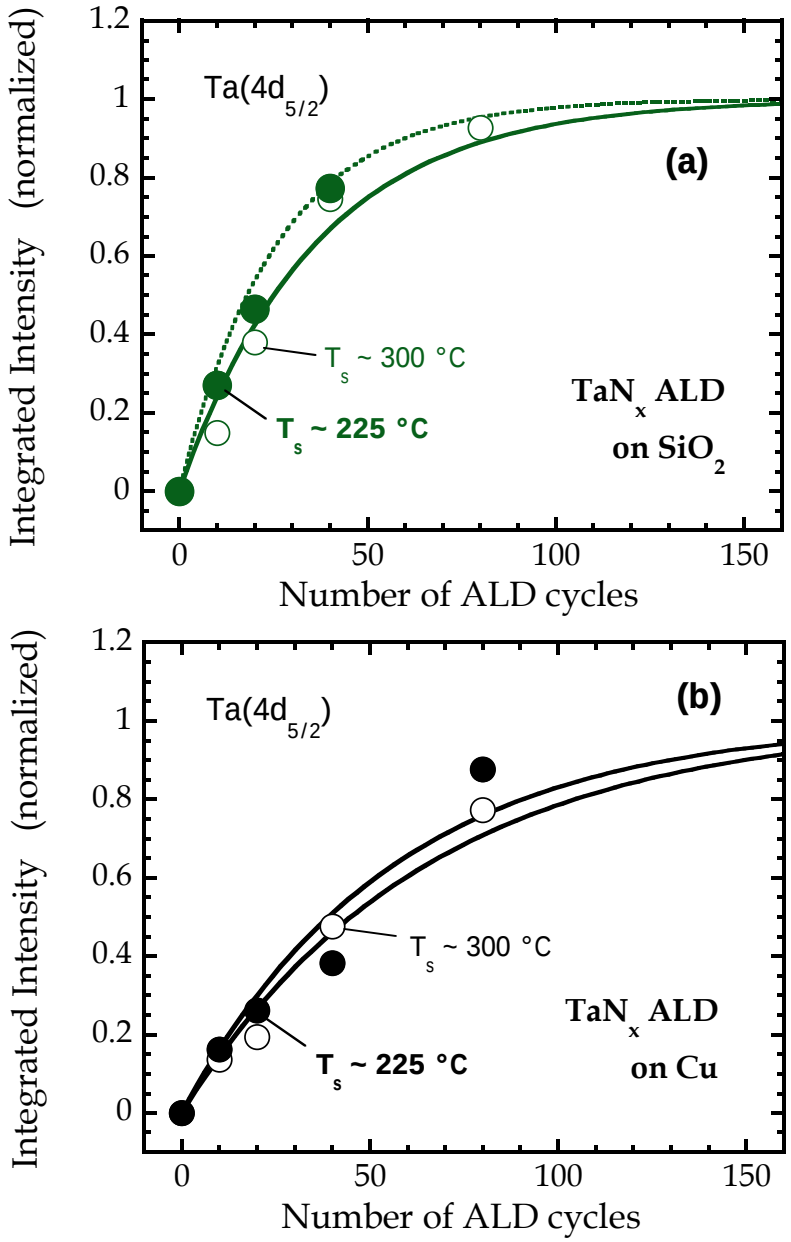

Figure 4S - 8 XPS integrated intensities of Ta($4d_{5/2}$) peak as a function of the number of ALD cycles for growth of TaN_x on **(a)** clean SiO_2 and **(b)** bare Cu at two substrate temperatures (T_s ~ 225 °C and 300 °C)

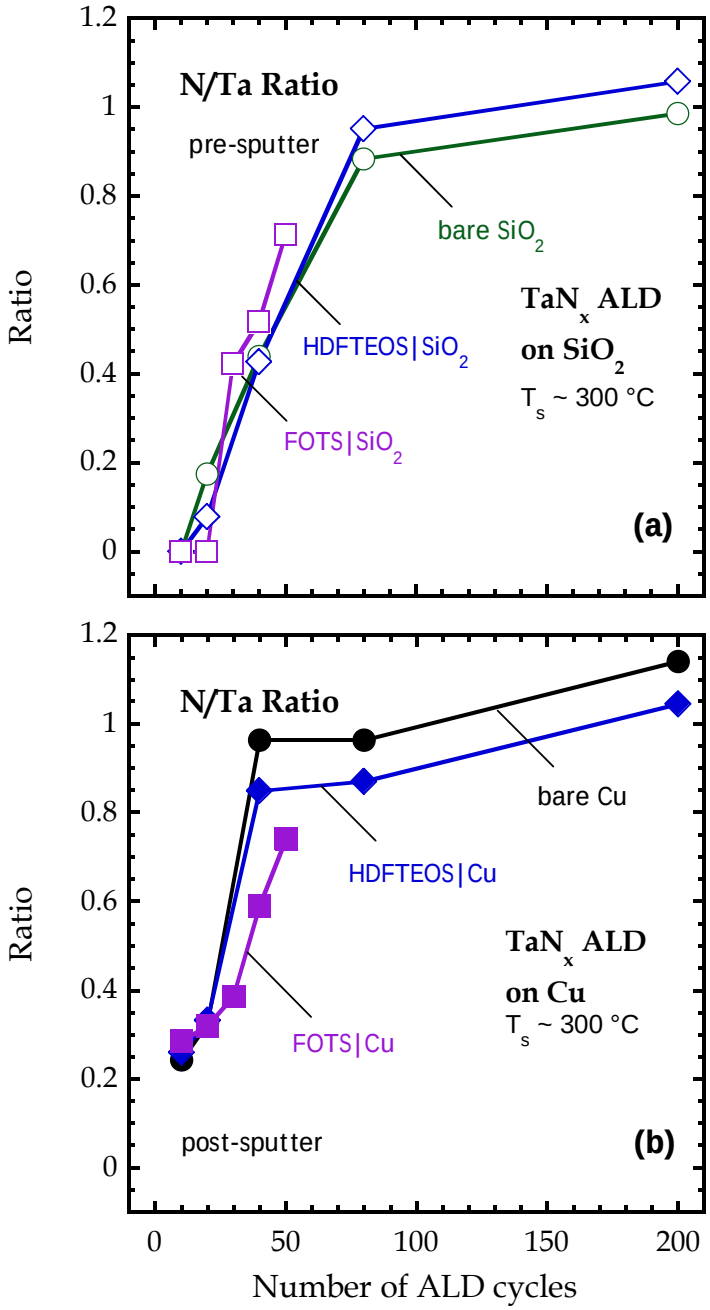

Figure 4S - 9 Elemental N/Ta ratio, computed using results from XPS, for TaN_x thin films on **(a)** SiO_2 and **(b)** Cu, as a function of ALD cycles

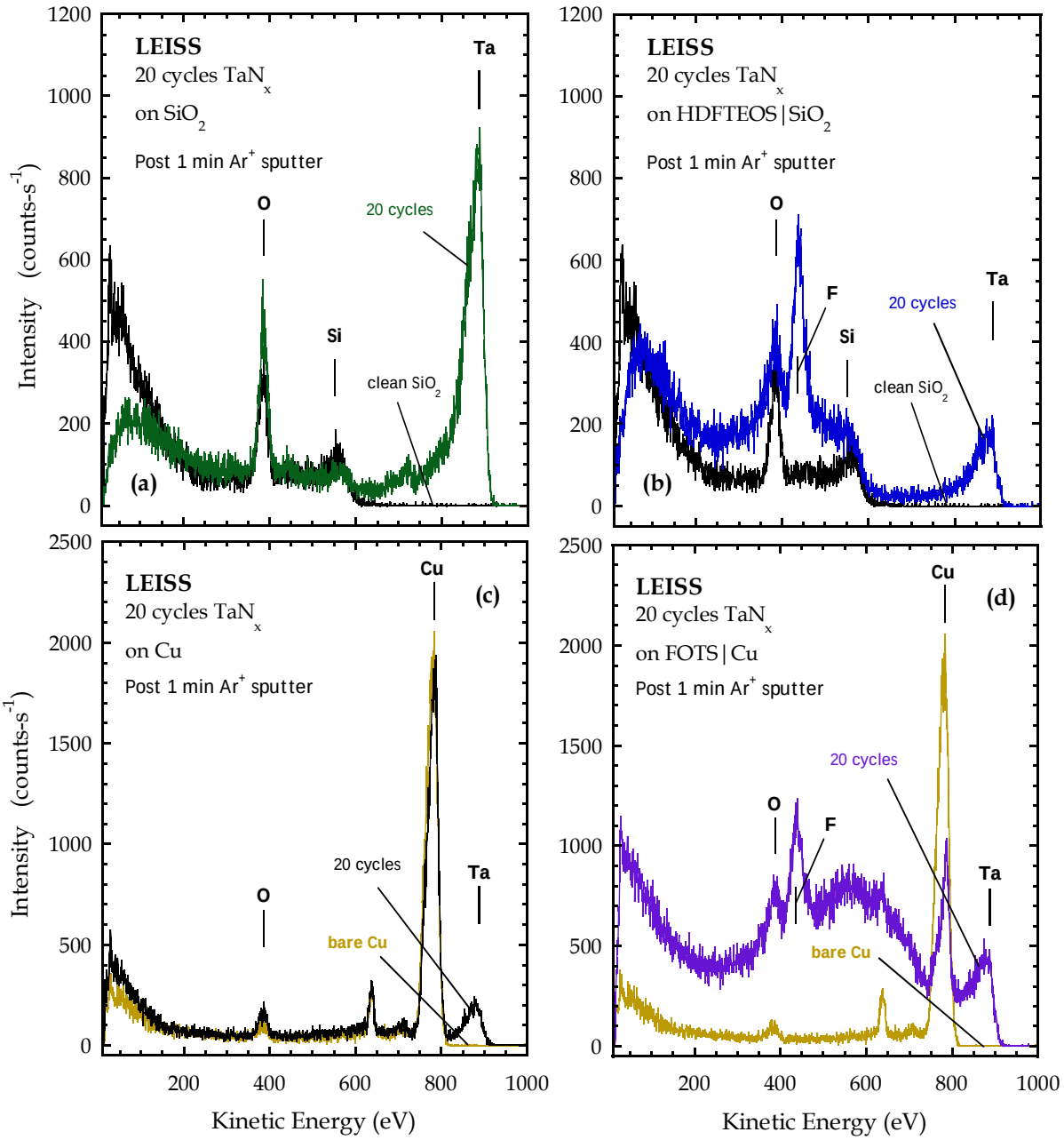

Figure 4S - 10 Representative spectra for LEISS for the **(a)** bare SiO_2 surface and 20 cycles of TaN_x ALD on bare SiO_2; **(b)** bare SiO_2 surface and that for 20 cycles of TaN_x ALD on HDFTEOS|SiO_2; **(c)** bare Cu surface and 20 cycles of TaN_x ALD on bare Cu; **(d)** bare Cu surface and that for 20 cycles of TaN_x ALD on FOTS|Cu

4.7.2.9 Model to fit thickness deposited per cycle

We used a model to fit to the data for the growth of TaN_x by ALD on SiO_2 surfaces modified by the SAMs. In previous work [S-4] we have used this model to successfully describe the effects of SAMs and other interfacial organic layers on the initial attenuation of the thickness deposited per cycle. The expression employed is as follows:

$$D = D'_{\infty}\{n + m(1- \alpha)[\exp(-n/m) - 1]\} \qquad [1]$$

where D is the film thickness, n is the number of ALD cycles, D'_{∞} is the deposited thickness per cycle as $n \rightarrow \infty$ (fixed to be the thickness deposited per cycle on bare SiO_2), and α and m are parameters. This form exhibits the following characteristics: $D|_{n=0} = 0$; $dD/dn|_{n=0} = \alpha D'_{\infty}$, and $dD/dn|_{n\rightarrow\infty} = D'_{\infty}$. Regarding the physical interpretation of α and m, the initial deposited thickness per cycle is a $\alpha D'_{\infty}$, while the growth rate approaches D'_{∞} with an exponential decay constant of m cycles. In order to fit the data shown in Fig. 4.5(a) we also have to account for the attenuation of the photoelectrons by the depositing thin film. The simplest assumption we can make is that the TaN_x thin film is uniform in thickness across the surface, which means that the integrated intensity for photoemission from the thin film is described by:

$$I = I_0[1 - \exp(-D/\lambda \cos\theta)] \qquad [2]$$

where I is the intensity of the thin film component [$Ta(4d_{5/2})$], with I_0 that for an infinitely thick film, D is the film thickness, and λ and θ are the attenuation length and takeoff angle of the photoelectrons.

4.8 Acknowledgments

This research was supported in part by the Semiconductor Research Corporation (Task 2149.001). This work was performed in part at the Cornell NanoScale Facility, a member of the National Nanotechnology Infrastructure Network, which is supported by the National Science Foundation (Grant ECCS-0335765). The authors would also like to thank Clay T. Long for technical contributions.

4.9 References

[1] S. George, Chem. Rev. **110**, 111 (2010).

[2] O.Van der Straten, S. M. Rossnagel, J. P. Doyle, and K. P. Rodbell, ECS Transactions, **1**, 51 (2006).

[3] X. Jiang and S.F. Bent, J. Phys. Chem. C **113**, 17613 (2009).

[4] P. Laibinis and G. Whitesides, J. Am. Chem. Soc. **113**, 7152 (1991).

[5] H. Kim, H.-B.-R. Lee, and W.-J. Maeng, Thin Solid Films **517**, 2563 (2009).

[6] A.J.M. Mackus, A.A. Bol, and W.M.M. Kessels, Nanoscale **6**, 10941 (2014).

[7] F.S.M. Hashemi, C.Prasittichai, and S.F. Bent, J. Phys. Chem. C **118**, 10957 (2014).

[8] C. Prasittichai, K.L. Pickrahn, F.S.M. Hashemi, D.S. Bergsman, and S.F. Bent, ACS Appl. Mater. Interfaces **6**, 17831 (2014).

[9] M.H. Park, Y.J. Jang, H.M. Sung-Suh, and M.M. Sung, Langmuir **20**, 2257 (2004).

[10] E.K. Seo, J.W. Lee, H.M. Sung-Suh, and M.M. Sung, Chem. Mater. **16**, 1879 (2004).

[11] X. Jiang and S.F. Bent, J. Electrochem. Soc. **154**, D648 (2007).

[12] K.J. Park, J.M. Doub, T.Gougousi, and G.N. Parsons, Appl. Phys. Lett. **86**, 051903 (2005).

[13] R. Chen, H. Kim, P.C. McIntyre, and S.F. Bent, Appl. Phys. Lett. **84**, 4017 (2004).

[14] H.-B.-R. Lee, W.-H. Kim, J.W. Lee, J.-M. Kim, K. Heo, I.C. Hwang, Y. Park, S. Hong, and H. Kim, Journal of The Electrochemical Society **157**, D10 (2010).

[15] M. Li, M. Dai, and Y.J. Chabal, Langmuir **25**, 1911 (2009).

[16] K. Park, Y. Lee, K.T. Im, J.Y. Lee, and S. Lim, Thin Solid Films **518**, 4126 (2010).

[17] H.-B.-R. Lee and H. Kim, ECS Trans. **16**, 219 (2008).

[18] A. Amassian, V.A. Pozdin, T.V. Desai, S. Hong, A.R. Woll, J.D. Ferguson, J.D. Brock, G.G. Malliaras, and J.R. Engstrom, J. Mater. Chem **19**, 5580 (2009).

[19] J. Huang, M. Lee, and J. Kim, J. Vac. Sci. Technol. A **30**, 01A128 (2012).

[20] A.S. Killampalli, P.F. Ma, and J.R. Engstrom, J. Am. Chem. Soc. **127**, 6300 (2005).

[21] M.J. Preiner and N.A. Melosh, Langmuir **25**, 2585 (2009).

[22] R. Chen, H. Kim, P.C. McIntyre, D.W. Porter, and S.F. Bent, Appl. Phys. Lett. **86**, 191910 (2005).

[23] R. Chen, H. Kim, P.C. McIntyre, and S.F. Bent, Chem. Mater. **17**, 536 (2005).

[24] J. Hong, D.W. Porter, R. Sreenivasan, P.C. McIntyre, and S.F. Bent, Langmuir **27**, 1160 (2007).

[25] R. Chen, and S.F. Bent, Chem. Mater. **18**, 3733 (2006).

[26] E. Färm, M. Vehkamäki, M. Ritala, and M. Leskelä, Semicond. Sci. Technol **27**, 074004 (2012).

[27] O. Seitz, M. Dai, F.S. Aguirre-Tostado, R.M. Wallace, and Y.J. Chabal, J. Am. Chem. Soc. **131**, 18159 (2009).

[28] E. Färm, M. Kemell, M. Ritala, and M. Leskelä, Chem. Vap. Deposition **12**, 415 (2006).

[29] S.E. Roadman, N. Maity, J.N. Carter, and J.R. Engstrom, J. Vac. Sci. Technol. A **16**, 3423 (1998).

[30] K.J. Hughes and J.R. Engstrom, J. Vac. Sci. Technol. A **30**, 01A102 (2012).

[31] A. Satta, J. Schuhmacher, C.M. Whelan, W. Vandervorst, S.H. Brongersma, A. Vantomme, M.M. Viitanen, H. H. Brongersma and W. F. A. Besling, J. Appl. Phys. **92**, 12 (2002).

[32] W. Zhang, R.K. Nahm, P.F. Ma, and J.R. Engstrom, J. Vac. Sci. Technol. A **31**, 061101 (2013).

[33] T.V Desai, S. Hong, A.R. Woll, K.J. Hughes, A.P. Kaushik, P. Clancy, and J.R. Engstrom, . Chem. Phys. **134**, 224702 (2011).

[34] K.J. Hughes, A. Dube, M. Sharma, and J.R. Engstrom, J. Phys. Chem. C **116**, 21948 (2012).

[35] A. Dube, M. Sharma, P.F. Ma, and J.R. Engstrom, Appl. Phys. Lett. **89**, 164108 (2006).

[36] A. Dube, M. Sharma, P.F. Ma, P.A.. Ercius, D.A. Muller, and J.R. Engstrom, J. Phys. Chem. C **111**, 11045 (2007).

[37] K.J. Hughes and J.R. Engstrom, J. Vac. Sci. Technol. A **28**, 1033 (2010).

[S-1] D. A. Shirley, *Phys. Re*v. *B* **5**, 4709 (1972).

[S-2] *Practical Surface Analysis: Volume I, Auger and X-ray Photoelectron Spectroscopy*, 2nd ed.; Seah, M. P., Briggs, D., Eds.; John Wiley and Sons: Chichester, England, 1990.

[S-3] H. S. Munro and C. Till, *J. Polym. Sci. Part A Polym. Chem.* **25**, 1065–1071 (1987).

[S-4] See, e.g., A. Dube, M. Sharma, P. F. Ma and J. R. Engstrom, Appl. Phys. Lett. **89**, 164108 (2006).

5. Techniques to modulate surface reactivity without the use of blocking layers

5.1 Abstract

With device feature sizes decreasing every generation, the appearance of three dimensional device architectures, along with the physical limitations of photolithography, substrate selective deposition has drawn significant interest over the past decade. Methods such as employing self-assembled monolayers (SAMs) as blocking layers and using intrinsic reactivity differences have shown some initial promise. But due to several drawbacks and limitations, a new technique to achieve selective deposition needs to be developed. Our group seeks to develop a general approach to achieve selective growth – employing an additional species that would prevent or reverse any adsorption events that might take place on the surface where growth is not desired, while allowing adsorption on the surface where growth is required. Species not present in the parent transition metal complex (molecular poisons, e.g. thiols) or species chemically similar to the ligands bound to the metal center (adsorption-reversal agents, e.g. amines) could be used to either block growth or effectively push the equilibrium towards an undissociated metal complex. Two different atomic layer deposition (ALD) reactors were used to study this idea: a conventional ALD tool, as well as a microreactor coupled to an ultrahigh vacuum analysis chamber. Different molecules (thiols and amines) were examined and two conditions showed promise for the first half ZrO_x ALD cycle.

5.2 Introduction

In Chapter 4, we discussed the use of organic self-assembled monolayers (SAMs) as blocking layers. While some success has been achieved with this approach, there are a number of disadvantages intrinsic to these methods. First, SAMs are very difficult to form defect free, and second, and perhaps more important, these masking layers themselves must be patterned or deposited selectively. The stability and effectiveness of this organic layer as a blocking agent is a strong function of the film deposition temperature [1]–[3], as well as the density of defect sites during the SAM deposition step. A second approach to selective area ALD relies on intrinsic reactivity differences between exposed surfaces, which, unfortunately, may be limited to a few special cases. With device feature sizes getting smaller every generation, a new technique for selective deposition needs to be developed. Here we seek to develop that general approach to achieving selective area growth.

Typical chemical specific analysis techniques of ultrathin ALD films (e.g. XPS, LEISS etc) require ultrahigh vacuum pressures (~10^{-8} to 10^{-10} Torr), while high throughput film depositions occur at orders of magnitude higher pressures (~ 10 to 10^{-2} Torr). This difference in pressure regimes indicate that most ALD films are analyzed *ex situ*, which poses many complications for ultrathin ALD films. A disadvantage to *ex situ* metrology is post deposition air exposure, which can drastically change surface composition and structure of the deposited thin film, as well as the underlying substrate. Ellipsometry is an analysis technique often coupled with ALD reaction chambers, because of the pressure regime it can be operated in. While ellipsometry can give useful thickness information, it lacks the chemical specificity that is often required when quality of the film deposited is often of

interest. XPS and LEISS, on the other hand, are surface sensitive techniques, which measure the elemental composition, chemical state and electronic state of the elements that exist within the material [4].

With these challenges in mind, a microreactor system coupled to our current analysis chamber (designed by Jiun-Ruey Chen) was used for this study (see Fig. 5-1). This micro-reactor allows us to do high pressure vapor phase depositions (at P_{μ} ~ 1- 10 Torr) and analyze the deposited films/substrates without an air-break, thereby giving us valuable information for ultrathin films. This microreactor enables the ability to *co-dose* several reactants (up to 3) onto a substrate at the same time. It also employs a curtain gas encapsulation concept that restricts the reactants to the sample surface. This minimizes any out diffusion into the chamber walls, which is important since the same "reaction chamber" is coupled to our UHV analysis system, and any 'contamination' will lengthen the pump-down and characterization time. We have done several characterization experiments to this microreactor system and determined it was able to deposit thin films (both ALD and CVD) in a confined manner, without reactants contaminating the chamber walls. Further details will be detailed in Jiun-Ruey's thesis.

The development of selective area growth has been identified as an important challenge. In some cases lithography is lagging behind the progress of other fabrication steps, and devices are also becoming more three-dimensional, highlighting these needs. Selective growth has long been practiced in a variety of thin film systems using chemical vapor deposition (CVD). However, it has not been as well developed in connection with ALD. Concerning any method of thin film deposition, the ability to achieve substrate – dependent selective area growth depends entirely on the ability to control the nucleation

stage of growth. That is, once the underlying substrate has been covered completely, growth should proceed independently of the starting surface's composition or structure. Thin film nucleation is often described in terms of a model displayed schematically in Fig. 5-2, which corresponds to homogenous nucleation. In this model, a number of processes are present that are relevant to thin film growth by techniques such as physical vapor deposition (PVD) and CVD. Some of these, however, are likely less, or not at all relevant to growth via ALD. For example, ALD by definition involves sequential, irreversible gas-surface chemical reactions. Thus, desorption of a film forming compound should not occur. On the other hand, surface diffusion is also possibly not as important due to the structure of the adlayers that are formed in ALD, particularly those representing steady-state growth—high coverages of adatoms and molecular fragments, with little "empty space" to facilitate facile diffusion. At low coverages, however, and on surfaces where the binding is less directional and the energetic corrugation is small (e.g., many transition metals) diffusion can play an important role. Clearly, the nature of nucleation in ALD is not captured by most of the classic models used to describe nucleation in processes involving continuous growth such as CVD and PVD. Thus, developing methods to control nucleation in ALD will require a different perspective.

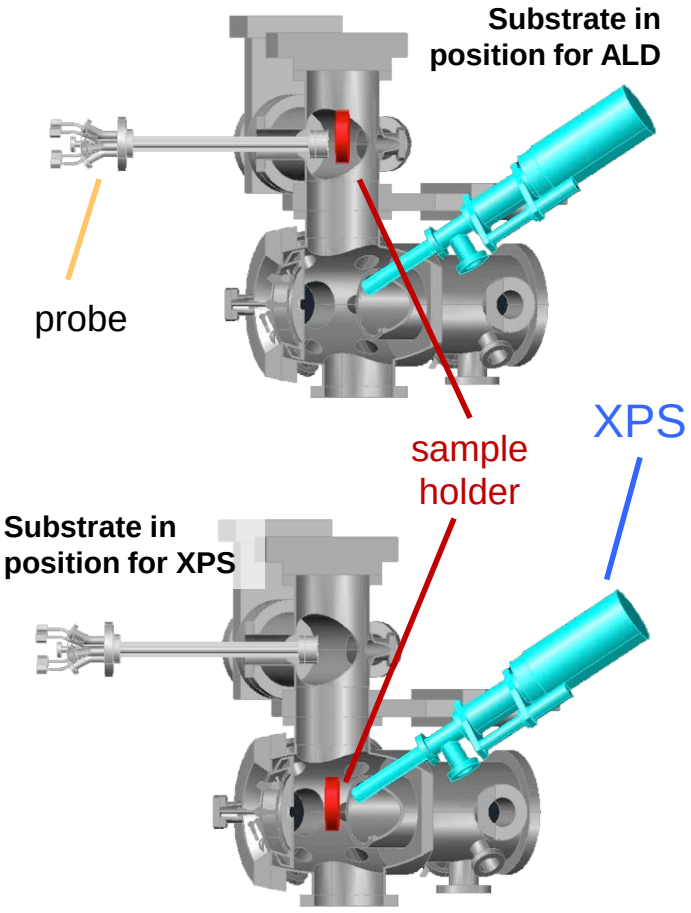

Figure 5 - 1 Schematic diagram of a microreactor probe coupled to an ultra-high vacuum analysis chamber [5], [6], enabling low-to-mid vacuum (p ~10^{-3} – 10 Torr) gas phase reactions and ultra-high vacuum (UHV, p <10^{-9} Torr) surface sensitive characterization to be performed without an air break.

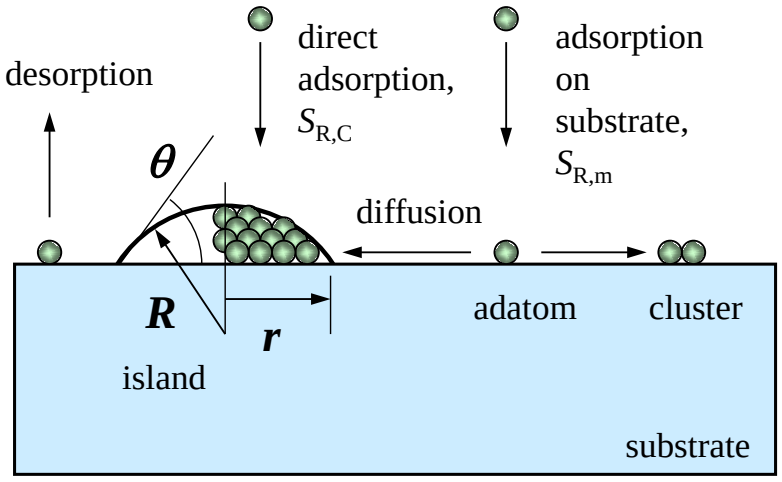

Figure 5 - 2 Atomistic processes considered in classic models for nucleation of a thin film on a foreign substrate [6]

To control nucleation in ALD, irreversible adsorption of the precursor molecule on the surface, where growth is not desired, must be prevented. There are two mechanisms that can prevent or strongly attenuate irreversible adsorption, namely: (*a*) the *intrinsic reactivity* of the surface, and (*b*) making adsorption *reversible*, via desorption or some surface reactions that produces a volatile product. Concerning the former mechanism, (*a*), thin film chemistries (precursor reactants) and reaction conditions are chosen such that chemisorption of one or more thin film precursors only occurs on the surface/feature of interest, and does not occur in other areas. There are few examples of surfaces of interest in micro- and nanoelectronics (metals, semiconductors and dielectrics) where this approach will work on unmodified bare surfaces. Perhaps the most common approach is to employ blocking layers in the form of self-assembled monolayers (SAMs), deposited on a surface where growth is not desired. Such a mechanism can be sensitive to defects, which lead to an incubation period concerning growth, and selectivity is eventually lost. Such a scenario can also be true for unmodified surfaces, where flat, atomically flat terraces may not be active for chemisorption, but step and kink sites may be. The latter mechanism, (*b*), however, concedes that material will build up (at least transiently) on areas of the substrate where growth is not desired, but adsorption can be reversed by species that have been added to the process. Reversal of adsorption, in this case, could depend on the density of adsorbed species, and/or the extent of their decomposition. A weakness of this approach is that poorly chosen reversal agents might lead to unintentional etching of areas of the substrate that one would seek to deposit a thin film on or perhaps leave untouched. Both approaches, (*a*) and (*b*), may have some utility for selective area thin film growth via ALD depending on the specifics of surfaces where one seeks growth, and where one does not.

A way to achieve selective growth is to employ *an additional species* that would prevent or reverse any adsorption events that might take place on the surface where growth is not desired. Species not present in the parent transition metal complex (molecular poisons, e.g. thiols) or species chemically similar to the ligands bound to the metal center (adsorption-reversal agents, e.g. amines) could be used to either block growth or effectively push the equilibrium towards an undissociated metal complex. For simplicity, we will refer to this additional species as *species "x"*.

To achieve selective deposition we believe the best approach involves modifying the standard typical ALD recipe: with a *co-exposure* of the substrate to both the transition metal complex and *species "x"*. We now discuss our examination of two approaches to achieve selectivity: (*i*) the use of adsorption reversal agents and (*ii*) the use of molecular blocking agents.

5.2.1 The use of adsorption reversal agents

In this scheme the primary concept is to employ species that would reverse any adsorption events that might take place on the surface where growth is not desired. Species not present in the parent transition metal complex could be "etchant" species, such as halogen containing gases. Alternatively, one might employ species similar if not essentially identical to the ligands bound to the metal center to effectively push the equilibrium towards an undissociated metal complex. A key factor concerning the reversibility of adsorption is the extent of decomposition of the precursor. There is likely a point-of-no-return concerning ligand loss, where removal of the adsorbed molecular fragment becomes essentially

impossible at the substrate temperature where ALD is conducted. In processes such as CVD, the substrate temperature can often be varied over a substantial range. This is not the case for ALD, where the so-called temperature window is relatively small, such that irreversible chemisorption is the only viable chemical reaction.

To achieve reversible adsorption we believe the best approach involves a *co-exposure* of the substrate to both the transition metal complex and molecules that can engage in ligand exchange reactions with the adsorbed transition metal species. If species are co-adsorbed onto a substrate with both metallic and dielectric surfaces, many species in the form of a protonated ligand, e.g., HL, that will dissociatively adsorb on a metal surface, while not adsorbing at all on a dielectric surface. A sufficiently high coverage of the ligand on the metal surface could act to reverse adsorption of a transition metal complex possessing the same or a similar ligand. This substrate – dependent reaction asymmetry is illustrated in Fig. 5-3.

The interactions indicated in Fig. 5-3 are best translated to a process where we seek to grow a dielectric selectively on a dielectric in the presence of an adjacent metal. In this chapter we will discuss below, the weak ligand–substrate interaction will be provided by a dielectric surface (SiO_2), and the strong interaction by a metal surface (Cu). Understanding and exploiting the asymmetry in the ligand-substrate interaction is at the heart of this approach.

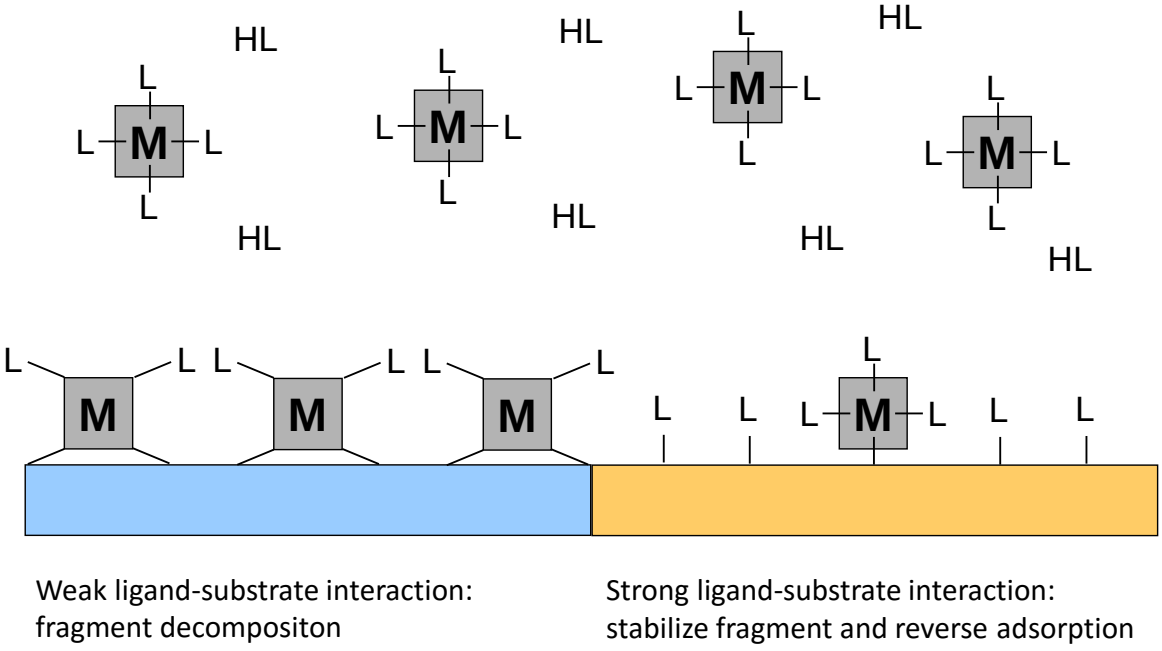

Figure 5 - 3 Substrate dependent asymmetry in ligand-surface interaction [6]

5.2.2 The use of molecular poisons

In rare cases does the chemistry of film deposition differ sufficiently on two surfaces naturally such that selective growth results. In most cases, some sort of substrate modification or pretreatment is required. The use of self-assembled monolayers (SAMs) as blocking layers has been explored by a number of investigators [3], [7]–[10], including our group [11], as a way to mask selected areas of a substrate. There are a number of potential drawbacks concerning the use of SAMs as blocking layers to promote selective area growth. First, for this approach to be attractive concerning single digit nanometer technologies, including growth on three-dimensional features, the SAM formation process itself must be selective. Second, the most successful versions of this approach have involved solution phase deposition of the SAMs, often requiring many hours for the self-assembly to be of sufficient quality. Third, one may wish to block growth on three-dimensional features, where curvature effects may render SAMs ineffective as a way to block growth. Fourth, the behavior of these blocking layers near nm-scale edges/boundaries of features is essentially unexplored, and these boundaries could be most susceptible to attack by the ALD precursors, rendering this approach unworkable for single digit nanometer technology. Fifth, SAM degradation over time could result in eventual loss of selectivity, as there is no mechanism to repair the blocking layer during ALD. Sixth, following deposition the SAM layer must likely be removed, a process that could possibly lead to unintended consequences. Because of these drawbacks, alternative methods to achieving selective area growth that involve tuning the intrinsic reactivity of a surface without using SAMs are worth considering.

The suppression of growth on a metal versus on a dielectric surface offers an opportunity to explore a new mechanism to promote selectivity. Transition metals, including elements such as Cu, Ru and Pt, have been long been studied for their catalytic activity, and all are used in actual commercial chemical processes. Catalysts can be poisoned by species present in a feedstock (sometimes at trace levels), where in most cases these species adsorb strongly to the metal, but do not bind to the high surface area support, which are often dielectrics such as SiO_2 or Al_2O_3. We propose that a similar idea can be pursued concerning selective area ALD growth, where *a species will be added to intentionally disrupt chemisorption on one surface* (the metal), *while not affecting growth on another* (the dielectric). Such a poison should possess certain characteristics: (i) it should adsorb strongly to the metal, and only weakly, if at all, to the dielectric; (ii) it should preferably adsorb intact (molecular chemisorption); (iii) it should effectively block chemisorption by the thin film precursor (likely a transition metal complex); and (iv) it should desorb from the surface in a subsequent purge cycle.

A possibility for transient, molecular blocking layers could be provided by chalcogen containing molecules. Sulfur is a well-known poison for many catalytic reactions on transition metal surfaces. For example, many petrochemical feedstocks must undergo hydrodesulfurization before additional chemical transformations can be attempted with transition-metal based catalysts. Possible molecules to consider here include H_2S, thiophene (C_4H_4S), and small volatile alkanethiols (*R*-SH). Here the binding of these molecules or molecular fragments at ALD process temperatures could prove to be an issue, as sufficiently strong binding is required for there to be effective blocking of the chemisorption of the transition metal complex. The use of H_2S could produce adsorbed S adatoms, S(*a*), in

general bind very strongly to many metal surfaces, and are well-known in the catalysis community for their ability to poison a variety of surface reactions. In such a scenario, S(*a*) could be removed subsequent to ALD using a moderate temperature anneal (possibly assisted by H_2) to thermally desorb these species.

Independent of the choice of the adsorption–reversal agent (molecular poison), a potential advantage of this approach is that the adsorption–reversal agent (molecular poison) is replenished each ALD cycle – thereby if defects appear in a blocking layer they can be potentially repaired/filled-in by subsequent exposures to the relevant species.

5.3 Experimental procedure

In this study, experiments and results will be presented in two different sections.

In the first section (Sec. 5.3.1), depositions are performed in a conventional viscous flow ALD reactor (Oxford FlexAL, Oxford Instruments, Oxfordshire, UK). Films deposited were analyzed *ex-situ*, using a variety of techniques that will be detailed in the following section. Results in this section include saturation curves regarding the first half ALD cycle of several precursors, as well as an attempt to use an adsorption reversal agent to achieve selectivity.

In the second section (Sec. 5.3.2), depositions were performed using the microreactor setup (*cf.* Fig. 5-1), coupled to a UHV analysis system. The first half cycle of ZrO_x ALD was studied, with the *co-dose* concept using several amines and a thiol.

The two substrate surfaces were explored, a dielectric surface – SiO_2 (chemical oxide) and a metal surface – Cu (~900Å Cu | Ta | SiO_2).

5.3.1 Conventional viscous flow ALD reactor

The first section of this study (Sec. 5.3.1) involves ALD using a conventional viscous flow ALD reactor (Oxford FlexAL, Oxford Instruments, Oxfordshire, UK). This ALD tool is located in a shared facility in Cornell Nanoscale science and technology Facility (CNF).

The first half ALD cycle was studied on the two different substrate surfaces: SiO_2 and Cu. Saturation curves were obtained for three different ALD precursors: pentakis(dimethylamido)tantalum {PDMAT, $\underline{Ta}[N(CH_3)_2]_5$}, tetrakis(ethylmethylamido)hafnium {TEMAH, $\underline{Hf}[N(CH_3)(C_2H_5)]_4$} and tris(dimethylamino)silane {3DMAS, $\underline{Si}H[N(CH_3)_2]_3$. These precursor molecules are shown in Fig. 5-4 below. For the saturation studies, the first half ALD cycle was performed on substrates, with nominal substrate temperatures of ~225 °C and ~250 °C for PDMAT (Ta) and TEMAH (Hf) respectively. Typical ALD conditions and steps were used, ALD chamber pressure during precursor exposures is ~ 80 mTorr, with 3 min Ar heating (99.9999% Ar, p = 200mTorr) before, and a relatively long 10s Ar purge after the precursor exposures. Various dose time of the ALD precursors were used, and the amount of precursor adsorbed onto the surface was determined using *ex-situ* x-ray photoelectron spectroscopy (XPS). One of our starting substrates (SiO_2, chemical oxide) is the same chemical signature as the SiO_2 film we are depositing using 3DMAS (Si), hence a different (dielectric) substrate surface is required to study the dose times for 3DMAS (Si). We deposited 250 ALD cycles of Al_2O_3 using trimethylaluminum [$Al_2(CH_3)_6$, TMA – exists as a dimer [12]] and oxygen (O_2) as precursors, at a substrate temperature of ~ 200 °C . This corresponds to a Al_2O_3 layer that is ~ 280 Å thick [based on growth rate (~1.1 Å /cycle) measured using spectroscopic

ellipsometry [SE; Woollam, Lincoln NE)]. This thickness was chosen because the underlying Si substrate is beyond the depth resolution of XPS (< 60 – 100 Å). This Al_2O_3 film acted as the starting dielectric substrate. SiO_2 deposition is a plasma enhanced (oxygen plasma) ALD process, so doing a first half cycle using 3DMAS would not result in any nucleation on the substrate surface, since the additional energy from the O_2 plasma is needed to activate the surface. Instead, multiple SiO_2 ALD cycles (0 – 100 cy, using 3DMAS and oxygen as precursors, at a substrate temperature of ~ 200 °C), using different 3DMAS dose time were deposited and the resulting film thicknesses were estimated using spectroscopic ellipsometry. From the ellipsometry fits, SiO_2 ALD growth rate can be estimated for each of the 3DMAS dose times studied.

Understanding the rates at which each precursor saturates different surfaces is important, since we can use the intrinsic reactivity differences between the substrates to push selectivity in the direction we desire. For example, we could choose dose times that do not saturate either substrate surface, but have the highest difference in the amount of precursor adsorbed onto the substrate surfaces.

An attempt was made to achieve selective growth in the conventional ALD tool in CNF by modifying the typical TaN_x ALD by introducing an adsorption reversal agent – dimethylamine [$(CH_3)_2NH$, DMA] around the exposure of the PDMAT precursor. This was an initial study of experimental conditions to explore selectivity without the use of self-assembled monolayers, so many conditions were attempted (different reactant doses, flow rates, substrate temperatures, PDMAT dose times, placement of the DMA dose step etc.) Due to the relatively slow turnover time to analyze samples using XPS (~ 3 samples every 2 days), most samples in this section of the study were analyzed using Wavelength Dispersive

X-ray spectroscopy (WDX, JEOL 8900 Microprobe, JEOL Ltd., Tokyo, Japan) (~3 samples every 90 min) at the Cornell Center for Materials Research facility. Because WDX is much more sensitive than Energy-Dispersive X-ray spectroscopy (EDX), with better elemental peak separations (see Chapter 2.4), using the Ta *M* edge, we can use a relatively thin layer of TaN_x ALD (20 - 40 ALD cycles, ~ 8 – 16 Å TaN_x) to probe the effectiveness of changing the typical TaN_x ALD recipe with the addition of DMA doses. Multiple (~ 3) WDX measurements were obtained and averaged for each sample analyzed. For further details on WDX, refer to Chapter 2. Some samples were placed in a custom-designed ultrahigh vacuum chamber [13], [14] for analysis using XPS.

Several different experimental conditions were explored. First, we looked at saturation curves on the substrate surfaces, by adding a short dose of DMA (5s) before and after the PDMAT dose step, without purges in between. Second, since the precursor explored here (PDMAT) is an amide, molecules such as DMA are of interest to reverse any adsorption of the metal organic precursor on the surface where it does not preferentially bind to (see Eqn 1 below).

$$M(N(CH_3)_a)_b + \text{substrate} \leftrightarrows [M(N(CH_3)_a)_{(b-n)} - \text{substrate}]_{ads} + n\text{DMA} \qquad [1]$$

Therefore, doses of DMA (1 – 100s) were introduced after the substrate surface is exposed to the metal organic precursor. Third, a combination of a DMA dose with the second half ALD cycle (NH_3 exposure) was additionally attempted. Table I below lists the experimental conditions attempted during the examination of DMA in the conventional ALD tool.

Table I: Experimental conditions used for TaN_x ALD study with DMA, using conventional ALD tool in CNF

Experiment	**Film(s) deposited**	**DMA dose / conditions**
A	½ cy TaN_x ALD - PDMAT exposures on SiO_2 and Cu	5s DMA before and after PDMAT dose
B	20 cy TaN_x ALD	DMA doses (1 – 100s) after PDMAT dose step (no purging in between)
C	20 cy TaN_x ALD	DMA doses (1 – 100s) after PDMAT dose step, combined with NH_3 dose

A typical TaN_x ALD dose has the following recipe:

1. Ar pre-heat

   Repeat *x* cycles
2. Dose PDMAT
3. Purge PDMAT
4. Dose NH_3
5. Purge NH_3

   Loop

For experiments sets mentioned in Table I, the recipes are modified in the following manner:

Experiment set A:

1. Ar pre-heat
2. *Dose DMA*
3. Dose PDMAT
4. *Dose DMA*
5. Purge

Experiment set C:

1. Ar pre-heat

   Repeat 20 cycles
2. Dose PDMAT
3. Purge PDMAT
4. *Dose NH_3 + DMA*
5. Purge

   Loop

Experiment set B:

1. Ar pre-heat

   Repeat 20 cycles
2. Dose PDMAT
3. *Dose DMA*
4. Purge
5. Dose NH3
6. Purge NH3

   Loop

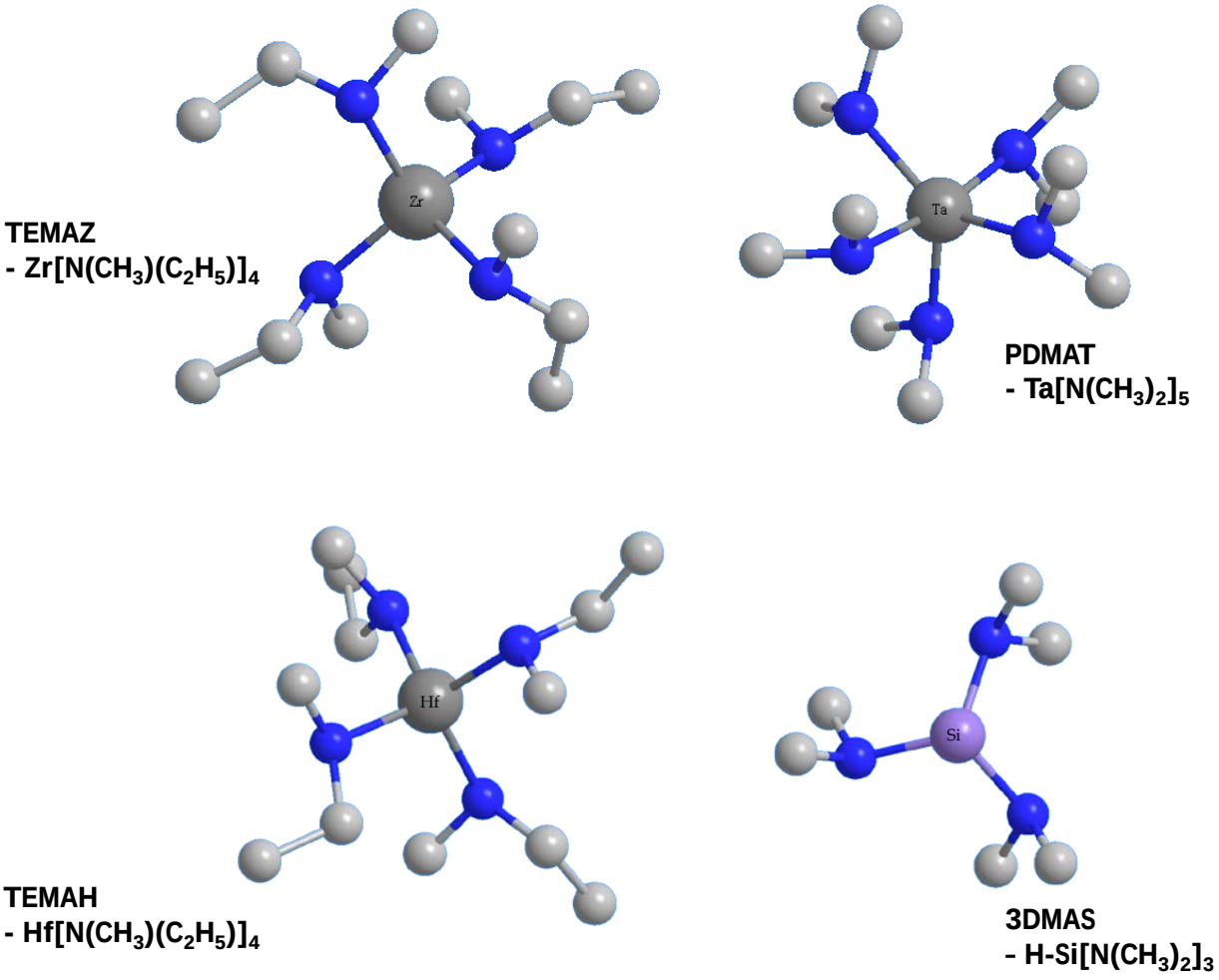

Figure 5 - 4 Ball-and-stick models (without H molecules for clarity) for ALD precursors used in this study: tetrakis(ethylmethylamino)zirconium (TEMAZ), pentakis(dimethylamido)tantalum (PDMAT), tetrakis(ethylmethylamido)hafnium (TEMAH) and tris(dimethylamino)silane (3DMAS)

5.3.2 Microreactor ALD system coupled to UHV analysis chamber

In the second section of this study (Sec. 5.3.2), we explored the first half cycle of thermal ZrO_x ALD using a Zr precursor – tetrakis(ethylmethylamino)zirconium ($Zr[N(CH_3)(CH_2CH_3)]_4$, TEMAZ), and the effect of co-dosing it with *species "x"* (an adsorption reversal agent or a molecular poison) using a ALD reactor coupled to a UHV analysis chamber (see Fig. 5-1). We investigated three adsorption reversal agents – ethylenediamine ($C_2H_8N_2$, EDA), diisopropylamine ($C_6H_{15}N$, DIPA) and triethylamine ($C_6H_{15}N$, TEA) and a molecular poison – ethanedithiol ($C_2H_6S_2$, EDT). In Fig. 5-5, we present all molecules representing *species "x"* in these studies.

We want to achieve deposition on the dielectric surface (i.e. SiO_2), while preventing TEMAZ adsorption on the metal surface (i.e. Cu). The amines were chosen because they are similar to the amido- ligands found on TEMAZ, with the goal of occupying active sites on surfaces where TEMAZ nucleation is not desired, and even possibly initiating a reversal of any TEMAZ that has bonded with the substrate surface where film growth is not desired. The molecular poison (EDT) was chosen because thiols (R-SH) react with metal surfaces such as Ag, Au, and Cu [15] and would act as a molecular blocking agent to prevent film growth. Different concentrations of the adsorption reversal agents (molecular poison) were delivered from a bubbler in a temperature controlled bath to the substrate surface using a carrier gas.

Substrate temperature was ~ 150 °C in all experiments, TEMAZ was kept at a bath temperature of 40 °C, adsorption reversal agents (molecular poison) were kept at various bath temperatures (and possibly diluted with N_2) to achieve necessary vapor pressures. Carrier

gases were N_2 (Airgas, 99.99%) for adsorption reversal agents (molecular poison), and He (Airgas, 99.999%) for TEMAZ. All delivery lines were heat traced after the bubblers. Unless specified otherwise, TEMAZ and adsorption reversal agents (molecular poison) exposures follow the exposure pattern in Fig. 5-6, with a 5 min TEMAZ exposure to ensure saturation on the substrate surfaces. Reactor pressure was maintained with a throttle valve at ~ 9 Torr for all experiments using the microreactor.

All samples in this section (Sec. 5.3.2) were placed in a custom-designed ultrahigh vacuum chamber [13], [14] for analysis using XPS. XPS is a powerful technique for analyzing thin films that are < 10nm thick and can give absolute densities/concentrations if appropriate calibration standards are used, and it holds the potential for depth resolution using angle-resolved XPS (ARXPS). For further details of this technique, refer to Chapter 2.

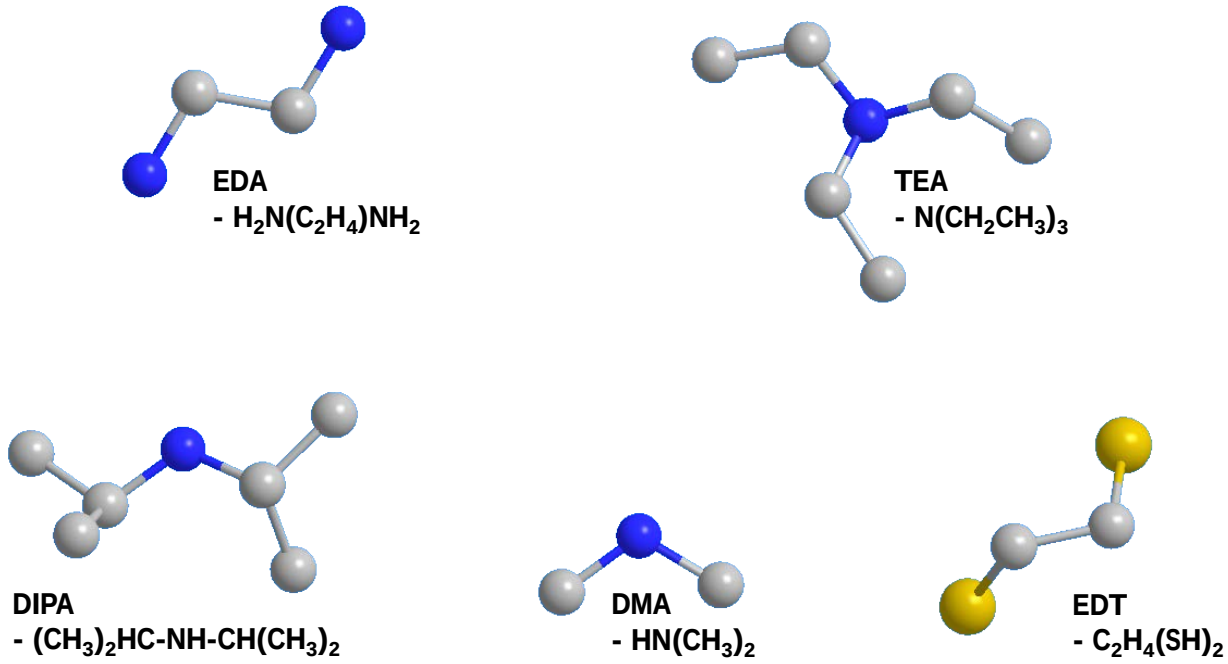

Figure 5 - 5 Ball-and-stick models (without H molecules for clarity) for *species "x"* used in this study: ethylenediamine (EDA), diisopropylamine (DIPA), dimethylamine (DMA), triethylamine (TEA), and ethanedithiol (EDT)

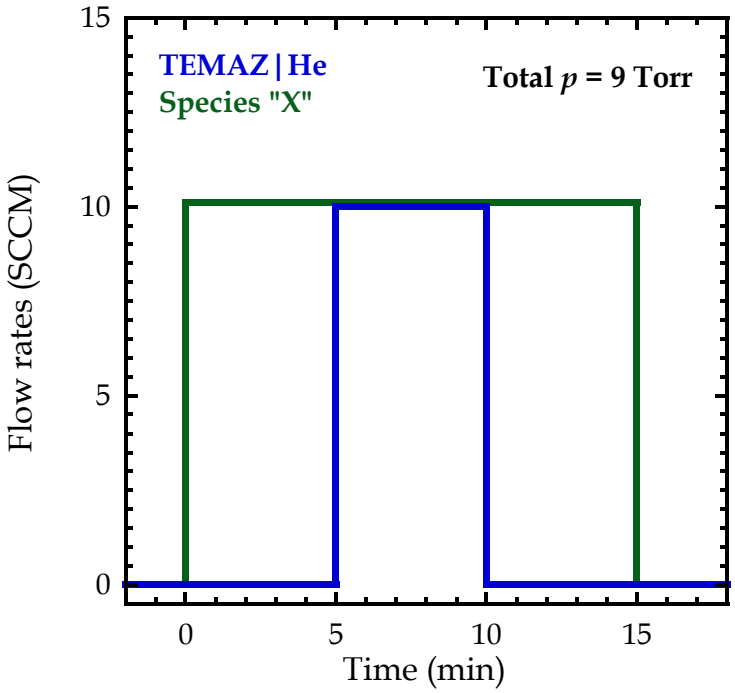

Figure 5 - 6 Exposure pattern for TEMAZ / *species* "*x*" experiments. *Species* "*x*" can represent N_2 (for TEMAZ only exposures), co-absorbates (for TEMAZ/amines co-exposures) or molecular poison (for TEMAZ/ thiol co-exposures)

5.4 Results

5.4.1 Conventional viscous flow ALD reactor

5.4.1.1 Saturation curves

The first half ALD cycle precursor [for PDMAT (Ta) and TEMAH (Hf)] exposures were performed on SiO_2 and Cu substrates. A series of precursor exposure times (0 – 5s) were studied on both substrate surfaces. During *ex situ* analysis of the samples, integrated Ta(4d) [Hf(4d)] XPS intensities were used as a signature for the amount of precursor nucleated on the substrate surface.

In Fig. 5-7 below, we present saturation curves for (a) PDMAT and (b) TEMAH nucleation on SiO_2 and Cu surfaces. The dotted lines are a fit to a simple model described below:

$$I = I_0[1 - e^{-kt}] \quad \text{----------} \quad [2]$$

where I is the XPS intensity, I_0 is the maximum XPS intensity (from fit), and k is the rate at which it reaches that maximum intensity (a larger k represents a shorter time to reach saturation). In Table II below, we present the fitted values for I_0 and k for each precursor on each surface.

Table II: Fitted values for I_0 and k to equation [2]

Precursor	**Substrate**	***I_0***		***k***	
PDMAT	SiO_2	6919	± 264	5.3	± 0.91
	Cu	6669	± 2696	0.26	± 0.13
TEMAH	SiO_2	5726	± 128	54	± 114
	Cu	6542	± 340	2.9	± 0.45

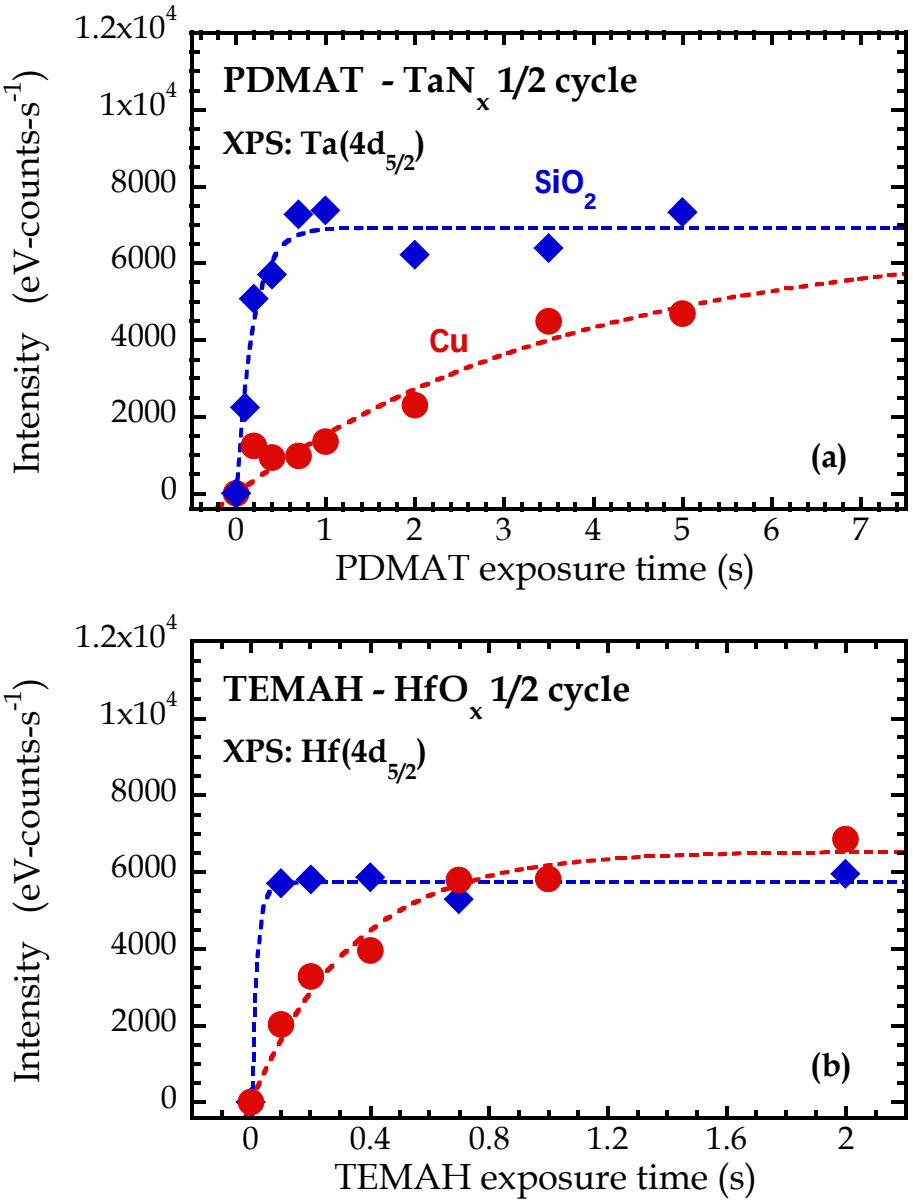

Figure 5 - 7 Integrated XPS intensities of **(a)** Ta(4d) peak for PDMAT exposure on SiO_2 (diamonds) and Cu (circles) and **(b)** Hf(4d) peak for TEMAH exposure on SiO_2 (diamonds) and Cu (circles)

For PDMAT saturation, the fits from our data showed close agreement on the two different substrates for the maximum (saturated) Ta(4d) XPS intensity (I_0, ~ 3.6% difference) at long exposure times. From Fig 5-7(a), we observe that PDMAT saturates differently on SiO_2 and on Cu, most likely due to the prevalence of hydroxyl (–OH) groups on the SiO_2 surface. Fits of the rate of saturation (k) for PDMAT on SiO_2 was ~ 20 times faster than that on Cu. For TEMAH saturation [*cf.* Fig. 5-7(b)], maximum (saturated) Hf(4d) XPS intensity differed slightly more between the two substrates (I_0, ~ 12% difference). The rates (k) for TEMAZ saturation on both substrate surfaces were an order of magnitude higher than the rates for PDMAT, implying a much higher reactivity of the TEMAH molecule compared to PDMAT. This can be further supported by the time at which the SiO_2 surface is saturated with each precursor as well: PDMAT saturates SiO_2 by ~ 0.7 – 1.0s, while TEMAZ saturated the SiO_2 surface at the shortest pulse time we investigated – 0.1s.

Obtaining a saturation curve for the SiO_2 precursor (3DMAS) was a little more complicated. We could not use the same model substrates as PDMAT and TEMAH (SiO_2 and Cu), since we would not be able to differentiate Si from 3DMAS or the SiO_2 substrate. With this in mind, we chose a different dielectric surface – Al_2O_3. This surface was deposited onto SiO_2 via ALD. A series of Al_2O_3 thin films (0 – 400 cy) were deposited on SiO_2 substrates; the thicknesses of the films were estimated using spectroscopic ellipsometry, and a growth rate was estimated (~1.1 Å /cycle). To use Al_2O_3 as the starting dielectric surface, we deposited a film thick enough such that the underlying SiO_2 substrate could be detected by XPS. The detection limit of XPS is implied from the inelastic mean free path (IMFP) of the detected electrons [16], [17], or the distance an electron can travel through a solid before losing energy. The excited electrons need to travel through the thickness of the

film, before being detected by the XPS analyzer. They are exponentially attenuated as a function of film thickness. We chose an Al_2O_3 thickness of ~ 280Å (250 Al_2O_3 ALD cycles). Substrate ($Al_2O_3|SiO_2|Si$) XPS did not reveal any Si peaks. Multiple cycles (0 – 50 cy) of SiO_2 (O_2 – plasma enhanced), with different 3DMAS dose times, were then deposited on the substrates. The deposited film thicknesses were then analyzed *ex situ* with spectroscopic ellipsometry. From the estimated film thickness data points, growth rates can be estimated for each 3DMAS dose time. In Fig. 5-8 below, we present the growth rate of SiO_2 on Al_2O_3 as a function of 3DMAS dose times. We observe that 3DMAS saturates the surface at dose times < 1s. Because of surface roughness, fitting spectroscopic ellipsometry thicknesses of thin films deposited on Cu is problematic. Future *ex situ* XPS analysis will result in a growth rate of SiO_2 on the Cu substrate, and a saturation curve for 3DMAS on Cu can be generated.

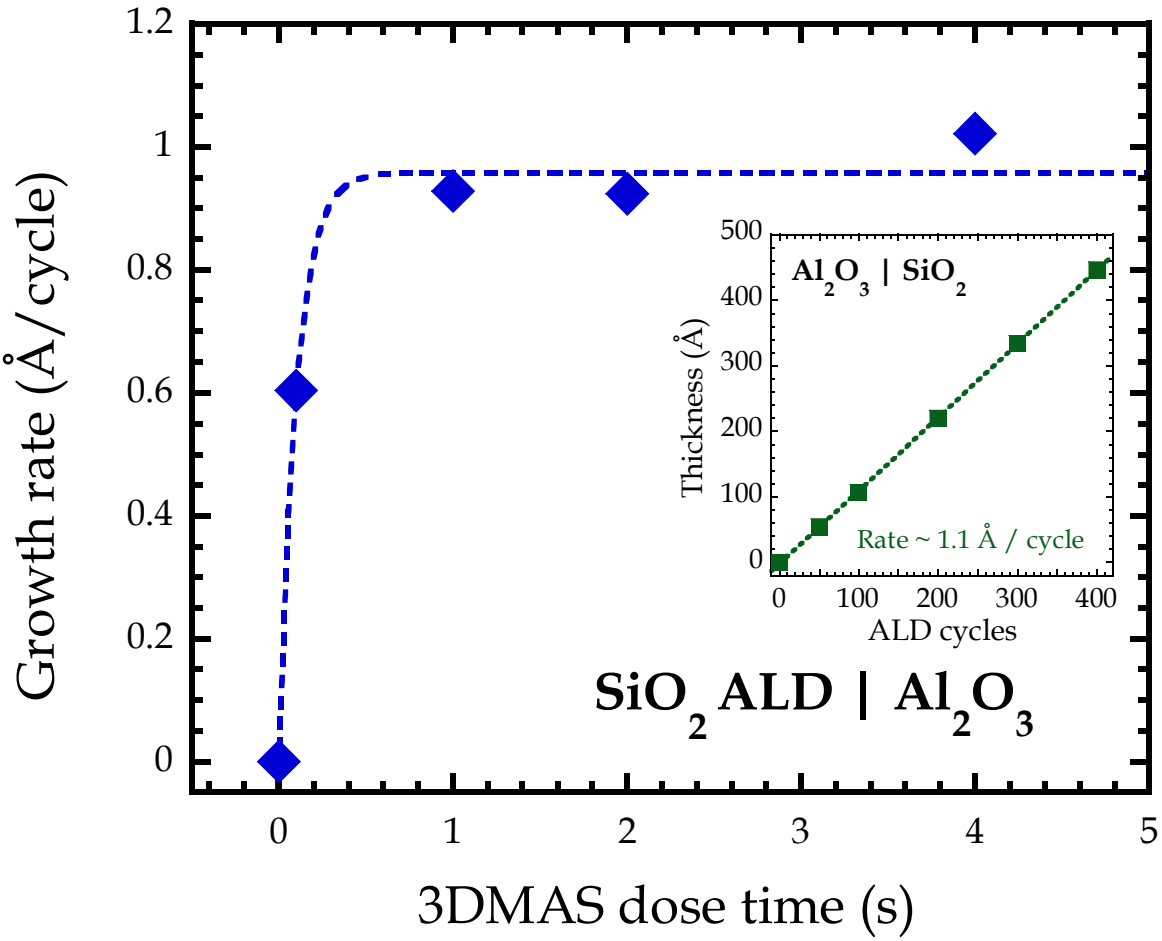

Figure 5 - 8 Estimated growth rate (from spectroscopic ellipsometry) of SiO_2 ALD using 3DMAS on Al_2O_3, **inset** shows experimental growth rate derived from ellipsometry fits of Al_2O_3 ALD on SiO_2 substrates

5.4.1.2 PDMAT/DMA exposures

Experiment Set A

Here we report the results for using DMA during the first ½ ALD cycle for TaN_x ALD. In Fig. 5-9 we present the integrated XPS Ta (4d5/2) intensity for PDMAT exposures on a Cu surface. This exposure was performed at a substrate temperature (T_s) of ~150 °C, lower than the reported ALD window for TaN_x. The typical PDMAT exposure step (dose PDMAT|purge) had been modified to include a pre- and post- DMA dose (dose DMA|dose PDMAT|doseDMA|purge). For comparison, a saturation curve for PDMAT deposited at ~225 °C on Cu has been included in Fig. 5-9.

First, we observed that changing the substrate temperature affected the amount of Ta adsorbed on the Cu surface for the PDMAT dose times studied. Decreasing the substrate temperature changed the surface energy of the Cu surface, decreasing the rate at which PDMAT saturate the Cu surface. Next, from the fits (to Eqn [2], solid lines), changing the typical PDMAT exposure step (using the conventional ALD tool in CNF) to include DMA doses did not result in significant observable changes in the amount of Ta chemisorbed on the surface.

Experiment Set B

Here we report the results for samples exposed to 20 ALD cycles of TaN_x ALD, dosing DMA right after a dose of PDMAT. Several DMA concentrations were explored by changing the flow rate of DMA, the amount of Ar gas used in the mixture and the ALD reactor pressure during the DMA dose step. All Ta *M* edge WDX results are presented in

Fig. 5-10 below, as a function of DMA partial pressure. The data points at zero DMA partial pressure represents the amount of Ta detected on each substrate without the use of DMA. We observe that using DMA did not affect the amount of Ta deposited on the SiO2 substrate, but changed the Cu surface and *enhanced* the deposition of TaN_x on Cu, which is the opposite of what we expected DMA to do on a metallic surface (we expected DMA to prevent deposition on the metallic surface).

Experiment Set C

Here we report the results for samples exposed to 20 ALD cycles of TaN_x ALD, dosing DMA during the second half ALD cycle (NH_3 dose). The idea here is for the NH_3 to react with the adsorbed PDMAT on the surface where TaN_x growth is preferred (dielectric – SiO2), and for DMA to react with any adsorbed PDMAT molecules on the surface where TaN_x growth is not preferred (metal – Cu). To aid comparison, all DMA dose concentrations have been converted to an 'exposure time' of NH_3, in units of partial pressure × time (mTorr • s). For a typical TaN_x ALD recipe, the NH_3 exposure is equivalent to 100 mTorr • s, and the Ta *M* edge WDX intensity was 12.73 and 7.1 counts per second (cps) for SiO_2 and Cu substrates respectively. From Fig. 5-11, we observed higher Ta intensities as a function of NH_3 doses on both substrates, and no selectivity was observed.

Using the conventional ALD tool in CNF, and modifying the typical TaN_x ALD recipe with doses of DMA did not achieve the intended substrate selectivity. Several possible reasons will be suggested in the discussion section.

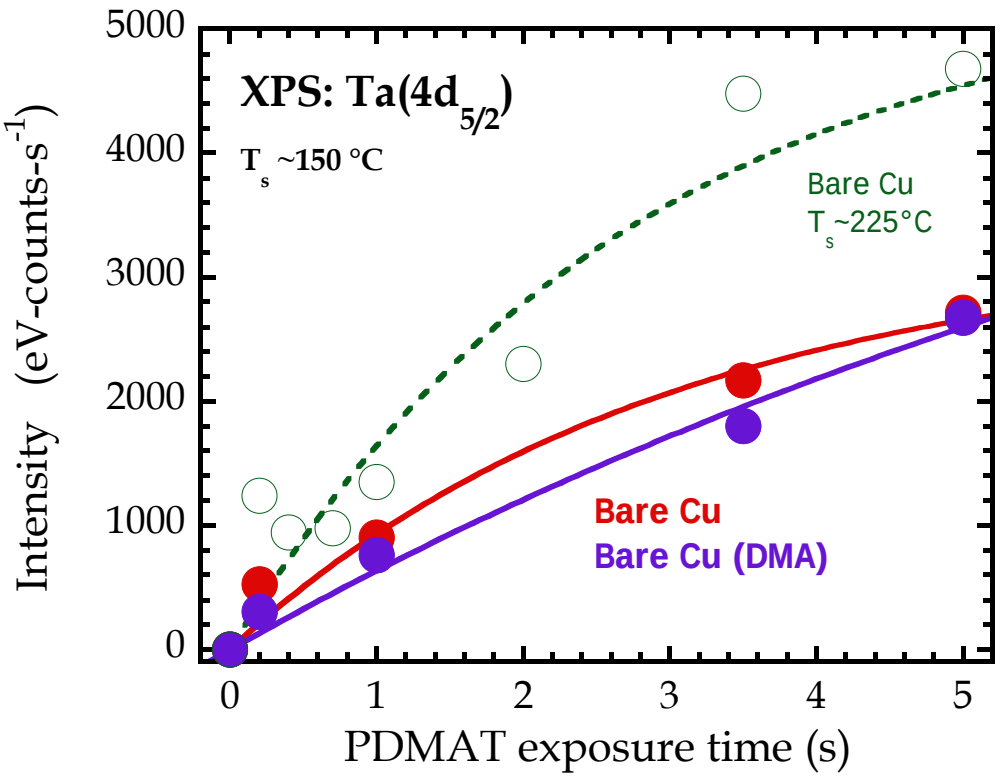

Figure 5 - 9 Integrated XPS intensities of Ta(4d) peak for PDMAT exposure on Cu (red) and Cu with DMA dose additions (purple) at T_s ~ 150 °C and PDMAT exposure on Cu (green) at T_s ~ 225 °C

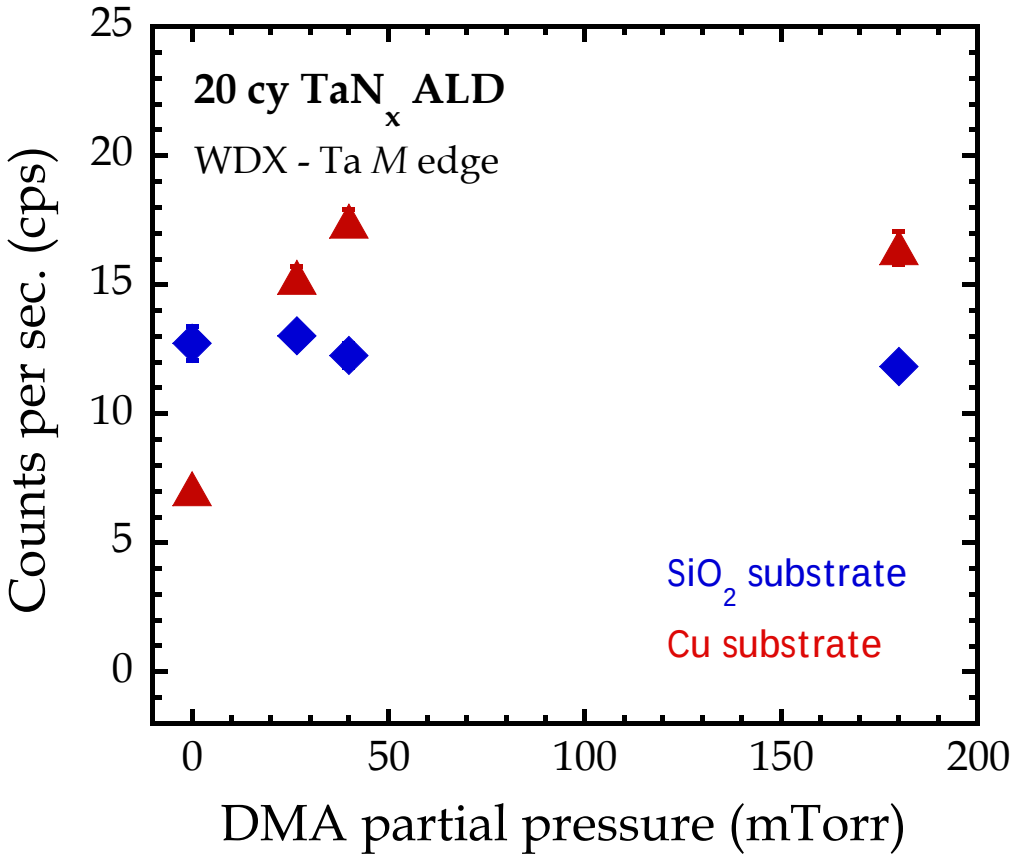

Figure 5 - 10 WDX Ta *M* edge counts for 20 cy TaN_x ALD on Cu (red) and SiO_2 (blue) as a function of DMA partial pressure. with a DMA dose right after PDMAT dose

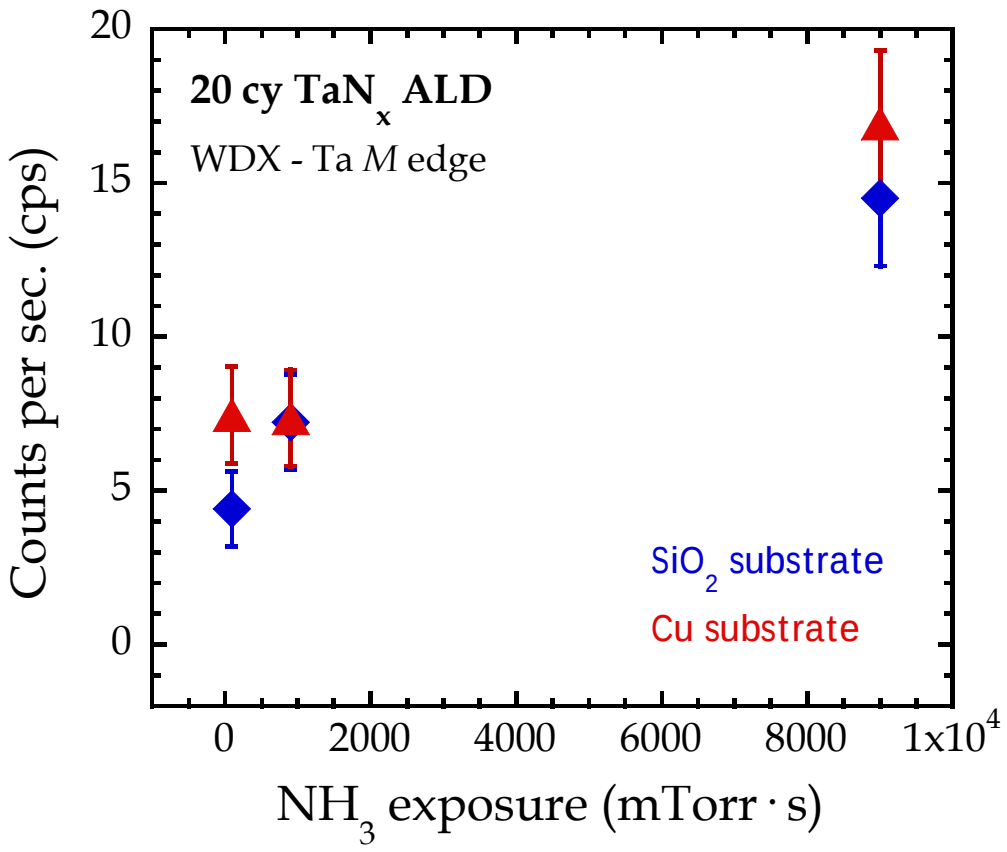

Figure 5 - 11 WDX Ta *M* edge counts for 20 cy TaN_x ALD on Cu (red) and SiO_2 (blue) as a function of NH_3 exposure (mTorr•s). with a DMA dose during the NH_3 dose

5.4.2 Microreactor ALD system

Amount of TEMAZ nucleation on different substrates were examined *in situ* using x-ray photoelectron spectroscopy (XPS), using Zr(3d) intensity as a signature. A saturation exposure of the first half ZrO_x ALD using TEMAZ was performed on bare SiO_2 and Cu for comparison with the cases with the co-exposures with co-absorbates (molecular poison). Different concentrations of these molecules were used, and their corresponding vapor pressure can be found in Table III.

In Fig. 5-12, we present the Zr(3d) XP spectra for half cycle TEMAZ exposure on bare SiO_2 and Cu surfaces, along with their respective peak fits. The Zr(3d) integrated intensity on both substrate surfaces are similar (~3.5% difference), implying a saturated TEMAZ exposure on both substrates, as well as an expected self-limiting first half ALD cycle. Surface densities of Zr atoms on the two substrate surfaces are calculated to be ~ 7×10^{14} atoms cm^{-2}. As a comparison, the surface density of Zr atoms on a monoclinic ZrO_2 surface is calculated to be ~1×10^{15} atoms cm^{-2}.

Next we explore the effect of a co-dose of *species "x"* and TEMAZ to achieve substrate – selective deposition on the two surfaces – dielectric (SiO_2), and metal (Cu).

5.4.2.1 Adsorption reversal agents

Three different amines were chosen for this study: a primary amine (ethylenediamine, EDA), a secondary amine (diisopropylamine, DIPA) and a tertiary amine (triethylamine, TEA).

For the primary and secondary amines (EDA and DIPA), desired selectivity was not achieved. In Fig. 5-13, we present the integrated XPS intensity for Zr(3d) peaks on SiO_2 and Cu surfaces for (a) EDA|TEMAZ and (b) DIPA|TEMAZ co-exposures. With a 'low concentration' of each of these amines, we saw a slight reduction of Zr(3d) feature on both substrates, and complete blocking on both substrates with a 'high concentration'. Based on these results, EDA and DIPA act as blocking agents on both surfaces, and possible mechanisms will be discussed in a later section.

For the tertiary amine (TEA), selectivity was achieved, using a low concentration of TEA, for the first half ZrO_x ALD cycle. In Fig. 5-14, we present the Zr(3d) XPS peaks for (a) SiO2 and (b) Cu surfaces, along with (c) integrated XPS intensity for Zr(3d) peaks for SiO_2 and Cu surfaces. During a TEMAZ co-exposure with a low concentration of TEA, we observed a decrease in the amount of Zr (~51% decrease) on the SiO_2 surface, and a complete blocking of TEMAZ nucleation on the Cu surface. With the high concentration of TEA, we observe TEA acting liking a blocking agent, preventing TEMAZ nucleation on both substrate surfaces.

Table III**:** Effective vapor pressures of reactants used, calculated using Antonie equation.

Molecule	Bath temperature (°C)	Concentration	Vapor Pressure (Torr)	Effective Partial Pressure (Torr)
TEMAZ	40		1.51×10^{-2}	1.51×10^{-2}
EDA	-10	Low	0.82	0.16
	0	High	1.95	1.95
DIPA	-10	Low	10.86	2.17
	-10	High	10.86	10.86
TEA	-10	Low	3.61	0.72
	-10	High	3.61	3.61
EDT	-10	Low	0.448	0.090
	0	High	0.997	0.997

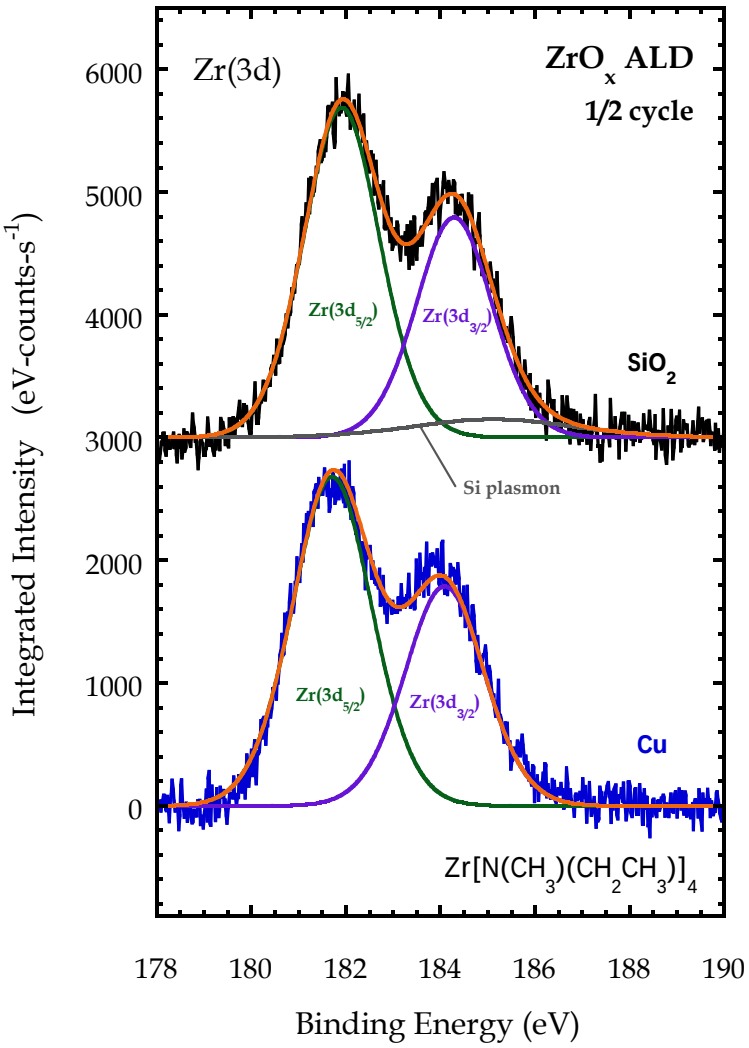

Figure 5 - 12 Zr(3d) XP spectra for TEMAZ exposure on (top) bare SiO_2 surface and (bottom) bare Cu surface, along with peak fits

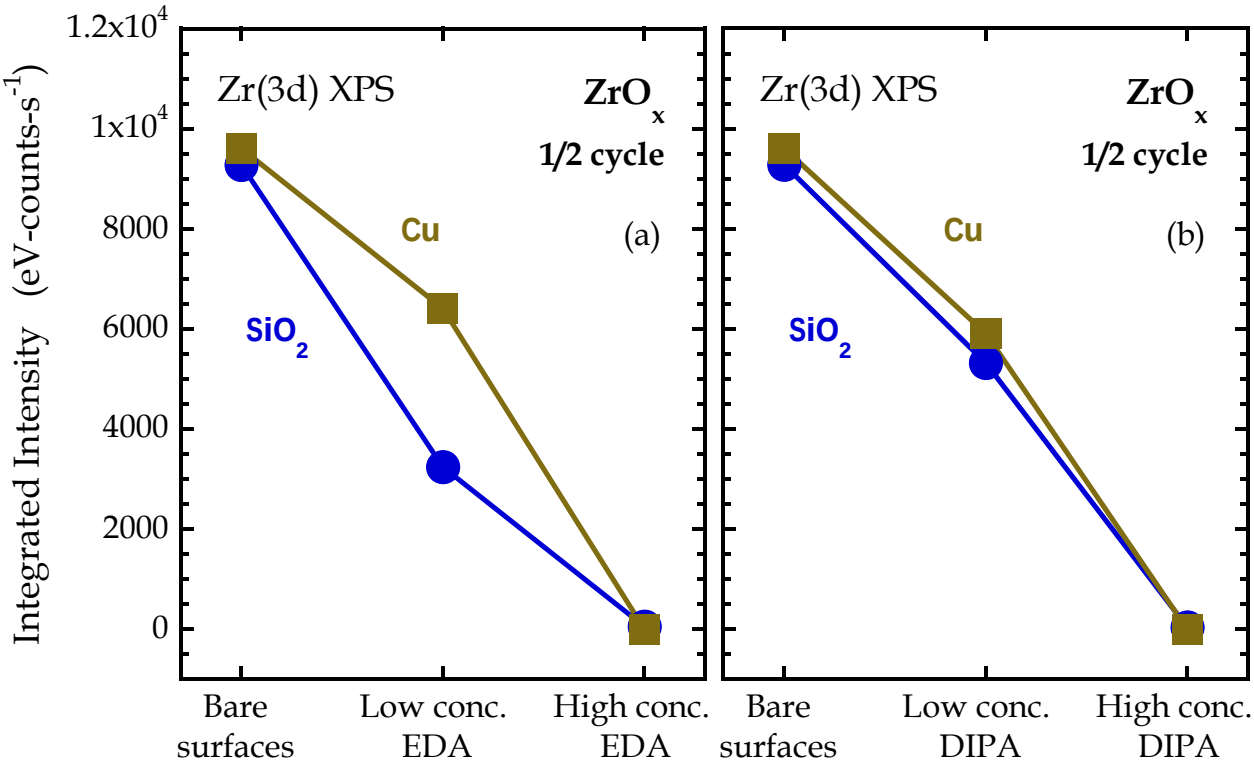

Figure 5 - 13 Integrated intensities of the peak from XPS associated with the thin film, Zr(3d), on **(a)** SiO_2 and **(b)** Cu surfaces, both bare substrates and for cases of EDA co-doses

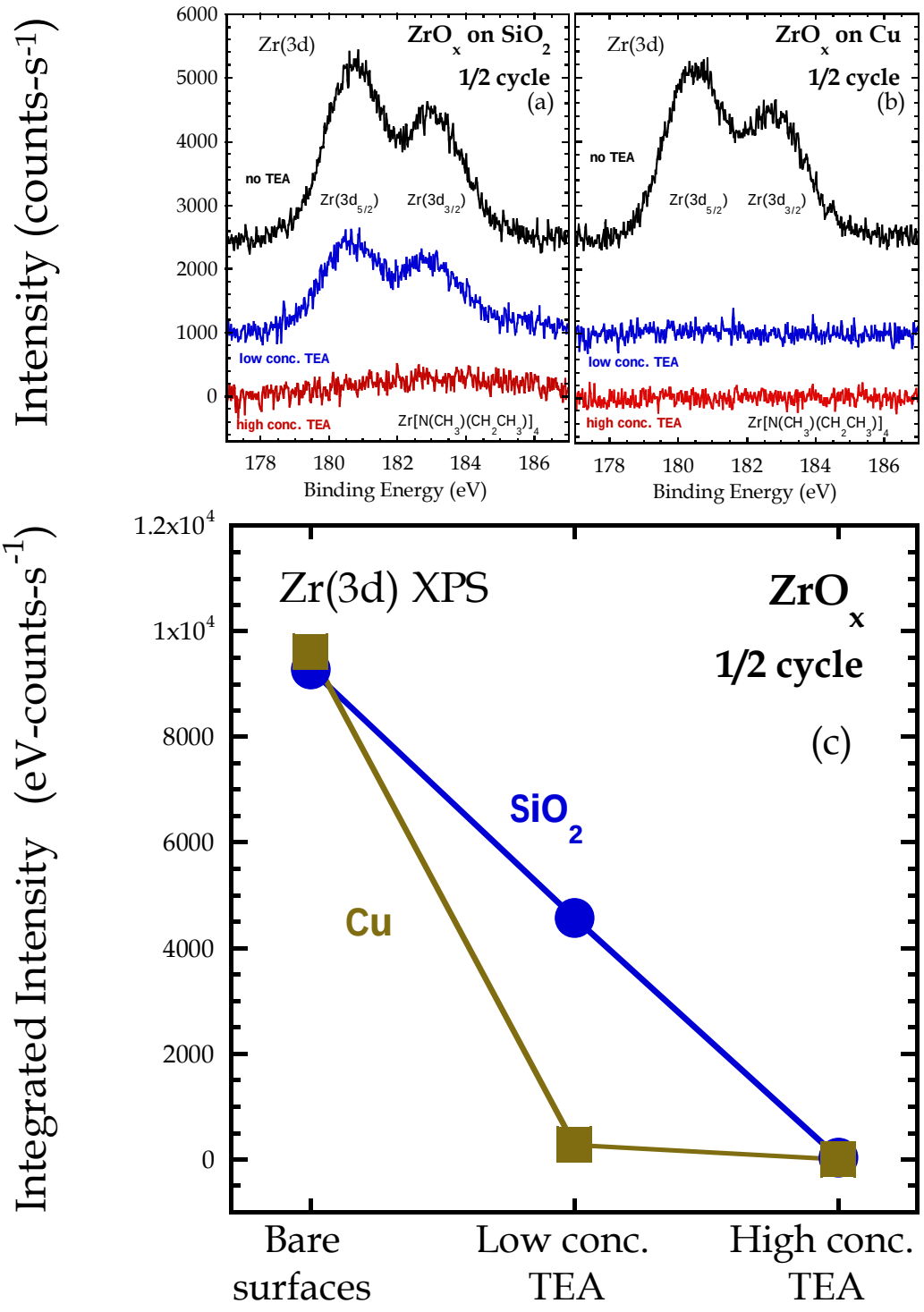

Figure 5 - 14 Zr(3d) XP spectra for co-exposures of TEMAZ|TEA on **(a)** SiO_2 and **(b)** Cu surfaces, and **(c)** integrated Zr(3d) XPS intensities on SiO_2 and Cu surfaces

5.4.2.2 Molecular poison

The molecular poison used in this study was ethanedithiol ($C_2H_6S_2$, EDT). Thiols are known to react preferentially on metallic surfaces, occupying active sites and creating a low energy surface where ALD precursors do not prefer to nucleate. In Fig. 5.15, we present the Zr(3d) XPS peaks for (a) SiO2 and (b) Cu surfaces for EDT|TEMAZ co-exposures, along with (c) integrated XPS intensity for Zr(3d) peaks for SiO_2 and Cu surfaces. The observations in Fig. 5.9 were similar to the results we observed for TEMAZ|TEA co-exposures (*cf.* Fig. 5.14). During a TEMAZ co-exposure with a low concentration of EDT, we observed a decrease in the amount of Zr (~24% decrease) on the SiO_2 surface, and a complete blocking of TEMAZ nucleation on the Cu surface. With the high concentration of EDT, we observed EDT acting liking a blocking agent, preventing TEMAZ nucleation on both substrate surfaces.

5.5 Discussion

5.5.1 ALD using a conventional viscous flow ALD reactor

The different rates at which the precursors nucleate on different surfaces can be used to develop experimental conditions to aid in selective deposition. Most ALD operate when the precursors saturate on substrates. However, from Fig. 5.7, we observe that there is an intrinsic ‘natural’ selectivity at short dose times. We could alter the typical ALD recipe in a way to exploit this intrinsic selectivity, as well as add certain chemistries to push selectivity

in the direction one desires. We have begun exploring some of these ideas, and initial work and results are presented in *Chapter 4* (using self-assembled monolayers) and the later portion of this chapter.

In this set of studies, we have investigated the effectiveness of a post-exposure of a reacted adlayer to an adsorption reversal agent (DMA), using a conventional ALD reactor. This approach met with little success. In hindsight one can identify possible weaknesses with such an approach. In the absence of co-adsorption, the transition metal complex will dissociate in the same way it does in conventional ALD. Most likely, a high coverage of a highly dissociated species will form. For the growth to be self-limiting, typically at least a single ligand needs to be retained by the complex at the end of the first half cycle, and it will only undergo additional reactions with the co-reactant (e.g., H_2O, NH_3) in the second half-cycle. We are unable to probe the effectiveness of co-adsorption using the ALD tool because of the tool's design. Because of safety reasons, metal-organic precursors (e.g. PDMAT etc.) and co-reactant gases (e.g., H_2O, NH_3, DMA etc.) are delivered from separate gas lines, and separated with a gate valve to prevent mixing of the gases within the lines (i.e. when flowing PDMAT, the gate valve from which the co-reactant gases are introduced have to be shut). This meant that DMA and PDMAT cannot be introduced to the substrate surface at the same time (i.e. no co-adsorption is possible). We have tried to mimic such conditions by filling the reaction chamber with DMA, followed by a dose of the PDMAT precursor, all at the same reaction chamber pressure. However, this pulse of PDMAT could have easily replaced the DMA molecules that have physisorbed on the substrate surface.

In addition, DMA is a relatively corrosive material. During the course of using DMA in the conventional ALD tool, a gas regulator (meant to handle DMA), a few mass flow

controllers, several check valves were damaged due to the chemical nature of DMA. While parts of the ALD tool were under service, this part of the research could not continue.

5.5.2 ALD using microreactor system

Because of the restrictions of the conventional ALD tool not allowing a co-dose of two reactants, a microreactor system that will allow a *co-dose* of more than one reactant was used for this section (*cf.* Fig. 5.1).

During this initial study of the first half ALD cycle using TEMAZ | *species "x"* co-exposures, we have identified two experimental conditions and chemistries where selectivity was observed. These observations were a co-dose of TEMAZ and a low concentration of TEA and a low concentration of EDT. However, we have also observed that these reactants act like a blocking agent when their concentrations were increased. We will attempt to hypothesize some explanations for such observations.

The idea of the co-dose of an ALD precursor and *species "x"* relies solely upon surface reactions, which means reactions between the precursor and *species "x"* occur only on the substrate surface, but not before in the gas phase. To prevent gas phase mixing and reactions, TEMAZ and *species "x"* were delivered via two separate delivery lines. However, there is a small volume (~ $1cm^3$) between the exits of these delivery lines and the substrate itself (see Fig. 5.16). Gas phase reactions could occur in this region and create molecules with chemistries that are unfavorable to nucleate on any substrate surface, thereby exhibiting the effect of a complete blocking of the chemisorption of the precursor on both substrate surfaces when a high concentration of *species "x"* was co-dosed. From the low flow rates of the reactants (~ 10 SCCM), the average residence time of the reactants (precursor and *species*

"x") is approximately 100ms. Comparing this residence time to an average ALD pulse time used in industry (<1s), 100ms is more than enough time for any unwanted chemistry to occur in the gas phase. One way to remove doubt that gas phase reactions are happening is to increase the flow rate of the reactants. This decreases the residence time of the reactant in the small volume. However to handle this increase in gas flows, a larger rough pump will be needed to handle the larger flow rates. Further ideas for future experiments are discussed in the following section (Sec. 5.6)

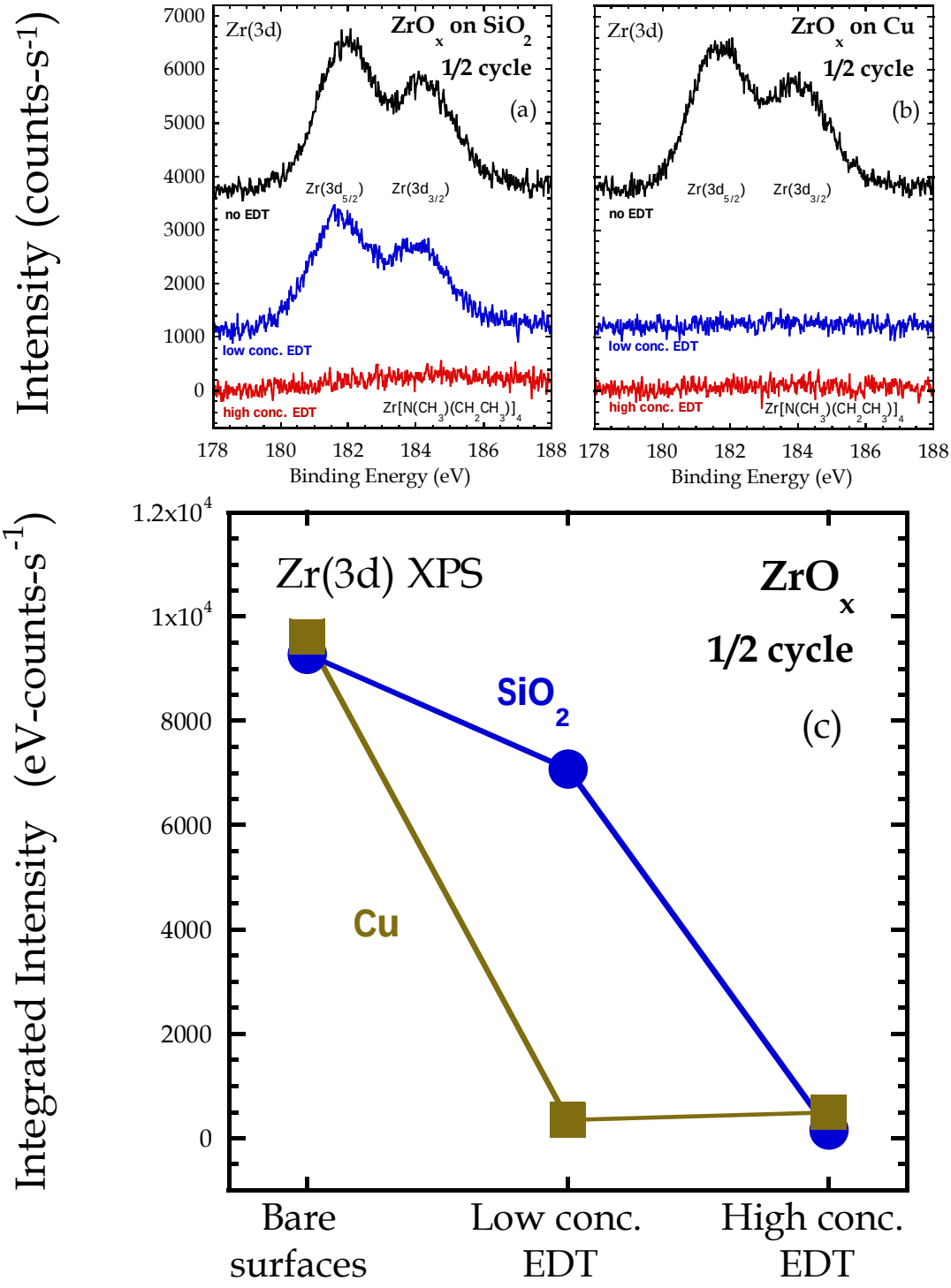

Figure 5 - 15 Zr(3d) XP spectra for co-exposures of TEMAZ|EDT on **(a)** SiO_2 and **(b)** Cu surfaces, and **(c)** integrated Zr(3d) XPS intensities on SiO_2 and Cu surfaces

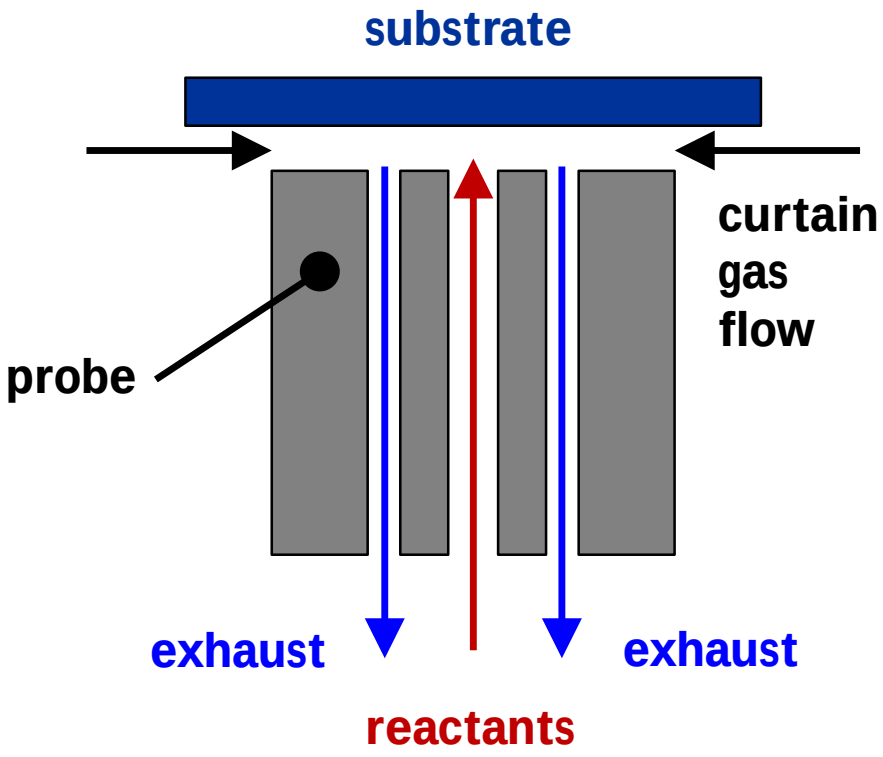

Figure 5 - 16 Schematic representation of gas flows in microreactor [5], [6]

5.6 Future work

Given the positive ½ cycle results for a co-dose using TEMAZ and low concentrations of TEA and EDT, we can move forward with these two molecules with multiple ALD cycles to study how long this selectivity can be maintained. With the flexibility of the microreactor system, we can easily modify the ALD cycle itself to push selectivity even further. For example, we know that an oxidized Cu surface is more susceptible to chemisorption of the metal organic precursor. And from previous work, we know that heating the Cu substrate to the ALD temperature of ~150 °C for 30 min reduces most of the Cu substrate (eliminates Cu^{2+} oxide). If we see that selectivity is lost after the *x* ALD cycles, we could do a flash anneal of the sample, before starting the set(s) of ALD cycles.

Further XPS analysis of the deposited film will also help us probe the possible mechanisms that resulted in the selectivity as well as the reason behind higher concentration of these *species "x"* acting like blocking agents. Nitrogen XPS data could suggest the number of ligands lost from the TEMAZ molecule, as well as indicate any amine (thiol) – substrate interactions. Oxygen XPS spectra, alongside binding energy of Zr(3d) XPS peaks could reveal the oxidation state of the chemisorbed TEMAZ molecule as well as chemical state(s) of the corresponding substrate(s). In addition, sampling gas molecules in the reaction zone and analyze them using a quadrupole mass spectrometer (QMS), we can probe gas–phase reactions and choose chemistries to avoid these unwanted reactions.

Another interesting effect is study selective deposition on an actual patterned substrate, to see if selectivity is achieved on the border of the dielectric/metal interface. ALD

precursors prefer to deposit next to an adsorbed precursor, so there may be some edge effects and we can study how we can reduce this 'spillage' using different chemistries etc.

This microreactor setup gives us a lot of control over a lot experimental parameters, including concentrations and flow rates of reactants, substrate temperatures, and spatial confinements. Given the ability for us to analyze these films at their initial growth stages without an air break, we can study each deposition cycle in detail and change the actual ALD cycle chemistry to push selectivity in the direction we desire.

5.7 References

[1] J. Hong, D. W. Porter, R. Sreenivasan, P. C. McIntyre, and S. F. Bent, Langmuir **23**, 1160 (2007).

[2] R. Chen, H. Kim, P.C. McIntyre, and S.F. Bent, Appl. Phys. Lett. **84**, 4017 (2004).

[3] X. Jiang and S.F. Bent, J. Phys. Chem. C **113**, 17613 (2009).

[4] W. Zhang, R.K. Nahm, P.F. Ma, and J.R. Engstrom, J. Vac. Sci. Technol. A **31**, 061101 (2013).

[5] J.-R. Chen, *Personal Correspondence*.

[6] J.R. Engstrom, *Personal Correspondence*.

[7] H. Kim, H.-B.-R. Lee, and W.-J. Maeng, Thin Solid Films **517**, 2563 (2009).

[8] A.J.M. Mackus, A.A. Bol, and W.M.M. Kessels, Nanoscale **6**, 10941 (2014).

[9] F.S.M. Hashemi, C.Prasittichai, and S.F. Bent, J. Phys. Chem. C **118**, 10957 (2014).

[10] R. Chen, H. Kim, P.C. McIntyre, and S.F. Bent, Appl. Phys. Lett. **84**, 4017 (2004).

[11] W. Zhang, and J.R. Engstrom, J. Vac. Sci. Technol. A **34**, 01A107 (2016).

[12] J.-O. Carlsson, J. Vac. Sci. Technol. B **9**, 2759 (1991).

[13] S.E. Roadman, N. Maity, J.N. Carter, and J.R. Engstrom, J. Vac. Sci. Technol. A **16**, 3423 (1998).

[14] K.J. Hughes and J.R. Engstrom, J. Vac. Sci. Technol. A **30**, 01A102 (2012).

[15] P. Laibinis and G. Whitesides, J. Am. Chem. Soc. **113**, 7152 (1991).

[16] C. J. Powell, A. Jablonski, S. Tanuma, and D. R. Penn, J. Electron Spectros. Relat. Phenomena **68**, 605 (1994).

[17] M. P. Seah and W. A. Dench, Surf. Interface Anal. **1**, 2 (1979).

6. Summary

This thesis revolves around investigations of atomic layer deposition (ALD) processes, how certainly metrology methods can now be used to determine the thin film continuity of these ultrathin ALD films, and initial attempts at modulating surface reactivity of different substrates to eventually achieve selective deposition without the use of photolithography steps.

We first began with a case study of a sputter depth profile of commercially deposited ultrathin (~ 5 and 10 Å) tantalum nitride (TaN_x) ALD films on three different substrates: thermally grown SiO_2; a Cu thin film grown by PVD; and a carbon(C)-doped SiO_2 porous low-κ (*cf.* Chapter 3). We employed *ex situ* angle-resolved x-ray photoelectron spectroscopy (ARXPS), low-energy ion scattering spectroscopy (LEISS) and atomic force microscopy (AFM) to determine the continuity of these thin films, and by implication, the abruptness of the thin film/substrate interface. On SiO_2 and low-κ we find similar results, both ARXPS and AFM indicate that smooth, uniform thin films are deposited, consistent with nearly layer-by-layer (LbL) growth of TaN_x on these surfaces. Examination of these films using LEISS reveals that while the 10 Å TaN_x thin films are continuous, the 5 Å TaN_x thin films are not continuous and may possess on the order of ~ 10% exposed substrate in the form of small sub-nm inclusions. On Cu the situation is quite different. The TaN_x thin films on these surfaces are not continuous, and our results point to a mixed layer of TaN_x and Cu forming during ALD. In all cases, if one were to rely solely on results from ARXPS, the picture would be incomplete as the results from LEISS are ultimately decisive concerning thin film continuity. We used a combination of ARXPS, LEISS and atomic force microscopy to

determine thin film uniformity and continuity of these films. The same techniques were applied to several other film stacks which were presented in the Appendix.

Next, we moved towards modulating surface reactivity to attempt selective deposition. A common approach to achieve selective deposition is to provide a masking material over areas of the substrate where deposition is not desired. In previous work self-assembled monolayers (SAMs) have shown promise as molecular-scale masks, preventing deposition at early stages of ALD deposition. With the appropriate choice of head groups, SAMs can be chosen to react selectively with one surface, while not reacting at all with another. For example, thiols (R-SH) react with metal surfaces such as Ag, Au, and Cu, while silanes (R-Si-X_3) react with hydroxylated (-OH) surfaces. SAMs also contain tail groups, which can effectively control the surface energy of the substrate as well as other properties. In addition, combining SAMs with ALD is a logical choice, since many substrate temperatures used for ALD are relatively low, which is important concerning the stability of SAMs and their ability to block growth.

In chapter 4, we examined the effect of two molecules that form self-assembled monolayers (SAMs) on the subsequent growth of TaN_x by atomic layer deposition (ALD) on two substrate surfaces, SiO_2 and Cu. The SAMs that the authors have investigated include two vapor phase deposited, fluorinated alkyl silanes: $Cl_3Si(CH_2)_2(CF_2)_5CF_3$ (FOTS) and $(C_2H_5O)_3Si(CH_2)_2(CF_2)_7CF_3$ (HDFTEOS). Both the SAMs themselves and the TaN_x thin films, grown using $Ta[N(CH_3)_2]_5$ and NH_3, were analyzed *ex situ* using contact angle, spectroscopic ellipsometry, x-ray photoelectron spectroscopy (XPS), and low energy ion-scattering spectroscopy (LEISS). First, we found that both SAMs on SiO_2 are nominally stable at T_s ~ 300 °C, the substrate temperature used for ALD, while on Cu, HDFTEOS

thermally desorbs, while FOTS is retained on the surface. The latter result reflects the difference in the head groups of these two molecules. Both SAMs strongly attenuate the ALD growth of TaN_x on SiO_2, by about a factor of 10, while on Cu, the SAMs have no effect on ALD growth. Results from LEISS and XPS are decisive in determining the nature of the mechanism of growth of TaN_x on all surfaces. Growth on SiO_2 is 2D and approximately layer-by-layer, while on the surfaces terminated by the SAMs, it nucleates at defect sites, is islanded, and is 3D. In the latter case, our results support growth of the TaN_x thin film over the SAM, with a considerable delay in formation of a continuous thin film. Growth on Cu, with or without the SAMs, is also 3D and islanded, and there is also a delay in the formation of a continuous thin film as compared to growth on SiO_2. These results highlight the power of coupling measurements from both LEISS and XPS in examinations of ultrathin films formed by ALD.

While using SAMs as blocking layers has shown some promise, there are a number of disadvantages intrinsic to using said method. First, SAMs are very difficult to form defect free, and second, and perhaps more important, these masking layers themselves must be patterned or deposited selectively. The stability and effectiveness of this organic layer as a blocking agent is a strong function of the film deposition temperature, as well as the density of defect sites during the SAM deposition step. A second approach to selective area ALD relies on intrinsic reactivity differences between exposed surfaces, which, unfortunately, may be limited to a few special cases. With device feature sizes getting smaller every generation, a new technique for selective deposition needs to be developed. Here we seek to develop that general approach to achieving selective area growth. We believe the best approach involves modifying the standard typical ALD recipe: with a *co-exposure* of the substrate to

both the transition metal complex and *species "x"*, which could be adsorption reversal agents and molecular blocking agents. Independent of the choice of the adsorption–reversal agent (molecular poison), a potential advantage of this approach is that the adsorption–reversal agent (molecular poison) is replenished each ALD cycle – thereby if defects appear in a blocking layer they can be potentially repaired/filled-in by subsequent exposures to the relevant species. In chapter 5, we presented some initial studies using this concept, studying the first few ALD cycles of ZnO_x ALD using tetrakis(ethylmethylamino)zirconium ($Zr[N(CH_3)(CH_2CH_3)]_4$, TEMAZ) as the precursor and three adsorption reversal agents – ethylenediamine ($C_2H_8N_2$, EDA), diisopropylamine ($C_6H_{15}N$, DIPA) and triethylamine ($C_6H_{15}N$, TEA) and a molecular poison – ethanedithiol ($C_2H_6S_2$, EDT) as *species "x"*.

During this initial study of the first half ALD cycle using TEMAZ | *species "x"* co-exposures, we have identified two experimental conditions and chemistries where selectivity was observed. These observations were a co-dose of TEMAZ and a low concentration of TEA and a low concentration of EDT.

Given the positive ½ cycle results for a co-dose using TEMAZ and low concentrations of TEA and EDT, we can move forward with these two molecules with multiple ALD cycles to study how long this selectivity can be maintained. With the flexibility of the microreactor system, we can easily modify the ALD cycle itself to push selectivity even further. For example, we know that an oxidized Cu surface is more susceptible to chemisorption of the metal organic precursor. And from previous work, we know that heating the Cu substrate to the ALD temperature of ~150 °C for 30 min reduces most of the Cu substrate (eliminates Cu^{2+} oxide). If we see that selectivity is lost after the *x*

ALD cycles, we could do a flash anneal of the sample, before starting the set(s) of ALD cycles.

7. Appendix

In this section, a method of determining actual substrate temperature is initially presented, followed by a few sputter depth profiles out group performed on commercially deposited films.

7.1 Sample heater calibrations

Substrate temperature is an important parameter in thin film deposition. In many cases, thermal energy from the substrate is needed to break apart the ligands stabilizing the reactants. Temperature is also vital when using organic compounds as a growth blocking layer (see Chapter 4). Due to experimental constraints, the exact temperature of the substrate cannot be measured during experiments. However, a thermocouple near the heater is available as a reference temperature – henceforth referred to as the Eurotherm temperature (**EU**). Sample heating in the UHV system in 312 includes a pyrolytic boron nitride heater (Invensys Eurotherm), located at the backside of the sample.

Two different platens were used for film deposition and analysis. Molybdenum platens (Thermionics Northwest) were used to hold samples (see Fig. 7-1). In these platens, the sample is held within a shallow well by a retaining plate secured by clips. With the exception of a narrow lip to prevent the sample from falling through, the well is open, so that the back of the sample is directly exposed to the sample heater, allowing efficient radiative heat transfer from the heated element in the manipulator and the back of the sample. The first sample holder (Fig. 7-1(a), henceforth referred to as “Sample Holder A”) incorporated three

wells designed to hold three 17 x 17 mm^2 samples along the axis of rotation of the manipulator. The second sample holder (Fig. 7-1(b), henceforth referred to as "Sample Holder B") held one single 4" wafer, with a 3" diameter circle exposed in the middle. Similar to Sample Holder A, the backside is also open so that efficient heat transfer from the heater is achieved.

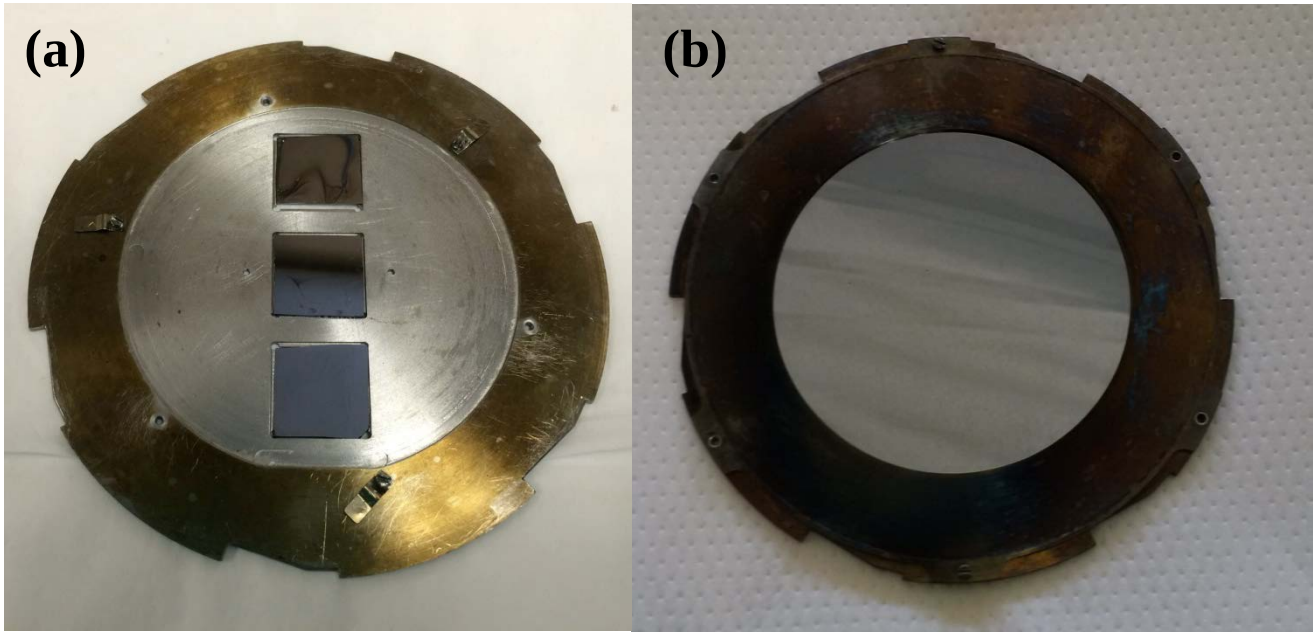

Figure 7 - 1 Molybdenum sample platens used in sample heater calibrations, one holds **(a)** three 17 x 17 mm^2 samples and an anther holds **(b)** one 100mm wafer

Since different deposition and analysis pressures exist, calibration curves need to be obtained in each case so the actual substrate temperature can be estimated. This was performed using a thermocouple brought into direct contact with the sample surface, for a series of reference temperatures (**EU**) as well as a series of pressures (HV ~ 10^{-7} Torr, deposition P ~ 9 Torr etc.).

Actual substrate temperature (**TC**) were obtained by attaching a thermocouple onto the sample transfer arm so that the thermocouple and the substrate surface made physical contact (see Fig. 7-2), while the sample is being heated at different conditions.

For temperature calibrations done in high vacuum, the sample holder A was used [Fig. 7-1(a)]; for calibrations done at 9 Torr, the sample holder B was used [Fig. 7-1(b)].

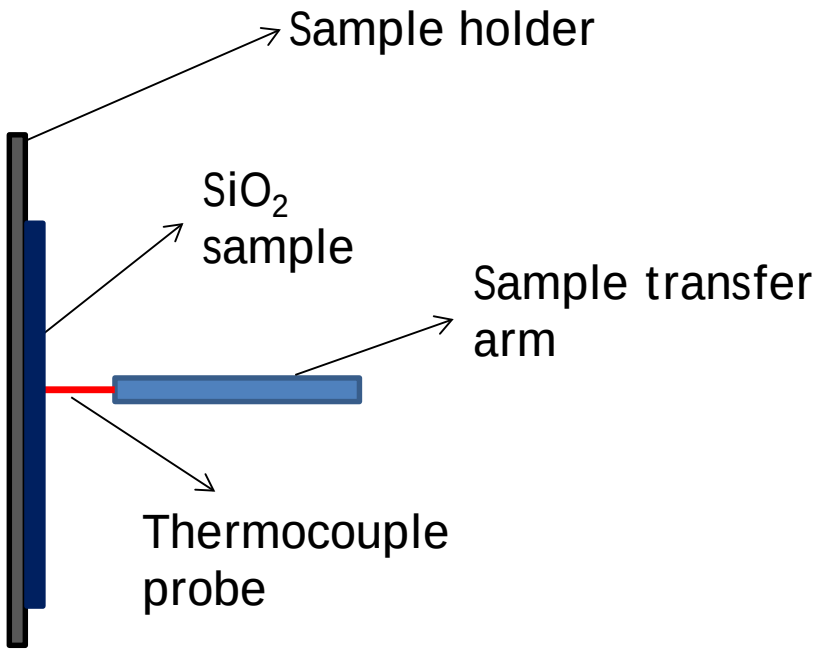

Figure 7 - 2 Figure illustrating method of obtaining substrate temperature measurements

7.1.1 Experimental Procedure

The thermocouple (type K, chromel–alumel) was secured to the sample transfer arm and brought to form a physical contact with the substrate surface. Thermocouple wires were connected via a 1.33" CF flange (#22), a nipple adaptor (1.33" to 2.75" CF), and a thermocouple feedthrough (MDC, #9312013). The sample (either a 17 x 17 mm^2 square coupon sample – when using the first sample holder, or a 100mm Si (100) wafer - when using second sample holder) faced the load-lock chamber (θ=123.5°), and the transfer arm was brought to touch the sample.

In the experiment for higher pressure deposition conditions (~9 Torr), the micro-reactor was retracted at the micro-reactor chamber. The micro-reactor gate valve is open so that the micro-reactor mechanical pump can be used to control the chamber pressure. Load-lock turbo pump was not used and its outlet was blanked off. Curtain gas (100 SCCM N_2) was flowed into the reaction chamber and pressure control was started to maintain the chamber pressure at ~ 9 Torr. Equilibrium temperature readings were obtained at different heater powers (**HP**, from 5.5 to 11.5%). In the experiment to simulate heating in high vacuum, the micro-reactor was retracted completely and the small gate valve closed. Chamber was pumped down using the load-lock turbo pump, obtaining a chamber pressure of ~ 10^{-7} Torr. No gas flow was used in this case.

7.1.2 Results

Temperature calibration curves for high vacuum pressure (P ~ 10^{-7} Torr) are shown in Fig. 7-3(a) and (b). Both temperature readings (substrate temperature - TC and reference temerpature - EU) rose with the increase in heater power (HP). Equations are displayed below and in the figures as well.

$$\boldsymbol{HP} = 2.74 + 0.03\,\boldsymbol{TC} - 5.9 \times 10^{-5}\boldsymbol{TC}^2 \qquad \text{- (1)}$$

$$\boldsymbol{EU} = 48.7 + 2.17\,\boldsymbol{TC} - 5.2 \times 10^{-3}\boldsymbol{TC}^2 \qquad \text{- (2)}$$

Temperature calibration curves for deposition pressure (P ~ 9 Torr) are shown in Fig. 7-3(c) and (d). Both temperature readings (substrate temperature - TC and reference temerpature - EU) rose with the increase in heater power (HP). Equations are displayed below and in the figures as well.

$$\boldsymbol{HP} = 2.84 + 4.4 \times 10^{-2}\,\boldsymbol{TC} - 1.14 \times 10^{-4}\boldsymbol{TC}^2 \qquad \text{- (3)}$$

$$\boldsymbol{EU} = -24.8 + 2.55\,\boldsymbol{TC} - 5.0 \times 10^{-3}\boldsymbol{TC}^2 \qquad \text{- (4)}$$

Using these equations, actual sample temperatures can be better controlled.

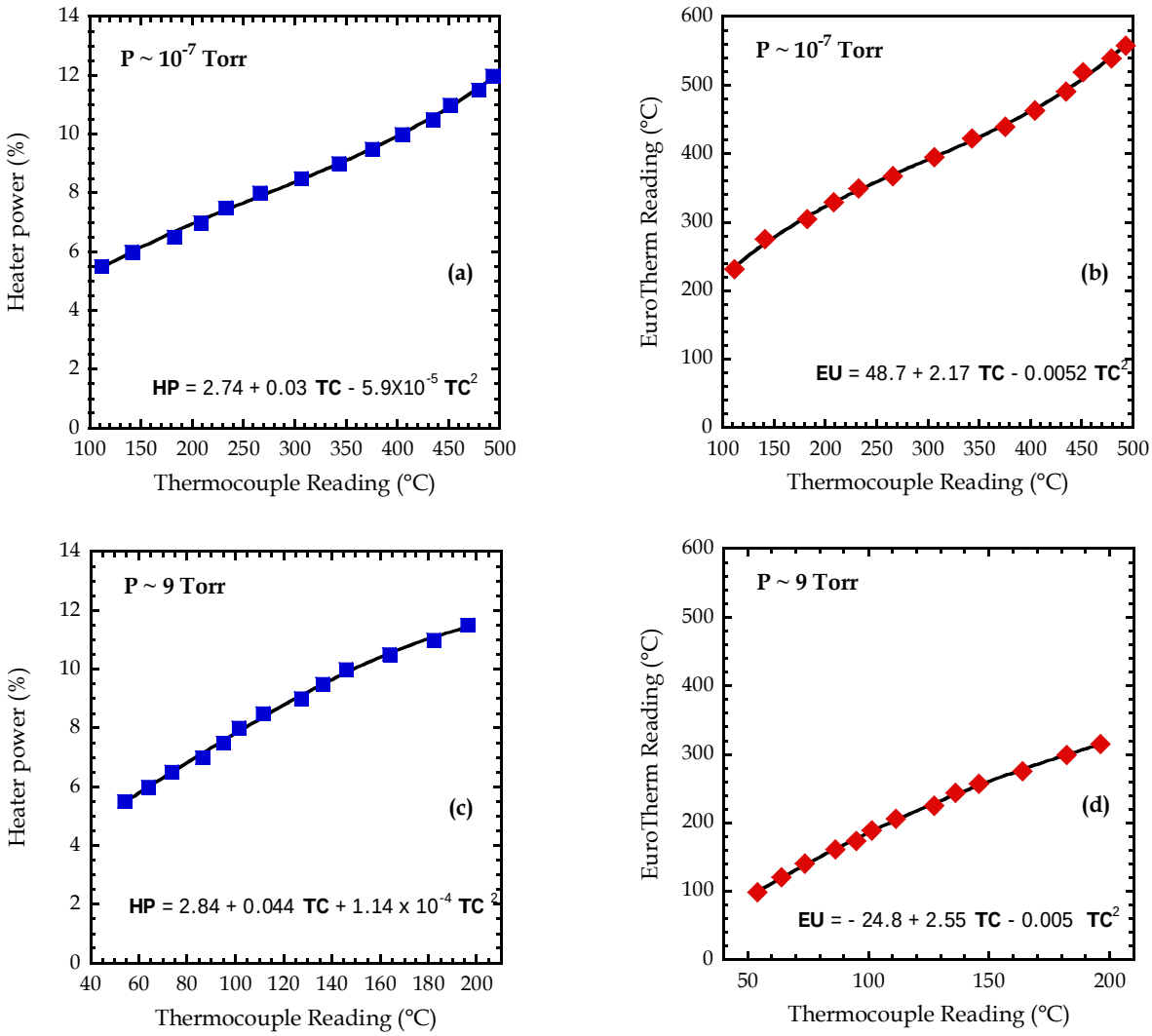

Figure 7 - 3 Temperature calibrations curves and equations for samples heated in [**(a) and (b)**] high vacuum pressure (P ~ 10^{-7} Torr) and [**(c) and (d)**] deposition pressure (P ~ 9 Torr).

7.2 *Ex-situ* sputter depth profiles of commercially deposited films

7.2.1 Introduction

With our experimental capabilities in Olin 312, several commercially deposited thin films were analyzed to determine thin film continuity and interface abruptness. In this chapter, three sets of sputter depth profile studies are described. First, we examined thin films of Co deposited via chemical vapor deposition (CVD) on substrates consisting of $TaN_x|SiO_2|Si$. Second, thin films of MnN_x deposited via atomic layer deposition (ALD) on low-κ substrates were investigated. Third, we examined the composition of two relatively thick films of TaN_x: One sample was 20 nm of ALD TaN_x on bare Si, another was 20 nm physical vapor deposited (PVD) TaN_x on SiO_2.

These sputter depth studies were a continuation of the work described in Chapter 3, where we probed the thin film continuity and interface abruptness of ultrathin films deposited via ALD using ex situ x-ray photoelectron spectroscopy (XPS) and low-energy ion scattering spectroscopy (LEISS). Using the appearance of the LEIS substrate peak, an idea of a continuous (or discontinuous film) can be indicated. Because the samples described in this chapter were analyzed *ex situ*, there is a contamination layer that exists on the sample, complicating the LEIS analysis of the thin film and substrate signals. For example, a discontinuous thin film could reveal no substrate LEIS signal due to the contamination layer covering the sample. Fig. 7-4 below shows model LEIS substrate signals for three different conditions: a case where the thin film is continuous and thicker than critical coverage (in blue), a case where the thin film is at the critical coverage (in black), and a case where the thin film is below critical coverage, or discontinuous (in red).

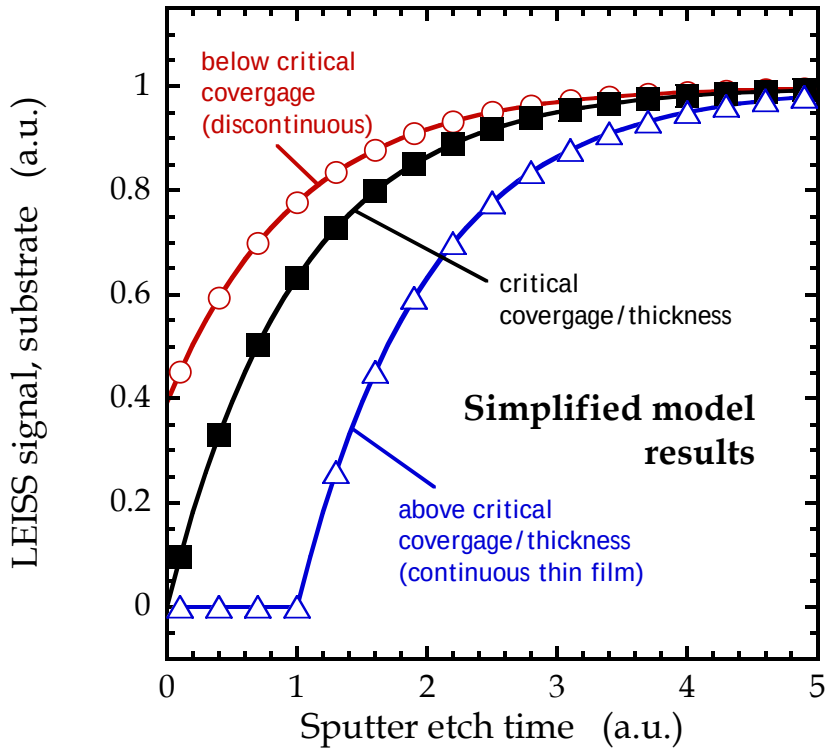

Figure 7 - 4 Model LEIS substrate signal as a function of sputter etch time, for three different thin film coverages [1].

7.2.2 Experimental procedure

For all experiments in the following sections (Sec 7.2.2 – 7.2.4), samples were cleaved into 17 × 17 mm^2 square samples and swept with a stream of dry N_2 before transferred and placed in a custom-designed ultrahigh vacuum chamber [2], [3] for analysis using XPS and LEISS. XPS is a powerful technique for analyzing thin films that are < 10nm thick and can give absolute densities/concentrations if appropriate calibration standards are used, and it holds the potential for depth resolution using angle-resolved XPS (ARXPS). LEISS has been shown to have extremely good surface sensitivity and is extremely useful in determining thin film continuity and interface abruptness of ultrathin films [4], [5].

Samples were analyzed first using fixed takeoff angle XPS, scanning in detail the regions corresponding to the elements of interest. This was followed by LEISS, using a primary beam of 1 keV He^+, scanning the entire range of kinetic energies (1-1000 eV). Subsequently, each sample was sputter etched for a fixed period of time using a (rastered - 10mm^2) 3 keV Ar^+ ion beam. XPS and LEISS spectra were collected again as described above. This procedure was repeated until most of the thin film had been removed by sputter etching.

7.2.3 CVD Co films on $TaN_x|SiO_2|Si$

We examined thin films of Co deposited via CVD on substrates consisting of $TaN_x|SiO_2|Si$. These Co thin films were of nominal thicknesses of 7, 10, 15 and 20 Å.

Using low energy ion scattering spectroscopy (LEISS), we found that the 7 Å thin film was likely not continuous. The 10 Å thin film was difficult to assign. A substrate peak was observed after a short Ar^+ sputter etch (1min, 3keV rastered over $10mm^2$), which is required to remove only the surface contamination layer, without doing significant damage to the underlying film or substrate [5], [6], suggesting the Co film is discontinuous. However, extrapolation of the substrate (Ta) signal gives a finite positive sputter time to reveal the substrate peak, suggesting the Co film is continuous. The 15 and 20 Å thin films were likely continuous. The LEIS integrated intensities of the thin film (Co) and substrate (Ta) signals are presented in Fig. 7-5 below.

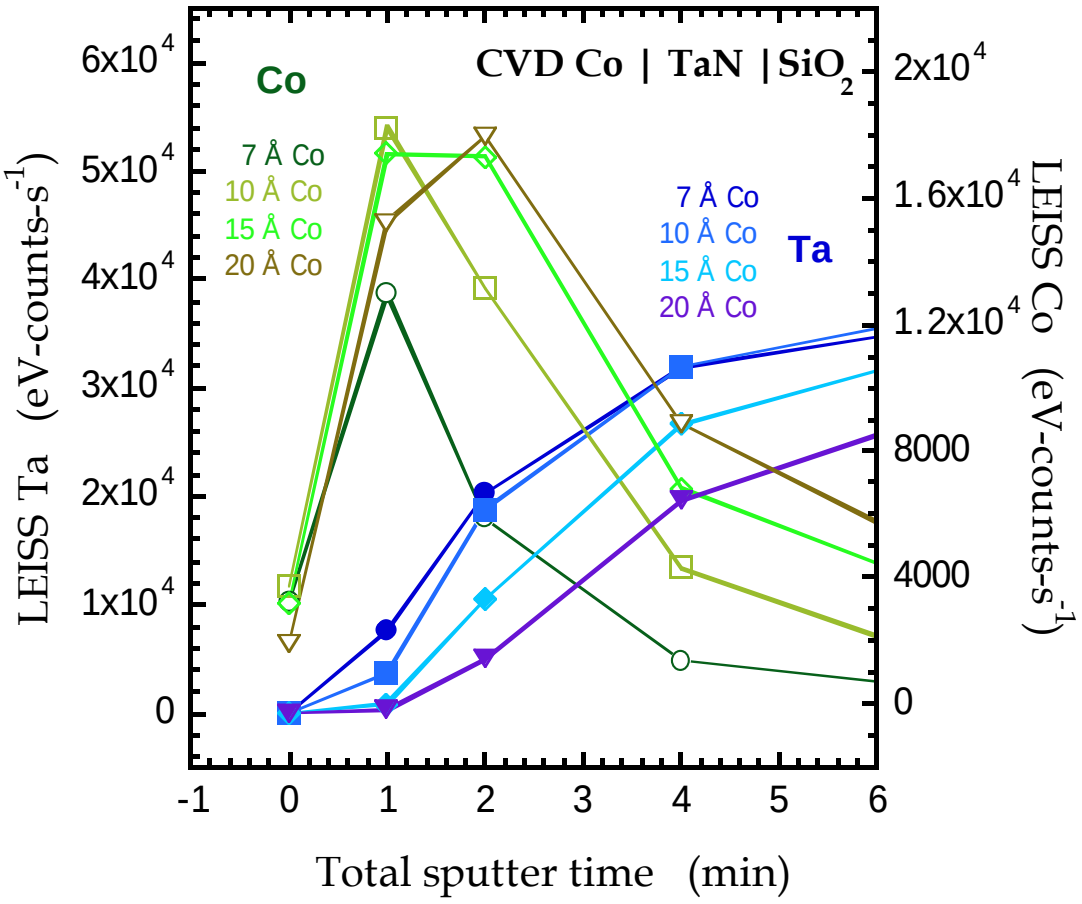

Figure 7 - 5 Integrated intensities of the LEISS Ta (substrate, left ordinate) and Co (thin film, right ordinate) peaks as a function of the total Ar^+ sputter etch time for nominal 7, 10, 15 and and 20 Å Co CVD thin films on TaN.

7.2.4 MnN on SiO_2

We examined thin films of MnN deposited via ALD on SiO_2 substrates. These MnN thin films were of nominal thicknesses of 5, 7, 10 and 13 Å. LEIS results are presented below in Fig. 7-6. For these ALD MnN thin films we found that the 5, 7, and 10 Å thin films were likely not continuous. Only the 13 Å thin film seemed to show an offset in the substrate Si LEISS peak vs. sputter etch time, which is a clear indicator of a continuous thin film.

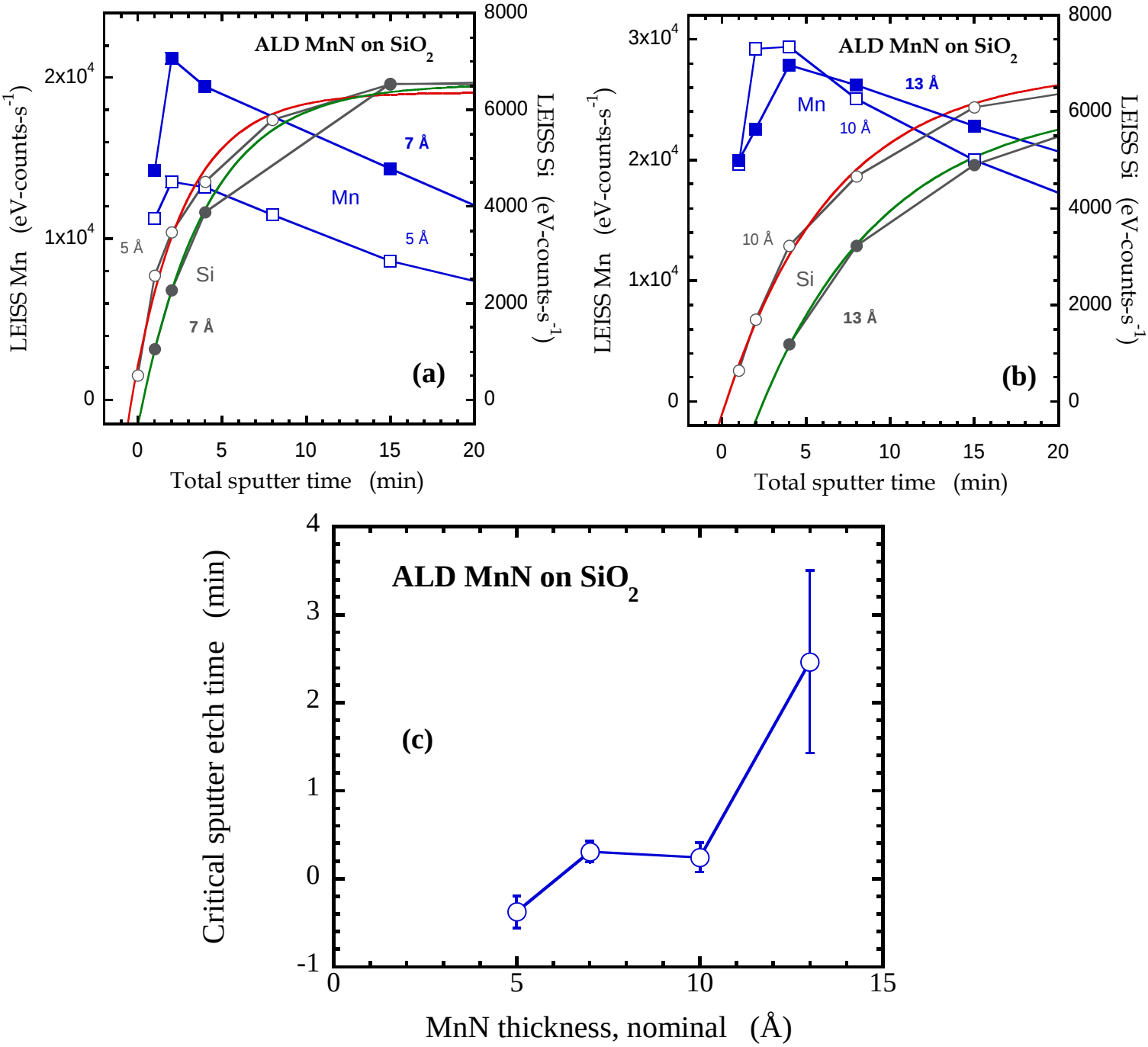

Figure 7 - 6 Integrated intensities of the LEISS Mn (thin film, left ordinate) and Si (substrate, right ordinate) peaks as a function of the total Ar^+ sputter etch time for **(a)** nominal 5 and 7 Å, and **(b)** 10 and 13 Å MnN ALD films on low-κ. Critical etch time to reveal substrate peaks are displayed in **(c)**.

7.2.5 Thick TaN_x on SiO_2 and Si

We examined the composition of two relatively thick thin films of TaN_x: One sample was 20 nm of ALD TaN_x on bare Si, another was 20 nm PVD TaN_x on SiO_2. We found significant differences in N content between ALD and PVD thin films. For the ALD TaN_x thin film we found that the ratio N:Ta was between 1.0 and 1.2 for as-received ALD sample. The upper limit in this case (1.2) assumes that atmospheric oxygen exchanges 1-for-1 with N in TaN_x. As the ALD TaN_x thin film is sputter etched we observed a continuous decrease in the ratio N:Ta, asymptotically approaching a value of ~ 0.5. At this time it is unclear if the decay in N:Ta with sputter etch time is intrinsic, or due to the preferential removal of N in the sputter etch process.

For the PVD sample we found values for the ratio N:Ta between 0.7 and 0.9 for as-received sample. Again the upper limit (0.9) assumes atmospheric oxygen exchanges 1-for-1 with N in TaN_x. Unlike the ALD thin film, we observed a rapid decay in the ratio N:Ta from 4 to 8 min of Ar^+ sputter etching, which could indicate the bulk of the TaN_x thin film is depleted of N.

These results are presented in Fig. 7-7 below.

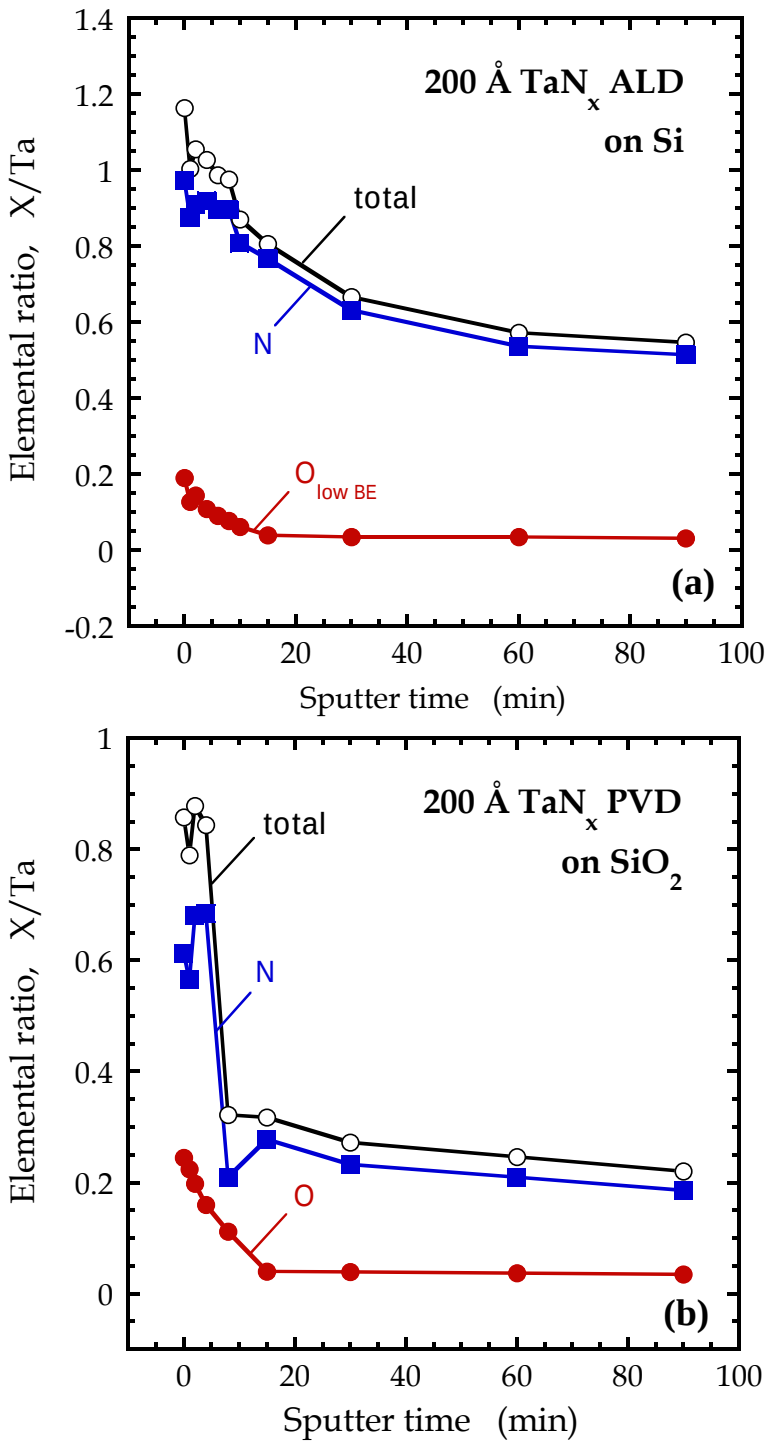

Figure 7 - 7 Calculated elemental ratios X / Ta (from XPS), for **(a)** 200 Å TaN_x ALD on Si and **(b)** 200 Å TaN_x PVD on SiO_2, where X can be either N (blue) or O (red) or N+O (total, black).

7.3 References

[1] J.R. Engstrom, *Personal Correspondence*.

[2] S.E. Roadman, N. Maity, J.N. Carter, and J.R. Engstrom, J. Vac. Sci. Technol. A **16**, 3423 (1998).

[3] K.J. Hughes and J.R. Engstrom, J. Vac. Sci. Technol. A **30**, 01A102 (2012).

[4] A. Satta, J. Schuhmacher, C.M. Whelan, W. Vandervorst, S.H. Brongersma, A. Vantomme, M.M. Viitanen, H. H. Brongersma and W. F. A. Besling, J. Appl. Phys. **92**, 12 (2002).

[5] W. Zhang, R.K. Nahm, P.F. Ma, and J.R. Engstrom, J. Vac. Sci. Technol. A **31**, 061101 (2013).

[6] W. Zhang, and J.R. Engstrom, J. Vac. Sci. Technol. A **34**, 01A107 (2016).